University of Lille
Graduate School of Biology and Health Sciences

UMR1167 - RID-AGE
«Risk factors and molecular determinants of aging-related disease»

Doctoral thesis for obtaining the degree of

Doctor of Philosophy of the University of Lille

In life and health science

Specialty: Molecular and cellular aspects of biology

Development of a 3D microfluidic in vitro model of pancreatic beta cells to mimic endocrine pancreatic function and study type 2 diabetes progression

by

Leonid Pliner

Publicly defended on December 6, 2024 in front of the jury composed of:

Pr Cécile Legallais Research director, CNRS, University of Technology of Compiègne	President of the jury
Dr Marie-Christine Durrieu Research director, Inserm, University of Bordeaux	Rapporteur
Pr Matthieu Raoux Professor, University of Bordeaux	Rapporteur
Dr Jean-Sébastien Annicotte Research director, Inserm, University of Lille	Director of thesis
Dr Anthony Treizebre Senior lecturer, University of Lille	Co-director of thesis

Université de Lille
Ecole doctorale Biologie-Santé de Lille

UMR1167 - RID-AGE
«Facteurs de risque et déterminants moléculaires des maladies liées au vieillissement»

Thèse de doctorat pour l'obtention du grade de

Docteur de l'Université de Lille

En science de la vie et de la santé

Spécialité : Aspects moléculaires et cellulaires de la biologie

Développement d'un dispositif in vitro microfluidique 3D de cellules bêta pancréatiques pour imiter la fonction endocrine du pancréas et étudier la progression du diabète de type 2

par

Léonid PLINER

Soutenue publiquement le 6 décembre 2024 devant le jury composé de:

Pr Cécile LEGALLAIS Research director, CNRS, University of Technology of Compiègne	Présidente du jury
Dr Marie-Christine DURRIEU Research director, Inserm, University of Bordeaux	Rapportrice
Pr Matthieu RAOUX Professor, University of Bordeaux	Rapporteur
Dr Jean-Sébastien ANNICOTTE Research director, Inserm, University of Lille	Director de la thèse
Dr Anthony TREIZEBRE Senior lecturer, University of Lille	Co-director de la thèse

Acknowledgements

Firstly, I would like to thank the jury members for taking part in my thesis defence. I am grateful to Professor Cécile Legallais for her valuable advices during the preceding CSI meetings and fruitful discussion during the defence. I am also extremely grateful to Professor Matthieu Raoux and Dr Marie-Christine Durrieu for taking their time to share their insightful and enthusiastic perspectives on my work in their reports. As accomplished scientists in their respective fields, my jury members are the people I look up to, and I saw my defence was a unique learning opportunity. It was a true honour and an enormous pleasure to present and discuss my thesis with them.

Secondly, I would like to thank my supervisors Dr Jean-Sébastien Annicotte and Dr Anthony Treizebre for providing their guidance and support to ensure that I can carry out my work in the most efficient way and have meaningful results. Despite this project not going in the anticipated direction with many obstacles encountered along the way, I am profoundly grateful to the dedication of my supervisors, who I could always rely on. I truly appreciate the time, enthusiasm and devotion, especially from Anthony. I am extremely grateful for each opportunity created for me by my supervisors to have a shot at getting as far as I can with this thesis. I am also incredibly happy to have defended with their help in preparation, and excited to start the next chapter of my life.

I would also like to thank the I-SITE ULNE PEARL programme coordinators Professor Frank Dumeignil and Mr Alexis Boulet as well as Marie Skłodowska-Curie EU Horizon 2020 research and innovation grant for providing me with such an exciting opportunity to take part in this mobility programme. I was impressed with how well everything was organised, despite the challenges faced at the beginning of the programme due to the sanitary crisis. Thanks to this programme I got to meet bright and talented fellow participants, with whom we had an exciting time during the doctoral training courses, which were useful, interesting and engaging. Also, I am extremely grateful to Mr Philippe Ducamp of EURAXESS for all the support with the administrative questions.

Additionally, I would like to thank the former members of UMR1283 for the warm welcome to the team, however short-lived. I thank Dr Cyril Bourouh, Dr Emilie Courty, Dr Flourine Barnaque and Ms Laure Rolland for teaching me the essential laboratory techniques and providing excellent advice during the scientific discussions. Furthermore, I would like to extend my gratitude to the members of UMR1167 for all their help and ever-present joyful mood, which has immensely brightened up my final year. My thanks also go to the BioMEMS team of IEMN, especially Ms Aude Sivery and Ms Marie Guilbert, who have delivered immeasurable help with microfluidics and cell culture, and with whom I enjoyed sharing the office. As well as this I would like to thank Mr Dickson Akoto for his hardworking attitude during his M1 internship. I extend my gratitude to all of the staff of IEMN.

As well as this, my huge thanks goes to the members of HCS Pharma. I deeply cherish the warm welcome to the team as well as all the support and resources availability, which was necessary for my work. I thank Dr Méryl Roudaut, Ms Vaihere Cheung, Dr Alejandra Mogrovejo Valdivia, Dr Elodie Vandenhaute, Mr Gaspard Delpouve, Dr Zied Sougir and of course Dr Nathalie Maubon for providing me with all the essential guidance concerning BIOMIMESYS® technology, teaching me the manipulation techniques and confocal image collection and processing. My thoughts are with you at these challenging times for the company and I wish you great success going forward.

I would also like to thank the fellow research collaborators, who were of incredible help for various aspects of my research activities. My special thanks goes to Dr Youness Carrout and the whole U1008 group for allowing me to use their facilities and teaching the required skills. Dr Carrout's guidance and scientific advice were invaluable for my work and I vastly esteem his input as well as his kindness. As well as this, I am deeply grateful to Dr Cedric Zobrist for his aid with rheological measurements, Mrs. Myriam Moreau for giving a hand with Raman spectroscopy, and Mr Antonino Bongiovanni for teaching me the spin-disc confocal microscopy. As well as this, I would like to thank Nathan Laneret for carrying out RNA isolation and qPCR. Also I would like to thank Dr Yannick Coffinier for his valuable insights during the CSI meeting as well as providing the resources and advice for my electrochemical activities.

I am also compelled to express my profound gratitude to the great teachers, who have encouraged my learning in the scientific fields at various stages of my education and who have inspired me to excel in my studies and choose the scientific career path. I thank my teachers, including Mrs Nina Trigub for her fun and engaging mathematics lessons, Mrs Elena Koshina for getting me to grasp and fall in love with physics, Mrs Zoya Sitnikova, Mrs Becky Miles and Dr Paul Hundal for structuring the foundations for my biology knowledge. I am also deeply grateful to the inspiring lecturers and scientists, including Dr Anthony Rossiter and Professor Mahdi Mahfouf for honing my interest in the most exciting engineering discipline — automated control systems, Professor Frederik Claeyssens and Professor Sheila MacNeil for promoting my aspiration to pursue practical skills in tissue engineering, biomaterial science and microfluidics, Dr Gavin Williams for introducing me to the Clean Room microfabrication and guiding my first steps in biosensor field, and of course, Professor Danny O'Hare for being a caring, charismatic and fascinating electrochemistry lecturer and supervisor.

Last, but certainly not least, I would like to thank my family and friends for the immense support that they have been giving me during some of the most challenging times in my life. I am profoundly grateful to my family for always believing in me, encouraging me and giving me all the opportunities in the world to fulfil my dream and become a scientist. Thanks, mom and dad, for constantly reminding me that where there's a will, there's a way. Thank you, grandma Lena, for your perpetual care and love, and grandpa Grisha for inspiring me to become a responsible and aspiring man and also for enabling my educational journey. I thank my best friends Pasha, Ted, Nick, Kolya, Yasha, Vlad B., Giuseppe, Marco, Kirill and Vlad V. for always having my back,

lightening up my mood and giving me relief even from far abroad. And of course, I am extremely grateful to have made such amazing friends as Andrea and Juanjo — we had an incredible time in Lille together and I'm looking forward for more memories with you.

“Don’t become a mere recorder of facts, but try to penetrate the mystery of their origin.”

Ivan Pavlov

“Is it not worth while […] to forget the selfish interests and to hope that in the end the good will benefit and survive, that throughout this continuous struggle for survival of the human race, through countless generations, progress will continue to be made, that we may still look forward in the end to a better world, a world where ills, both human and social, will be controlled, and where man, the best of man, will be the conqueror?”

Selman A. Waksman

Table of Contents

Résumé en Français

Le diabète de type 2 (DT2) se caractérise par une hyperglycémie persistante, due à une fonction (sécrétion d'insuline) et une masse (diminution de la prolifération ou sénescence accrue) inadéquates des cellules bêta du pancréas face à une résistance périphérique à l'insuline. La perte de masse et de fonction des cellules bêta joue un rôle majeur dans la pathogenèse du DT2. Contrecarrer cette perte représente une voie prometteuse pour des traitements alternatifs du DT2. Bien que plusieurs études aient démontré un effet délétère des tissus périphériques, y compris le tissu adipeux, sur les cellules bêta, les mécanismes moléculaires précis de ce dysfonctionnement lié à l'interaction des organes restent à découvrir.

Il est bien établi que la progression de la maladie résulte de la perturbation de la communication homéostatique entre plusieurs organes. Toutefois, les approches actuelles, comme l'expérimentation animale, ne permettent pas de définir avec précision les conséquences de ces interactions sur la physiologie et la maladie. Il est donc crucial de développer des modèles in vitro capables de récapituler ces interactions et d'identifier de nouvelles cibles thérapeutiques contre le diabète. Le développement de ces approches est également encouragé par la règle des 3R (Replace, Reduce, Refine) de la Commission Européenne (Directive 2010/63/EU) régissant l'utilisation des animaux.

Cette thèse s'est concentrée sur le développement d'outils in vitro imitant le microenvironnement pour modéliser la communication entre le tissu pancréatique et adipeux. Tout d'abord, des matrices extracellulaires synthétiques ont été utilisées pour faciliter la culture tridimensionnelle (3D) des cellules bêta, améliorant la pertinence du modèle par rapport à la culture en deux dimensions (2D), en fournissant des repères mécaniques. Une matrice hydrogel poreuse contenant des biomolécules clés, comme l'acide hyaluronique, le collagène et le motif de la fibronectine, a été synthétisée. Les échafaudages ont été évalués par des expériences rhéologiques et de relaxation sous contrainte pour caractériser leurs propriétés viscoélastiques et les comparer aux données des tissus biologiques. Leur composition chimique a été confirmée par spectroscopie Raman. La porosité a été étudiée par microscopie électronique. La fonctionnalité biologique a été évaluée avec des cellules MIN6 (cellules de souris sécrétant de l'insuline), en comparant la réponse à la sécrétion d'insuline, la viabilité et la prolifération en 3D par rapport à la culture standard en 2D.

Deuxièmement, plusieurs méthodes microfluidiques ont été développées pour imiter la circulation des nutriments par perfusion du milieu, incluant un modèle d'écoulement des fluides, un contrôle numérique, ainsi que l'estimation du volume et de la résistance du système. Le contrôle automatisé de la pression a permis d'alimenter en fluide les puces microfluidiques. Des puces commerciales et conçues sur mesure ont été utilisées.

Enfin, des tentatives ont été faites pour développer un réseau de biocapteurs permettant la surveillance continue du glucose et de l'insuline dans le système microfluidique. Des réseaux de

microélectrodes ont été fabriqués et caractérisés par des techniques électrochimiques, puis modifiés avec des flocons d'oxyde de graphène pour améliorer la détection des analytes.

En somme, ce travail pose les bases d'un modèle microfluidique 3D in vitro, qui pourra être développé pour étudier les événements moléculaires du DT2 dans un contexte de dialogue entre plusieurs organes.

Abbreviations

2D : two-dimensional

3D : three-dimensional

3Rs : Replacement, Reduction, and Refinement

ACC : acetyl-CoA carboxylase

ADH : hydrazide cross-linker

AFM: atomic force microscopy

AGE : advanced glycation end-products

AKT : protein kinase B

AMP : adenosine monophosphate

AMPK : adenosine monophosphate-activated protein kinase

ANOVA : analysis of variance

ATP : adenosine triphosphate

BSA : bovine serum albumin

CAD : computer automated design

CE : counter electrode

CMC : carboxymethyl cellulose cryogel

CNC : computer numerical control

CNS : central nervous system

COC : cyclic olefin copolymer

DAPI : 4',6-diamidino-2-phenylindole

DMSO : dimethyl sulfoxide

DNA : deoxyribonucleic acid

ECM : extracellular matrix

EDCI : carbodiimide reagent

ELISA : enzyme-linked immunosorbent assays

EPS : electric pulse stimulation

ESCs : embryonic stem cells

FAS : fatty acid synthase

FFA : free fatty acids

FGF19 : fibroblast growth factor 19

FGF21 : fibroblast growth factor 21

FOXO1 : forkhead box protein O1

G6Pase : glucose-6-phosphatase

GAGs : glycosaminoglycans

GCK : hexokinase-glucokinase

GIPR : glucose-dependent insulinotropic polypeptide receptor

GLP-1 : glucagon-like peptide-1

GLUT : glucose transporter

GO : graphene oxide

GSIS : glucose-stimulated insulin secretion

GWAS : genome-wide association studies

HA : hyaluronic acid

HFD : high-fat diet

HPA : hypothalamus-pituitary-adrenal

HPLC : high-performance liquid chromatography

HSL : hormone-sensitive lipase

HSPGs : heparan sulfate proteoglycans

HUVECs: human umbilical vein endothelial cells

IL-6 : interleukin 6

INSR : insulin receptor

IRS : insulin receptor substrate

KATP : ATP-sensitive potassium

KRB : Krebs buffer solution

LOD : limit of detection

LPL : lipoprotein lipase

LVR : linear viscoelastic region

MAPK : mitogen-activated protein kinase

MEA : microelectrode array

MEK-ERK1/2 : MEK–extracellular signal-regulated kinase1/2

MGWAS : metagenome-wide association study

MMP : matrix metalloproteinases

MTT : 3-(4,5-dimethylthiazol-2-yl)-2,5-diphenyltetrazolium bromide

NAD(P)H : nicotinamide adenine dinucleotide phosphate

NAFLD : non-alcoholic fatty liver disease

NKX6.1 : Nkx6 homeobox 1

OCR : oxygen consumption rate

OOC : organ-on-chip

OSTE+ : thiol–ene–epoxy

PC : poly(carbonate)

PDE3B : phosphodiesterase 3B

PDK1 : phosphoinositide-dependent kinase-1

PDMS : poly(dimethylsiloxane)

PDX1 : insulin promoter factor 1

PEG : poly(ethylene glycol)

PEPCK : phosphoenolpyruvate carboxykinase

PGC-α : co-activator peroxisome proliferator-activated receptor-γ coactivator α

PI3K : phosphoinositide-3-kinase

PID : proportional-integral-derivative

PIP3 : phosphatidylinositol-trisphosphate

PKA : protein kinase A

PKC : protein kinase C

PLA : poly(lactic acid)

PLGA : poly(lactic-co-glycolic acid)

PMMA : poly(methyl methacrylate)

PTFE : poly(tetrafluoroethylene)

PP2A : protein phosphatase 2A

RE : reference electrode

RGDS : arginine-glycine-aspartic acid

RNA : ribonucleic acid

SDK : software development kit

SEM : scanning electron microscope

SGLT2 : sodium-glucose transport protein 2

SPARC : Acidic and Rich in Cysteine

SREBP-1c : sterol regulatory element-binding protein 1c

T2D : type 2 diabetes

TAZ : transcriptional co-activator with PDZ-binding motif

TGF-β : transforming growth factor β

TIMP : tissue inhibitors of metalloproteinases

TR-FRET : time-resolved F√rrster resonance energy transfer

TSPs : thrombospondins

UKPDS : UK Prospective Diabetes Study

UV : ultraviolet

WE : working electrode

YAP : yes-associated protein

cAMP : cyclic AMP

hiPSCs : human pluripotent stem cells

mTORC1 : rapamycin complex 1

qRT-PCR : quantitative reverse transcription polymerase chain reaction

Table of Figures

1. Introduction

1.1 Diabetes type 2 and glucose homeostasis

1.1.1 Overview of type 2 diabetes

Type 2 diabetes mellitus (T2D) is a chronic metabolic disorder characterised by hyperglycaemia resulting from insulin resistance, inadequate insulin secretion, or both [1]. Insulin is produced in beta-cells, which are found in islets of Langerhans in pancreas, and is secreted in response to elevated blood glucose levels. It is a crucial molecule signalling to the organism's cells to uptake glucose from the blood, thus responsible for maintaining glucose homeostasis. In T2D, the organism's cells become less responsive to insulin, leading to reduced glucose uptake and utilisation. As a result, the pancreas initially compensates by increasing insulin production to maintain normal blood glucose levels. However, over time, the pancreas may fail to produce sufficient insulin to overcome the resistance, resulting in the decrease of beta-cell mass and persistently elevated blood glucose levels [2].

The prevalence of T2D has been increasing across the globe at an alarming rate in the recent years. According to the International Diabetes Federation, approximately 537 million adults (20-79 years) were living with diabetes globally in 2021. This number is projected to reach 643 million by 2030 and 783 million by 2045 [3]. Around 90% of these cases are attributed to T2D [4]. Interestingly, T2D prevalence varies across different regions and populations. In 2021, the Western Pacific region was reported to have the highest number of adults with diabetes (206 million), followed by the South-East Asia region (90 million) and the Europe region (61 million) [3]. Countries with the highest number of diabetic adults include China, India, and the United States [5] (Figure 1.1.1).

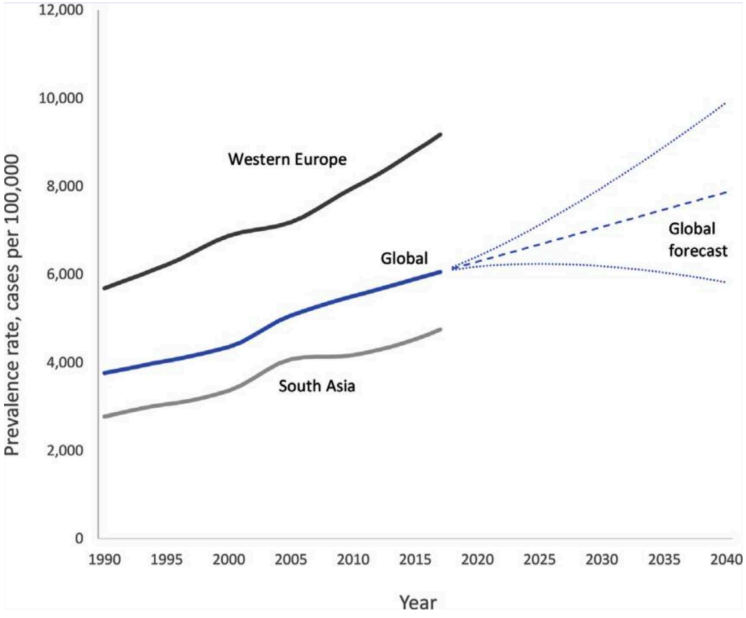

Figure 1.1.1 Epidemiology of T2D.
Adapted from Khan *et al.* 2020, [5].

Such growing rate of T2D prevalence poses significant health, social, and economic challenges globally. T2D is associated with numerous complications, including cardiovascular disease, neuropathy, nephropathy, and retinopathy [6]. These complications can lead to increased morbidity, disability, and premature mortality, which significantly impacts individuals' quality of life and imposes a substantial burden on the healthcare systems [7]. In 2021, diabetes caused an estimated 6.7 million deaths worldwide, with almost half of these deaths occurring in people under the age of 60. The global healthcare spending for diabetes was estimated at $966 billion in 2021, and this figure is expected to rise to $1054 billion by 2045 [3]. The economic burden of T2D is considered to extend beyond the direct medical costs, since the condition can also lead to lower productivity, absenteeism, and early retirement [8].

The increasing prevalence of T2D is driven by several factors, including genetic, population growth, ageing, urbanisation, and the rise in obesity and physical inactivity [9]. Obesity, in particular, is a major risk factor for T2D, with studies showing that the risk of developing T2D increases with increasing body mass index [10]. The adoption of sedentary lifestyles and the consumption of energy-dense, nutrient-poor diets have contributed to the global obesity epidemic and, consequently, the rise in T2D [11].

To address the global impact of T2D, it is required to take a multifaceted approach that involves prevention, early detection, and effective management. Lifestyle modifications, such as adhering to a healthy diet, engaging in regular physical activity, and maintaining a healthy body weight, are considered integral to prevent and manage T2D [12]. As well as this, early screening and diagnosis of T2D can enable timely intervention and the prevention of complications [13]. Furthermore, the effectiveness of T2D management depends on the access to affordable and quality healthcare, including medications, self-management education, and support [14].

At the time of writing this thesis, there exist multiple pharmacological antidiabetes agents, such as metformin, sulphonylures, incretin mimetics, dipeptidyl peptidase-4 (DPP-4) inhibitors, etc. However, these therapies are limited by lack of significant impact on the disease progression, and side effects, such as weight gain and hypoglycaemia [15]. Despite extensive research, the complexity of T2D and its multifactorial nature have hindered a complete understanding of the disease pathophysiology and hence limited the drug discovery [16]. Current research methods present a gap in combing large-scale population screening with more in-depth although less representative animal and *in vitro* models to the specific microphysiological characteristics and inter-organ causality of T2D. Therefore, there is a need for better insight into the progression of T2D.

Furthermore, the complexity of T2D implies that it remains necessary to identify new targets for the therapeutic agents at multiple levels of the pathological process. For this, all of the various aspects of T2D, including insulin resistance, insulin secretion, and glucose homeostasis — need to be addressed [17]. Therefore, there exists an increasing demand for efficient drug screening techniques to support the development and evaluation of new medications. These techniques include high-throughput screening, computer-aided drug design, and advanced *in vivo* and *in vitro*

models that can better replicate the complex physiopathology of T2D [18-20]. The development of innovative drug screening methods is crucial for accelerating the discovery of new therapeutic agents and ultimately improving the management and treatment of T2D [21].

1.1.2 Physiology of pancreatic islets of Langerhans

Pancreas is a spongy elongated gland located below the stomach, about 15 cm long and 2.5 cm thick (Figure 1.1.2A). It is both an exo- and endocrine organ responsible for the secretion of digestive enzymes and hormones regulating blood sugar levels. The endocrine function is performed by islets of Langerhans — spherical cell clusters, comprising about 2% of the pancreatic mass and uniformly scattered across the organ, often more highly present in the tail region [22] (Figure 1.1.2C). Islets maintain glucose homeostasis by controlling the blood glucose levels within a stable narrow physiological range, typically between 3.9-6.1 mmol/L in fasting conditions [1]. This is achieved through the production of hormones that regulate glucose uptake, production and utilisation across various tissues. The islets contain several cell types (Figure 1.1.2B), primarily β-cells producing insulin, α-cells producing glucagon, δ-cells producing somatostatin and other cell types. The corresponding distributions of these cells are around 50% beta, 40% alpha and 5% delta with the total cell number ranging from a few to 3,000 cells in a single pancreatic islet [22, 23]. The mean islet diameter has recently been demonstrated to be 108.92 μm [24].

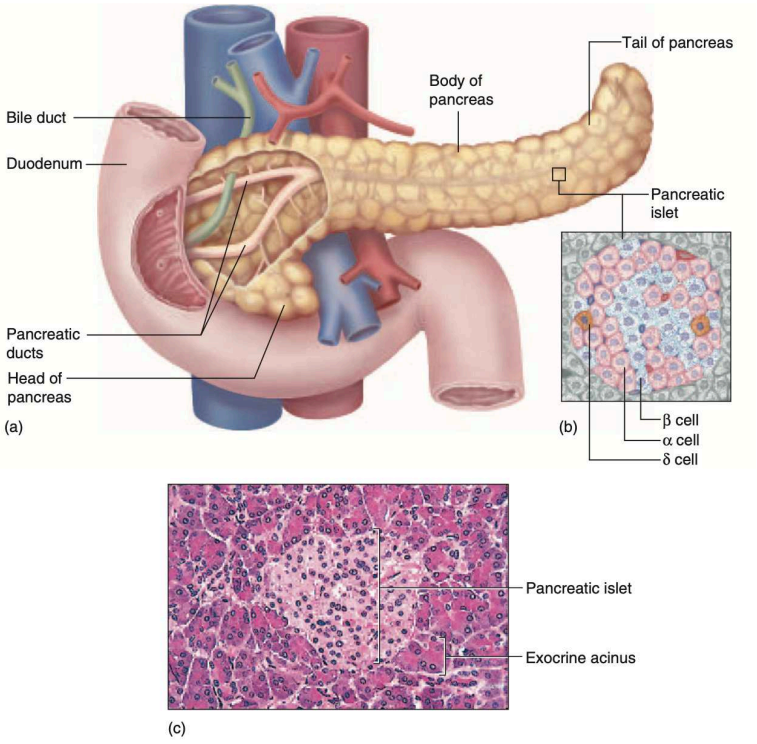

Figure 1.1.2 Physiology of islets of Langerhans.
A - diagram of pancreas and its positioning relative to duodenum and the surrounding organs. **B** - cell types in the pancreatic islet of Langerhans. **C** - histology of the pancreatic islet. Adapted from Saladin 2004 [22].

The islets of Langerhans are innervated by both sympathetic and parasympathetic systems, influencing glucagon secretion during hypoglycaemia. Sympathetic innervation plays a critical role in establishing and maintaining islet architecture and function, particularly in determining the localisation of non-β cells, which are essential for overall islet structure and function. Pancreas is also highly vascularised with an intricate network of blood vessels providing up to 20% of the pancreatic blood supply to ensure efficient oxygen and nutrient delivery to the islets as well as to facilitate the transport of the secreted hormones. Notably, the islets are exposed to the systemic and not the portal glucose concentration [23].

β-cells are polygon-shaped cells with an average diameter of 13-18 μm, containing approximately 10,000 secretory granules, each storing insulin at a concentration of around 1.6 x 10^{-18} mol. Glucose metabolism in β-cells is unique, allowing them to act as glucose sensors and adjust insulin secretion according to blood glucose levels (Figure 1.1.3). Glucose is transported into β-cells by the low affinity glucose transporters (GLUT) 1 and 2 as well as hexokinase-glucokinase (GCK). Consequently, glucose metabolism in mitochondria leads to an increase in intracellular adenosine triphosphate (ATP), which inhibits K^+ ATP sensitive channels, causing membrane depolarisation. This is followed by opening of voltage-gated L-type Ca^{2+} channels, allowing calcium influx and triggering the release of insulin [25]. The secretion pattern is observed in 2 phases, characterised by an initial transient response of pre-docked insulin granules and followed by a more sustained release, mobilising insulin reserve pool [26, 27].

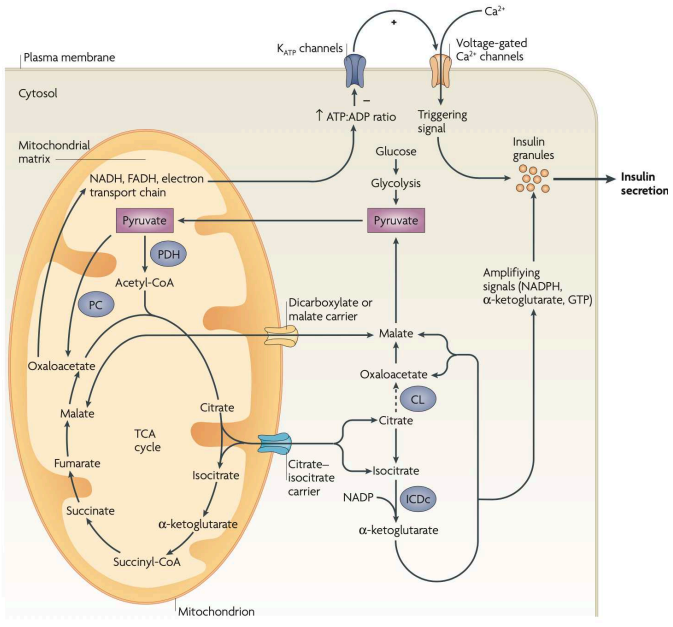

Figure 1.1.3 Insulin secretion by β-cells.
The diagram depicts the molecular mechanisms of glucose metabolism in β-cells, which trigger insulin secretion. Adapted from Mouio and Newgard 2008 [32].

Insulin secretion by the β-cells increases during and immediately following a meal in response to elevated blood glucose and amino acid levels. This hormone facilitates cellular uptake of these nutrients for storage or metabolism. Insulin enhances the synthesis of glycogen, fat, and

protein by preventing the release of glucose from liver, inhibiting the breakdown and secretion of fats and facilitating amino acid uptake to the muscle tissue, while counteracting the actions of glucagon [28].

The latter is secreted by the α-cells between meals when blood glucose levels decline. In the liver, glucagon stimulates glycogenolysis (the breakdown of glycogen) and gluconeogenesis (the synthesis of glucose), resulting in the release of glucose into the bloodstream. In adipose tissue, it promotes fat catabolism and the release of free fatty acids (FFA). Additionally, glucagon responds to elevated amino acids after a high-protein meal, promoting amino acid absorption for gluconeogenesis [28, 29]. Somatostatin secretion is upregulated by the δ-cells after the meal in order to regulate the digestion and to moderate the activity of the islets as a paracrine messenger [30].

1.1.3 Metabolic circuits

The activity of pancreatic islets affects function of multiple organs in the body. For instance, insulin exerts profound effects on metabolism by interacting with the cells in other organs through both direct and indirect mechanisms. These actions are mediated by complex signalling cascades in multiple tissues, primarily skeletal muscle, liver, and adipose tissue, with additional effects on the central nervous system and pancreatic α-cells. Generally, in target cells insulin physiological effects are mediated through the insulin receptor (INSR) which is a heterotetrameric receptor tyrosine kinase expressed on the cell membrane. When insulin binds to INSR, it triggers a conformational change that leads to autophosphorylation and activation of the receptor's kinase domains. Activated INSR recruits and phosphorylates various scaffold proteins, most importantly the insulin receptor substrate (IRS) family, which then activate downstream effectors such as phosphoinositide-3-kinase (PI3K). PI3K generates phosphatidylinositol-trisphosphate (PIP_3), which recruits and activates phosphoinositide-dependent kinase-1 (PDK1) and protein kinase B (AKT) — key nodes in the insulin signalling cascade. This signalling pathway (Figure 1.1.4A) is regulated by various feedback mechanisms and can be attenuated by receptor internalisation and dephosphorylation. The insulin signalling cascade branches into mitogenic and metabolic pathways, with the latter requiring lower insulin concentrations and being the focus of metabolic regulation in insulin-responsive tissues such as muscle, liver, and adipose tissue (Figure 1.14B) [31].

In skeletal muscle, insulin stimulates glucose uptake. This is triggered by translocation of GLUT4 glucose transporters from intracellular storage vesicles to the plasma membrane. The insulin signalling cascade begins with insulin binding to its receptor, triggering a series of phosphorylation events, regulating GLUT4 vesicle trafficking. This process, along with insulin-induced actin remodelling, promotes the translocation of the vesicles to the cell membrane, which in turn, facilitates glucose uptake [34]. Insulin also promotes glycogen synthesis in muscle by reducing inhibitory phosphorylation of glycogen synthase. This enzyme helps to convert glucose into glycogen [35]. Physical activity of muscles, in turn, has paracrine effects on other tissues through the release of exerkines. For instance, interleukin 6 (IL-6) enhances insulin secretion in

islets in response to glucose stimulus, as well as promoting lipolysis and fatty acid oxidation in fatty acids in adipose tissue and improving insulin sensitivity in liver. In addition to this, fibroblast growth factor 21 (FGF21) and irisin enhance β-cell function by promoting insulin gene expression, while also stimulating browning of white fat, increasing thermogenesis in adipose. In the liver, these exerkines regulate glucose metabolism and reduces hepatic lipid accumulation. Another factor secreted during exercise, myonectin, upregulates fatty acid uptake in adipose tissue and liver, reducing circulating lipid levels. This protects β-cell from lipotoxicity and improves their function by modulating insulin secretion [36].

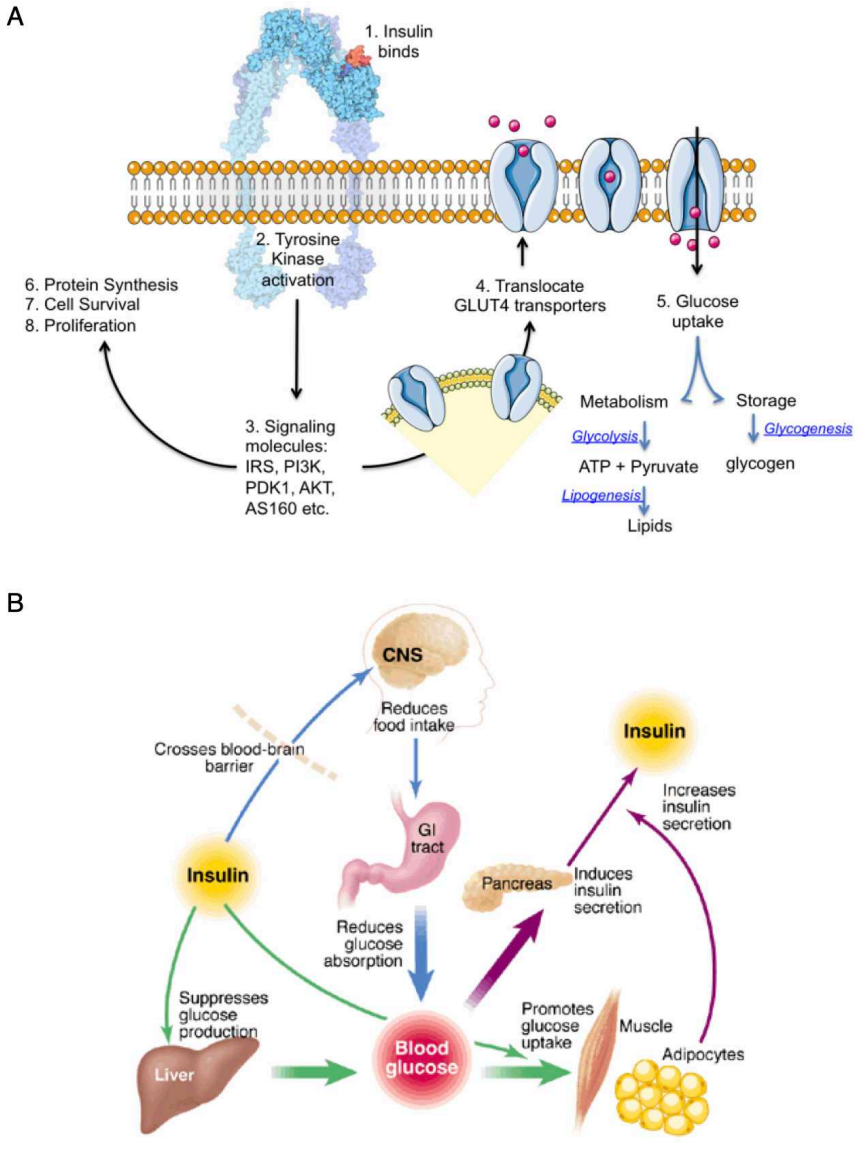

Figure 1.1.4 Insulin action.
A - mechanism of insulin action on target cells, triggering glucose uptake. Adapted from https://pdb101.rcsb.org/global-health/diabetes-mellitus/managing/non-pharmacological (visited on 05.09.2024). **B** - glucose homeostasis. Adapted from Riaz 2014 [33].

In the liver, insulin exerts multiple effects on hepatic glucose production and lipid metabolism. Directly, insulin inhibits the transcription of gluconeogenic enzymes like phosphoenolpyruvate carboxykinase (PEPCK) and glucose-6-phosphatase (G6Pase) by promoting the phosphorylation and nuclear exclusion of the transcription factor forckhead box protein O1 (FOXO1). Insulin also stimulates glycogen synthesis through mechanisms similar to those in muscle. As well as this, insulin promotes lipogenesis in the liver by activating the transcription factor sterol regulatory element-binding protein 1c (SREBP-1c). The latter upregulates genes involved in fatty acid synthesis, including acetyl-CoA carboxylase (ACC) and fatty acid synthase (FAS). Insulin also acutely activates ACC through dephosphorylation, likely via inhibition of adenosine monophosphate (AMP)-activated protein kinase (AMPK). Additionally, insulin stimulates protein synthesis in the liver through activation of the mammalian target of rapamycin complex 1 (mTORC1) pathway [37].

In adipose tissue, a critical action of insulin is the suppression of lipolysis. This occurs primarily through the activation of phosphodiesterase 3B (PDE3B), which degrades cyclic AMP (cAMP). Reduced cAMP levels lead to decreased protein kinase A (PKA) activity, resulting in reduced phosphorylation of hormone-sensitive lipase (HSL) and perilipin. HSL hydrolyses triglycerides stored in adipocytes into FFA, while perilipin coats lipid droplets. The action of insulin through PDE3B pathway is not completely determined, however it was shown to impede the lipolytic processes [31]. Furthermore, insulin stimulates glucose uptake in adipocytes through GLUT4 translocation, similar to the mechanism in muscle. As well as this, lipogenesis is promoted by insulin in adipocytes by activating SREBP-1c. This ramps up lipoprotein lipase (LPL) activity, facilitating the uptake and storage of circulating lipids [38].

A key indirect effect as a consequence of insulin action is the suppression of hepatic gluconeogenesis, regulated by adipose tissue lipolysis. By inhibiting lipolysis, insulin decreases the release of FFA and glycerol into the blood circulation. This has two major implications for hepatic glucose production. Firstly, reduced fatty acid availability leads to decreased activation of pyruvate carboxylase, a key gluconeogenic enzyme. Secondly, decreased glycerol availability limits substrate for gluconeogenesis, as glycerol is a direct gluconeogenic precursor [39].

Leptin is a hormone secreted by adipocytes in response to insulin. It acts in the brain, signalling for energy balance and metabolism. It suppresses the hypothalamus-pituitary-adrenal (HPA) axis and prevents lipolysis and gluconeogenesis during starvation and diabetic ketoacidosis. Leptin also has an antidiabetic effect by reducing glucagon secretion by α-cells [40]. Furthermore, leptin has been shown to positively influence β-cell activity by inhibiting insulin secretion via cAMP/PKA and phospholipase C/protein kinase C (PKC) pathways [41, 42], promoting proliferation and inhibiting apoptosis by increasing fatty acid oxidation [43].

Adiponectin is another adipose-secreted hormone involved in glucose homeostasis. It promotes fatty acid oxidation and glucose uptake, while suppressing gluconeogenesis in muscle and liver. Current research on adiponectin action on pancreatic cells is conflicting. On the one hand, adiponectin promotes insulin secretion by increasing the exocytosis of insulin granules, at

the same time promoting β-cell differentiation. However, its effect on insulin secretion appears to be dual, depending on the existing glucose concentration. Additionally, adiponectin exhibits anti-apoptotic effects by activating PI3K-Akt and MEK–extracellular signal-regulated kinase1/2 (MEK-ERK1/2) pathways. However, it is still uncertain whether adiponectin directly activates AMPK in β-cells [44].

In the pancreas, insulin acts on the α-cells to suppress glucagon secretion, which serves as another indirect mechanism for reducing hepatic glucose production. This occurs through activation of PI3K and phosphodiesterase-mediated degradation of cAMP in α-cells, similar to insulin's action on adipocytes. The resulting decrease in PKA activity leads to reduced exocytosis of glucagon-containing granules [45].

Glucose metabolism has long been recognised to be also regulated by the central nervous system (CNS). Insulin plays a significant role in appetite suppression by crossing the blood-brain barrier and acting on neurons and glial cells. Deletion of neuronal insulin receptor gene *Insr* in mice was demonstrated to lead to obesity and hepatic insulin resistance, emphasising insulin's role in appetite modulation [46]. CNS insulin signalling also affects peripheral metabolism. For example, intracerebroventricular insulin can suppress hepatic glucose production in rodents and nasal insulin enhances this suppression in humans [47, 48]. However, physiological increases in brain insulin levels do not consistently affect hepatic glucose production across species, and mechanisms linking insulin action on CNS and peripheral insulin action remain unclear [31].

The gut-brain-liver axis further regulates glucose metabolism, with gut-derived hormones like incretins or fibroblast growth factor 19 (FGF19) enhancing glucose tolerance via HPA axis suppression [49]. As well as this, the gut microbiome may influence CNS control of insulin action through mechanisms such as acetate production, which stimulates insulin secretion. Studies in rodents suggest that gut nutrient sensing impacts CNS regulation of metabolism, though similar mechanisms in humans remain to be confirmed [50, 51]. Overall, CNS regulation of glucose metabolism involves complex, integrated mechanisms with potential therapeutic implications, especially for conditions like diabetes and obesity.

1.1.4 Metabolic disorders and type 2 diabetes

Evidently, pancreatic endocrine signalling acts on multiple organs, which in turn triggers feedback signalling from those organs to regulate pancreatic action. The disruption of these processes can result in several metabolic disorders influencing multiple systems in the organism. T2D is considered to be a multi-organ homeostatic failure, with symptoms manifesting in pancreas, liver, muscles, adipose and other tissues.

In pancreas, during T2D, β-cells undergo several significant changes, impacting their survival and function. Firstly, a progressive loss of β-cell mass is often observed. This is a consequence of decreased cell proliferation and increased apoptosis [52] and actual reduction of cell mass. The origins for apoptotic pathway include: glucotoxisity caused by elevated blood sugar levels [53], lipotoxicity caused by elevated FFA circulation [54] and inflammation caused by signalling of inflammatory cytokines [55]. Furthermore, a decreased electrical activity of the β-

cells is observed during T2D. This is attributed to the disruptions in sensitivity of ATP-sensitive potassium (KATP) ion channel, efficiency of Ca^{2+} influx and mitochondrial function — which leads to impaired membrane depolarisation and, consequently, insulin secretion ability [56-58]. In addition to this, the biphasic activity of the β-cells is disrupted in T2D. The first rapid phase is often lost, while the second sustained phase appears diminished. This is linked to several factors, such as: reduction of insulin granule pool, reduced sensitivity to glucose, changes in incretin expression and impaired exocytosis [59-62].

One of the precursors of T2D can be the loss of sensitivity to insulin in several organs, known as insulin resistance (Figure 1.1.5). This condition is characterised by an impaired ability of target tissues to respond normally to insulin, resulting in decreased glucose uptake, reduced suppression of endogenous glucose production, and impaired lipolysis suppression. This typically leads to compensatory hyperinsulinemia by the β-cells, creating an amplified feedback loop, that can eventually result in β-cell failure and T2D. It is currently regarded that insulin resistance occurs due to a combination of both decreased INSR expression in the target cells and impaired insulin signal transduction [31]. Recent research has identified mechanisms for active regulation of surface insulin receptor expression, such as the ubiquitin ligase MARCH1, which may play a role in insulin resistance [63]. Overall, the understanding of insulin resistance has evolved from a focus on receptor binding to a more complex model involving defects in multiple aspects of insulin signalling and action.

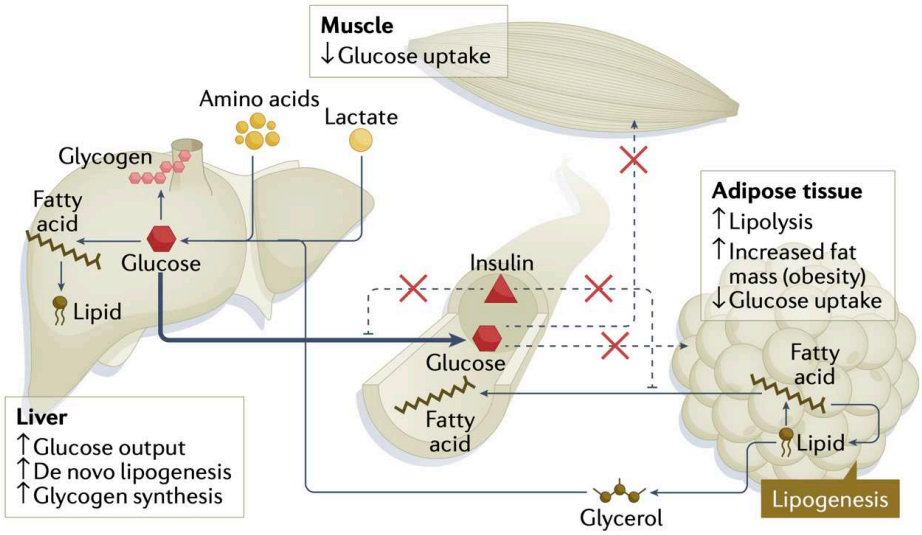

Figure 1.1.5 Insulin resistance.
Diagram depicting the complex inter-organ glucose homeostasis disruption as a result of insulin resistance. Adapted from James *et al.* 2021 [64].

Skeletal muscle insulin resistance affects insulin-stimulated glucose uptake controlled by GLUT4 translocation. This resistance significantly impacts whole-body glucose turnover, as skeletal muscle is a major site of insulin-stimulated glucose disposal. Research has shown that the primary defect in muscle insulin resistance lies in glucose transport, which consequently affects glycogen synthesis and glycolysis [65]. The underlying mechanisms involve defects in the insulin

signalling cascade, particularly at the levels of the INSR, IRS1, PI3K and AKT. Decreased INSR tyrosine kinase activity, reduced surface INSR content, and impaired IRS1 tyrosine phosphorylation are observed in insulin-resistant muscle [66]. Blunted insulin stimulation of IRS1-associated PI3K activity is also consistently observed. While distal effectors like AKT often show impaired activation in muscle insulin resistance, it's unclear whether these are independent defects or secondary to proximal signalling impairments. Interestingly, insulin resistance in skeletal muscle does not affect mitogenic signalling through mitogen-activated protein kinase (MAPK) [31]. Further research is needed to fully understand the relative contributions of specific signalling defects to impaired insulin-stimulated glucose uptake in muscle.

Insulin resistance in liver disturbes the balance between the gluconeogenesys, glycogenolysis and glycogen synthesis, leading to increased hepatic glucose production. INSR signalling cascade is disrupted, while alterations occur in transcriptional regulation. FOXO1 remains active in insulin-resistant hepatocytes, promoting the expression of PEPCK and G6Pase, which increases gluconeogenesys [67]. Similarly, glucose production is ramped up as a result of increased activity of the transcriptional co-activator peroxisome proliferator-activated receptor-γ coactivator 1α (PGC-1α) [68]. As well as this, elevated net lipogenesis in liver is observed during insulin resistance. Accumulation of intrahepatic lipids, particularly ceramides, leads to interference with insulin signalling due to activation of protein phosphatase 2A (PP2A), which dephosphorylates and inactivates AKT [31]. This lipotoxicity-induced insulin resistance is often associated with non-alcoholic fatty liver disease (NAFLD), a common comorbidity in T2D [69].

Similar to muscle and liver, the insulin receptor tyrosine kinase activity is reduced in insulin-resistant adipocytes. Normal action of insulin to inhibit lipolysis is impaired. As a result, an increase of lipolysis is observed, despite the presence of insulin. However, the causality and precise molecular mechanisms of adipocyte insulin resistance remain largely unexplained. For instance, it is unclear whether insulin resistance in suppressing adipose lipolysis is mainly due to increased lipolysis, decreased re-esterification of fatty acids, or both. [31]. Also, in insulin-resistant conditions, adipokine secretion by the adipocytes is altered, which further promotes insulin resistance in other organs. Reduced production of adiponectin as well as increased secretion of leptin, glycerol FFA is observed. This negatively impacts insulin secretion by the β-cells and glucose uptake in other organs [70]. Elevated leptin may also may lead to leptin resistance in other organs, which not only further exacerbates glucose homeostasis disruption, but also may result in obesity [71].

Obesity itself is one of the major risk factors related to T2D. It has long been established that the abundant fatty acid circulation in blood negatively influences glucose control and promotes insulin resistance [72-74]. Molecules such as leptin, adiponectin, chemerin, omentin and vaspin are involved in insulin-dependent regulation of adipose tissue and can be important in linking obesity and T2D [75]. Obesity has been shown to lead to pancreatic exhaustion affecting β-cell life cycle and insulin secretion thus leading to T2D development [76]. However, the specific molecular changes inducing insulin resistance in adipocytes are largely unestablished [31].

Therefore, there exists a gap in the current understanding of the islet-adipose cross-talk and the particular molecular event sequences at the core of T2D progression.

Pancreatic islets play central role in glucose homeostasis and insulin regulation, and therefore it is crucial to understand their microenvironment, when considering the metabolic disorders. Pancreatic tissue function is influenced by the structure of the extracellular matrix (ECM), which surrounds the islets and provides them with structural and biochemical support.

1.2 Extracellular matrix in pancreas

1.2.1 Structure and composition of pancreatic tissue

Pancreatic ECM is characterised as loose connective tissue, comprised of reticular and collagenous fibres coated with glycoproteins, that form an interconnected network between each other and the cells. Collagens, laminins and fibronectin — are the main constituent proteins of the pancreatic ECM ensuring mechanical stability, flexibility and adhesion [22]. The ECM composition in the pancreas is dynamic and varies between different regions and during different physiological and pathological states. Adult human islets *in vivo* are suspended in incomplete capsules made up of a single layer of fibroblasts and their associated collagen fibres. This capsule forms the periinsular basement membrane (Figure 1.2.1A and C), in which the islets are surrounded by the ECM and acinar cells. Within the islet, the extensive microvasculature is associated with its own perivascular basement membrane (Figure 1.2.1B) [77].

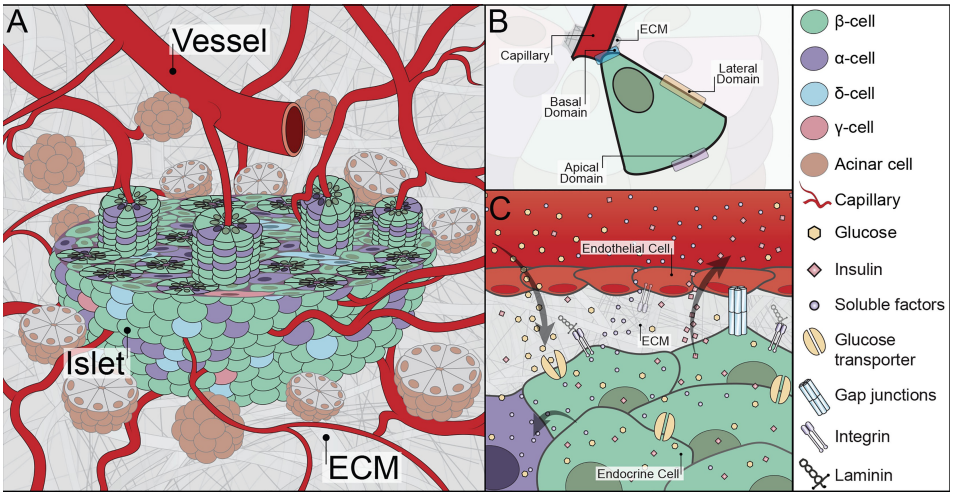

Figure 1.2.1 Structure of islet tissue.
A - illustration of periislet membrane. **B** - illustration of organisation of a vascularised islet. **C** - illustration of cell-cell and cell-matrix interactions in islet tissue. Adapted from Patel *et al.* 2022 [78].

Collagens are structural fibrous proteins and they are the most abundant proteins in the pancreatic ECM. Type I and IV collagens are predominantly found in the interlobular regions,. Type IV collagen forms planar hexagonal non-fibrillar networks in the basement membrane [77]. Type V and VI collagens are also present in smaller quantities. These fibrillar proteins and their arrangement dictate the tensile strength of the tissue, provide a scaffold for cell adhesion and

regulate cell fate [79]. While less abundant than in other organs, elastin fibres also contribute to the elasticity of pancreatic tissue, particularly in blood vessels and ducts [22].

Fibronectin is an adhesive glycoprotein, that is widely distributed throughout the pancreatic ECM and it plays a crucial role in cell-matrix adhesion. It contains multiple binding domains for other ECM structural components and cell surface receptors, such as arginine-glycine-aspartic acid (RGDS) cell adhesion motif, thus facilitating cellular attachment to the ECM [80]. In fibronectin, the RGD sequence appears as an extended, flexible loop situated between two β-strands. The cells use heterodimeric transmembrane protein receptors, known as integrins, to mediate binding to RGDS [77].

Laminins are cross-shaped heterotrimeric adhesive glycoproteins, consisting of three polypeptide chains linked by disulfide bonds. Akin to the fibrobectin, they are essential components of the basement membrane, forming networks that interact with cell surface receptors. In the pancreas, laminin-111 and laminin-332 are particularly important for maintaining the structural integrity and shape of acini and islets [81].

Glycosaminoglycans (GAGs) are also integral components of the pancreatic ECM. These molecules are comprised of linear disaccharide chains, glucosamine and uronic acid. Hyaluronic acid (HA), a non-sulfated GAG, is abundant in the ECM of pancreatic islets. HA interacts with cell surface receptors like CD44, influencing cell behaviour, such as Ca^{2+} signalling and tissue remodelling [82, 83]. Similarly, the disaccharide chains form covalent bonds with core proteins to produce structures known as proteoglycans. The examples of such are heparan sulfate proteoglycans (HSPGs), including perlecan and agrin, — crucial components of the intracellular basement membrane. HSPGs play vital roles in growth factor sequestration and presentation, affecting cellular signalling and differentiation [84, 85].

Matricellular proteins, including thrombospondins (TSPs), tenascins, and Secreted Protein Acidic and Rich in Cysteine (SPARC), are important regulators of cell-matrix interactions during the development of the pancreas. TSP-1 and TSP-2 are expressed in the pancreas and regulate cell-matrix interactions, angiogenesis, and transforming growth factor β (TGF-β) activation [86]. Tenascin-C is expressed during pancreatic organogenesis and is upregulated in inflammation and cancer. It modulates cell adhesion and migration, influencing tissue remodelling by interacting with cell surface receptors and other ECM components [87]. SPARC regulates collagen and fibronectin assembly and influences cell-ECM interactions by promoting growth factor signalling during tissue remodelling and repair [88].

ECM remodelling enzymes play a crucial role in maintaining the dynamic nature of the pancreatic ECM. Matrix metalloproteinases (MMP), including MMP-2, MMP-9, and MT1-MMP, are secreted by pancreatic satellite cells. These enzymes degrade ECM components, facilitating tissue remodelling and cell migration [89]. Tissue inhibitors of metalloproteinases (TIMP) regulate MMP activity and are crucial for maintaining ECM homeostasis [90].

Thus, the pancreatic ECM is a rather complex structure, comprised of diverse macromolecules. The ECM is important for both structural support and functional regulation of

cellular processes in the islets of Langerhans. Understanding the molecular composition and organisation of the pancreatic ECM is therefore essential for determining its influence on pancreatic function during the disease progression. There is an opportunity for research focusing on the interactions between specific ECM components and pancreatic cells to broaden our knowledge of pancreatic biology and to find potential therapeutic targets for pancreatic disorders, such as pancreatic cancer, T1 and T2D.

1.2.2 Significance of the ECM

ECM plays a crucial role in tissue development and function. It provides not only structural support, but also mechanical and chemical cues for the cells, regulating cellular behaviour, growth and differentiation through dynamic binding to the cells [91]. The influence of ECM on pancreatic islet cell differentiation, attachment and proliferation has long been known [92]. The key interactions between the ECM molecules and cells occur through integrin receptor binding. The latter facilitates mechanotransduction — the process of cell converting mechanical stimulus into the electrochemical activity and signalling cascades, influencing regulation of gene expression and transcription factors [79]. In addition to this, integrins are linked to the intracellular cytoskeleton via a series of anchoring molecules, thus bridging it to ECM (Figure 1.2.2). Cytoskeleton is in turn connected to the nuclear envelope, hence mechanical signal can be transferred directly to the nucleus. Mechanical stimulus can therefore can affect the survival, growth and differentiation of cells [93-95].

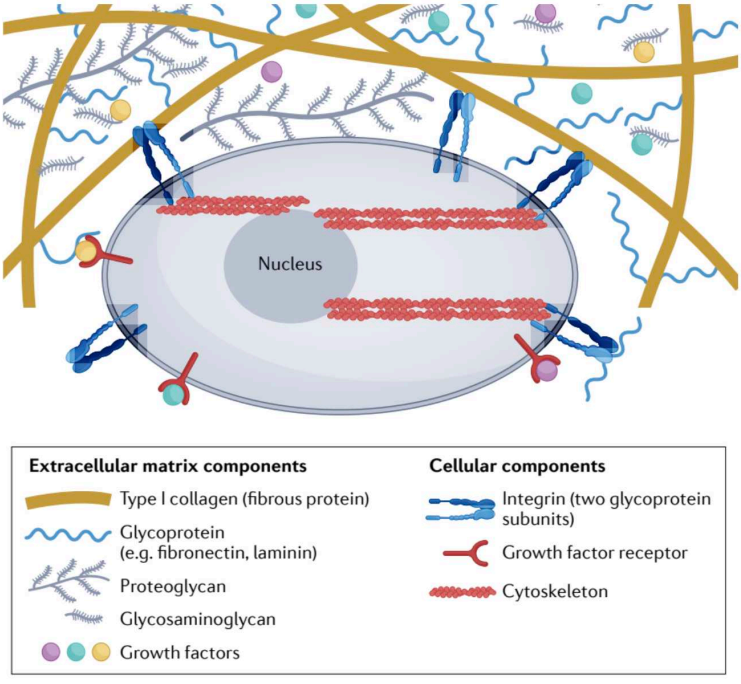

Figure 1.2.2 Cell-matrix interactions.
The diagram illustrating cell attachment to the macromolecules of ECM. Adapted from Lou and Mooney 2022 [95].

One of the mechanotransduction mechanisms in cells involves mechanosensitive ion channels, such as PIEZO1. This membrane protein converts the mechanical forces, such as shear stress or stretch into electrical signals, by non-selectively activating the flow of Ca^{2+}, K^{+} and Na^{+} ions across the cell membrane [96, 97]. In pancreatic β-cells, PIEZO1 together with its agonist, Yoda1 [98], have been linked to insulin secretion, since membrane depolarisations triggered by PIEZO1 lead to activation of voltage-gated Ca^{2+} channels, which in turn stimulate insulin release. At the same time, PIEZO1 expression was found to be increased in T2D patients and diabetic mice models, with notable translocation of the protein from membrane to nucleus, which has lead to dysregulation of insulin response to high glucose stimulation [99].

The mechanical forces can be also transduced into biochemical signals via soluble regulatory factors, such as Yes-associated protein (YAP) and transcriptional co-activator with PDZ-binding motif (TAZ). The YAP/TAZ signalling pathway is a key mediator of mechanotransduction, with its activity closely linked to substrate stiffness and cytoskeletal tension. YAP and TAZ function as mechanosensors, translating mechanical cues from the extracellular environment into transcriptional changes. YAP/TAZ localisation and activity were demonstrated to be regulated by ECM stiffness and cell shape. On stiff substrates, YAP/TAZ localise to the nucleus and are transcriptionally active, while on soft substrates, they are sequestered in the cytoplasm and inactive [100]. This mechanism has been shown to play an important role in pancreatic development. For instance, YAP is highly expressed in pancreatic progenitors and its expression decreases as differentiation progresses. Inactivation of YAP was found to be necessary for proper endocrine cell differentiation [101, 102]. This is because YAP directly regulates key pancreatic transcription factors, including insulin promoter factor 1 (PDX1), which is crucial for β-cell development and function [103].

Interestingly, mechanical cues have also been shown to influence cell metabolism by modulating mitochondrial dynamics and function through cytoskeletal interactions [104]. Mitochondria are organised into dynamic networks within the cells and their shape is dictated by the two antagonistic mechanisms: fission and fusion. The first leads to fragmentation of the mitochondria into smaller round-shaped organelles, while the second — to connection and elongation [105]. These processes are typically triggered by the energy demand and supply, however, a link to mechanotransduction mechanism also exists, since the cytoskeletal interactions with actin filaments and microtubules also influence the shape and positioning of the mitochondria [106, 107]. Recent studies involving proteomic analysis of β-cells cultured on nano-topographic surfaces demonstrated strong effects of the mechanical cues on the calcium dynamics, mitochondrial structure and metabolic activity via remodelling of the actin cytoskeleton. In particular, the nanostructure surfaces influenced the increased calcium handling protein expression, decreased cristae formation, upregulated mitochondrial fusion and downregulated fission proteins. All of these changes have implications on the insulin secretion in the β-cells [108, 109].

The role of ECM is increasingly recognised as an important factor in the pathophysiology of T2D. One of the key observed changes during the disease, is the increased deposition of collagen type I and III, leading to fibrosis. This impairs islet cell communication and reduces vascularisation, affecting nutrient and oxygen supply to β-cells [110]. The altered ECM composition disrupts integrin signalling, leading to decreased cell adhesion and impaired insulin secretion [111]. Additionally, chronic hyperglycemia contributes to the accumulation of advanced glycation end-products (AGE) in the pancreatic ECM, causing β-cell dysfunction and apoptosis [112, 113]. Excessive HA content in the diseased ECM also plays a role in islet inflammation by recruiting and activating immune cells [114]. The understanding of these changes provides insights for new therapeutic strategies, such as targeting ECM remodelling enzymes in T2D drug development, or using ECM-mimetic materials for islet transplantation and β-cell preservation in type 1 diabetes (T1D) management.

Consequently, the positive impact of ECM on islet survival and function has been taken advantage of in T1D research. T1D is an autoimmune disorder during which the β-cells are targeted by the host's immune system. The condition is most commonly treated with an artificial pancreas, which injects doses of exogenous insulin into the patient's bloodstream, calculated based on blood glucose measurements [115]. As an alternative, islet transplantation aims to restore endogenous insulin secretion of the T1D patient. However, the need for improving the success rate of islet transplantation has lead to the development of 3D encapsulation methods, which provided isolated islets with biomechanical cues for prolonged insulin secretion and viability. Different matrix engineering approaches, such as polymer scaffolds, protein hydrogels and decellularised matrices — have been investigated.

Synthetic polymer matrices, such as poly(ethylene glycol) (PEG), poly(lactic acid) (PLA), and poly(lactic-co-glycolic acid) (PLGA) were historically used as a standard bio-inert tissue engineering solution to encapsulate the islets. These materials are suitable for transplantation thanks to their controlled degradation profiles, non-adherent nature, lacking natural interactions with cells, and low toxicity. They prevent protein absorption and cell-mediated degradation, making them suitable for long-term islet encapsulation [116-120]. As an alternative to the synthetic materials, natural-derived polysaccharides, such as agarose and alginate — have also been used for 3D islet cultures [121, 122]. Despite their highly customisable mechanical properties, such hydrogels often fail to replicate the biochemical complexity of the native ECM, which ultimately limits their ability to mimic the *in vivo* behaviour of islet cells through integrin binding interactions. As a consequence of their non-adhesive nature, apoptosis can be induced in the encapsulated cells over prolonged culture durations [123, 124].

To address this problem, Daoud *et al.* showed that incorporating ECM components like collagen and laminin significantly enhanced the survival and functionality of human islets *in vitro* [125]. Similarly, Nagata *et al.* found that rat islets cultured in an ECM-derived scaffold exhibited improved insulin secretion, in contrast to classic 2D culture [126]. Hydrogels composed of discrete soluble ECM components, such as laminin, nidogen, collagen I, III, and IV, mimic the

native peri-islet ECM [127-130]. These hydrogels preserve islet function and suppress cell death. These functionalisation strategies can be useful in developing novel 3D *in vitro* islet models for T2D research. However, challenges arise due to the artificial assembly of ECM proteins, which may not fully replicate their native conformations. For instance, collagen IV requires laminins and nidogens for proper chain assembly. Therefore, there remains a need for a more integrated and biomimetic approach that combines essential structural and functional elements of the ECM to improve the efficacy of these models.

In contrast to the bottom up synthesis of scaffold materials, there exists a top down approach, which involves the use of decellularisation of the native ECM. The encapsulation of islets within decellularised hydrogels has been shown to sustain insulin secretion function [131-133]. These hydrogels naturally contain a broad spectrum of biomolecules, peptides, and growth factors, therefore providing a complex and native-like microenvironment for islet culture, that impacts islet behaviour. Furthermore, such scaffolds have been shown to support the differentiation of stem cells into insulin-producing β-cells, making them a suitable *in vitro* model of pancreas for T2D research [134, 135]. Recently, several works were reported by Kim *et al.* describing novel bioprinting approaches for *in vitro* islet reconstruction, involving decellularised ECM inks [136, 137]. However, the careful processing decellularised ECM remains a challenge, as the cell removal protocols can disrupt ECM integrity and affect hydrogel properties [138].

In addition to chemical composition, the mechanical properties of a biomimetic matrix should be considered. Thanks to its diverse composition and structure, ECM exhibits viscoelastic mechanical properties — consisting both of solid and liquid phase and capable non-linear response to progressive loading in addition to characteristic transient dissipation of applied constant strain (stress-relaxation) [139]. The rate of stress-relaxation by ECM as well as its stiffness are unique for each tissue type, accommodating the tissue function. Dissimilar microenvironment can negatively impact the functionality and viability of β-cells and adipocytes. Hence, when engineering a matrix for *in vitro* model pancreatic tissue, it is important to match the corresponding mechanical properties of the native tissue [95, 140].

The complexity of pancreatic ECM and its impact on β-cell function need to be acknowledged in the research of the T2D progression. Various research methodologies, including human studies, animal models, and cell culture techniques, have been employed to investigate the pathophysiology of T2D. The consideration of ECM impact on the β-cells in these models is important in order to improve the physiological relevance and therefore results interpretation.

1.3 Overview of research approaches for diabetes pathology

1.3.1 Human studies

Human studies mainly focus on large population screening aiming to determine the risk factors leading to T2D as well as the effective prevention and treatment strategies. For example, a large study in 2007 established a risks score for T2D development in German population, using

non-invasive methods linking to lifestyle (diet, activity, habits, history of hypertension and physical appearance) [141]. By analysing data from 84,941 female nurses from 1980 to 1996 Hu *et al.* has shown that overweight or obesity, lack of exercise, poor diet quality, smoking and alcohol consumption were independently associated with increased risk of T2D in women [142]. Another landmark multicentre clinical trial by Knowler *et al.* demonstrated that lifestyle intervention or metformin could prevent or delay the onset of T2D in high-risk individuals with impaired glucose tolerance. This study enrolled 3,234 participants and found that lifestyle intervention reduced the incidence of T2DM by 58% compared to placebo, while metformin reduced it by 31% [12]. Also, metagenome-wide association study (MGWAS) of gut microbiota deoxyribonucleic acid (DNA) sequencing analysis by Qin *et al.* has reported distinct differenced in gut microbiota of T2D-diagnosed and healthy individuals [143].

As well as this, T2D is explored in the context of genetic inheritance. Thus, it has been established that the risk of developing T2D for the individuals with 1 parent affected was 40%, while for those with both parents affected — 70%. Interestingly, there's a stronger case for inheriting the condition from mother rather that from father [144, 145]. A recent twin pair genotyping and phenotyping study has demonstrated a strong heritability of T2D [146]. Several meta-analysis articles, including genome-wide association studies (GWAS) helped identifying the specific genes involved [147, 148]. A landmark study by Scott *et al.* [149] analysed data from 26,676 T2D and 132,532 control individuals and identified 128 independent T2D risk variants. Nevertheless, the extent of influence of hereditary versus epigenetic factors is yet to be established.

Additionally, T2D management strategies have also been studied in the context of cardiovascular disease, which is a complication of T2D [150]. Thus, the UK Prospective Diabetes Study (UKPDS) was an important trial that established how glycemic control played a critical role in reducing microvascular complications of T2D [151]. Recently, cardiovascular outcome trials have demonstrated the benefits of antidiabetic agents. The EMPA-REG OUTCOME trial showed that empagliflozin, an inhibitor of sodium-glucose transport protein 2 (SGLT2), reduced the mortality in T2D patients who had been diagnosed with cardiovascular disease [152].

Furthermore, personalised approaches to T2D management are emerging. ADOPT trial compared the long-term glycemic effects of different antidiabetic agents and found that the results were dependent on patient-specific characteristics, indicating the need for tailored therapy [153]. This finding was supported by the PREDICT1 study, which has identified large inter-individual variability between patients' responses to identical meals. The results of this trial have highlighting the advantages of personalised nutritional algorithms for T2D management [154].

1.3.2 Animal studies

Additionally, there exists a number of animal models for pharmacological and pathophysiological T2D research, ranging from smaller sized animals, such as zebra fish and rodents, to large sized animals, such as pigs and primates. While small animal studies benefit from low cost, ability for genetic manipulation and relatively high throughput, the physiology and

anatomy are distinct from human. On the other hand, large animals offer better relevance to humans in terms of physiology and pharmacokinetics, nevertheless presenting higher costs and much lower scale and time efficiency [18].

Rodent models remain a popular choice due to genetic homology with humans [155]. Environmental T2D factors research has led to the development of high-fat diet (HFD) model, where rodents are fed a diet containing 45-60% of total calories from fat. This model has become a gold standard for obesity-induced insulin resistance and glucose intolerance in rodents [156]. Such approach is good at mimicking the natural T2D progression in humans due to poor nutrition and lifestyle, however it is also prone to high variability in metabolic responses between individual animals. Also, HFD is costly and time-consuming, as it takes 12-16 weeks to induce the condition. In contrast, there exists a pharmacologically induced strategy — gold-thioglucose treated mice were also shown to become obese and diabetic in shorter time [157]. As well as these, such genetically induced models as KK mice, hIAPP mice, Leptin-receptor-deficient *db/db* mice and GK rat have been invaluable in discovering the roles of insulin resistance, inflammation, dietary fat content, exercise, and potential treatments for T2D [158]. For instance, the groundbreaking work by Coleman on *ob/ob* and *db/db* mice led to the discovery of leptin and its receptor, revolutionising our understanding of energy homeostasis and obesity-related diabetes [159]. More recently, Portha *et al.* investigated the role of epigenetic modifications in the intergenerational transmission of diabetes risk in GK rats, exploring the influence of genetic and environmental factors in T2D [160].

Some phenomena are difficult to replicate in small animal models, hence larger animals are used. For instance, pigs and primates have more similar incretin systems to humans. Thus, Renner *et al.* reported generation of a transgenic pig model expressing a dominant-negative glucose-dependent insulinotropic polypeptide receptor (GIPR), similar to a mutation found in some human T2D patients. This model has been useful in studying role of incretin hormones in glucose homeostasis [161]. Similarly, islet amyloid deposition, observed in human T2D patients, does not naturally occur in rodent models. Therefore, aging rhesus monkey model was used to study the relationship between the amyloid formation and β-cell loss in T2D progression [162]. Furthermore, the longer lifespan of monkeys has enabled more detailed investigation of the T2D chronic effects [163].

An important advantage of animal models is the control of food intake and nutrient proportioning as well as genetic and surgical manipulations, that would be unethical or impossible in human subjects. Moreover, these models enable detailed molecular biology and histology evaluation *ex vivo*, to examine tissue-specific changes that occur during disease progression. It is worth noting, however, that animal models have significant limitations in extrapolation of the results to human biology. The intricate interplay of genetic, environmental, and lifestyle factors in human T2D makes it challenging to completely replicate in any single animal model. Additionally, species-specific differences in metabolism, insulin sensitivity, and β-cell function can lead to contradictions between animal study results and human clinical outcomes.

1.3.3 Cell culture studies

Cell culture studies have been instrumental in advancing our understanding of T2D physiopathology and in the development of novel therapeutic approaches. These studies involve various cell types, including established cell lines, primary cells and stem cells. Cell culture research investigates the molecular, differentiation and epigenetic processes at the core of insulin resistance, β-cell dysfunction and other aspects of T2D. The main advantages of the cell culture techniques include the microenvironment control, high throughput of the experiments and a wide variety of assays to study cells' activity and gene expression.

Immortalised cell lines are widely used in T2D research due to their ease of cultivation and genetic manipulation. Pancreatic β-cell lines, such as INS-1 and MIN6, have been extensively used to study insulin secretion mechanisms and β-cell dysfunction in T2D. These cell lines retain many characteristics of native β-cells, including glucose-stimulated insulin secretion [164, 165]. Hohmeier *et al*. developed the INS-1 832/13 subclone, which exhibits enhanced glucose responsiveness and stability, making it a valuable tool for investigating β-cell function in T2D contexts [166]. EndoC-βH cell line, developed by Scharfmann group, is a more representative β-cell model to human biology, compared to the rodent lines, mentioned above [167]. These cells have been utilised to study the effects of gluco- and lipotoxicity [168, 169], as a T2D model, as well as inflammation [170, 171] to model T1D. Nonetheless, the robustness of insulin response of EndoC-βH lines remains a limiting factor.

The most commonly employed insulin-responsive cell lines include 3T3-L1 adipocytes, L6 myotubes, and HepG2 hepatocytes [172-174]. These cells have been instrumental in elucidating the insulin signaling pathway and its alterations in T2D. For instance, Zeng *et al.* used 3T3-L1 adipocytes to demonstrate the role of protein tyrosine phosphatase 1B in modulating insulin sensitivity, providing insights into potential therapeutic targets for T2D [175].

While cell lines offer convenience and reproducibility, they may not fully recapitulate the complexity of primary cells. Therefore, researchers often employ primary cells isolated from human or animal tissues to validate findings from cell line studies and to investigate T2D pathophysiology in a more physiologically relevant context. Glucose-stimulated insulin secretion (GSIS) studies have been extensively performed using isolated rodent islets. For instance, Henquin *et al.* used isolated mouse islets to elucidate the complex interplay between glucose metabolism, ATP production, and calcium signalling in the regulation of insulin secretion. Their work helped to refine our understanding of the stimulus-secretion coupling in β-cells [176]. Furthermore, rodent models are useful for exploring diet-specific implications on the T2D pathophysiology. Mosser *et al*. isolated islets from mice subjected to high fat diet, to investigate the compensatory increase in β-cell mass and function that occurs in response to obesity-induced insulin resistance [177]. Isolated rodent islets have also been instrumental in studying the effects of various pharmacological agents on β-cell function. Ahren *et al.* used mouse islets to investigate the mechanisms by which glucagon-like peptide-1 (GLP-1) receptor agonists enhance insulin secretion, contributing to the development of this important class of diabetes medications, such as

incretin mimetics [178]. The regulation of β-cell mass through proliferation and apoptosis has been extensively studied using rodent islets. For instance, Kitamura *et al.* investigated the role of the transcription factor FOXO1 in β-cell proliferation and survival using isolated mouse islets [179].

Primary human islets are considered the gold standard for studying β-cell function and dysfunction in T2D. These cells provide a more accurate representation of human β-cell biology compared to rodent islets or immortalised β-cell lines. Marselli *et al.* used laser capture microdissection to isolate β-cells from pancreatic sections of T2D and non-diabetic donors, enabling the study of gene expression changes associated with T2D at the cellular level [180]. El-Assad *et al.* used isolated human islets to study the role of lipid signalling in the amplification of GSIS, uncovering the importance of glycerolipid/FFA cycling in this process and the contribution of lipotoxicity to β-cell disfunction [181]. Primary human skeletal muscle cells have also been used to study insulin resistance mechanisms in T2D patients. Ciaraldi *et al.* utilised these cells to demonstrate that insulin resistance in T2D involves defects in both insulin signalling and glucose transport activity [182].

In recent years, stem cell-based approaches have gained prominence in T2D research. Human pluripotent stem cells, including embryonic stem cells (ESCs) and human induced pluripotent stem cells (hiPSCs), can be differentiated into various cell types relevant to T2D, such as pancreatic β-cells, adipocytes, and hepatocytes. Kroon *et al.* described a first milestone in the field, showing that human ESC could be differentiated into pancreatic endoderm cells. When transplanted into mice, these cells further differentiated into insulin-producing cells that were capable of responding to glucose and maintaining normoglycemia in diabetic animals. This study provided proof-of-principle for the potential of stem cell-derived β-cells in diabetes treatment [183]. Pagliuca *et al.* developed a protocol to generate functional pancreatic β-cells from hiPSCs, providing a renewable source of human β-cells for disease modelling and drug screening [184]. Nair *et al.* focused on improving the maturation of stem cell-derived β-cells by recapitulating the natural clustering of endocrine cells during organogenesis. By reaggregating differentiated cells into islet-like clusters, they achieved enhanced β-cell maturation and function. This approach highlighted the importance of three-dimensional (3D) organisation and cell-cell interactions in β-cell development and function [185]. Recently Hogrebe *et al.* provided a detailed protocol for generating insulin-producing β-cells from multiple hiPSCs by systematising the previous studies. This comprehensive guide covered all aspects of the differentiation process, from stem cell maintenance to β-cell characterisation [186]. Nonetheless, the stem cell-derived islets often remain functionally immature [187, 188].

Understanding the trade-offs of each cell model is important for experimental design and results interpretation in T2D research. The specialised β-cell lines, such as INS-1, MIN6, and EndoC-βH — are excellent for studying insulin secretion mechanisms, with EndoC-βH offering the advantage of human origin. Nonetheless, the cell lines often show reduced glucose responsiveness, compared to the primary cells. The latter provide more relevant responses,

however, they are limited by availability, donor variability, and short survival in culture. In contrast to that, stem cell-derived models, including hiPSCs, offer an advantage of generating unlimited quantities of human β-cells and the ability to study patient-specific disease mechanisms. However, the differentiation protocols are often complex, time-consuming and expensive, while the insulin secretion output is yet to match that of the primary islets. Therefore, the choice of the appropriate model depends on the specific research question, balancing physiological relevance, reproducibility and practicality.

1.3.4 Identified gaps in current methods

The cross-talk between specific organs can be treated as a 'black box' — a term in engineering, which refers to a system, to which there are known inputs and outputs, however, the mechanism relating the former to the latter is unknown. In the case of T2D, there remains a substantial gap in the current understanding of the disease pathophysiology and the complete sequence of specific molecular events at each stage of the disease progression remains unknown. Current approaches involving human and animal studies for *in vivo* research and cell culture studies for the *in vitro* research are directed towards the discovery of the various disruptions in the metabolism during T2D. Nonetheless, these methods have their disadvantages in clearly uncovering the black box mechanisms in glucose homeostasis and demonstrating the link between the different organs triggering T2D.

Human studies, while crucial for understanding of T2D, face significant challenges. The extent of experimental manipulations is limited by ethical concerns. The high cost and time demands, due to the chronic nature of T2D, limit the scope of these studies. Also, the restricted access to organs hinders direct disease observation and relies on indirect measurements. The inability to manipulate key variables in humans, such as gene expression or specific metabolic states, makes it challenging to establish clear cause and effect relationships in disease mechanisms. Moreover, high environmental and genetic heterogeneity among human populations complicates the evaluation of specific factors, influencing T2D.

Animal models, while offering more experimental manipulations and better control over the conditions, also lack the capability for detailed evaluation of chemical signalling between different organs in real time. Moreover, the relatability of the animal experimentation results to human biology is limited due to dissimilarities in organ function. For instance, recent transcriptomic studies have demonstrated, that there are differences in gene expression of islet endocrine cells between humans and mice [189, 190]. Additionally, the arrangement of and β-cells has been shown to differ in various mammalian species. For instance, rodent islets contain α-cells in the periphery and β-cells in the inner core, while monkey and human islets possess a more random organisation and higher percentage of α-cells [191, 192]. This arrangement has been shown to have the implications on the Ca^{2+} signalling patterns and electrical signal propagation due to cell to cell contacts. This in turn affects the insulin secretion coordination within the islet. During exposure to high glucose, in rodents the membrane potentials of the β-cells display synchronised oscillations across the entire islet, whereas in human islets such pattern is still debated and more

localised synchronisation is observed [193-195]. The reasons for such variability in islet architecture between the species are not clear, however, changes in human islet organisation have been linked to the development of T2D [196]. Furthermore, it has been shown that the level of islet vascularisation is higher in rodents, compared to humans. At the same time, during T2D the density of islet vasculature increases [197]. As well as this, there are notable differences between the ECM in rodent and human islet basement membranes. In particular, the membrane is single-layered in rodents and double-layered in humans, with the inner layer containing both laminin-411/421 and −511/521, while the outer layer — only −511/521. The latter has been demonstrated in numerous studies to impact insulin secretion and survival of the β-cells [198-201].

Cell culture models, while providing an excellent range of the molecular biology manipulations, lack the complexity of T2D condition and struggle to replicate the long-term, systemic nature of its development. These models offer oversimplified perspective, using single cell types and lack the hormonal, neural, metabolic, etc. inputs that influence cell function *in vivo*. The two-dimensional cultures used by most *in vitro* models fail to recapitulate the complex three-dimensional architecture of native tissues, since the ECM component is often neglected. This is particularly relevant for pancreatic islets, where the 3D arrangement can influence function and communication. Furthermore, cell cultures cannot adequately model the effects of systemic insulin resistance on β-cell function and mass. The progressive decline of β-cells in T2D is partly is influenced by peripheral insulin resistance, exhibited by other tissues. This cross-talk is hard to replicate in isolated systems. Additionally, immortalised cell lines may not accurately represent the behaviour of the primary cells, which are typically short-lived and less available. Hence, there is a need for the development of more biologically relevant models with an increased capacity for microphysiological examination and analysis.

1.3.5 The '3Rs' initiative

In modern days there is an increasing ethical demand in the society to minimise animal experimentation in science. The 3Rs initiative, which stands for Replacement, Reduction, and Refinement, is a widely accepted ethical framework aimed to lessen the animal use and suffering in scientific research. Proposed by Russell and Burch in 1959, the 3Rs have become a guiding principle for the humane use of animals in experimentation [202]. The ultimate goal of this initiative is to promote the development and implementation of alternative methods that can replace, reduce, or refine animal use in research, testing, and education [203].

Replacement insists on non-animal methods in research, that are capable of providing comparable or superior scientific results. This includes *in vitro* techniques, such as cell and tissue cultures, and *in silico* approaches, such as computer modelling and simulation. For instance, the use of hiPSCs has shown promise in replacing animal models for toxicity testing and drug discovery [174]. Similarly, the development of organ-on-chip (OOC) systems has the potential to replace animal testing in such fields as drug development and disease modelling [205].

Reduction focuses on minimisation of the number of animals used in the experiments, while still achieving robust and reliable results. This is possible to accomplish by careful experimental design, statistical analysis, and data sharing. For instance, the use of factorial designs and power analysis can help optimise sample sizes and reduce animal numbers [206]. Additionally, the establishment of data repositories and collaborative networks can encourage the sharing of animal data, which can help reducing redundant experiments [207]. Another example of Reduction are non-invasive imaging techniques. For instance, positron emission tomography and single-photon emission computed tomography enabled longitudinal studies of β-cell mass in the same animal, hence reducing the total number of animals required for that study [208].

Refinement involves modifying experimental procedures in order to minimise the pain, suffering, and distress experienced by animals, at the same time improving their welfare. This includes the appropriate use of anaesthesia and analgesia, environmental enrichment, and humane endpoints [209]. In neuroscience research, the development of microelectrode arrays and optogenetic techniques has lead to less invasive and more precise manipulation of neural activity, which in turn reduced animal distress [210]. Environmental enrichment strategies, such as providing hiding spaces and nesting materials, were also useful in improving the welfare of laboratory animals [211] and has already been employed in diabetes studies with rodents [212].

The successful implementation of the 3Rs initiative has been seen across several disciplines. For instance, in toxicology, the development of high-throughput *in vitro* screening methods has significantly reduced the use of animals in chemical safety testing [213]. In vaccine development, *in vitro* and *in silico* methods are being employed more often for antigen discovery and vaccine candidate selection. As well as this, novel vaccine delivery systems and adjuvants are implemented, aiming to enhance vaccine efficacy and minimise large animal distress [214]. Furthermore, the establishment of national and international 3Rs centres, such as the NC3Rs in the United Kingdom and the Center for Alternatives to Animal Testing in the United States, has promoted the dissemination and implementation of 3Rs principles worldwide [215].

Therefore, the 3Rs initiative is a significant step towards promoting a more humane use of animals in the scientific research. The 3Rs is aimed to transform the way the research is conducted by encouraging the development and adoption of alternative methods, optimising experimental design, and improving animal welfare. At the same time, 3Rs initiative maintains scientific rigour and ensures ethical standards in research. As the scientific community continues to embrace the 3Rs, further solutions are expected to be implemented across various disciplines, including T2D research.

The increased demand for reduction of animal studies and quest for higher relevance to human biology have led to the emergence of microfluidic OOC platforms, as promising tools for studying pancreatic function and disease mechanisms. These *in vitro* platforms are aimed to address the challenges, currently encountered by the traditional 2D cell culture and animal approaches.

1.4 Approaches to microfluidic pancreas-on-chip devices

1.4.1 Advantages of microfluidic organ-on-chip devices

OOC devices (Figure 1.4.1) have recently demonstrated increased use cases in meeting the demand for generating more accurate *in vitro* physiological systems. Taking advantage of microfabrication and microfluidic techniques, these systems are aimed to recreate 3D microenvironment for cultured cells. As a result of this, the cellular response to the environment appears representative of the function of the organ, that this cell type is a constituent of.

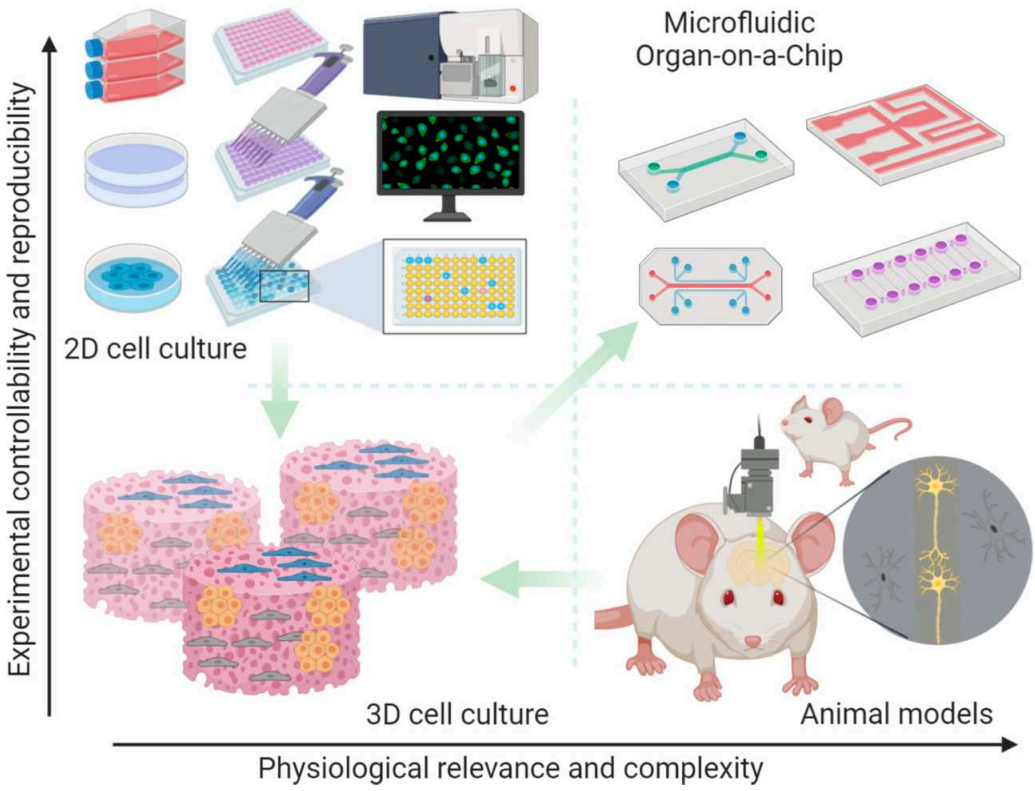

Figure 1.4.1 Advantages of organ-on-chip platforms.
Organ-on-chip technology is a bridge between classic models and relevance to human physiology. Adapted from Ma *et al.* 2021 [216].

In microfluidic systems, flow typically occurs in the laminar regime, where fluid moves in parallel layers with little to no mixing between them. Laminar regime simplifies the flow modelling, allowing it to be predicted with Poiseuille's law, which makes assumptions such as constant density and negligible height variation. Hence, the main parameter in microfluidic systems is the resistance to flow, which illustrates the increased dominance of viscous forces. Here it is particularly significant, since the high surface-to-volume ratio in microfluidic geometries has a large effect on the flow behaviour as a result of friction between the fluid and the microchannel walls [216].

There exists an array of different materials, from which the microfluidic devices are made. The most common rapid prototyping material at the early stages of research is poly(dimethylsiloxane) (PDMS). It is a soft elastomer with high optical transparency, cured by cross-linking. PDMS is gas permeable, which allows long-term cell culture. The material is also flexible, making it suitable for fabricating valves and pumps in more advanced microfluidic OOC devices. Inorganic materials, such as silicon, glass and ceramics have been utilised in early microfluidic device applications due to their high chemical resistance, however are less commonly used these days due to complicated and expensive fabrication. Instead, rigid thermoplastic polymers are preferred thanks to their scalability for mass production and low cost. The examples of these are poly(methyl methacrylate) (PMMA), poly(carbonate) (PC), cyclic olefin copolymer (COC) and poly(tetrafluoroethylene) (PTFE). The microfluidic geometries are produced within these materials by such techniques as hot embossing, laser ablation and injection moulding. PMMA and COC are most popular because of their transparency, while PTFE is inert and biofouling resistant. Rigid polymers are more durable compared to PDMS, however are less easy to bond and hence require thermobonding or glue to avoid leaks [217].

One of the main advantages of OOC devices is that they provide a high level of control over experimental conditions. For instance, such parameters as flow rate, pressure, O_2 and CO_2 levels can be precisely controlled. This enables a more precise investigation of specific aspects of organ function and drug effects. Furthermore, microfluidic systems can be integrated with biosensors for real-time, non-invasive analyte monitoring. This can help obtaining dynamic, high-resolution data, that is challenging to implement in other models. Also, by integrating with other technologies such as imaging and multi-omics analyses, OOC systems provide comprehensive analytical information about the molecular processes and drug responses. Their ability to support long-term culture also enables the study of chronic disease progression and long-term drug effects, addressing limitations of traditional *in vitro* models [216].

The technology's potential to reduce animal testing aligns well with ethical considerations in research, supporting the 3R principles. Moreover, OOC models can provide faster, more relevant and cost-effective screening of drug candidates, compared to animal studies. Therefore, this technology has a potential to accelerate the drug development pipeline and reduce overall research and development costs [216]. Additionally, these systems have excelled at modelling complex barrier tissues, such as the blood-brain barrier, allowing for more accurate prediction of drug penetration and efficacy in challenging physiological contexts [218]. OOC systems also offer unique opportunities for personalised medicine. By incorporating patient-derived cells or hiPSCs, these platforms can be tailored to reflect individual patient characteristics, enabling personalised disease modelling and drug screening [219].

Furthermore, two or more OOC systems can be connected to represent the cross-talk between multiple organs. These multi-organ models enable the study of complex inter-organ communications, allowing to investigate disease pathophysiology more broadly [220]. Thus, OOC devices provide a silver lining approach to modelling T2D, offering to improve the understanding

of the disease progression and hence lead to more accurate predictions of drug efficacy and toxicity.

1.4.2 Pioneering pancreas-on-chip works and their development

There already have been several works developing pancreas-on-a-chip models. Some of the earliest microfluidic islet chips have been reported by the group of R. Kennedy. In 2003-2009 studies several glass devices were described, capable of hosting single mouse islets in dedicated chambers and performing electrophoresis-based competitive fluorescence anisotropy immunoassay of insulin and Ca^{2+} flux measurement in short 40-minute experiments under extremely low flow rates. Insulin biphasic and oscillatory secretion was observed in response to step glucose concentration increase [221-223].

In addition to this, a 2004 study by Rocheleau et al. presented a PDMS microfluidic setup trapping single mouse islets into a 150 μm wide clamp and subjecting them to graded glucose concentration stimuli (Figure 1.4.2). The work revealed the glucose concentration threshold of 6.6 mM required to initiate Ca^{2+} membrane depolarisation leading to insulin release. This was demonstrated by live cell imaging of nicotinamide adenine dinucleotide phosphate (NAD(P)H) autofluorescence and intracellular Fluo-4 labelled Ca^{2+} ions. It was also observed how the depolarisation oscillation was damped the further it propagated to the centre of the islet. This suggests strong coupling to the average glucose concentration around specific cells, impacting the ATP-sensitive K^{+} ion channels, which balance membrane depolarisation [224]. Later the group have also reported fatty acid oxidation measurement in single islet-on-chip, obtained by confocal imaging of electron transfer flavoprotein autofluorescence [225]. In their most recent study the group has reported a PMMA microfluidic chip capable of additionally measuring the oxygen consumption rate (OCR) of individual pancreatic mouse islets in response to glucose stimulation. The device used a sensor placed in an optically clear microwell on a thin glass coverslip to provide high temporal resolution. Results showed that glucose-stimulated OCR is determined by glycolytic flux through pyruvate kinase and is independent of calcium activity in the 1st phase [226].

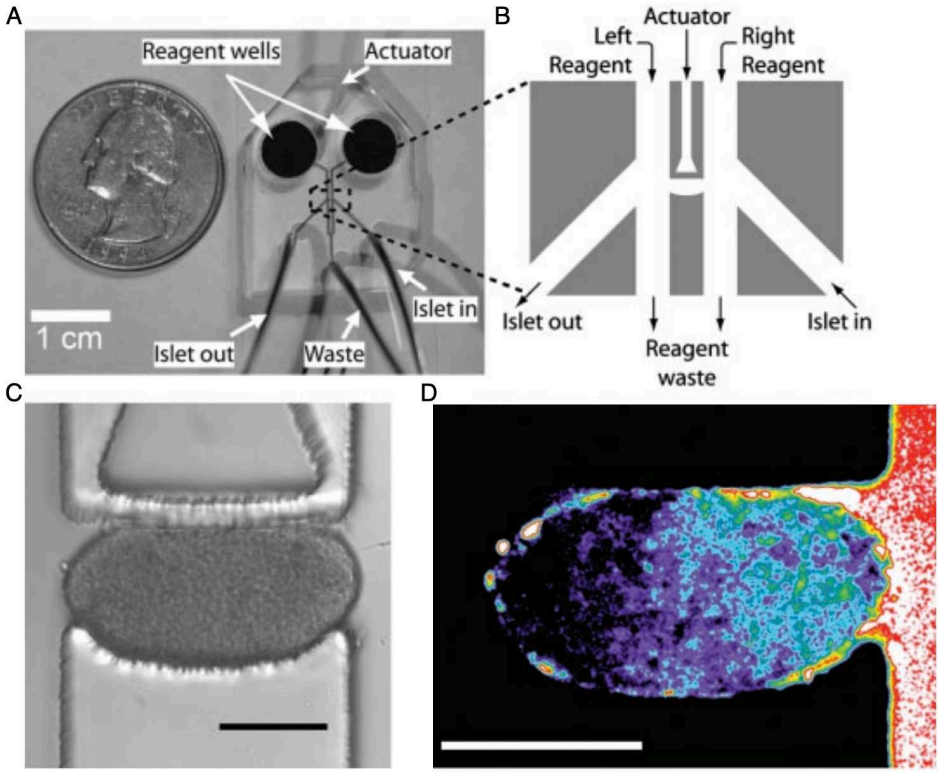

Figure 1.4.2 Pioneering islet-on-chip work by Rocheleu et al.
On of the first islet-on-chip models used to study the calcium fluxes across the cell membranes of isolated mouse islets. A - photograph of the microfluidic device. B - schematic of the microfluidic geometry, enabling islet trapping. C - light microscope image of a trapped islet. D - confocal fluorescence microscopy of glucose-stimulated islets. Scale bar = 150 µm. Adapted from Rocheleu *et al.* 2004 [224].

The long-term islet-on-chip models were validated in the works of Yong Wang. The devices produced by soft lithography technique with PDMS featured microfluidic channels and traps to immobilise human and rodent pancreatic islets (50-400 µm), enabling local microenvironment control (O_2, glucose and CO_2), and live cell imaging. The works demonstrate that is possible to improve the metabolic activity and survival of human pancreatic islets in vitro in view of islet transplantation [227-230].

M. Roper group has contributed with severals studies describing microfluidic devices, capable of delivering temporal gradients of glucose concentration, such as ramps and sinusoid, to isolated mouse islets achieved via microfluidic mixing. They were able to study the coherent pulsate nature of insulin release in response to varied glucose stimulation. This was shown by tracking Ca^{2+} oscillations correlated to insulin signalling as well as fluorescence immunoassay on chip [231-234]. Furthermore, a 2019 collaboration study with K. Parker group presented a complex PC chip, which hydrodynamicly trapped human cadaveric islets integrated with mixing microchannels for continuous fluorescence anisotropy insulin immunoassay [235]. In the most recent study the group has described an inverse dependence of glucagon secretion as human pancreatic islets on chip were subjected to high and low glucose concentrations. Exometabolome samples were collected and post processed with time-resolved Förster resonance energy transfer

(TR-FRET) sandwich immunoassay. The dynamics of glucagon secretion, however, was observed as highly variable between samples ranging from bursts to sustained to none [236].

1.4.3 Alternative approaches

A novel method to on-chip monitoring of pancreatic islets' activity has been demonstrated in the works of the J. Lang group (Figure 1.4.3A, B and C). Slow potentials, arising as β-cells' membrane depolarisations in response to glucose, were recorded using platinum black electrodes and electrochemical transistors in direct contact with isolated islets cultured in integrated microfluidic devices. It was confirmed that the frequency and amplitude of these electrophysiological signals depended on glucose concentration, manifesting in the biphasic response to the increase of the latter, and linked to insulin secretion [237-242]. These findings were strengthened by the similar works also involving microelectrode arrays for islets' electrical interrogation or impedance measurements [243-247].

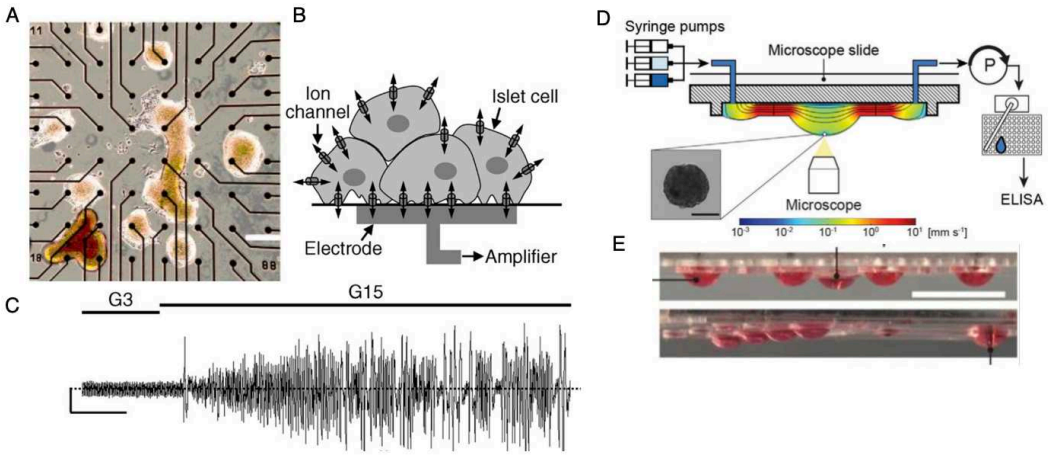

Figure 1.4.3 Alternative approaches to pancreas-on-chip.
A, **B** and **C** - light microscope image, schematic and recorded signal (respectively) from the experiment of J. Lang group on electrical activity of islets. Adapted from Lebreton *et al.* 2015 [238]. **D** and **E** - schematic and photographs (respectively) of hanging-drop microfluidic pancreas-on-chip system developed by P. Misun group. Adapted from Misun et al. 2020 [250].

The effects of fluid flow on the islets were investigated by Jun *et al.* The chip in their work mimicked interstitial flow with the aid of an osmotic pump and endothelial cells seeded around the islet wells was comprised of PDMS-based concave microwells, 500 μm in width. The optimised flow conditions in the chip were reported to preserve the shape and viability, while improving the insulin secretion activity of isolated rat islet spheroids for up to a month. This was due to the proximity of secreted soluble factors to the islets and the promotion of diffusion-mediated interactions between them [248].

Lee et al. have recently developed a 'microphysiological analysis platform' for human pancreatic 1.1B4 β-cell line. The device has been innovatively fabricated with a grey-scale SU-8 photolithography approach for the PDMS mould master and the geometry involved a dedicated 800 μm hemispherical compartments for spheroid formation as well as surrounding microfluidic perfusion chambers separated by a 2 μm micropatterned perfusion barrier. The latter was

engineered to replicate the nutrient diffusion and gas exchange across blood vessels, while also facilitating reduced gravity-based hydrodynamic liquid flow, which promoted spheroid formation. The work has linked the hyperglycaemia and hyperlipidemia-induced apoptosis of β-cells to caspase-mediated pathway elicited by reactive oxygen species. However, the drawbacks of the study include the unaltered viability of spheroid cells compared to two-dimensional (2D) monolayer, dictated by an occurrence of a necrotic core, which has been confirmed by difference in glucose-induced Ca^{2+} signal between the inner and outer cells [249].

In contrast to hydrodynamic traps and hemispherical wells commonly used for on-chip islet cultures and pseudo-islets organisation, a hanging-drop-based perfusion system was presented by P. Misun group in several recent studies (Figure 1.4.3D and E). Such microfluidic devices were composed of 3 mm openings at the bottom of the PDMS structure, inducing a drop of approximately 600 μm in height, containing single islets. Despite being more technically challenging to implement, the setup was claimed to be advantageous, since it was enabling quicker switching between the applied glucose concentrations, reduced chip wall absorption effect, better tissue oxygenation and shorter sampling intervals. These factors contributed to more detailed insulin secretion information for both phases. Additionally, thanks to enhanced flow and volume regulation, the sample-to-sample variability was decreased. This approach, however, presents a trade-off between *in vivo* relevance and sample precision, since single islets for each hanging drop are used, simply suspended in liquid [250, 251].

1.4.4 Three-dimensional cultures

As opposed to 2D and hanging drop models, a vascularised 3D model attempting to enhance the physiological relevance of a pancreas-on-chip has been presented in 2021 in the collaborative work by M. Sandler and C. Huges groups. A PDMS microfluidic chip used in the study consisted of a large culture chamber interconnected with two parallel microchannels on each side (Figure 1.4.4A). The vascularisation was achieved by injecting a fibrin hydrogel containing endothelial and stromal cells together with isolated cadaveric human islets and allowing 5-7 days for vessel formation under the flow from one side channel to another across the culture chamber (Figure 1.4.4B and C). Maintained number of β-cells and α-cells after a week in the chip was reported compared to native islets and in contrast to simple islet suspension. Insulin-secreting capability of the vascularised islets was confirmed and validated with an architecture-mimicking simulation model, however, without the suspension islets control. Additionally, vessel-delivered mononuclear white blood cells were shown to induce morphological and vital changes to the islets, thus linking the model to T1D [252].

A more recent study by Quintard *et al.* reported a microfluidic platform for vascularising pancreatic islet spheroids also using endothelial vessel network to mimic the perivascular basement membrane. Human pancreatic islets were hydrodynamicly trapped in wells and encapsulated with human umbilical vein endothelial cells (HUVECs) and fibroblasts, embedded in fibrin hydrogel, similar to M. Sandler's work. The microfluidic device was made from COC, and supported long-term culture for up to 30 days under continuous perfusion. Functional assays,

including GSIS, demonstrated improved insulin response in vascularised islet spheroids compared to static and non-vascularised cultures. The approach enhanced organoid growth and function but required precise control of hydrogel deposition due to cell loss during polymerisation and intricate thickness management [253].

Another 3D hydrogel culture approach has been recently demonstrated by C. Stabler group, who have produced a PMMA chip by computer numerical control (CNC) milling and CO_2 laser cutting (Figure 1.4.4D-F). Described setup enabled dynamic glucose conditions and continuous *in situ* viability monitoring and calcium signalling of cultured islets. Furthermore, two versions of the chip have been evaluated: a fully enclosed chip and an open one with a permeable perfluoroalkoxy membrane. The chips sustained viable and functional rodent or human islets in alginate hydrogel for more than 10 days, in contrast to rapidly deteriorating islets in static condition. However, the permeable chip appeared to dampen and delay the insulin response compared to the enclosed chip and no biphasic curves were observed. The authors explain the latter as the result of altered glucose diffusion through the gel [254].

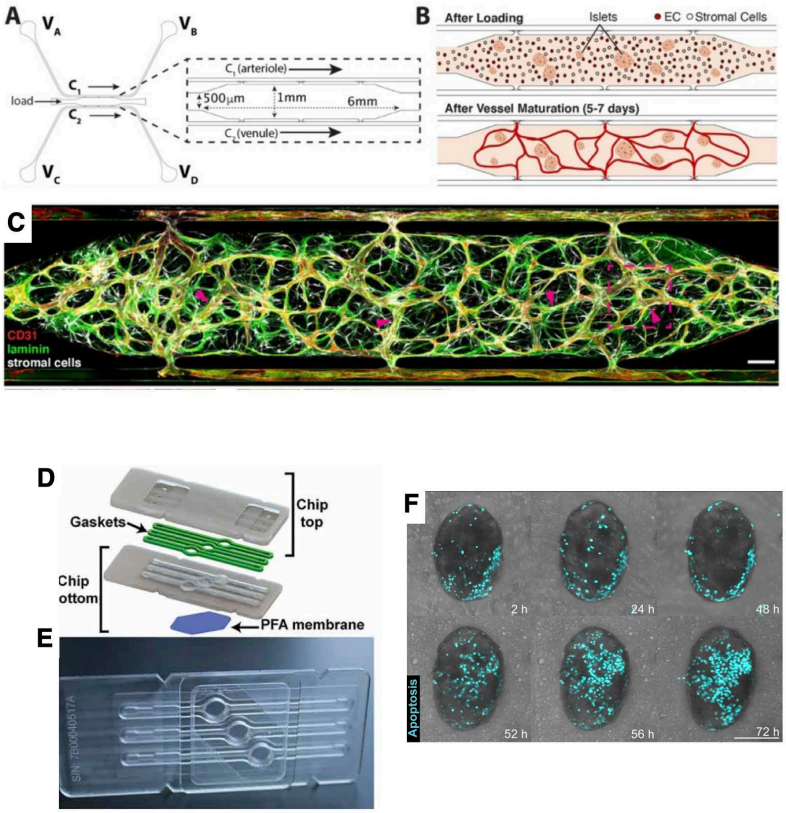

Figure 1.4.4 Three-dimensional pancreas-on-chip models.
A, **B** and **C** - microfluidic chip layout, experimental schematics and confocal fluorescent image (respectively) of a vascularised chip developed by M. Sandler group. Endothelial cells (red) were introduced to the chip in a pre-filled fibrin gel and were able to form a vascular network after 5 days of maturation. Adapted from Bender *et al.* 2024 [252].
D and **E** - schematic and photograph of a microfluidic chip, produced by C. Stabler group, containing alginate hydrogel-seeded islets (**F**). Adapted from Patel *et al.*2021 [254].

In addition to this, a study with involving a 3D scaffold on chip and integrated biosensor was published by J. Ramon group in the same year. Isolated mouse pancreatic islets were seeded on carboxymethyl cellulose cryogel (CMC, a hydrogel porosyfied by freezing as a result of water molecules nucleation) of stiffness reportedly about 0.7 kPa, incorporated into a microfluidic chip. The islets preserved the characteristic expression of PDX1 and were not significantly different from suspension control evaluated in static condition. Also they were demonstrated to be functional after 24 hours of perfusion with the aid of surface plasmon resonance sensor utilising immobilised antibodies for insulin detection [255]. Previously, such sensors have been employed for simultaneous detection of insulin, glucagon and somatostatin in sampled islet secretive solutions. Nonetheless, the disadvantage of this sensor is low temporal resolution due to permanently binding antibodies [256].

1.4.5 Multi-organ models

Moreover, lab-on-a-chip technique allows the incorporation of multiple organ models within a single chip. For instance, Park et al. co-cultured GLUTag cell line and INS-1 β-cell line in dedicated chambers on a single chip to create a small intestine-pancreas model. After three days of co-culture, both cell lines remained viable and formed 3D aggregates. In comparison to static 2D culture, GSIS results demonstrated a more intense and faster saturating insulin response to high glucose by the β-cells in presence of GLUTag cells, which were contributing to this effect by producing GLP-1 [257].

Furthermore, a 2017 study featured the coupling of human pancreatic islets and liver spheroids from HepaRG cell line in dedicated 2D compartments on a single biochip. The physiological feedback loop between islet signalling insulin in response to glucose changes and hepatocytes uptaking glucose and secreting albumin in response to insulin changes has been confirmed over the course of up to 15 days [258].

Similarly, in a 2020 study (Figure 1.4.5), E. Leclerc group has demonstrated a combination of 2 chips: pancreatic and liver from their previous works [259-261]. The set-up featured a pancreatic biochip with an array of wells to trap isolated rat islets and a liver biochip with microchambers for hepatic HepG2 cells' attachment — both made from PDMS. After 5 days of perfusion together they examined the tissues with quantitative polymerase chain reaction (qPCR), immunostaining and sampled media with enzyme-linked immunosorbent assays (ELISA) and enzymatic sensors - and compared with separate chip perfusions. While the results confirmed improved hepatocyte function and expression, the islets' expression appeared negatively impacted. This could be due to mismatch of islet number compared to the number of hepatocytes with imbalanced secretions or due to lack of other tissues represented in the system. This finding suggests that for relevant microphysiological system the proportion of cells and their signals should also be considered. In addition to this, in a more recent rat islet on-chip evaluation the group has demonstrated the increased lipid metabolism in a 3D vs 2D comparison as well as a

higher sensitivity of the 3D cultures to GLP-1 and isradipine stimulation. This was done by studying the exometabolome of the islets with mass spectrometry [262].

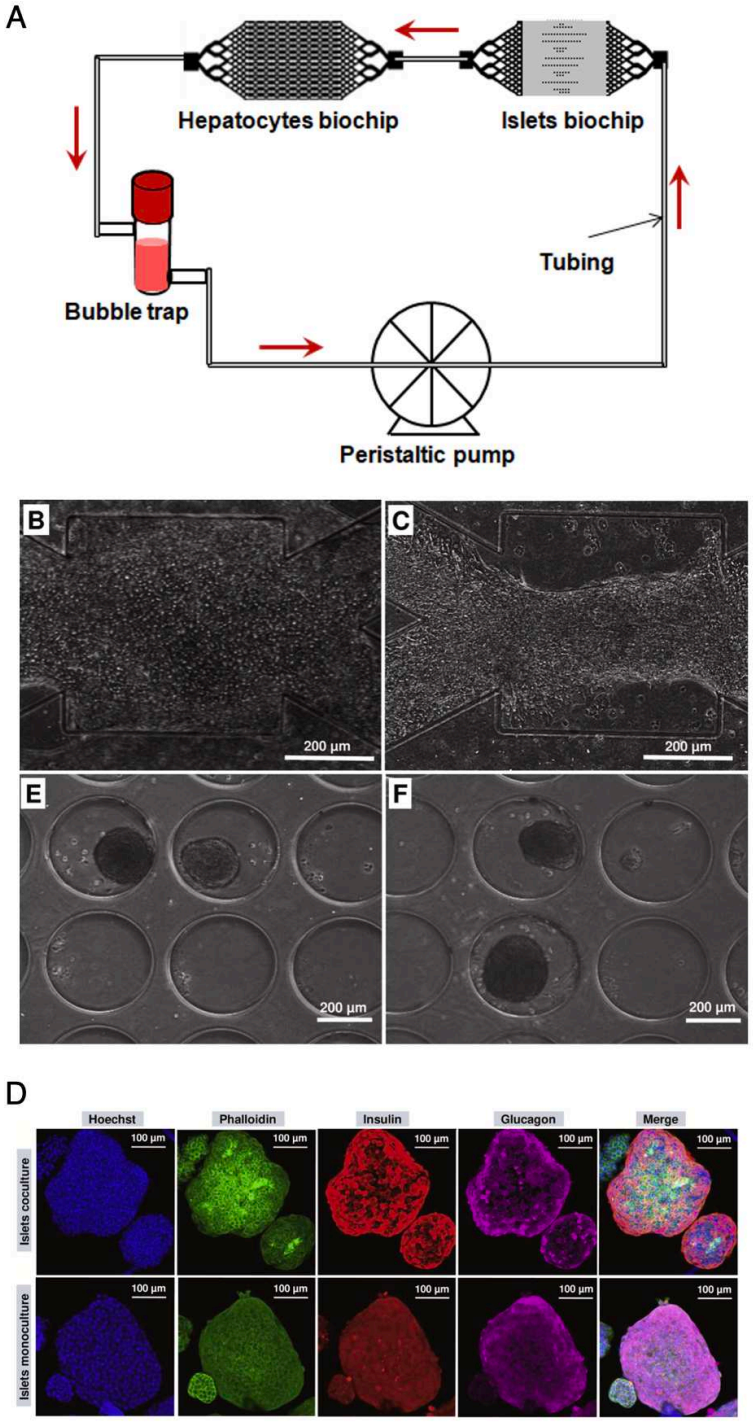

Figure 1.4.5 Multi-organ-on-chip model.
A pancreas-liver model reported by E. Leclerc group combined 2 chips into a connected microfluidic system (**A**): hepatocyte chip (**B** and **C**) and islet chip (**E** and **F**). **D** - confocal fluorescent images of co-cultured islets. Adapted from Essaouiba et al. 2020 [259].

Successful islet differentiation on chip has been reported by Hirano et al in 2017. A 30-day protocol has been performed on a closed-channel chip which included dedicated non-adherent microwells with hiPSCs. In a series of time-depended media alterations previously described by the group, it was possible to achieve 95% PDX1 expression among the cells by the day 13, confirming pancreatic lineage and 35% INS expression by the day 20, characteristic to beta-cells. The functionality of the induced islets has been confirmed by GSIS experiment [263]. These results were later confirmed in a similar study by Qin et al., who have reported a 4-layer device promoting islet formation from hiPSCs, growth and viability. The organoids exhibited higher β-cell gene and protein expression, including PDX1, Nkx6 homeobox 1 (NKX6.1), insulin and C-peptide. Also the GSIS and Ca^{2+} influx were improved, compared to static culture [264]. Expanding upon this work, the group went on to co-culture hiPSC-derived islet and liver organoids on a single chip for more than 30 days. The chip consisted of corresponding tissue type compartments featuring microwells connected via microchannels and was perfused via peristaltic pump in a closed loop manner. The organoids were first differentiated to liver and pancreatic lineages on separate chips, as described in the preceding work, and were then transferred to the co-culture chip at 1:1 ratio. In contrast to E. Leclerc work, this study demonstrated enhancements in both cell types. QPCR and ribonucleic acid (RNA) sequencing revealed improved hepatic and islets' gene expression, significant down-regulation of apoptosis-related genes and up-regulation of cell type-specific genes as well as lipid and glucose metabolism genes in the co-culture compared to mono-culture. Furthermore, the multiorganoid system improved insulin secretion in islets and boosted glucose consumption by liver microtissues. Under hyperglycaemic conditions, mitochondrial function and decreased glucose metabolism ability were initially observed, similar to the pathological changes in T2D, however, alleviated by metformin [265].

A novel pneumatic microfluidic device featuring both human primary liver and islets has been recently reported by V. Lauschke group. Multi-chamber chip was fabricated as a sandwich of thiol–ene–epoxy (OSTE+), PMMA and PDMS parts and operated in a cyclic fashion of air pumping and withdrawal to pneumatically push the liquid back and forth across the chambers. This operation mode was applied in order to emulate the *in vivo* blood circulation initiated by heartbeat. The flow rate to the culture chambers could be individually tuned by altering the resistance in the corresponding microchannels. High glucose exposure caused significant transcriptomic changes in islets, indicating of β-cell stress, pancreatic dedifferentiation, metabolic alterations and unfolded protein response. In liver cultures induction of lipogenesis, down-regulation of insulin response genes and counter-regulation of transcriptional programmes has been observed. While confirming the interlinked nature of the pancreas-liver axis, the authors, however, did not demonstrate the long-term dynamics of these responses, as only a 1h long high-glucose condition was applied. It is also unclear to what extent the pneumatic system was prone to liquid evaporation, which could be a limiting factor for long-term studies with such set-up [266].

As well as these, a muscle-pancreas-on-chip has been presented by the previously mentioned J. Ramon group. Developing further their setup, the group has co-cultured insulin secreting MIN6

cells in CMC gel together with C2C12 myoblasts in fibrin/Matrigel® matrix. In the preliminary separate static evaluations, MIN-6 were shown to from 3D spheroids, possess similar levels of PDX1 expression and insulin response as in 2D culture. Myoblasts, on the other hand, were demonstrated to remodel the matrix fibres, initially cast in a PDMS master with 2 pillars, into an aligned tissue, exhibiting uniaxial tension, which in turn contributed to aligned myotubes formation post-differentiation. In addition to this, muscle tissue functional contractility was confirmed under electric pulse stimulation (EPS). The pre-formed microtissues were then placed into two dedicated connected chambers on a PDMS chip. The group reports a 3-hour long 'training' on chip, involving EPS muscle tissue stimulation during the second hour, using graphite electrodes. The plasmon resonance sensor previously reported by the group has been used in this study with an updated design and featuring immobilised insulin and IL-6 antibodies, and it had to be replaced every 20 minutes. Maximum IL-6 response was observed immediately at the beginning of stimulation, rapidly declining after, whereas a similar insulin response was recorded with a 40-minute peak delay and a less steep drop. Combined with the confirmation of this result by applied post-stimulus muscle tissue media as well as IL-6 to separately cultured MIN-6 cells, these findings demonstrate the IL-6 time-delayed insulin dependency. The observed phenomenon describes how exercise triggers paracrine activity of pancreatic islets to stimulate glucose uptake into muscle [267].

Additionally, Liu et al. developed a 3D double-organ chip that integrated both adipose tissue and pancreatic islets to examine the interaction between these tissues in pathological conditions and evaluate the efficacy of drugs. The chip consisted of two chambers - adipose, with a diameter of 6 mm and height of 2 mm; and islet, with a diameter of 8 mm and height of 2 mm. The chambers were separated from channels by a PC membrane with a pore size of 10 μm to prevent fluid from directly impacting the tissues. Insulin secretion, islet cell damage, and inflammatory response were analysed by measuring the secretion of inflammatory factors, such as adiponectin, IL-6, and interleukin 1β. The results indicated that inflammation, triggered by the lipopolysaccharide can affect the function of pancreatic islets and the presence of fat tissue can amplify this response. Liraglutide reduced the inflammatory response of both fat and pancreatic islets, which can improve the function of islets by reducing the stimulation by lipopolysaccharide and adipose tissue [268, 269].

The development of pancreas-on-chip models has enabled significant advancements in T2D studies in a controlled microenvironment. However, to fully harness the potential of these systems, real-time monitoring of insulin dynamics is essential. Biosensors can be integrated within OOC platforms, enabling precise and continuous measurement of insulin secretion and metabolic responses. It is therefore important to consider the existing insulin detection techniques when selecting a suitable option, that can be used for on-chip monitoring.

1.5 Biosensing approaches for insulin detection

1.5.1 Overview of biosensing techniques

Insulin, with a molecular weight of approximately 5.8 kDa [270], is produced by the pancreas and plays a significant role in carbohydrate and fat metabolism. Normal fasting blood insulin levels are around 50 pM [271], while levels exceeding 70 pM can suggest T2D [272]. The detection of insulin is complicated by its low concentrations, large molecular size, and interference from other biomolecules like glucose and uric acid. Several methods have been developed, including immunoassays, optical and electrochemical methods. ELISA has become the gold standard in T2D research due to its high throughput and reliability. However, it is a relatively high cost technique, involving considerable sample preparation, which can be time-consuming and may affect the overall efficiency of the assay. Another standard technique is high-performance liquid chromatography (HPLC) combined with mass spectrometry. It provides high specificity and sensitivity, achieving limit of detection (LOD) of about 1.8 μIU/mL (10.8 pM) [273]. Nonetheless, it also requires extensive sample preparation and processing steps to isolate insulin from other proteins, which adds to the complexity and time required for the analysis.

Alternative insulin biosensors are emerging aiming to simplify the detection process and reduce the costs, while improving the accessibility and size of the setup. An example of such technique is electrochemical sensors, employing voltammetric and amperometric techniques to monitor insulin oxidation in the liquid [274]. The electrochemical sensors often require surface modifications to improve the specificity due to competing electroactive substances in biological samples, such as ascorbic acid. For example, a nickel-doped carbon composite electrode achieved an LOD of 40 pM [275], while a guanine/NiOx-modified glassy carbon electrode demonstrated an LOD of 22 pM at pH 7.4 [276]. Another notable example is a silica gel-modified carbon paste electrode that demonstrated an LOD of 36 pM [277]. Other sensors have reported insulin monitoring with such surface modifications as reduced graphene oxide (GO) [278], silver nanoflower (Figure 1.5.1) [279], carbon nanotubes [280], $Ni(OH)_2$ [281] and molecular imprinting [282, 283]. Thus, electrochemical sensors exhibit a promising potential in integration with the microfluidic OOC system to monitor the secreted insulin in real time, provided the selectivity and sensitivity of the electrode is optimised.

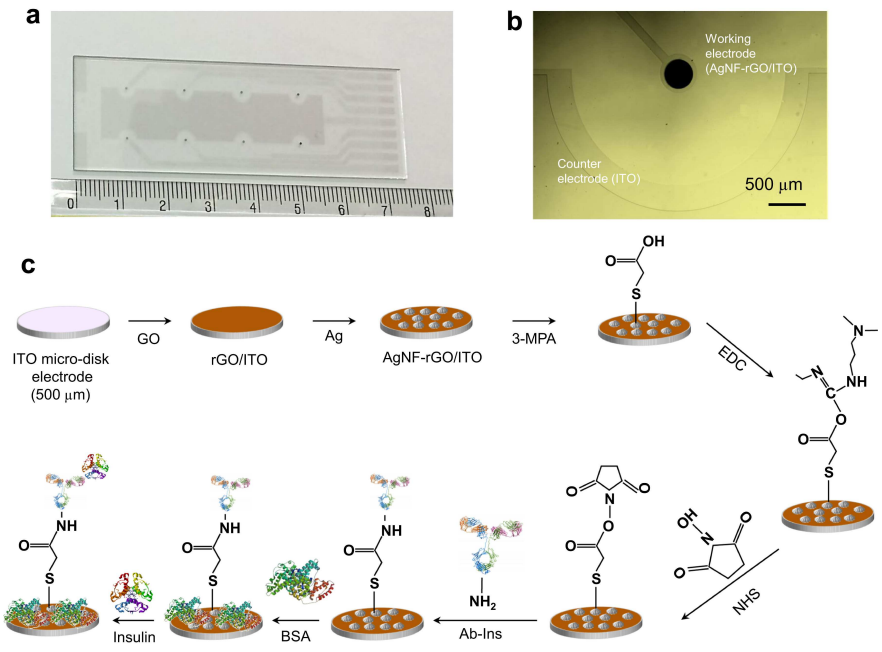

Figure 1.5.1 Electrochemical insulin sensor.
An electrochemical sensor reported by Yagati et al. featured an array of microelectrodes with silver nanoflower-modified surface. **A** - photograph of the array, **B** - microscope image of the microelectrode. **C** - process diagram for surface modification. Adapted from Yagati *et al.* 2016 [279].

1.5.2 Principles of electrochemical sensors

An electrochemical biosensor converts the information about a biochemical reaction into an electrical signal by tracing the electron transfer kinetics, usually at metal-solution interface [284]. Such biosensors typically operate in ionic aqueous media, making them a suitable candidate for microfluidic devices, where such interface can be ensured. The main benefits of electrochemical biosensors are low cost, ease of use and ability to perform continuous measurements. Various surface modifications with nano-structures or enzymes have enabled monitoring of wide range of analytes [285]. These sensors are used to trace the reduction-oxidation (redox) reaction at the electrode interface once a potential is applied: O + ne- ⇄ R. Such reaction depends on mass transport which includes diffusion of the species down the concentration gradient, migration of the charged species and convection of electrolyte fluid. These phenomena can be summarised in the following equation, which uses Nernst-Planc equation [286-289] to describe diffusion and migration, while also including fluid flow element:

$$J_i = -D_i\left(\nabla C_i - \frac{nF}{RT}C_iE\right) + uC_i \qquad (1.1)$$

where, J_i is the flux, D_i is the diffusion coefficient and C_i is concentration of species i, u is the fluid velocity, n is the number of electrons transferred in a redox reaction, E is the applied

potential, F is the Faraday constant, R is the universal gas constant and T is the temperature in Kelvin.

A typical electrochemical cell features working, counter and reference electrodes (WE, CE and RE respectively), interfacing with electrolyte solution. CE is set by potentiostat to produce electric field balancing WE. The RE feeds the WE potential back to the potenetiostat [285]. When a potential is applied to electrode the electron transfer becomes initiated and faradaic current is generated, which can be related to the concentration of the oxidised/reduced species. This process can be described by Nernst equation [286, 287]:

$$E = E^o - \frac{RT}{nF} ln \frac{C_O}{C_R} \tag{1.2}$$

where, E^o is a standard potential of the redox, C_o and C_R are respectively the concentrations of the oxidised and reduced species. Thus, there exists a specific potential for a particular molecule's redox and a peak current is expected at this potential. Voltammetry is a common electrochemical technique and it is used for comparison of so called 'fingerprints' of redox reactions. It consists of applying various potentials to the cell and recording the current to identify the characteristic peaks on voltage-current curves [289].

Typically, there also arises a capacitive current due to a double layer formed at the electrode surface from charged ions. Once the potential is applied the capacitive current adds to the faradaic current. The timescale of charging of the double layer is associated with the size of the electrode. Historical attempts to enhance the mass transport resulted in the development of ultra-microelectrodes (or simply, microelectrodes). Unlike regular electrodes, to which the mass transport is assumed to be perpendicular with semi-infinite planar diffusion (or one-dimensional), the microelectrodes are characterised by rather spherical distribution of the diffusion fields towards the edges of the electrodes [290]. This feature contributes to the improvements in sensitivity, detection time and signal-to-noise ratio. This is usually observed in voltammetry, as the distribution of mass transport gets better, the current-voltage curve approaches the shape of a perfect sigmoid [291]. As a consequence, the faradaic current is more dominant and the characteristic peaks are easier to identify.

In order to increase the signal and to enable simultaneous tracing of multiple analyses, arrays of microelectrodes are often used. An important consideration for the arrays is the electrode density, since it can affect the distribution of diffusion. For instance, in a study comparing two set ups of gold multi-microelectrode arrays for chromium(VI) detection with high and low microelectorde densities, the effects of the electrode size and separation have been demonstrated to influence the cyclic voltammetry response. It was found that lower density contributes towards better analytical signal (Figure 1.5.2) [292]. It has been argued, that for the array signal described above to be achieved the separation has to be many times larger, than the microelectrode's radius [291], however, there has there is a compromise between the overall array size and the preferred diffusional regime.

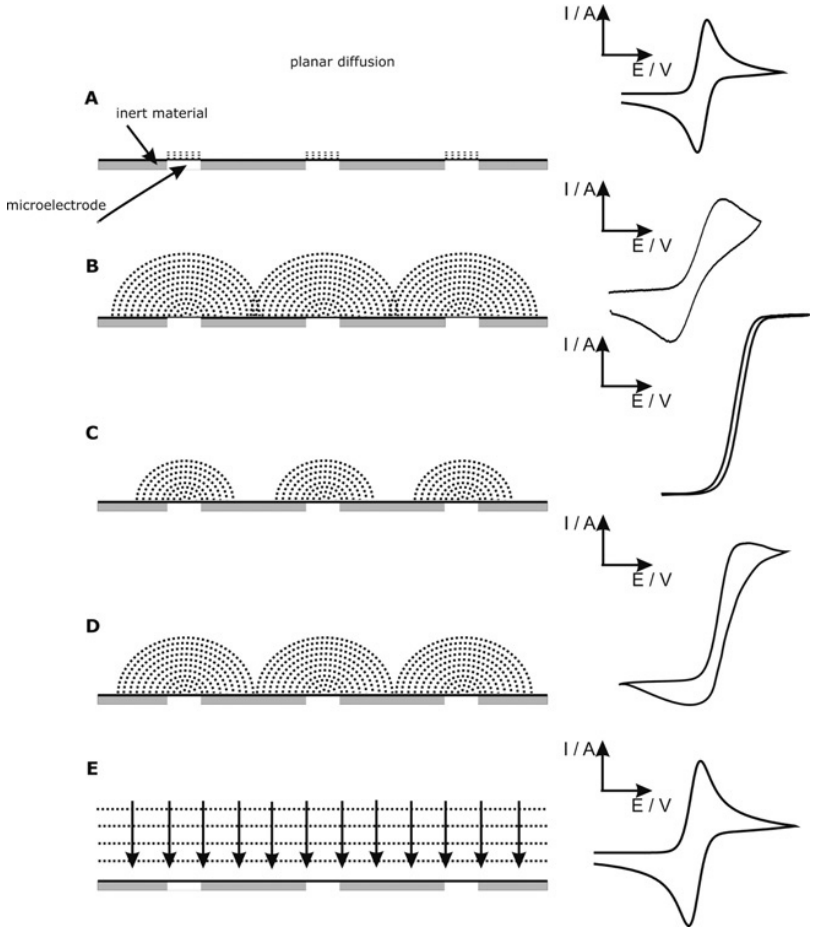

Figure 1.5.2 Different diffusional regimes depending on the array configuration and corresponding cyclic voltammograms.
A - planar diffusion profile resulting from the diffusion layers that as small relative to the electrode size. The voltage-current curve is peak-shaped.
B - overlap of the neighbouring diffusion zones influencing a mix between planar and hemispherical regimes, thanks to smaller electrode size. The voltage-current curve has better features and depends on the scan rate.
C - no overlap in the diffusion zones thanks to the appropriate microelectrodes' size and spacing. The voltage-current curve is sigmoid-shaped with clear current saturation plateaux, depending on the analyte concentration.
D - overlap of the diffusional zones due to decreased spacing between the neighbouring microelectrodes. The voltage-current curve is again scan-rate dependent and has peaks.
E - planar diffusion regime due to high density of the microelectrodes. The voltage-current curve is peak-shaped.
Adapted from Hood *et al.* 2009 [292].

2. Previous Results of the Group

2.1 Synthetic extracellular matrix

In this study we used a synthesised ECM matrix created with BIOMIMESYS® technology, developed by our collaborator, HCS Pharma (HCS Pharma, France). Previously a similar composition biomimetic hydrogel scaffold had been tested with adipocytes. The matrix was functionalised with adipose ECM components, including hyaluronic acid, collagen I, collagen VI and the cell-binding domain of fibronectin — RGDS, for the 3D culture of human and murine adipocytes (Figure 2.1A).

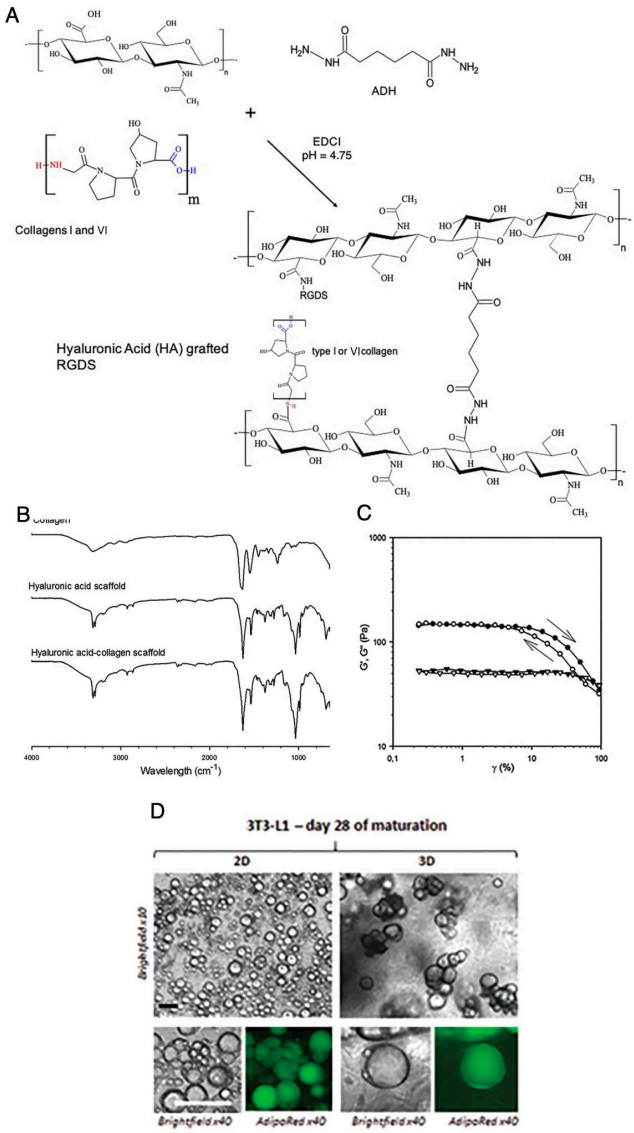

Figure 2.1 BIOMIMESYS® and adipocytes.
A - molecular diagram of BIOMIMESYS® synthesis (adapted from Roudaut *et al.*, 2024 [293]). **B** - FTIR characterisation of collagen, HA scaffold and the cross-linked HA-collagen scaffold. **C** - rheological measurements of the scaffold. **D** - bright field and AdipoRed-stained fluorescence images of 3T3-L1 cell line on 2D and scaffold after 28 days of maturation culture, scale bar 100 µm. B, C and D adapted from Louis *et al.*, 2017 [294].

The scaffold was characterised in terms of its elastic properties with a rheological oscillatory sweep technique (Figure 2.1C). It had a Young's modulus of 0.45 ± 0.05 kPa, which is similar to the mechanical properties of native adipose tissue ECM (1.5-3 kPa) [295]. For chemical bonds characterisation, Fourier-transform infrared spectroscopy (FTIR) was used (Figure 2.1B). It confirmed the successful incorporation of collagen into the scaffold, as evidenced by the presence of the amide III band at 1,240 cm^{-1} and the difference in intensity between the amide I band at 1,624 cm-1 and the band at 1,033 cm^{-1}. Morphological characterisation was performed with scanning electron microscopy (SEM). The scaffold had a homogeneous porous network with pore sizes ranging from 70 to 170 μm in diameter and a thickness of 2 mm, while the swelling ratio was measured to range from 50% to 70%. In functional biological tests with 3T3-L1 cells, scaffold's porosity provided a physiologically relevant microenvironment that supported the growth and differentiation of preadipocytes into mature adipocytes. The latter formed multicellular aggregates with in vivo-like organisation, reaching up to 120 μm in diameter after 4 weeks of maturation. Compared to 2D cultures, adipocytes grown in the 3D scaffold exhibited significantly higher lipogenic activity (up to 20-fold at day 28 for human white preadipocyte cultures) and differentiation rates, as well as a 3- to 7-fold higher expression of adipocyte-specific genes such as FABP4 (Figure 2.1D). The 3D cultured adipocytes also displayed a reduced sensitivity to lipogenesis inhibitors and a better regulated lipolysis, compared to 2D cultures. These findings suggest that the ECM-functionalised hydrogel scaffold provides a robust and physiologically relevant 3D culture system for studying adipocyte biology and metabolic regulation [294]. It was therefore hypothesised that such scaffold could be utilised for creating a 3D model of pancreatic tissue in this project.

2.2 Perfused islets

As a preliminary study to this thesis, islet on-chip perfusion had been carried out by the research group. In this experiment, two separate wells of an ibidi® μ-Slide III 3D perfusion chip (ibidi GmbH, Germany) were pre-seeded with 50 and 25 isolated mouse islets and perfused in parallel. The protocol involved 30 minute starvation with low glucose (2.8 mM) Krebs buffer solution (KRB), followed by 60 minutes of high glucose (20 mM) treatment another 30 minutes of low glucose treatment. After this a solution of 30 mM KCl was supplied for 15 minutes to stimulate maximum depletion of insulin by the islets. All of the solutions were perfused at 10 μl/ min and the outgoing liquid was sampled each 2 minutes. The collected samples were post-processed with mouse insulin ELISA kit to produce a continuous plot of the secreted insulin concentration over time (Figure 2.2). The expected behaviour of the islets would manifest in direct response to the hyperglycaemic condition with upregulation of insulin secretion. It was found, however, that insulin secretion pattern was opposite to the expectation with higher secretion observed during low glucose treatment and no secretion over the course of high glucose exposure. On the other hand, it appeared that KCl stimulation correlated with higher insulin concentrations.

These controversial results suggested that further repetitions with proper investigation of microfluidic environment were required, including estimation of volume and mixing dynamics of the perfused solutions.

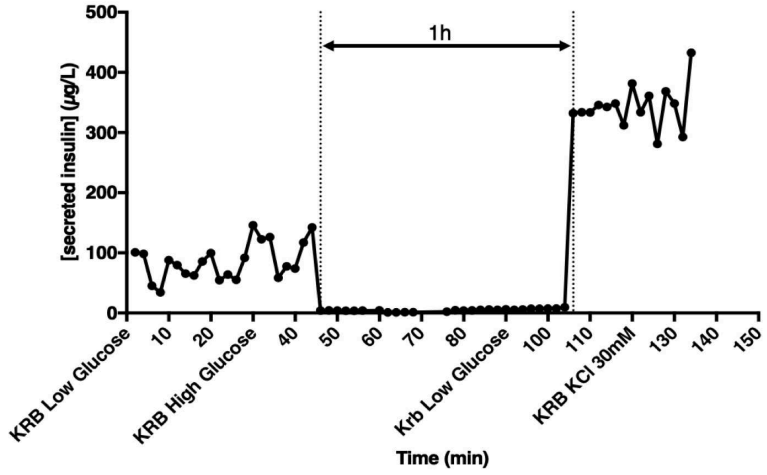

Figure 2.2 Islets on chip.
Preliminary study with perfused islets showing the GSIS insulin concentration results as collected during the experiment.

3. Objectives

The Micro3DBeta project aimed to develop an advanced microfluidic platform for the three-dimensional culture of pancreatic islets, enabling the research of the islets' response to various chemical and biochemical stimuli in a more physiologically relevant context. As a higher aim, the model was also to feature organoids from both pancreatic and adipose tissues to explore the chemical signaling between the two tissues — their cross-talk (Figure 3.1A). Microfabrication techniques were to be employed to produce a multi OOC device with connected microfluidic perfusion. The platform design was to allow precise control over the perfusion of islet cultures, while simultaneously integrating a quantification process for monitoring islet secretion through temporal and dynamic sampling. Electrochemical, impedance, and other sensors were proposed to be used for tracing specific biomarkers in targeted biochemical pathways. The system was required to be capable of high-throughput experimentation and automation to demonstrate how different input conditions affect the cellular responses in healthy conditions versus T2D.

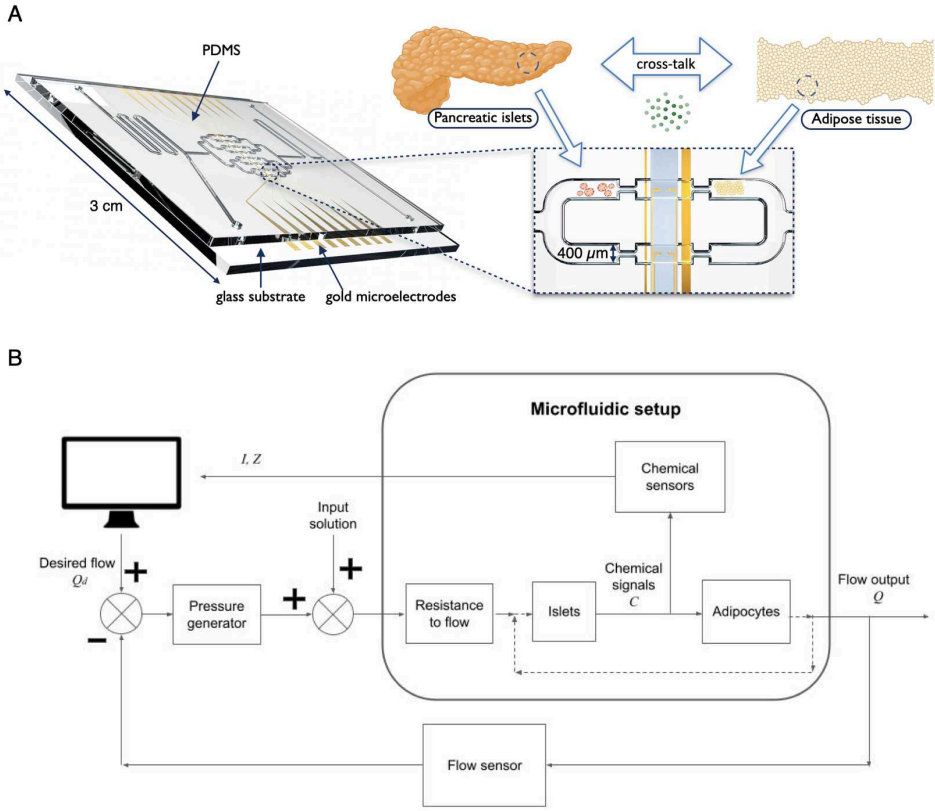

Figure 3.1 Micro3Dbeta concept.
A - microfluidic chip concept (*diachip*, not to scale) demonstrating the PDMS geometry on glass substrate, containing microelectrode array. Pancreatic cells along with adipocytes to be cultured in dedicated chambers, and solution to be monitored via biosensors placed in dedicated detection zones. **B** - block diagram, representing the automated perfusion system developed in this thesis.

In order to improve the microphysiological relevance, the organoids were to be cultured on the chip in 3D within synthetic biopolymer matrices engineered to mechanically represent the

organs of origin *in vivo* for improved cell differentiation, longevity, and signalling. The matrices were to be developed in collaboration with HCS Pharma based on BIOMIMESYS® hydro-scaffold technology. The main requirement for the 3D ECM was to meet the physiological relevance by achieving fidelity to the native pancreatic ECM. This would be done by synthesising the matrix from the biomolecules naturally occurring in the pancreas, including HA, collagens and fibronectin motif, — in order to resemble the chemical composition of the tissue. As well as this, the matrix would need to provide the accurate mechanical cues to the β-cells, hence it would require to exhibit similar viscoelastic properties and have stiffness equivalent to that of the native pancreatic tissue. Therefore, the synthesised ECM was to be validated by chemical characterisation and mechanical tests, such as rheology and stress-relaxation. Furthermore, it was essential for the matrix to accommodate formation of islets within its structure, hence its porosity had to fall within the range of naturally occurring islets — 20 to 400 μm [296]. The morphological aspects were to be verified with micro-scale imaging, such as SEM. Finally, the ECM scaffolds were expected to improve the viability and function of the cultured β-cells. For this, the matrix was to be tested with an insulin-secreting cell model. As a first confirmation step, a cheap and easy to maintain mouse-derived cell line MIN6 was planned to be used. ECM performance was to be compared with traditional 2D cell culture by carrying out short- and long-term interrogations with viability and GSIS assays. This 3D approach was intended to provide more accurate insights into β-cell function and dysfunction, contributing to a better understanding of the mechanisms underlying T2D.

Microfluidic diabetes-on-chip system (will be referred to as simply '*diachip*' elsewhere in this thesis) that was being developed in this PhD work, has been conceptualised as a multipurpose device with an extensive functionality. The proposed characteristics of the *diachip* included: perfusion of various liquids towards 3D cell cultures of islets or β-cells and adipocytes, chemical signal detection, capability of live-cell imaging, high-throughput scalability and automation of experiments. Therefore, the concept of the system consisted of several parts (Figure 3.1B) and featured:

- *pressure generator or peristaltic pump* — actuator to support perfusion;
- *input solution* — to supply nutrients to the cells and generate various environmental conditions;
- *substrate* — the bottom part of the *diachip*;
- *cell culture chambers* — dedicated cavities with 3D organoids for each tissue type representing respective organs;
- *chemical sensors* — devices for specific chemical signal detection;
- *flow sensor* — to monitor the microfluidic flow;
- *computer* — for automated control.

The microfluidic circuit was intended to further improve the microphysiological *in vitro* model by providing it with perfusion, mimicking the nutrient and signal gradients of the blood

flow. It was required to enable precise flow control with the use of pressure generator, flow sensor and automated input regulation in the real time. This would involve microfluidic system characterisation in terms of its volume and pressure to flow transfer function, as well as development of digital algorithms for input control and compensation. The microfluidic geometry of the *diachip* was planned to be incorporated with 3D ECM and was required to support long-term perfusion from several days up to a couple of weeks.

The *diachip* was to be produced at microfabrication facilities. Microfluidic geometry was to be designed using computer automated design (CAD) software, such as Autodesk Fusion 360, and to be produced by CNC machining of master mould for PDMS — a biocompatible transparent and fairly inexpensive material. The dimensions of the *diachip* were to be dictated by the microfabrication constraints, such as substrate size or photolithographic mask dimensions. Several parallel flow channels were proposed to be fit on a single *diachip* in order to increase the experimental capacity. For transparency required for live-cell imaging, glass was proposed as the substrate material.

Finally, the *diachip* was to feature biosensors for on-chip monitoring of the analytes involved in β-cell activity. In particular, it was planned to continuously trace glucose and insulin concentrations using an electrochemical amperometry in the microfluidic system in mM and nM range respectively. Biosensorial microelectrodes were to be fabricated with photolithography techniques and to reside in a dedicated detection chamber cavity of the microfluidic chip in order to avoid biofouling. In order to guarantee accuracy, an optimal mass transport around the microelectrodes had to be ensured. For this, it was first required to experimentally validate the appropriate electrode size and spacing, considering the sensitivity range. The microelectrodes were to be characterised in standard electrochemical solutions to confirm the geometrical parameters, using linear sweep voltammetry technique. An important objective would be to achieve high specificity, conductivity and non-fouling aspect of the electrode surface. It was therefore planned to be modified with carbon nano-structures. The characteristic reaction potentials were then to be determined from current-voltage peaks derived from cyclic voltammetry, during the exposure of the electrodes to the target analytes.

4. Materials and Methods

4.1 Extracellular scaffold fabrication and characterisation

4.1.1 Scaffold fabrication

The hydrogel scaffold was prepared as previously described [294]. The synthesis of BIOMIMESYS® Adipose Tissue scaffolds was carried out in two main stages. First, HA (9067-32-7, Baoding Faithful Industry Co., Ltd, China) was fully dissolved in pure water at a concentration of 3.64 µM. This solution was then supplemented with 10 mg of the RGDS motif (91037-65-9, Cayman Chemicals, U.S.A.), 7.22 µmol of type I collagen (c-136157, Santa Cruz Biotechnology, Inc., U.S.A.), and 2 µmol of type VI collagen (ab7538, Abcam, U.K.). The mixture was stirred for 1 hour until a uniform solution was achieved. In the second step, a hydrazide cross-linker (ADH, TCI Europe, Belgium) was dissolved in deionised water at a concentration of 103 mM and added to the solution, while the pH was adjusted to 4.75 with 1 M HCl (Fisher Scientific, France). The carbodiimide reagent (EDCI, TCI Europe, Belgium) was then dissolved in deionised water and introduced into the reaction mixture, which was left to gel for 2 hours under gentle stirring. The resultant hydrogels were dialysed against deionised water to eliminate any unreacted ADH and EDCI. Afterward, the purified hydrogel was cast into 96-well plates, frozen and lyophilised during 24 hours using a freeze dryer (Crios, Cryotec, France; capacity: 3 kg ice/24 h, T = 55°C). Finally, the hydrogel-loaded plates were sterilised under ultraviolet (UV) light for 30 minutes. (Figure 4.1.1).

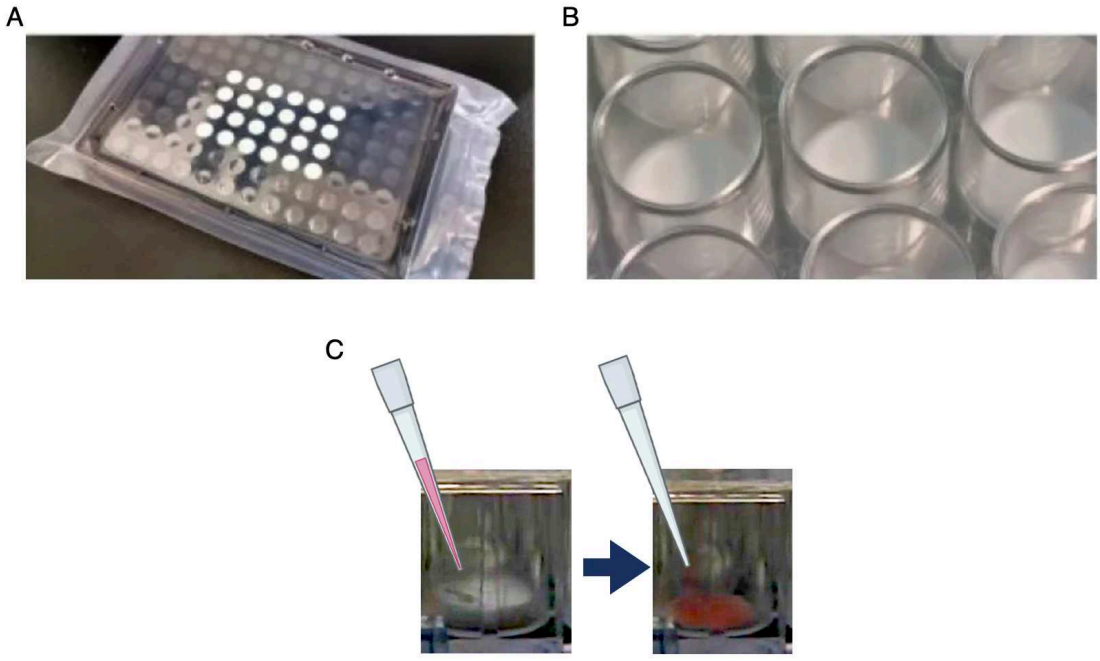

Figure 4.1.1 BIOMIMESYS® treated plates.
A, **B** - photographs of BIOMIMESYS® scaffolds after synthesis on 96-well plates. **C** - hydrogel formation after application of cell culture media to ready-to-use scaffolds. Photographs adapted from https://hcs-pharma.com/biomimesys/biomimesys-adipose-tissue/ (visited 07.08.2024).

4.1.2 *Rheological measurements*

The scaffold in hydrogel form consisted of both the liquid and solid phases and was hence considered to exhibit viscoelastic behaviour. For solid materials the shear stress, τ , is directly proportional to the shear strain, γ , with the rate of proportionality G — shear elastic modulus:

$$\tau = G\gamma \tag{4.1}$$

However, for the viscoelastic materials, shear modulus G^* is complex and includes storage modulus, G' , representing the elastic component (stored energy), and loss modulus, G'' , representing the viscous component (dissipated energy) — related in a Pythagorean theorem:

$$G^{*2} = G'^2 + G''^2 \tag{4.2}$$

$$\tan(\delta) = \frac{G'}{G''} \tag{4.3}$$

where, δ is the phase angle representing the phase shift between the two components. $\delta = 0°$ for a completely elastic material and 90° for totally viscous accordingly.

To investigate this relationship, a rheometric oscillation experiment was performed in a logarithmic amplitude sweep on scaffolds hydrated with media, fixed between two parallel plates. In this experiment the samples were deformed in an oscillatory manner while the amplitude of the oscillation was increasing and then decreasing. Such procedure allows to record the shear stress while varying the strain and relate to the storage and loss moduli (Figure 4.1.2).

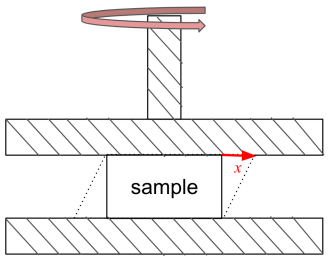

Figure 4.1.2 Rheometric oscillation experiment.
In rheological experiment the scaffold sample was contained between 2 parallel plates and subjected to rotational deformation with amplitude *x(t)*.

As the top plate rotates with the angular frequency ω , the imposed deformation, x , and hence the strain are given by:

$$x(t) = x_0 \sin(\omega t) \tag{4.4}$$

$$\gamma(t) = \gamma_0 \sin(\omega t) \tag{4.5}$$

where, x_o and γ_o are the respective amplitudes of the oscillation. At the same time the shear stress is out of phase with the strain:

$$\tau(t) = \tau_0 \sin(\omega t + \delta) \tag{4.6}$$

$$\tau(t) = \tau_0 \sin(\omega t)\cos(\delta) + \tau_0 \sin(\delta)\cos(\omega t) \quad (4.7)$$

From (4.1) and (4.3), the moduli relationship can be also deduced as:

$$G' = \frac{\tau_0 \cos(\delta)}{\gamma_0} \quad (4.8)$$

$$G'' = \frac{\tau_0 \sin(\delta)}{\gamma_0} \quad (4.9)$$

Therefore, the shear stress exhibited by the samples in this experiment relates to the loss and storage moduli as follows [297]:

$$\tau(t) = G'\gamma_0 \sin(\omega t) + G''\gamma_0 \cos(\omega t) \quad (4.10)$$

Rheological measurements were performed using Discovery HR10 from Ta Instruments (New Castle, U.S.A.), using a Peltier plane and a 25 mm plane geometry, sustained at 37°C. The scaffold was subjected to shear stress with an oscillation measurement in a logarythmic amplitude sweep from 1 to 500 Pa at a frequency of 1 Hz. Optimal gap between the plates for the samples used in this study was found to be 100 μm. Shear modulus *G** was determined as the square root of the sum of squares of the shear storage *G'* and loss *G"* moduli recorded in the linear viscoelastic region (LVR). The loss factor tan(δ) was obtained by taking the ration of *G"* to *G'*.

4.1.3 Stress-relaxation investigation

For the stress-relaxation experiment, two sets of samples, shaped to fit a 6-well plate, were prepared in two separate synthesis processes as described earlier. On day 1 following each synthesis, one plate from each batch (Batch 1 and Batch 2) was tested. Additionally, another plate from Batch 2 was stored at 4°C and evaluated on day 30 after synthesis. A third plate of Batch 2 samples was filled with cell culture media and incubated at 37°C, 5% CO_2 for 7 days.

TA.XTplusC Texture Analyser (Stable Micro Systems, U.K.) was used to perform the stress-relaxation measurements. For this, a spherical probe with a 6 mm diameter was connected to a 5g load cell. The experiment involved rapidly applying mechanical strain with the probe onto the biomaterial, which was placed between two parallel plates, and holding this deformation for 60 seconds before releasing it. During the process, the force exerted by the biomaterial against the probe was recorded (as shown in Figure 4.1.3).

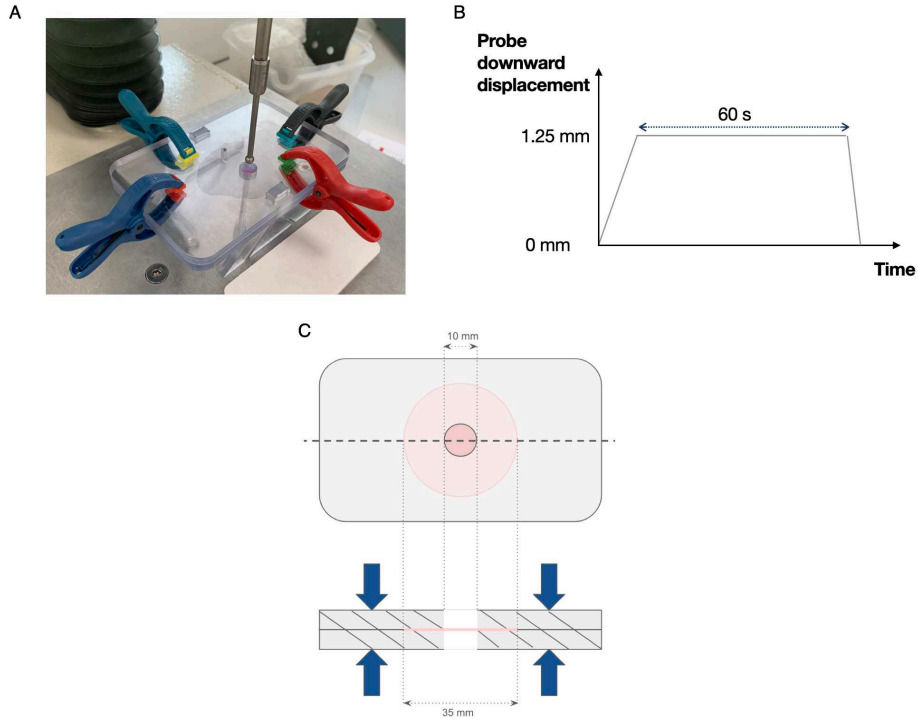

Figure 4.1.3 Stress-relaxation experiment.
A - photograph showing scaffold sample clamped between 2 parallel plates and spherical probe of the texture analyser. **B** - the spherical probe was used to swiftly apply stress onto the scaffolds through an opening and sustain it for 60 s, while the relaxation response of the samples was being recorded. **C** - schematic demonstrating top and section view of the plates and the opening of 10 mm in diameter, exposing the sample to the probe, not to scale.

The time-series data collected during the experiment was processed using a custom Python program that incorporated the Statsmodels, SciPy, and Scikit-learn libraries for model fitting and evaluation [298-300]. For data processing and visualisation, the Pandas, NumPy, and Matplotlib libraries were employed [301-303]. The data signal was filtered using lowess smoothing and subsequently fitted to a two-exponential model using non-linear least squares curve fitting. The quality of the model fit was assessed based on the R^2 value and the mean square error of the residuals. The fitted models were then normalised around their peak value. The code is provided in the Appendix 2.

4.1.4 Chemical characterisation with Raman spectroscopy

Raman spectra were collected for the scaffold and its individual components: HA, RGDS, and collagens type I and VI, over a spectral range of 380–3800 cm^{-1} using the HR Evolution spectroscope (Horiba Scientific, Japan). HA and RGDS were measured in their powder form, while the collagen samples were obtained by freeze-drying 2 mL of type I and type VI collagen at -50°C for 24 hours. The scaffold samples were prepared as previously described. For HA, RGDS, and type I collagen, a 632.8 nm laser was used as the excitation source, coupled with a 100x objective lens, focusing 15 mW of power at the sample's air interface under ambient conditions,

creating an approximately 1 μm² laser spot. The spectrometer was equipped with a diffraction grating of 300 grooves/mm, yielding a spatial resolution of 2 wavenumbers per pixel. Before data collection, the system was calibrated using the Raman line of silicon at 520.7 cm^{-1}. Single spectral acquisitions of 120 seconds were recorded for each sample. In contrast, type VI collagen spectra were acquired using a 785 nm laser, with two spectral acquisitions of 100 seconds each. Data processing was conducted using LabSpec 5 software (Horiba Jobin Yvon). To eliminate fluorescence interference, an 8th-degree polynomial baseline correction was applied. The average spectra were generated from three specimens of each material.

4.1.5 Surface characterisation with scanning electron microscopy

Fresh non-reconstituted scaffolds were visualised in their dry state using a scanning electron microscope ULTRA 55 (Carl Zeiss Microscopy GmbH, Germany) operated at 10 keV, with a working distance of approximately 12 mm. Pore measurements were conducted using ImageJ software. To identify the pores, the 'Band Pass Filter' tool was first applied for smoothing, followed by pixel intensity histogram thresholding using the ‘Li Thresholding’ method [304] , which distinguished the fibres (foreground) from the pores (background). The resulting binary image was then analysed using the ‘Analyse Particles’ function. Porosity was determined by calculating the ratio of the total pore area to the overall area of the SEM image, expressed as a percentage.

4.2 Cell culture procedures

4.2.1 MIN6 cell culture

MIN6 cells (AddexBio, U.S.A.) were cultured in complete MIN6 medium, consisting of DMEM with a glucose concentration of 4.5 g/L (31966-021, Gibco, U.S.A.). The medium was supplemented with 15% foetal bovine serum, 100 μg/ml penicillin-streptomycin, and 55 μM β-mercaptoethanol (M6250, Sigma Aldrich, U.S.A.). The cells were maintained at 37°C in an environment containing 5% CO_2. On day 0 of the experiment, cells were detached from a T75 flask using trypsin and seeded into 96-well plates at a concentration of 100,000 cells per well. For the 3D condition, the 96-well plates were preloaded with the matrix in each well, and the seeding process was performed in two steps. Initially, 30 μl of cell suspension was pipetted directly onto each matrix and incubated for 15 minutes. Then, 170 μl of culture medium was added to each well. All plates were incubated under the same conditions as previously described for a duration of 7 days, with media changes occurring every two days. Optimal cell seeding density was determined in a pilot 7-day evaluation, details provided in Appendix 3.

4.2.2 MIN6 metabolic activity and viability assessment

For the shirt-term 2D vs. 3D experiment, the metabolic activity of the MIN6 cells was evaluated on the days 0, 3 and 7 with resazurin reduction assay. For the long-term experiment, the assay was performed on the days 7, 14 and 21. Resazurin sodium salt (B21187, Fisher Scientific,

France) was dissolved in deionised water to create a 1 mM working solution, which was then sterilised using a 0.22 μm syringe filter. Before performing the assay, fresh media was added to each well. Following this, 100 μl of the resazurin solution was introduced into each well, and the samples were incubated for 4 hours at 37°C in an atmosphere with 5% CO_2. After incubation, 100 μl of media was collected from each well into a sampling plate, and fluorescence was measured using an Infinite 200 PRO microplate reader (Tecan Group Ltd., Switzerland). The fluorescence signal was recorded with excitation at 550/9 nm and emission at 590/20 nm. For the shirt-term experiment, a standard curve was produced based on Hills saturation curve. The curve was used to determine the cell number, dependent on the fluorescence value, reflecting the overall metabolic activity of the cells in the sampled wells. To achieve this, the assay was conducted using a range of different cell concentrations (0, 10, 20, 40, 100, 200, and 400 $x10^3$ cells per well) on day 0, after full cell attachment to the well bottom had been confirmed. No standard curve was made for the long-term evaluation.

Additionally, in the short-term, cell viability was assessed using 3-(4,5-dimethylthiazol-2-yl)-2,5-diphenyltetrazolium bromide (MTT) assay. Measurements were taken on day 3 and 5 of the culture period. During this, 20 μL of MTT (475989, Sigma Aldrich, U.S.A.) solution (5 mg/mL in PBS) was added to each well of a 96-well plate containing either 2D or 3D cultures. The plate was then incubated at 37°C, 5% CO_2 over the course of 4 hours. After this, the supernatant was discarded, and 150 μL of dimethyl sulfoxide (DMSO) was added to each well, with the plates then incubated at room temperature for 20 minutes. Absorbance was recorded at 540 nm. Each experimental set included 6 data points: 1 control and 5 samples from cell cultures. The results were expressed as a percentage of viability relative to day 3.

4.2.3 Immunostaining and fluorescence imaging

For fluorescence imaging, after 7 days of culture, the wells containing cell-loaded scaffolds and the chamber slides (Lab-Tek™ II CC2™ Chamber Slide, 154941, Thermo Fisher Scientific, France) were filled with a 4% paraformaldehyde fixing solution in phosphate-buffered saline (PBS) and left at room temperature for 20 minutes. Following fixation, blocking was carried out using a 1% BSA blocking buffer. Guinea pig anti-insulin primary antibodies (IR00261-2, Agilent Technologies, U.S.A.) were then added and incubated overnight at 4°C. After this, the cells were washed with PBS 4 times and incubated with anti-guinea pig secondary antibodies conjugated to 647 nm (A21450, Invitrogen, U.S.A.) for 1 hour at room temperature to visualise intracellular insulin. Nuclear staining was performed using 4',6-diamidino-2-phenylindole (DAPI) for 15 minutes, followed by thorough washing with PBS. Confocal imaging was performed with a Zeiss Axio Observer Z1 inverted microscope (Carl Zeiss Microscopy GmbH, Germany), equipped with a CSU-X1 spinning-disc unit (Yokogawa Electric Corporation, Japan) and a sCMOS PRIME 95B camera (Teledyne Photometrics, U.S.A.). Two-dimensional slides were imaged with a 40x objective lens. For the three-dimensional scaffold samples, a z-stack was acquired, comprising 100-200 images focused on a series of equally spaced planes along the z-axis with a 63x objective

lens. Image processing was performed using ZEN Microscopy Software (Carl Zeiss Microscopy GmbH, Germany). A single 2D projection image was created from the z-stack by selecting the maximum intensity of the pixels at each x-y coordinate, resulting in a pseudo-3D image viewed from above. Additionally, 3D reconstruction images were generated from the z-stacks. Control experiments that omitted primary antibodies were conducted to evaluate the specificity of the staining.

For live/dead staining and fluorescence imaging performed in long-term experiment as well as the multi-3D experiment, the procedure consisted first of a 15-minute staining with Hoechst (1/ in culture media) and Draq7 (1/ in culture media) in the incubator. This was followed by 4 washes with culture media and a 20-minute fixation in paraformaldehyde (4%) in PBS, kept at room temperature. Afterwards, the samples were washed with PBS 4 times and kept at 4°C prior to imaging. Confocal imaging with z-stack was performed with ImageXpress Micro Confocal system (Molecular Devices) using 10x objective lens.

4.2.5 RNA extraction and qPCR analysis

RNA samples were isolated using the TRIzol reagent (15596026, Invitrogen, U.S.A.). Before the extraction process, hydrogel scaffolds were placed in an Eppendorf tube along with TRIzol and homogenised with a 1-mL syringe fitted with a 19G needle to achieve effective disruption of the scaffolds. Following homogenisation, 200 µL of chloroform was introduced, and the samples were shaken vigorously for 10 seconds, then allowed to incubate at room temperature for 3 minutes. Centrifugation at 12,000 g for 15 minutes at 4°C was conducted to facilitate phase separation. The aqueous phase was then carefully transferred to a new tube, where 500 µL of isopropanol was added to precipitate the RNA. The samples were incubated at room temperature for 15 minutes and subsequently centrifuged at 12,000 g for 10 minutes at 4°C. The RNA pellet was washed twice with 1 mL of 75% ethanol, air-dried, and resuspended in 10-20 µL of RNase-free water. mRNA expression was quantified following reverse transcription using quantitative reverse transcription polymerase chain reaction (qRT-PCR) as previously outlined [305], employing FastStart SYBR Green master mix (Roche, Switzerland) on a LC480 instrument (Roche, Switzerland). The qRT-PCR data were normalised to the levels of endogenous cyclophilin reference messenger RNA (mRNA). Results were presented as relative mRNA levels of specific gene expression, calculated using the formula $2^{-\Delta Ct}$. A comprehensive list of primers is included in Table 4.2.5.

Gene Name	Gene symbol	Species	Primer
Cyclophilin	*Cyclo*	Mouse	ATGGCACTGGCGGCAGGTCC
			TTGCCATTCCTGGACCCAAA
Insulin1	*Ins1*	Mouse	GCCAAACAGCAAAGTCCAGG
			GTTGAAACAATGACCTGCTTGC
Insulin2	*Ins2*	Mouse	CAGCAAGCAGGAAGCCTATCT
			CAGGTGGGAACCACAAAGGT
Solute carrier family 2 (facilitated glucose transporter)	*Slc2a2*	Mouse	GTGACATCCTCAGTTCCTCTTAG
			GTCCAGAAAGCCCCAGATACC
Proprotein convertase subtilisin/kexin type1	*Pcsk1*	Mouse	TGATGATCGTGTGACGTGGG
			GGCAGAGCTGCAGTCATTCT
Glucagon-like peptide 1 receptor	*Glp1r*	Mouse	GTTTCCTCACGGAAGCGCCA
			AAGGAACCTGGGGGCCCATC
Urocortin 3	*Ucn3*	Mouse	TGATGCCCACCTACTTCCTG
			CTGTGTTGAGGCAGCTGAAG
Pancreatic and duodenal homebox 1	*Pdx1*	Mouse	CCCCAGTTTACAAGCTCGCT
			CTCGGTTCCATTCGGGAAAGG
v-maf musculoaponeurotic fibrosarcoma oncogene family, protein A	*MafA*	Mouse	CCTGTAGAGGAAGCCGAGGAA
			CCTCCCCCAGTCGAGTATAGC
Homebox protein Nkx6.1	*Nkx6.1*	Mouse	TCAGGTCAAGGTCTGGTTCC
			GTCTCCGAGTCCTGCTTCTT
Glucagon	*Gcg*	Mouse	AGGCCGAGGAAGGCGAGACT
			GGAGCCATCAGCGTGCCTGC
Somatostatin	*Sst*	Mouse	TCCGTCAGTTTCTGCAGAAGTCTC
			GTACTTGGCCAGTTCCTGTTTCCC

Table 4.2.3 List of primers used for qRT-PCR analysis.

4.2.4 Isolated mouse islets culture

All animal experiments complied with European Union guidelines and French ethical regulations (animal house agreement no. 59-350294, project approval no. APAFIS#2915-201511300923025v4). Five-week-old male C57BL/6J mice were housed under a 12 h light/dark cycle and fed a normal diet for 12 weeks as previously described [306].

Mouse pancreatic islets were isolated by injecting the pancreas with collagenase type V (1.5 mg/mL, Sigma Aldrich, U.S.A.) and digesting for 10 min at 37 °C. Islets were purified using a

polysucrose density gradient (1119, 1100, 1080, and 1060 g/mL from histopaque 1119, Sigma Aldrich, U.S.A.), collected between the 1100 and 1080 gradients, and handpicked for purity. Isolated islets were incubated for 24 h at 37 °C and 5% CO_2 in RPMI 1640 with Glutamax (61870044, Gibco, U.S.A.) supplemented with 10% fetal bovine serum and 100 pg/mL penicillin-streptomycin. 50 islets were seeded onto a well in the ibidi® µ-Slide III 3D perfusion slide (80376, ibidi GmbH, Germany) prior to perfusion experiment and kept in low glucose (2.8 mM) solution.

4.2.5 Glucose stimulated insulin secretion and insulin quantification

For the shirt-term 2D vs. 3D static experiments with MIN6 cells, GSIS was performed on the days 3 and 7 of culture. For the long-term evaluation, GSIS was performed on the days 7, 14 and 21. During this, MIN6 cells underwent a 1-hour starvation period using Krebs-Ringer bicarbonate buffer (KRB) supplemented with 0.5% bovine serum albumin (BSA, A7030, Sigma Aldrich, U.S.A.). Subsequently, cells were exposed to 2.8 mM and then 20 mM of glucose, each treatment lasting 1 hour. Insulin content was determined after cell lysis with 180 mM HCl and 75% ethanol, followed by neutralisation with 1 M Na_2CO_3. Following each treatment phase and lysis, the supernatant was collected from the wells and transferred to collection 96-well plates, kept on ice. The plates were then stored in at -20 °C until insulin quantification. The experiment was repeated twice. The static GSIS procedure is summarised in the Figure 4.2.1.

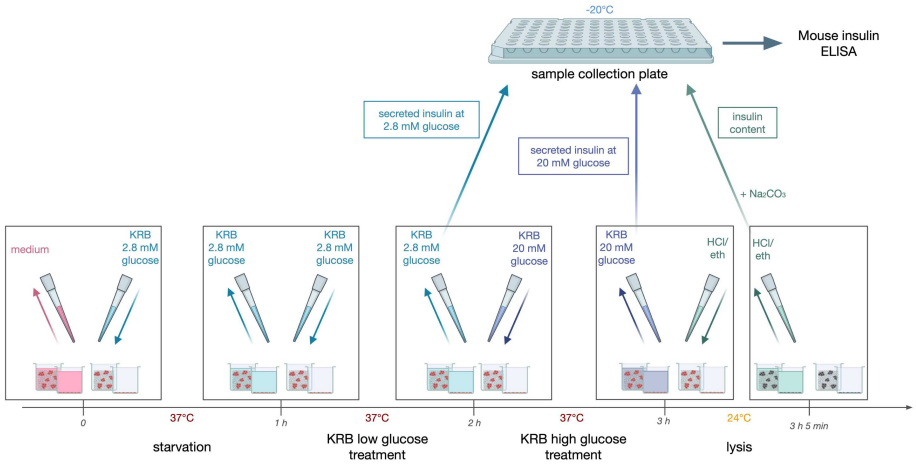

Figure 4.2.1 Process diagram of GSIS protocol for static culture.

For the perfusion experiment (setup presented in the section 4.3.1, Figure 4.3.1) with isolated mouse islets, the seeded ibidi® µ-slide III 3D perfusion was supplied with KRB low glucose solution (2.8 mM) for 30 minutes, followed by change of the supply test-tube and the perfusion of KRB high glucose solution (16.8 mM) for 60 minutes. Subsequently, another change of tube to low glucose solution and perfusion for 30 minutes took place. All solutions were supplied at 10 µl/ min flow rate and the output liquid was sampled onto a 96-well plate placed on ice for 1 minute every 2 minutes. At the end of perfusion the islets were lysed and neutralised with the

corresponding solutions for content collection, which was then diluted and added to the plate, which was stored at -20 °C until insulin quantification.

Secreted and content insulin concentrations from the collection plates were evaluated using mouse insulin-specific ELISA (10-1247, mouse insulin ELISA kit, Mercodia, Sweden). Cubic polynomial linear regression algorithm was used to establish interpolated calibration curves of ELISA absorbance vs. insulin concentration, based on the calibrator solutions supplied in the kit. Appropriate dilutions were applied to the collected samples, such that the concentration readings would fall within the calibration curve range recommended by the supplier, to improve the accuracy of the real insulin concentration estimation. Results were expressed as a percentage of insulin content.

4.2.6 Alternative culture surface treatments for 3D spheroid generation

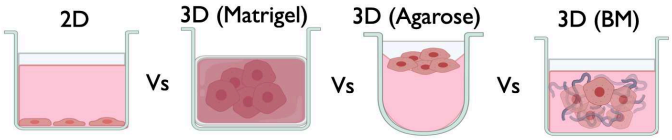

Figure 4.2.2 Classic cell culture (2D) and alternative 3D approaches.
BM - BIOMIMESYS® hydrogel scaffold.

To prepare the Matrigel® matrix for the alternative approaches of 3D culture experiment, the Matrigel® matrix was thawed overnight by at 4°C. After this, the vial was gently swirled to ensure proper dispersion of the gel. Next, 60 µL of the Matrigel® matrix was added to each well of a pre-chilled 96-well plate at a concentration of 8 to 11 mg/mL and spread evenly with a pipet tip. The plate was then incubated at 37°C, 5% CO_2 for 30 minutes to allow the Matrigel® matrix to set. All media that came into contact with the Matrigel® matrix was pre-chilled or kept ice-cold. The Matrigel® matrix itself was maintained on ice throughout the entire process to prevent excessive drying during the gelation phase. MIN6 cells were re-suspended in the MIN6 culture medium to achieve a final cell density of 20,000 cells per well, and 67 µL of the prepared cell suspension was pipetted into each well of the pre-coated 96-well plate. The plate was then incubated at 37°C, 5% CO_2 for 30 minutes. MIN6 cell culture media was added to the Matrigel® matrix to achieve a final concentration of 0.8 to 1.1 mg/mL (10%). A volume of 73 µL of the Matrigel® matrix medium mixture was gently added to each well by pipetting it down the side to avoid disturbing the cells or the gelled Matrigel matrix. The medium needed to be thoroughly chilled to ensure homogeneous mixing and even deposition of the Matrigel® matrix onto the cells in culture. The cultures were maintained for 2 days, with the Matrigel® matrix medium mixture (10%) replaced on the day 2.

To produce agarose coating, 1.5% wt/vol agarose solution was prepared using 2-hydroxyethylagarose and MIN6 cell culture media (45 mg per 3 mL). The solution was heated to 90°C. After this, 100 µL of the agarose solution was added to each well and left to set at room temperature for at least 1 hour. Subsequently, each well was seeded with 100 µL of media

containing 20,000 cells. The plate was returned to the incubator until the spheroids reached approximately 500 µm in diameter. The media was changed on the day 2, with 100 µL added to each well and an equal volume removed.

4.2.7 Statistical analysis

Data are expressed as mean ± standard deviation or standard error of the mean. A two-sided Grubbs test was consistently conducted to detect outliers, utilising Prism 10.0 (GraphPad Software). Statistical analyses were carried out using either a two-tailed unpaired Mann-Whitney U-test or a two-way analysis of variance (ANOVA) followed by Fisher's LSD tests. Statistical significance was accepted at $p < 0.05$ (*$p < 0.05$, ** $p < 0.01$, *** $p < 0.001$, and **** $p < 0.0001$).

4.3 Microfluidic setups, procedures and chips

4.3.1 Single channel setup

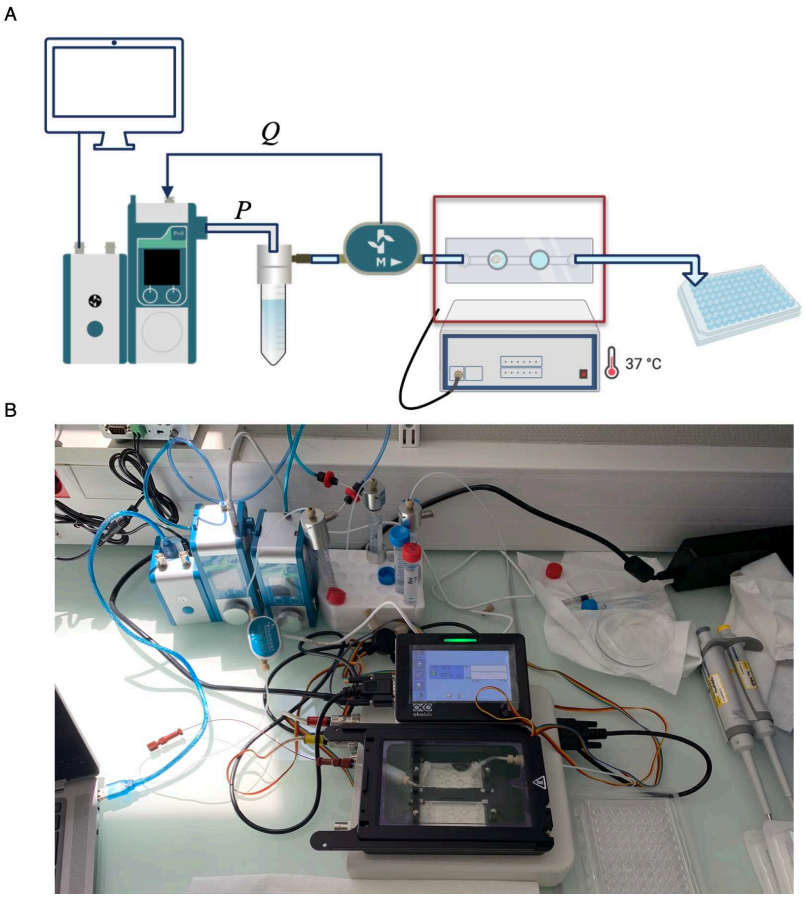

Figure 4.3.1 Microfluidic experiment setup.
A - Schematic depicting the key elements in the microfluidic setup, including pressure generator, fluid reservoir, flow sensor, microfluidic chip, temperature controller and sample collection plate. **B** - photograph of the setup with the pressure generator connected to a computer.

In microfluidic experiments the setup involved a pressure generator connected by air tubing to a test-tube with an input liquid, which in turn was connected by liquid tubing to a flow sensor followed by a microfluidic chip and outlet tubing. For various chips, the choice of connected tube diameter was between 0.13, 0.3 and 0.8 mm, depending on the required resistance to flow. The fluid flow was directed in an open-loop fashion towards a separate test-tube or a 96 well plate for post-processing. Pressure control was carried out with Fluigent™ Pressure Unit for pressure generation and Flow Unit (Fluigent, France) for flow measurement. For cell culture experiments on chip in particular, the chip was contained within a chamber with controlled temperature, sustained at 37°C (H301-T-UNIT-BL-PLUS, Okolab, Italy). The setup is depicted in Figure 4.3.1.

Fluigent™ equipment was digitally controlled, when connected to a computer using the software development kit (SDK) provided. The functions such as 'set pressure to a desired input value' and 'read flow measurement' were utilised by Python algorithms, developed in this thesis for specific experiments described below. The Python scripts for the specific experiments are available in the Appendix 4.

4.3.2 Q-P experiment

In Q-P experiment a range of varying pressure inputs from 0 to 1000 Pa was applied to a microfluidic circuit through Fluigent™ Pressure unit. During this, the pressure and flow rate readings were collected from the sensors. The pressure step was 1 Pa and the sampling rate was 0.1 s. A Python algorithm was used to automate the process, which consisted of the following steps:

1) The pressure input set to a new value, starting at the minimum value in the range.
2) 5 second wait time allowed for the input to settle.
3) Real pressure and flow rate readings sampled for 5 seconds.
4) New pressure input set by increasing the current pressure by the step value.
5) Steps 2-4 repeated until the maximum pressure in the range is reached.

4.3.3 Volume estimation experiment

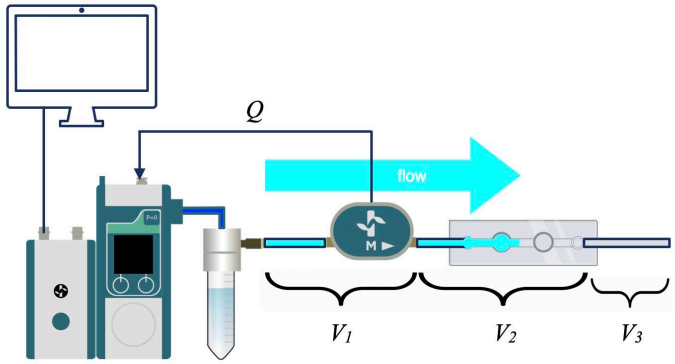

Figure 4.3.2 Volume estimation experiment.
Schematic depicting the process for estimating the volume of a microfluidic system. As the pressure generator applies fluid flow across the tubes of known length (segments V_1 and V_3), the flow rate Q is recorded over time to determine the volume of the segment of interest, V_2.

Volume estimation experiment (Figure 4.3.2) was developed to determine the volumes of complex chip geometries and it consisted of 3 steps. First, the coloured liquid/culture medium was pushed through the circuit by applying positive pressure, until it crossed the flow sensor and pressure was put to zero. The volume of the liquid pushed through the circuit was calculated using the known lengths and diameters of the tubes and noted as V_1. Second, positive pressure was applied into the system to continue pushing the liquid through the segment of interest, during which the flow rate was recorded over time at the sampling rate 0.1 s and stored by a python script. The volume of the second push of liquid could be estimated the sum of flow rates multiplied by the sampling rate. This volume was then noted as V_2. Finally, the remaining length of the tubes of known diameter leading to the waste reservoir was used to calculate the remaining volume, V_3. The total volume of the system could then be estimated as the sum of V_1, V_2 and V_3.

4.3.4 Bifurcation setup

Bifurcation setup (Figure 4.3.3) included a split into two parallel channels. The setup comprised of a Fluigent™ pressure generator connected to a reservoir with red dye-coloured water. The reservoir was connected to Fluigent™ OMI High Resistance chip with a tube of 0.8 mm in diameter and 43 cm in length. The chip was then connected to Fluigent™ Flow Sensor with a 7 cm long soft tube of 0.8 mm in diameter to record the total flow rate for the system, Q_T. The flow sensor was linked to a 90° bidirectional flow divider with a tube of 0.3 mm in diameter and length of 32.5 cm. The two outlets of the flow divider were supplying the liquid to two parallel channels on Ibidi® µ-slide III 3D perfusion with two tubes of diameter 0.3 mm and length 11.5 cm. The outlet tubing of the µ-slide channels were followed by the corresponding flow sensors to measure the flow rate on each channel, Q_1 and Q_2. Finally the channels were connected to corresponding waste collection reservoir, each with a 30 cm long tube of 0.8 mm in diameter.

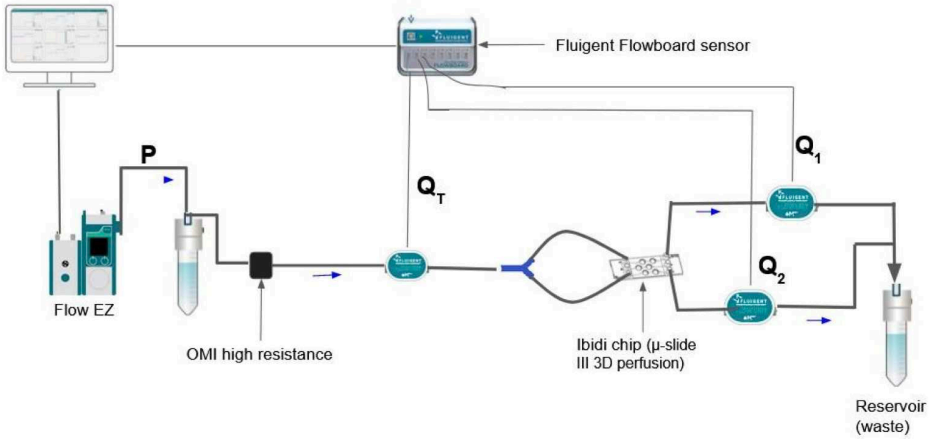

Figure 4.3.3 Bifurcation setup.
Schematic, produced by Dickson Akoto for his M1 internship report, depicting the microfluidic system arrangement with 2 branching channels.

4.3.5 *Hydrogel scaffold chip fabrication and testing under flow*

A microfluidic chip was designed in order to evaluate the synthetic biomaterial matrices' performance under flow conditions. The chip geometry was confined to the dimensions of a microscope slide (75 x 25 mm) and featured a single input branching to 4 cell culture wells and to 4 corresponding outputs, all connected by microfluidic channels. After several versions the optimal parameters for the chip were chosen as follows: 60 µl and 4 mm wide wells; 100 µm wide and 200 µm thick channels. A sandwich design was implemented aiming to maintain sufficient height of the liquid columns inside the wells, dictated by the hight of the input microchannels. It consisted of 2 parts: top with the channels and bottom with the wells — aligned and sealed together and attached to the glass substrate. The resulting liquid filling volume of the wells was therefore approximately 30 µl. A CAD of the chip was modelled in Fusion 360 software (Figure 4.3.4).

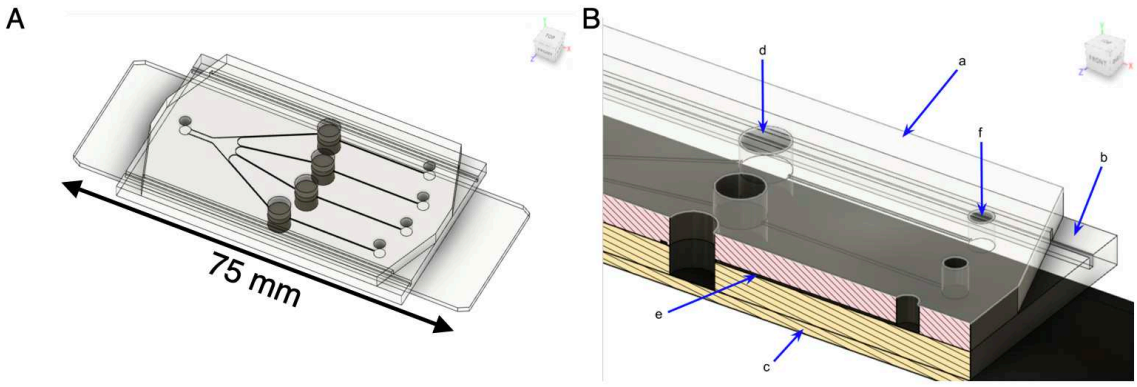

Figure 4.3.4 Microfluidic chip CAD for scaffold experiments.
A - Assembly view. **B** - Section: **a** - top part, **b** - bottom part, **c** - glass substrate, **d** - cell culture and scaffold well, **e** - microchannel, **f** - flow output.

The chip was fabricated from PDMS (SYLGARD™ 184 Silicone Elastomer Kit, Dow Inc., U.S.A.) with monomer : cross-linker mixing ratio 17 : 1, using an aluminium master mould, produced by CNC milling. For cross-linking, the uncured PDMS was mixed, degased in vacuum and poured into the aluminium mould master, which was left in 70°C oven for 2 hours. Bonding of the parts together and to the glass has been ensured by depositing thin uncured PDMS layer between the assembled cured parts with a brush and treating solidified surfaces with corona plasma for 1 minute each. Hydrogel solution was then deposited into the wells, after which the chips were frozen, lyophilised, and sterilised with UV radiation. Glass coverslip or adhesive tape were attached on top of the wells to seal the chips. The process is summarised in Figure 4.3.5.

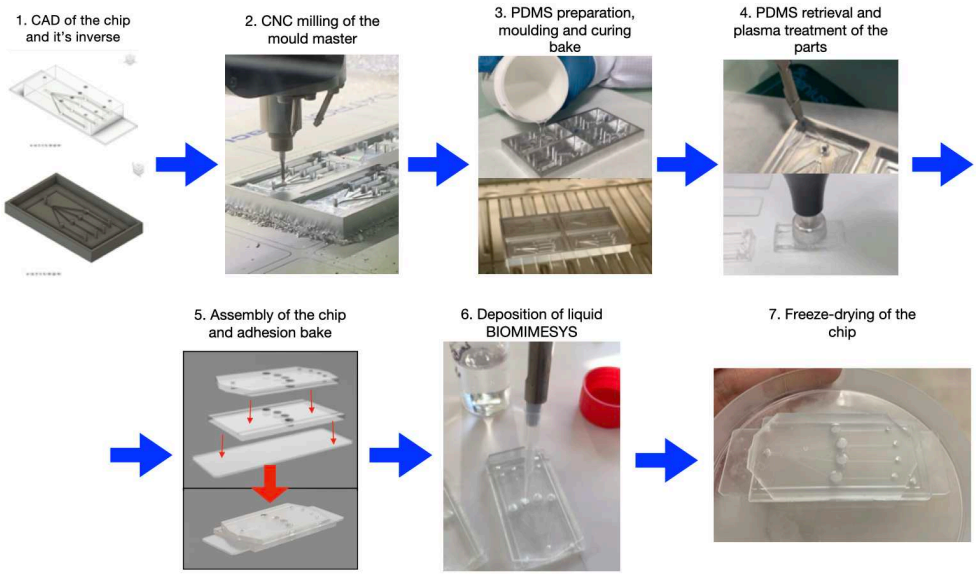

Figure 4.3.5 Hydrogel scaffold chip fabrication.
The process involved CAD creation and CNC milling of a mould master for the chip. Next, PDMS was cured producing the mould geometry. The chip was then assembled and cured for adhesion of the parts. After this, liquid BIOMIMESYS® solution was applied to the dedicated cell culture wells of the chip and it was liophilised. Chip design underwent several alterations to improve the detachment from mould master as well as microfluidic resistance characteristics, hence some images of the mould may differ from the resulting chip.

Both biomaterial-treated and empty chips were tested in a microfluidic perfusion setting in the Q-P experiment with PBS. Quadratic linear regression algorithm was applied to pressure and flow rate readings to determine the unique Q-P relationships for each chip in order to compare the contribution of the hydrogel scaffold matrix to the resistance to flow.

4.4 Microelectrode fabrication and characterisation

4.4.1 Microelectrode array design

Microelectrode array (MEA) with specific geometrical parameters was designed to determine the optimal electrode size and density, considering the effect of diffusion zones and flow in order to maximise the signal and minimise the detection time. The design criteria was based on the works of [307] and [308] (Figure 4.4.1A), the core parameter of which was a dimensionless scan rate, σ , for a cyclic voltammetry experiment:

$$\sigma = \frac{nFa^2}{4RTD}\frac{\partial v}{\partial t} \tag{4.11}$$

where, v is the potential and a is the radius of the electrode. Assuming single-electron reaction (n = 1), bioincubation temperature (T = 310 K), quasi-steady state of reaction at a slow

scan rate ($\partial v/\partial t$ = 1 mV/s) and using diffusion coefficient for insulin as $D = 5 \cdot 10^{-10}$ m²/s [309] - gives the dimensionless scan rate related to the electrode radius roughly as following:

$$\sigma = 2 \cdot 10^7 \cdot a^2 \tag{4.12}$$

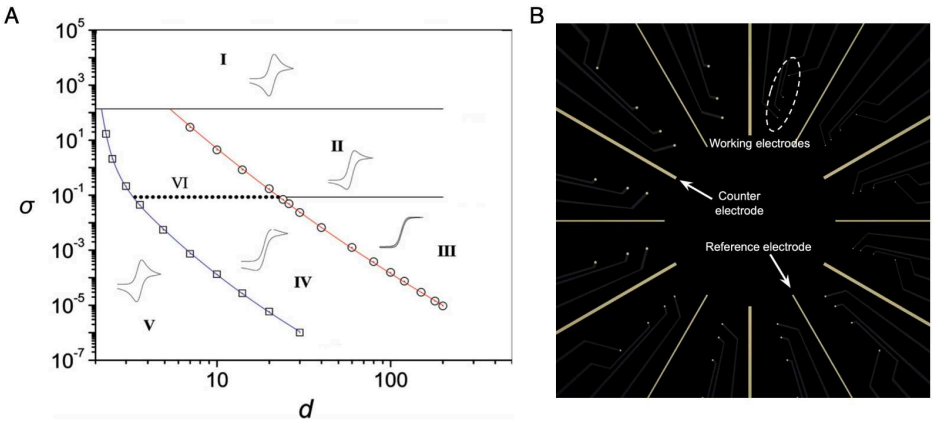

Figure 4.4.1 Microelectrode array for parameters optimisation.
A - Design criteria for σ and *d* expressed in terms of *a*. Adapted from Guo and Lindner, 2009 [307]. **B** - layout of microelectrode evaluation array, featuring working microelectrodes, counter electrodes and reference electrodes.

A range of 20-50 µm was selected as the typical microelectrode diameter, which according to (4.12) corresponds to σ between 0.0020 and 0.0125. Using the zone diagram provided by [307], it can be referenced that the sweet-spot range for the electrode centre-to-centre spacing distance, d , would be 30a-50a in terms of the electrode radius. Therefore the evaluation radius was chosen as an arithmetic sequence, while the spacing distance range between the neighbouring electrodes — as the geometric sequence for the i^{th} term:

$$a_i = 10 + \frac{15}{2}(i - 1) \tag{4.13}$$

$$d_i = 15a\left(\frac{5}{3}\right)^{i-1} \tag{4.14}$$

	d		
a	15*a*	25*a*	42*a*
10.0 µm	150.0 µm	250.0 µm	420.0 µm
17.5 µm	262.5 µm	437.5 µm	735.0 µm
25.0 µm	375.0 µm	625.0 µm	1050.0 µm

Table 4.4.1 Microelectrode evaluation array testing parameters

The resulting values of *a* and *d* for the evaluation array are given in Table 4.4.1. In addition to the working electrodes described here, reference and counter electrodes have also been included in the layout. The array was designed in a circular shape featuring 4 sets of electrodes of each

radius and corresponding spacing. The spacing $d = 15a$ was selected as the starting point outside of the referenced range in order to verify the referenced guidelines.

In addition to the working electrodes, reference and counter electrodes of the respective widths of 30 and 60 µm were also added in the layout (Figure 4.4.1B). The arrangement included a pair of these electrodes for each set of working electrodes, lying at equal distance apart from each other.

4.4.2 Array microfabrication

The MEA microfabrication process is summarised in Figure 4.4.2. As the first step, an array was deposited onto a glass substrate. For this, a 1000 nm layer of negative resist AZ nLOF 2020 (diluted, MicroChemicals GmbH, Germany) was spin coated onto a 3 inch glass wafer, exposed to UV light for 3.5 s in hard contact mode at 10 mW/cm², constrained by the first photomask in MA6/BA6 mask aligner (SÜSS MicroTec SE, Germany). The samples were heated at 110°C to ensure the cross-linking reaction and developed in AZ 326 MIF (MicroChemicals GmbH, Germany) for 30 s and consequently rinsed with deionised water and blow-dried using nitrogen gun. Next, 10 nm of Ti and 500 nm of Au were deposited by vacuum thermal evaporation performed with MEB 550 SL (PLASSYS, France) evaporator. Finally, lift-off process involved two cycles of 70°C heated ultrasonication in SVC-14 photoresist stripper (Kayaku Advanced Materials, Inc., U.S.A.), 20 minutes each, followed by deionised water rinsing and nitrogen blow-drying. Photomasks' KLayout designs are provided in the Appendix 5.

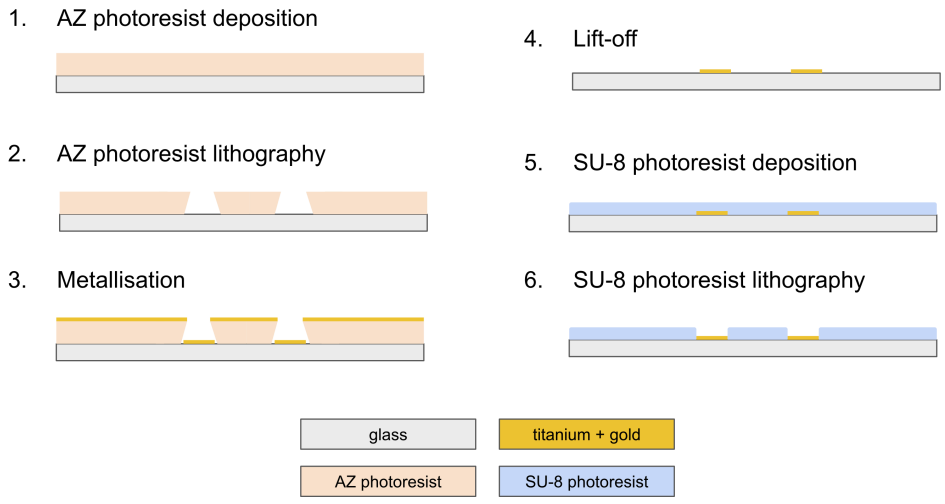

Figure 4.4.2 Array microfabrication process.
Diagram depicting the stages of microelectrode array fabrication, including AZ photoresist deposition and lithography by UV light through a photomask, followed by metallisation and lift-off. Next, SU-8 deposition and photolithography was performed to produce the insulating layer with defined geometry on top of electrode tracks.

Second step involved the fabrication of the passivation layer to cover and insulate the electrode tracks, while exposing the working surfaces. The process has been optimised for the glass substrates in order to achieve the required insulating layer thickness and feature resolution. The samples were first pre-baked for 10 minutes at 200°C hotplate to evaporate any remaining

solvent and water molecules. After this, the samples were cooled using blow-dry gun and placed onto the spin coater. 2 mL of SU-8 2002 negative photoresist (Kayaku Advanced Materials, Inc., U.S.A.) was then dispensed at moderate speed to ensure a thin uniform puddle covering all the sample area. The spin coating process involved an open 500 rpm spin for 10 s followed by closed-lid 1050 rpm spin over the duration of 30 s. Then the samples were placed onto 100°C hotplate for 2 min and then moved to 40°C hotplate to reduce the film stress effect during soft bake. Next, the samples were aligned with mask aligner to match the electrode pattern of the second photomask with the previously deposited tracks. This was followed by 3 s long hard contact UV exposure. Subsequently the samples underwent 90 s post-exposure bake as the temperature was ramped from 75 to 95°C , after which the samples were let cool down at room temperature. Finally, the development was performed in SU-8 developer (Kayaku Advanced Materials, Inc., U.S.A.) over the course of 2 minutes, whilst the beaker containing the samples was agitated at 170 rpm, followed by rinsing with isopropyl alcohol and deionised water and nitrogen blow-drying. Thickness of the SU-8 features was confirmed using Dektak XT diamond stylus profilometer (Bruker Corp., U.S.A.).

A PDMS ring was also fabricated similar to the process described in Section 4.3.5, and attached to the array in order to contain liquids for electrochemical experiments.

4.4.3 Electrochemical characterisation

Slow scan linear sweep voltammetry was employed to test the electrodes separately and pairwise in 2 mM solution of $K_3[Fe(CN)_6]$ in 1 M of KCl (Sigma Aldrich, U.S.A.). For this, PalmSens4 potentiostat (Palmsens B.V., Netherlands) was used, connected to the electrodes with 2 working electrode channels, as well as corresponding channels for the counter and reference electrodes (as shown in the Figure 4.4.3 A), and the signal was recorded with PS Trace software. The experiment was designed to record the current produced in ferricyanide reduction reaction to ferrocyanide as the potential was decreased from 0.25 V to -0.55 V in the forward sweep and vice versa in the backward sweep. The scan rate was set to 1 mV/s to ensure the quasi-steady state. The devices were cleaned with deionised water and pure ethanol before use.

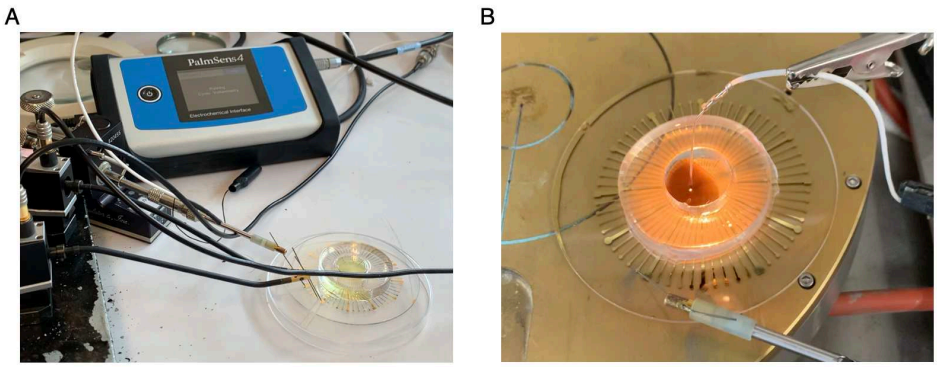

Figure 4.4.3 Electrochemical experiments.
A - The setup for $K_3[Fe(CN)_6]$ reduction voltammetry experiments with probes connecting PalmSens potentiostat channels to the corresponding working, counter and reference electrodes of the array, exposed to ferrocyanide/potassium chloride solution. **B** - graphene oxide deposition setup with a Pt reference electrode.

4.4.4 Graphene oxide deposition

Microelectrode surface modification was performed with GO deposition. GO flakes (Sigma Aldrich, U.S.A.) were dispersed in ultrasonic water bath and diluted in deionised water to obtain a suspension of 0.5 mg/mL. MEA samples were cleaned in 30% HCl and then 70% ethanol to remove excess salts from the surface, followed by rinsing with deionised water and blow-drying. The electrodes were then exposed to the GO suspension as the applied potential was swept from 0 to 0.75 V in a cyclic voltammetry regime for 100 cycles at 0.1 V/s (the setup is shown in the Figure 4.4.3 B). The deposition was then confirmed with SEM imaging.

5. Results

5.1 Generation of 3D model of pancreas with synthetic extracellular matrix

5.1.1 Chemical characterisation of the scaffold

Synthetic extracellular matrix BIOMIMESYS® used in this project, was comprised of integral connective tissue components, such as HA, collagens type I and VI and RGDS, — covalently cross-linked with each other. HA was used to ensure the swelling of the scaffold, collagens were chosen to provide the structural stability, whereas RGDS — for cell adhesion and growth factor binding properties.

In order to confirm the chemical composition and bond formation, Raman spectroscopy was performed on the scaffold and its major chemical constituents: HA, type I and type VI collagens and RGDS. The average spectra of 3 specimen each are presented in Figure 5.1.1. The spectrum of collagen type VI is presented in the range of 380-2800 cm^{-1}, due to limited Si sensor sensitivity at higher wavenumbers for the laser configuration employed.

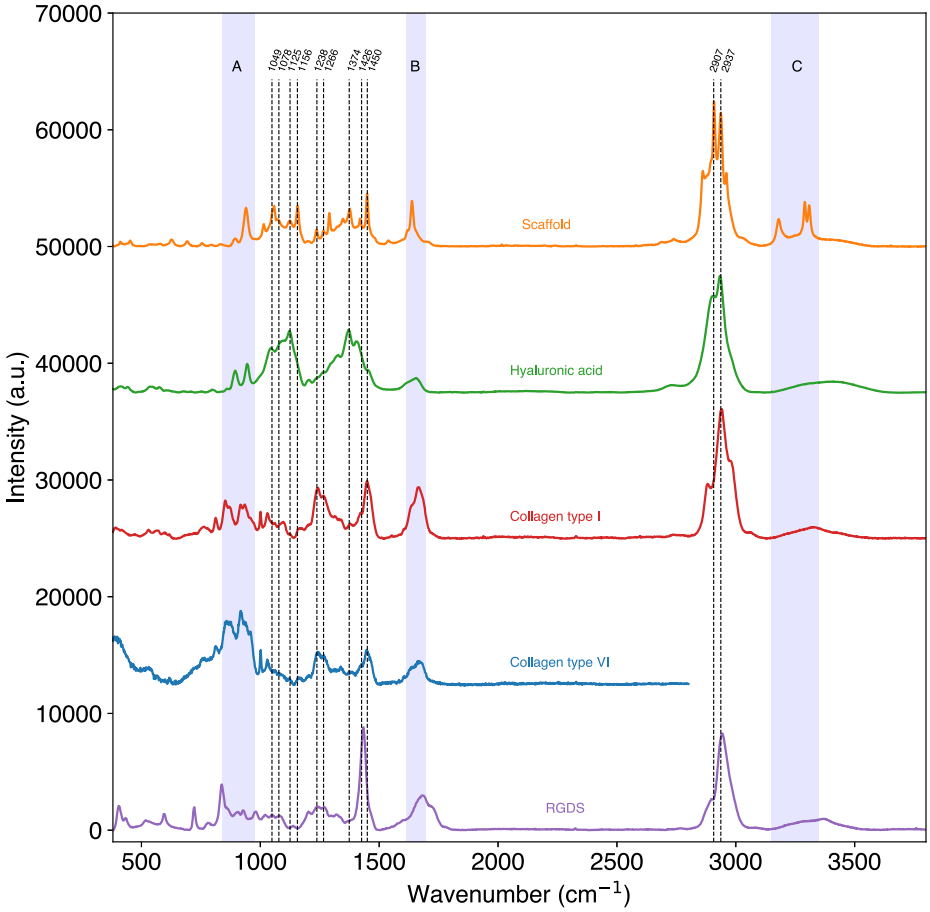

Figure 5.1.1 Raman spectroscopy of BIOMIMESYS® scaffold and its constituents. Raman spectroscopy profiles of collagen type I (red), hyaluronic acid (green) and the scaffold (yellow) were obtained. The highlighted regions correspond to the C-C and C-O-C stretching bands (**A**), the amide I band (**B**), and the N-H stretching bands (**C**). Three samples of each material were prepared, and spectra were collected under dry conditions at ambient temperature. Fluorescence noise was eliminated using polynomial baseline correction, and the average spectrum for each chemical is presented (n=3).

The spectral patterns of both collagen types were similar thanks to their comparable chemical compositions. Amide bands were observed in the spectra of HA, RGDS, collagens, and the scaffold. For example, amide I band was observed in the region of 1630-1690 cm^{-1}, resulting from the C=O stretching vibration. While this peak appeared at higher wavenumber for HA, RGDS, and collagen samples, it was downshifted to 1640 cm^{-1} in the scaffold, indicating a conformational change from β-sheet to α-helix [310]. Additionally, amide III peaks at 1238 cm^{-1} and 1266 cm^{-1} were present in all spectra, corresponding to C-N stretching and N-H bending vibrations. N-H in-plane deformations were also found in the scaffold spectrum at 1426 cm^{-1}, similar to the collagens' and RGDS spectra.

The peaks at 890 cm^{-1} and 938 cm^{-1} bands appeared in the scaffold spectrum and were associated with the breathing of proline ring and C-C stretching of the collagen and RGDS backbone, respectively. Together with the peak at 1125 cm^{-1}, these can also be linked to the stretching of the C-O-C glycosidic bond, forming the polysaccharide backbone of HA. Furthermore, the peak at 1049 cm^{-1} has both appeared in HA and as a shoulder in the scaffold spectrum, attributed to the C-O stretching vibration of the alcoholic group (-OH). Similar vibrations were inherited by the scaffold from RGDS, observed at 1078 cm^{-1}. The peak at 1374 cm^{-1}, arising from C-H and CH_2 out-of-plane deformations, was seen in both HA and scaffold spectra, together with the CH stretching peak at 2907 cm^{-1}. The scaffold also inherited CH_3 and CH_2 deformation peaks at 1450 cm^{-1} and 2937 cm^{-1} from collagen.

A distinct peak at 1156 cm^{-1}, corresponding to C-N stretching, indicated the formation of new cross-links between the carbonyl and amine groups of HA and collagen. A significant peak at 1296 cm^{-1} in the scaffold spectrum resulted from the twisting of CH_2 methylene groups of the cross-linking agent ADH. In addition to this, a group of high-intensity peaks in the 3150-3350 cm^{-1} region in the scaffold's spectrum can be assigned to N-H stretching, originating from urea linkages of EDCI/NHS formed between the polysaccharide chains during the synthesis. These findings confirmed the expected chemical composition of the scaffold as well as the cross-linking of the key components [311-313].

5.1.2 Morphological characterisation of the scaffold

Physical structure of cell-free scaffolds was studied using SEM in order to evaluate the porosity — an important aspect for adhesion, integration and growth of biological cells. The biomaterial was characterised as a mesh of irregularly distributed, thin, interlinked, non-uniform, concave-shaped structures of varying sizes, resulting from the cross-linking of the HA and collagen fibres. The space between these fibres formed a homogeneous network of highly open and interconnected. The pores appeared evenly distributed throughout the entire scaffold volume, as evident from top, bottom and cross-sectional images (Figure 5.1.2 B, D and C respectively).

The pore diameters were measured ranging from 1.82 to 135.07 μm and the average porosity was determined as 47.76 ± 4.48%, providing sufficient volume for structural support of biological cells. The scaffold was therefore demonstrated to exhibit the appropriate morphology for 3D cell culture application.

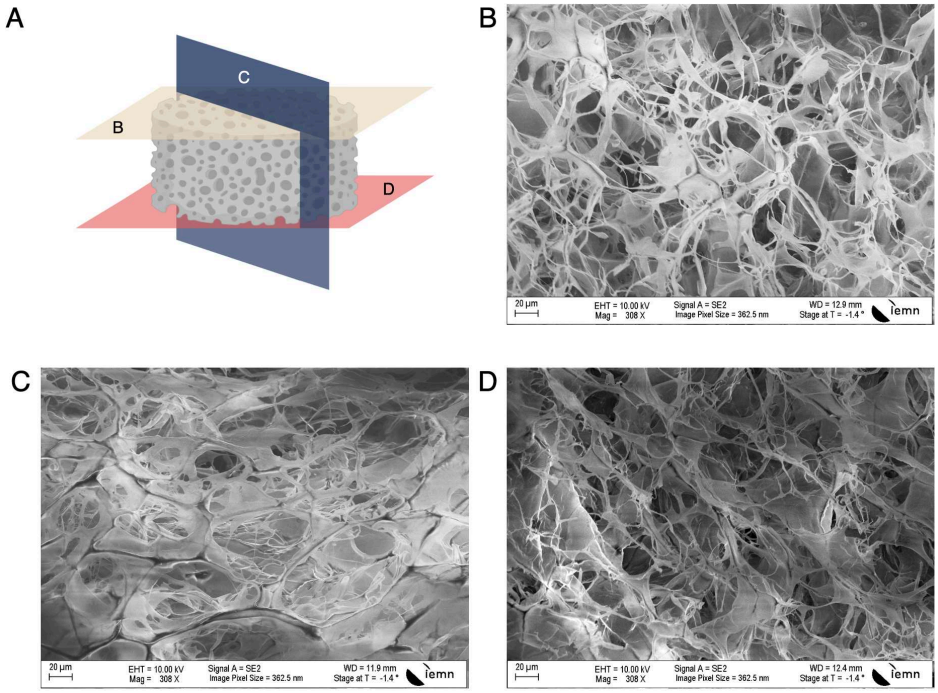

Figure 5.1.2 Morphological characterisation of the scaffold.
SEM images, as illustrated in schematic **A**, reveal the microstructure of the top (**B**), section (**C**), and bottom (**D**) of the scaffold. Prior to imaging, the scaffolds were freeze-dried. Sputter coating was not necessary, as the fibres were detectable at 10 kV with minimal charging effect. The porosity of the scaffold was assessed by examining the open areas between the fibres.

5.1.3 Mechanical characterisation of the scaffold: shear stress

In order to compare the mechanical stiffness properties of the synthesised scaffold with native pancreatic ECM, a shear stress rheological investigation was carried out. This allowed to decompose the complex viscoelastic properties of the biomaterial into solid and liquid phases, represented by shear storage (*G'*) and loss (*G''*) moduli, respectively. The moduli were recorded during the rheological oscillatory deformation experiment and presented in Figure 5.1.3.

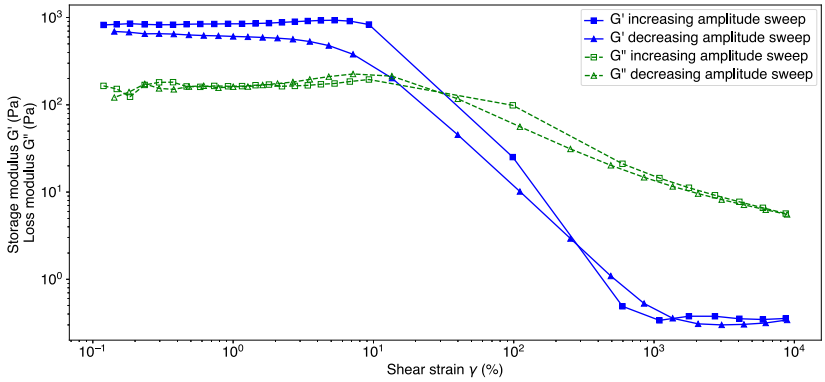

Figure 5.1.3 Rheological evaluation of the scaffold.
Log scale plot for rheological response of scaffold to oscillatory strain.

For small deformation amplitudes (<10%) no change in either of the moduli was observed, indicating that scaffold structure remained stable. This region was identified as LVR. In this region the storage modulus was larger than the loss modulus, confirming the gel-like properties of the biomateial. Deformation region was identified after the consequent crossing of the curves of *G′* and *G”*. It corresponded to the changes in the fibre alignment and cross-linking, protein unfolding and bond breakage. However, by observation the hysteresis was minimal as the backward sweep curves returned close to the original values of *G'* and *G”*, suggesting that the fibres of the scaffold remained intact, allowing the biomaterial to preserve its properties after significant deformations.

Using equations (4.2) and (4.3), provided in Section 4.1.2, the shear modulus G^* was found 815.37 ± 165.08 Pa and the average loss factor $\tan(\delta) = 0.187$. These parameters were also used to deduce the material's stiffness, described by the Young's Modulus, *E*. For that, Poisson's equation was applied:

$$E = 2(1 + \nu)G^* \tag{5.1}$$

where *v* is the Poisson's ratio and for hydrogels is equal to 0.5 [314]. Hence, using (5.1) the elastic modulus of the scaffold was estimated as 2446.1 ± 495.23 Pa. Noteworthy, these results differed from the preliminary data provided in Section 2.1 due to an altered fabrication process, despite similar composition [294]. The synthesis therefore can be controlled to obtain the desired stiffness of the scaffold.

5.1.4 Mechanical characterisation of the scaffold: stress-relaxation

Stress-relaxation tests were also performed with the aim to obtain further insight into the dynamic non-linear behaviour of the viscoelastic biomaterial, arising due to its complex composition in response to a constantly applied tensile stress. In nature, biological tissues consist of a variety of organic and inorganic molecules, specific to the tissue type and each material exhibits unique behaviour when experiencing mechanical stress.

In the stress-relaxation experiment, the scaffold was subjected to a constant strain by applying a fixed deformation and maintaining it for 60 seconds, while the stress was measured. The biomaterial's response is illustrated in Figure 5.1.4A. The behaviour was characterised as a dynamic non-linear relaxation to a steady state from an initial value. This transient response is evident from the fact that the initially steep negative gradient converged to zero over time.

A Generalised Maxwell model [315] (depicted in Figure 5.1.4B) was used to mathematically describe the behaviour of the scaffold by spring-dashpot elements connected in parallel. Springs were used to represent the elastic properties of the scaffold, while dashpots — viscous. It was determined that second-order model featuring two parallel elements adequately captured the relaxation response observed. The model can be expresses as following:

$$\sigma(t) = \sigma + \left(\frac{\eta_1}{E_1} + \frac{\eta_2}{E_2}\right)\frac{d\sigma}{dt} + \frac{\eta_1\eta_2}{E_1E_2}\frac{d^2\sigma}{dt^2} \tag{5.2}$$

where σ is the stress, η_1 and η_2 are the viscosity coefficients of the corresponding dashpot element and E_1 and E_2 are the corresponding spring coefficients. The model had an exponential solution, that consisted of 2 exponential elements. It was expressed as:

$$F(t) = Ce^{-\frac{t}{T_1}} + \left(F(t=0) - C - F_{ss}\right)e^{-\frac{t}{T_2}} + F_{ss} \tag{5.3}$$

where $F(t=0)$ is the initial reaction force, F_{ss} is the steady state force and C is the parametric coefficient and T_1 and T_2 are the time constants, describing the speed of relaxation of the biomaterial. These are equivalent to the the ratios η/E of differential model (5.2).

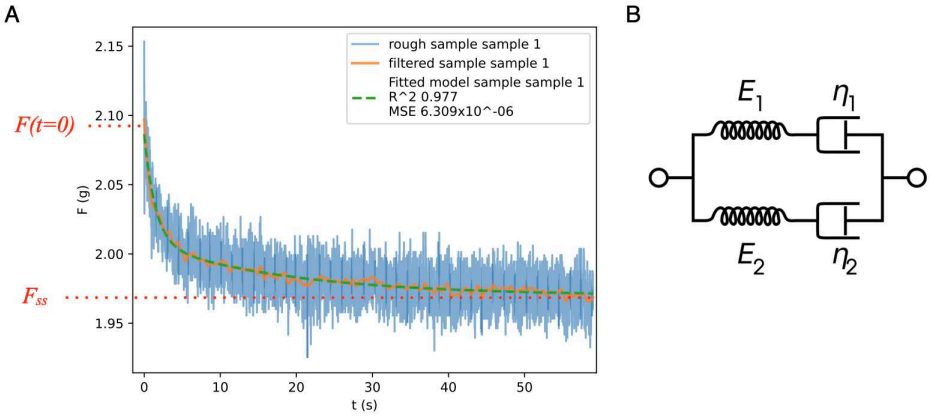

Figure 5.1.4 Stress-relaxation response of the scaffold.
A - time series data of the force exerted onto the texture analyser probe by the scaffold. This data was first filtered using lowess function to remove the noise. It was then fitted to double exponent model by using the parameters for $F(t=0)$ as the initial value and F_{ss} as the steady state value. The latter was obtained by taking the average of the final 15% of the series. **B** - Generalised Maxwell model defined as parallel arrangement of 2 series spring-dashpot elements with the corresponding spring and viscosity coefficients, E and η , respectively. The stress and strain in this model have second order differential relationship with a 2 exponent solution, used for data fitting.

The experimental time series data of fresh samples from Batches 1 and 2 tested at days 1 and 30 after synthesis, were processed and fitted to the model (5.3), and then normalised against the maximum value (as shown in Figure 5.1.5A). The parameters were demonstrated to be repeatable across all samples, obtaining a more aggressive T_1 = 36.43 ± 3.10 and a steadier T_2 = 1.49 ± 0.36, with the reaction force stabilising at F_{ss} = 0.8850 ± 0.0076 (normalised against the initial force). This behaviour was also found to be consistent across batches and reproducible after one month of storage at 4°C, as presented in Figures 5.1.5 B, C, and D.

Interestingly, a slight degradation in the mechanical stability was observed in some samples incubated in cell culture medium at 37°C, 5% CO_2 for one week (Figure 5.1.5E). The samples' maximum force was lower and the relaxation pattern was less stable with more oscillations, which did not conform as well with the model (5.3) as the fresh samples. These findings suggest fibre realignment and possible cross-link degradation resulting in stronger influence of the liquid phase of the scaffolds. However, this result needs to be confirmed, since only one repetition was done.

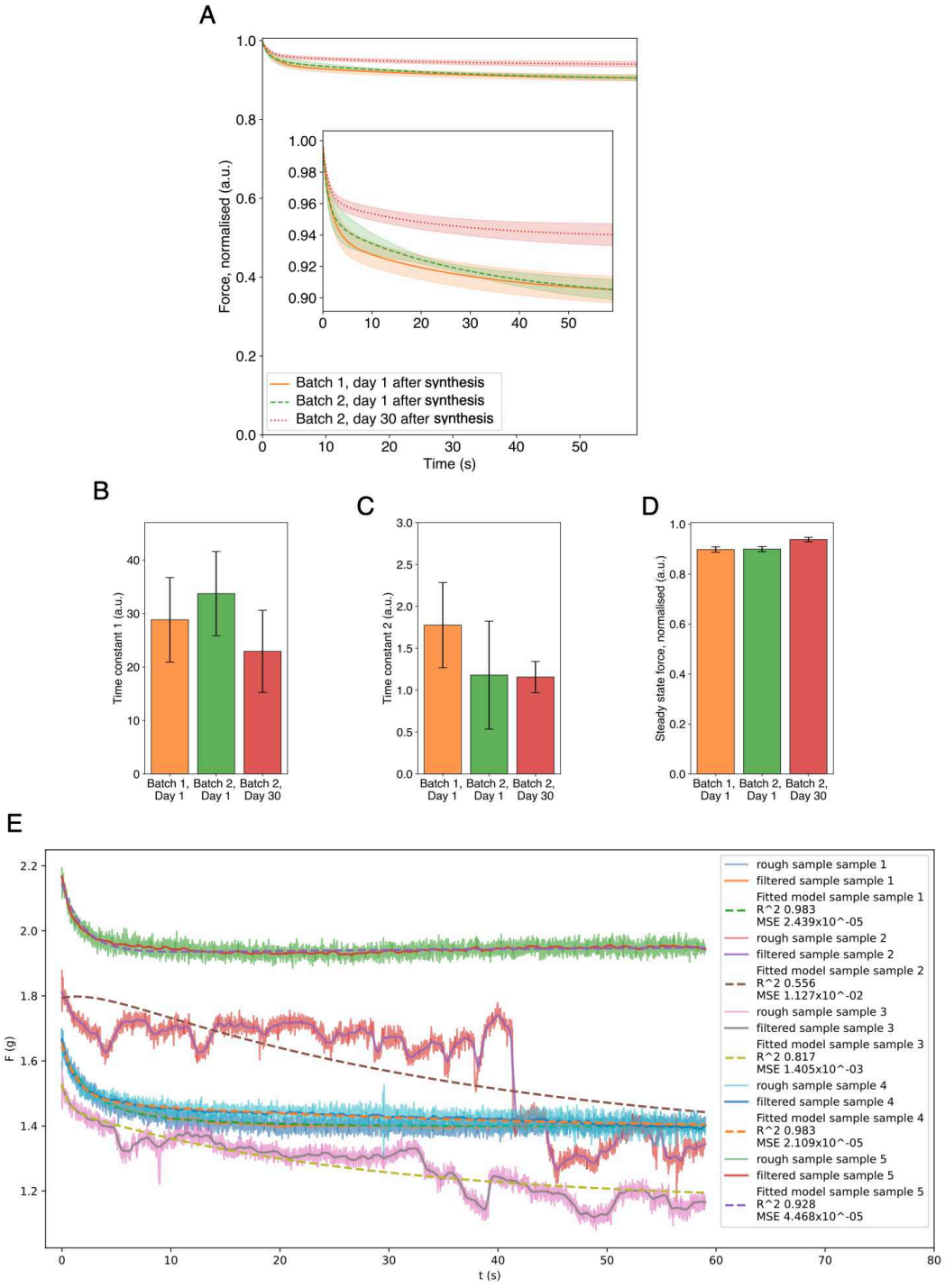

Figure 5.1.5 Stress-relaxation characteristics of the scaffolds.
A - average normalised fits and standard deviation bands for the relaxation responses of Batch 1 (orange, $n = 6$), Batch 2 on the first day after synthesis (green, n = 4) and Batch 2 after 30-day preservation at 4°C post synthesis (red, $n = 6$). **B** and **C** - T_1 and T_2 parameters comparison between the same samples, respectively. **D** - relaxation steady state comparison. Averages and standard deviation bars are presented. **E** - Batch 2 after 7-day preservation at 37°C, 5% CO_2 post synthesis.

5.1.5 Short-term 3D culture of MIN6 cells

MIN6 is a mouse-insulin secreting cell line based on the insulinoma derived from transgenic mouse and it has been shown to have similar properties to isolated pancreatic islets. At this stage a tradeoff between the cost-effectiveness and the relevance to human biology was made in favour of the cheaper and more readily available cells with insulin secretion capability in order to demonstrate the effectiveness of the scaffolds [316, 317]. The cells were cultivated on classical plastic surface and scaffold-treated 96-well plates over the course of 1 week.

The proliferation and viability of MIN6 cells was assessed over a one-week incubation period by measuring metabolic activity through the resazurin assay, as illustrated in Figure 5.1.6A and MTT assay, presented in Figure 5.1.6B. The growth rates displayed a similar pattern for both 2D and 3D cultures. A rapid increase in metabolic activity was observed by day 3 compared to day 0, followed by a more gradual growth rate by day 7. Nonetheless, the overall proliferation rate was observed to be higher in the 3D culture than in the 2D culture. Cells seeded on the scaffold reached 400% proliferation by the day 3 and 550% by the day 7, in contrast to a steadier increase of 260% and 320% in the classic culture on the same days, relative to day 0 metabolic activity. This difference can be attributed to the fact that confluence was reached in the 2D culture. In MTT assays, cells in the 2D culture exhibited the same metabolic rates at both day 3 and day 5 (Figure 5.1.6B). Conversely, the metabolic activity of MIN6 cells in the 3D culture has improved significantly from day 3 to day 5, indicating that 3D culture could enhance MIN6 cell viability over time.

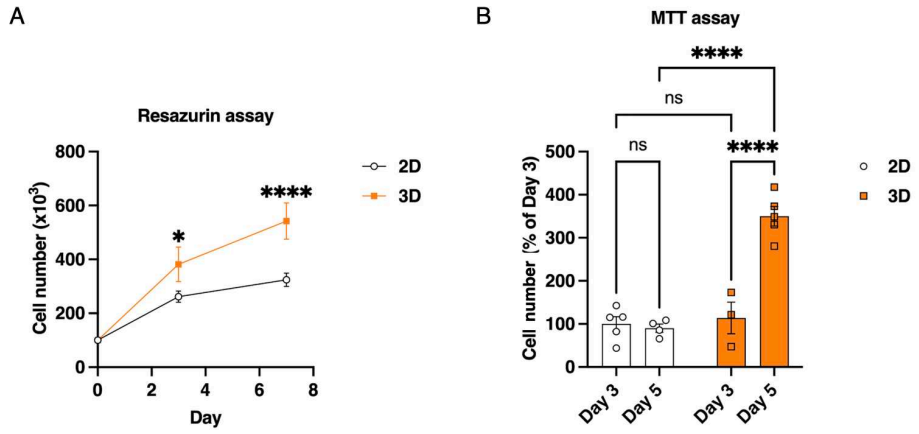

Figure 5.1.6 MIN6 proliferation after 7 days of culture in 2D and on scaffold.
MIN6 cells were cultured on classic plastic surface (2D) and on scaffolds (3D) in 96-well plates for 7 days, initially seeded 10^5 cells/well. **A** - proliferation rates, assessed with resazurin assay on days 3 and 7 (n=3). Standard curve was produced to correlate fluorescence intensity to cell number by testing the activity of cells seeded at a range of concentrations and the assay performed after cell sedimentation on day 0. **B** - proliferation rates, assessed with MTT assay on days 3 and 5 (n=3-5). Averages with standard deviations are presented for the obtained cell number data, * p<0.05, **** p<0.0001.

After a week of culture, MIN6 cells seeded on the classic plastic 2D surface reached confluence, spreading uniformly across the entire available area (Figure 5.1.7A). In contrast, z-stack immunofluorescent imaging of the 3D culture, as shown in Figures 5.1.7B, C, D, and E, revealed the formation of clustered spheroid structures by MIN6 cells that expressed insulin at the protein level. Clusters consisting of 20-40 cells were observed to have been scattered throughout the entire scaffold volume. The clusters exhibited a rather asymmetrical shape in the x- and y-directions, while appearing oblate in the z-direction, with widths varying between 40 and 120 µm and thicknesses ranging from 20 to 40 µm. These findings suggested that the cells had migrated, adhered, and divided within the scaffold's pores, effectively distributing themselves throughout the available 3D space during the week-long culture period.

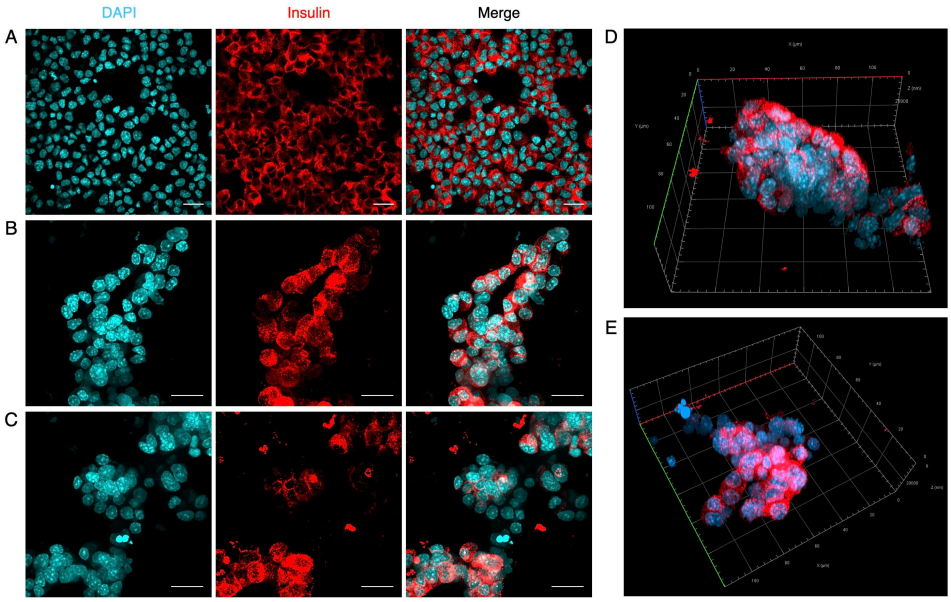

Figure 5.1.7 Confocal imaging of MIN6 after 7 days of culture in 2D and on scaffold. Immunofluorescence confocal imaging of MIN6 cells showed a high degree of confluence in 2D cultures and the formation of clusters in 3D cultures after 7 days. The cells were fixed and stained to visualise nuclei (cyan) and insulin (red). **A** - images of 2D samples, obtained from a single focal plane, scale bar = 20 µm. For the images **B**-**E**, confocal spin disc microscope was used to take a stack of images at 100-200 focal planes in z-direction, spaced by 0.2 µm. **B** and **C** - maximum intensity projection images of z-stack, depicting examples of β-cell clusters. Scale bar = 20 µm. **D** and **E** - 3D space reconstructions of z-stack confocal fluorescence images of MIN6 spheroids.

To determine whether gene expression of MIN6 cells could be influenced by 2D or 3D culture conditions, the mRNA levels of essential β-cell identity genes (*Ins1, Ins2, Slc2a2, Pcsk1, Glp1r, Ucn3, Pdx1, Mafa, Nkx6.1*) along with other pancreatic islet genes (*Gcg, Sst*) were measured using qRT-PCR. Although most of the gene expressions were found comparable in MIN6 cells cultured in both 2D and 3D for 3 and 7 days, an increase in the transcription factor *Nkx6.1,* a crucial gene for insulin secretion and β-cell identity, was observed in the 3D environment at day 3 when compared to the 2D culture (Figure 5.1.8). These findings indicate that 3D culture conditions may have biological effects on the transcriptome of MIN6 cells.

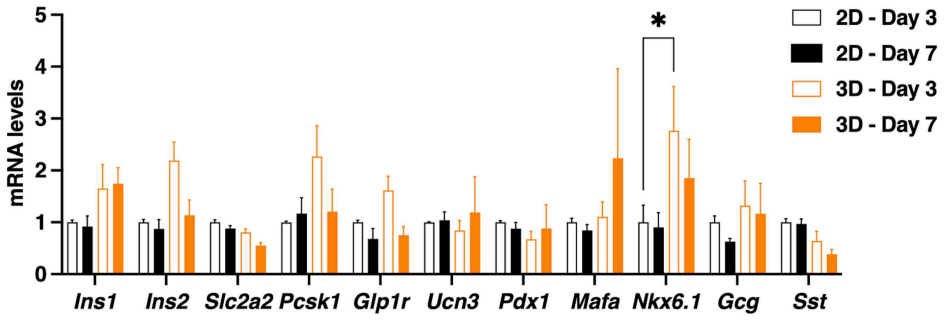

Figure 5.1.8 mRNA expression of key β-cell identity genes.
Ins1, Ins2, Slc2a2, Pcsk1, Glp1r, Ucn3, Pdx1, Mafa, Nkx6.1 and other pancreatic islet genes (*Gcg, Sst*) in MIN6 cells cultivated in 2D and 3D for 3 and 7 days. Results are displayed as means +/- standard error. * $p<0.05$

The regulation of insulin secretion by MIN6 cells in response to varying glucose concentrations was assessed through a GSIS experiment, as shown in Figure 5.1.9. Both 2D and 3D culture conditions displayed a sustained increase in insulin secretion under 20 mM glucose on both day 3 and day 7 (Figures 5.1.9A and B, respectively). Despite the higher cell numbers, insulin content remained similar between MIN6 cells cultured in either 2D or 3D at both day 3 (Figure 5.1.9C) and day 7 (Figure 5.1.9D). When normalised against the total insulin content (Figures 5.1.9E and F), the percentage of secreted insulin remained consistent after 7 days in 2D, although the magnitude of the response diminished over time. In the 3D culture, MIN6 cells continued to respond to 20 mM glucose stimulation, although their response also decreased compared to day 3. Overall, these findings indicate that the insulin secretory activity of MIN6 cells was analogous for 2D and 3D cultures in the short term, confirming that the scaffold-seeded cells maintained their functionality.

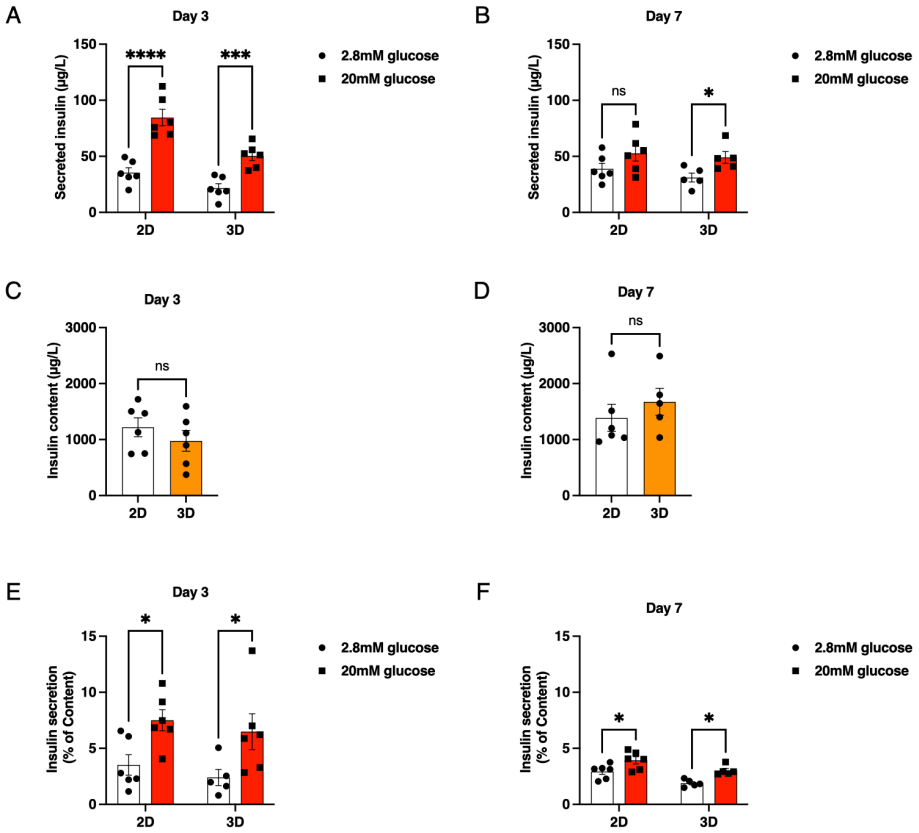

Figure 5.1.9 Insulin secretion in response to glucose at days 3 and 7 of MIN6 culture in 2D and on scaffold.
Values of secreted insulin concentration after 2.8 and 20 mM glucose stimulation (**A-B**) were normalised against total insulin content in each well (**C-D**) and displayed as percentage of content (**E-F**). Average and standard error of the mean values are presented (n=6). *$p < 0.05$, *** $p < 0.001$ and **** $p < 0.0001$.

5.1.6 Long-term 3D culture of MIN6 cells

Next, the long-term effectiveness of the BM scaffold was assessed in a 3-week-long evaluation in order to explore the potential of the synthesised matrices to sustain prolonged viable and functional β-cell cultures. MIN6 cells were seeded in 2D 96-well plate and in 3D scaffold-treated plate at the density of 10,000 cells per well and were sustained in culture for 21 days. GSIS, live/dead staining and resazurin viability assay were performed every 7 days, starting on the day 7.

Metabolic activity data obtained in the resazurin (displayed in Figure 5.1.10A) assay indicated different proliferation patterns for the two culture conditions. 2D culture was characterised with high rate in the beginning, peaking on the second week and declining by day 21. Nonetheless, it was observed that the metabolic activity was significantly higher on the hydrogel scaffold cultures on the days 14 and 21, compared to the first week. In addition to this, a substantial decline in living cells and increase of dead cells was observed on the 2D day 14images, compared to the 3D — and even more so on the day 21, where most of the cells appeared dead (Figure 5.1.10B).

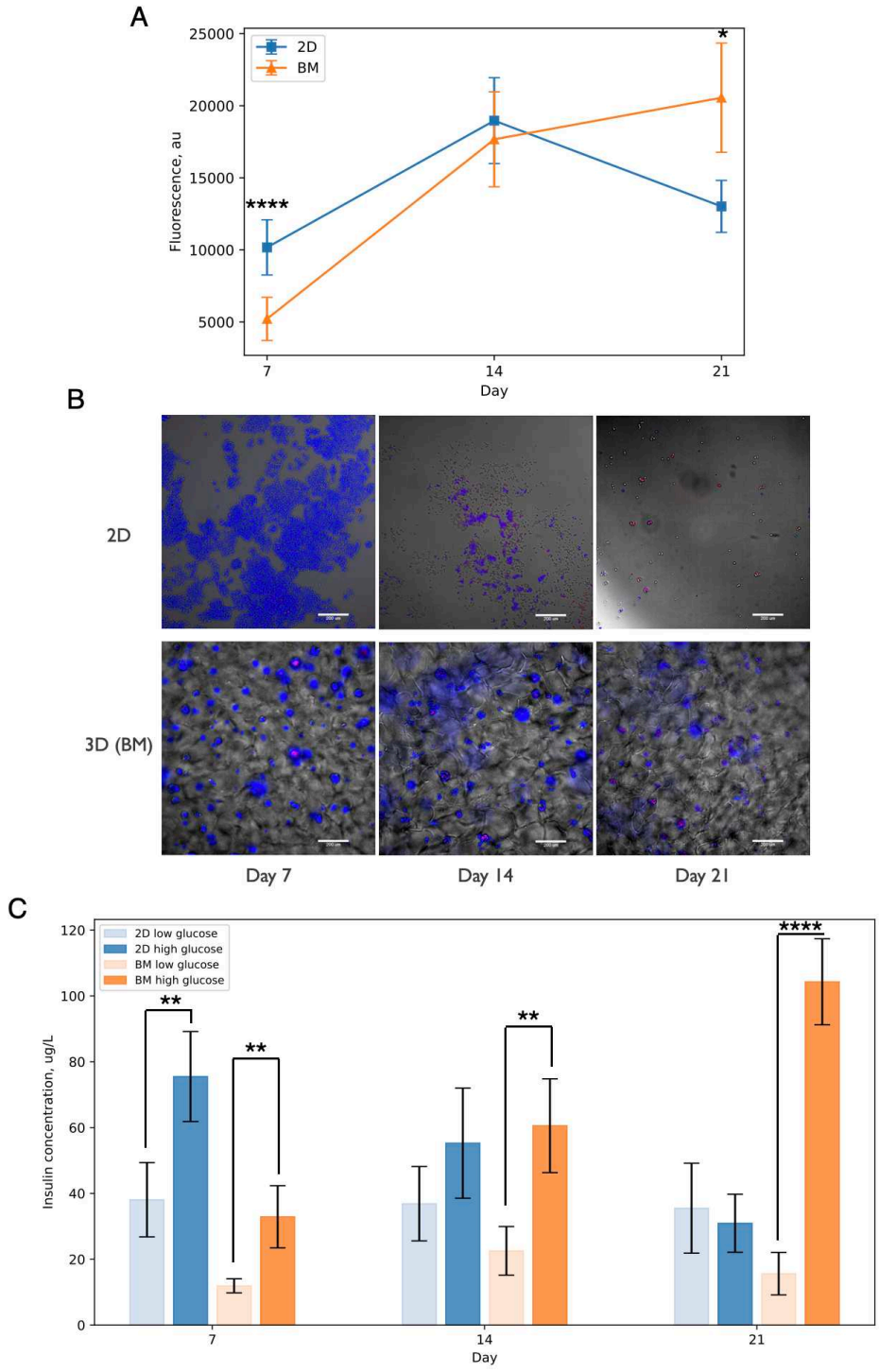

Figure 5.1.10 Evaluation of MIN6 culture in 2D and on scaffold during 3 weeks. MIN6 cells were cultured on classic plastic surface (2D) and on scaffolds (3D, BM) in 96-well plates for 21 days, initially seeded 10^4 cells/well. Interrogations were performed on the days 7, 14 and 21. **A** - proliferation rates, assessed with resazurin assay (n=3-6). **B** - live (hoecst, blue)/ dead (draq7, red) staining. Bar = 200 µm. The images were taken at the centre of the wells, not accurately capturing the distribution of the cells. **C** - values of secreted insulin concentration after 2.8 and 20 mM glucose stimulation. Average and standard deviation values are presented (n=4-5). ** $p < 0.01$ and **** $p < 0.0001$.

GSIS results, displayed in Figure 5.1.10C, demonstrated a progressive decrease in 2D cultured cells' capacity to secrete insulin over time. In contrast, insulin secreting activity of the MIN6 cells cultured in 3D appeared to be sustained throughout the entire duration of the experiment with an improved response on the day 21. It was characterised by a significantly higher insulin secretion during high glucose treatments, in comparison to the low glucose, with a noticeable drop at low glucose on the day 21. Overall these findings strengthened the hypothesis, that BIOMIMESYS® hydrogel scaffold would best benefit the long-term studies with insulin secreting cells, which is one of the requirements for *diachip*.

5.1.7 Other 3D culture approaches with MIN6 cells

Short term experiment has also been performed with other strategies for 3D cell culture to compare the performance of BIOMIMESYS® hydrogel as well as classic 2D as the control. Two gold standard techniques for *in vitro* organoid generation were evaluated, including Matrigel® and agarose well plate treatment [318, 319]. In this evaluation, 20,000 cells were seeded per well and left in culture for 2 days, followed by GSIS and nuclei staining with Hoechst and Draq7 to represent the live and dead cells respectively. Imaging and GSIS results are presented in Figure 5.1.9 A and B respectively.

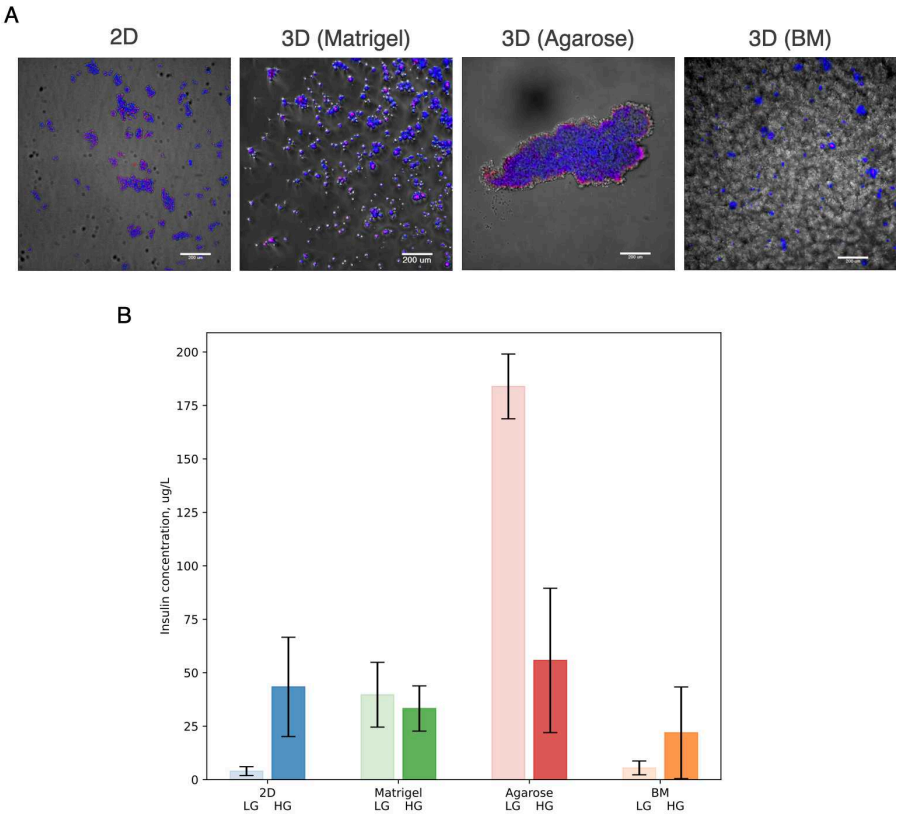

Figure 5.1.11 2D vs different 3D approaches of MIN6 culture.
A - Live (hoecst, blue)/dead (draq7, red) nuclei staining of MIN6 cultures after 2 days. For Matrigel® and BIOMIMESYS® (BM) maximum intensity projection images of z-stacks are used. Bar = 200 µm. **B** - Insulin secretion. LG - low glucose treatment, 2.8 mM. HG - high glucose treatment, 20 mM. Average and standard deviation values are presented (*n*=3-6).

It was observed, that agarose coating influenced the organisation of MIN6 cells into a large oval clusters, 50-100 μm thick. This was attributed to the non-adherent properties of the agarose gel. On the other hand, smaller sized spheroids (20-150 μm) were scattered throughout all the volume of the matrix in both Matrigel® and hydrogel scaffold. However, in the case of Matrigel®, the cells were rather integrated in the gel substance, whereas in case of the scaffolds — cells were growing into its pores and attaching to the fibres.

No necrotic core was observed in the live/dead fluorescence images of the agarose samples, indicating the sufficient nutrient supply to the majority of the cells in the organoid. On the contrary, dead cells, represented by the red signal, appeared to be distributed around the edges of the clusters. More dead signal was detected from the Matrigel® samples, mostly at the spheroid core, compared to the BIOMIMESYS® scaffolds, suggesting a less efficient nutrient diffusion across the Matrigel® gel and decreased availability for the core cells.

ELISA data presented in Figure 5.1.9B, confirmed the positive correlation between the glucose concentration and average insulin secreted by MIN6 cells for the 2D and in part for scaffold samples, although the significance could not be demonstrated for the latter. On the contrary, Matrigel® matrix has contributed to high insulin secretion in both low and high glucose treatment, further indicating the impaired nutrient gradient as well as abundance of sugars in the gel. Finally, the agarose data yielded controversial results with a decreased insulin secretion for the high glucose treatment. It was hypothesised, that free floating cells, which hadn't adhered to agarose coating, were present in the supernatant collection. Thus, this ELISA data could not be used to infer about the true insulin secretion for the agarose condition. Therefore, Matrigel® and agarose conditions were not carried forward to further experiments.

5.2 Microfluidic circuits

5.2.1 Establishment and confirmation of fluid flow mathematical model

Microfluidic circuits in this project comprised of:

a) pressure generator — to produce flow by creating a pressure difference with the atmospheric pressure;

b) microfluidic element — to direct the flow and facilitate the microenvironment for the pancreas-on-chip model;

c) flow sensor — to measure the flow and feed the measurement back into the system.

The fluid volumetric flow rate (or simply, flow), Q , is generated when a pressure P is applied and it shows the volume of fluid dispensed per unit time. In a microfluidic setting fluid's energy is dissipated in shear with the walls of the geometry containing the fluid due to viscosity. This can be described as a resistance to the flow, R. To model the flow in the system, the flow was assumed to be in a laminar regime, constant across varying geometries and only depend on the pressure.

$$Q = A_1 u_1 = A_2 u_2 \tag{5.4}$$

where, A and u are respectively the cross-sectional area and fluid velocity perpendicular to this area - varying for geometries 1 and 2. The fluid was assumed to be incompressible of constant density, ρ. The hight variations were ignored thus no change in the potential energy was taken into account. Therefore from Bernouli equation and resistance to flow, pressure can be related to the flow the following way:

$$P = \rho \frac{u^2}{2} + RQ \tag{5.5}$$

The resistance to flow can be modelled using Poiseuille's law for a long pipe of length x and diameter d, where $x>>d$. Since the setup consists of multiple pipes connected together and a microfluidic chip, assuming other geometries can also be modelled, as sets of n pipes connected in series, the relation (2) becomes:

$$P = \rho \frac{Q^2}{2\overline{A}^2} + Q \frac{128\mu}{\pi} \sum_{i=1}^{n} \frac{x_i}{d_i^4} \tag{5.6}$$

where μ is fluid dynamic viscosity and $\overline{A}$ is an average cross-sectional area. By observation, a quadratic relationship is expected according to this model, where there exit a quadratic and a linear coefficient for Q: a and b, respectively.

An experiment ('Q-P experiment') determining this relationship was performed during which for varying pressure, the output flow was measured by collecting multiple flow rate readings. The data was then fit to a polynomial linear regression of the form $y = ax^2 + bx + c$. Despite the collected datapoints conforming with the quadratic polynomial, the resulting coefficient a for the quadratic term was lower from the expected value by several orders of magnitude. This is a consequence of the assumptions taken regarding the pipe flow and the average area, which don't describe the microfluidic chip geometry precisely. On the other hand, the linear term coefficient b proved to be close to the corresponding expected value. This observation is influenced by the fact that for small geometries shear forces become dominant. In addition to this, an offset zero-intersept term c had emerged, which could be related to error in the measurement and influence of the hight variation in the setup pipes adding potential energy. Q-P experiment was used multiple times to reestablish the relationship between the pressure and the flow in further procedures when the geometry was varied (i.e. pipes were added/removed or shortened). For instance, in one example of the setup the relationship appeared as such (Figure 5.2.1):

$$P = 0.03Q^2 + 3.60Q - 1.23 \tag{5.7}$$

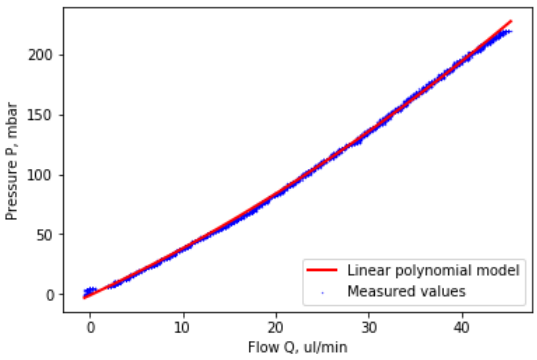

Figure 5.2.1. The pressure-flow model of a microfluidic circuit.
A single channel of ibidi® chip was connected with microfluidic tubing to Fluigent™ pressure generator and flow sensor. Pressure was changed in small increments, while flow was recorded, collecting 11,049 datapoints in total. The data was fit to a 2nd degree polynomial regression to describe the *P*-*Q* relationship.

It was observed that for low volume microfluidic chips, the quadratic coefficient *a* was often found to be close to 0 and hence it could be neglected in more complex microfluidic circuits, such as bifurcations. Conversely, the linear term *b* is directly associated with resistance. Importantly, for more precise control of the flow via pressure adjustments, the resistance to flow had to be increased by using smaller diameter tubes and lesser volume microfluidic chips. Thus, flow fluctuations arising from pressure fluctuations could be limited as well as providing more range for pressure accuracy.

5.2.2 PID control of the flow

One of the project's objectives was aiming to develop an automated microfluidic platform for high-throughput experimentation. An automatic control method involving a proportional-integral-derivative (PID) compensation protocol has been developed for the system in order to carry out steady flow supply to the cells. Such compensators are typically employed in automated systems enabling stable closed-loop control, based on the error between the desired parameter value and measured output value. The error is processed in a mathematical function of the controller containing proportional, integrative and derivative transformations, outputting a new input parameter value to regulate the dynamics of the system in the real time [320].

The native digital control of pressure generator equipment was characterised with a slow oscillatory transient response with a large initial overshoot to almost twice the desired input value. The settling time to reach the steady state flow rate was longer than 10 seconds (Figure 5.2.2A). It was obvious that despite the flow rate measurement, the initial conversion from a desired input flow to the desired input pressure was outside of range in the real relationship of *Q* and *P*. In case of a hypothetical random disturbance introduction during future experiments, such as bubbles or leak, the native control may disrupt the steady state fluid flow, which may be detrimental to the cultured cells or introduce an erroneous cue to their signalling.

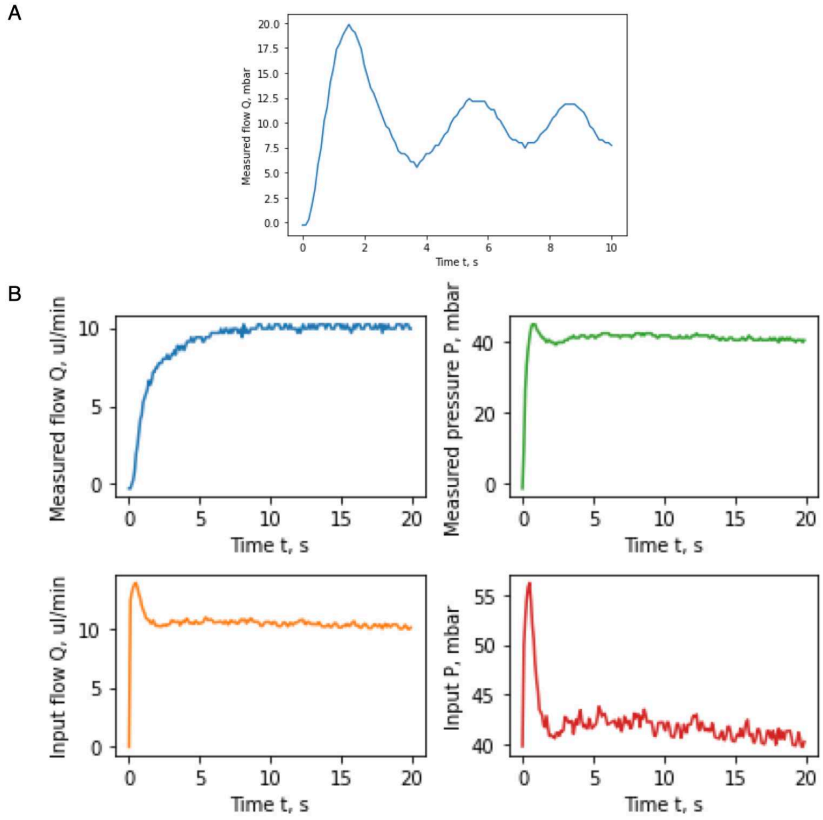

Figure 5.2.2. PID control of the flow.
A - native control of the Fluigent™ system. The measured Q in the system has high oscillation and long settling time. **B** - digital PID control. The graphs presented in this section demonstrate the measured Q and P as well as the controlled input. The overshoot over the target flow is removed and the steady state is reached faster.

Digital PID control introduced to the setup took advantage of the experimentally determined Q-P relationship. Assuming error E_j as the difference between the instantaneously measured flow reading j and the desired flow input, with the time gap $T_{sampling}$ between the measurements, the PID controller C_j takes the following discretised form:

$$C_j = K_p E_j + K_i \sum_{i=1}^{j} E_i T_{sampling} + K_d \frac{E_j - E_{j-1}}{T_{sampling}} \tag{5.8}$$

$$P_{j+1} = aC_j^2 + bC_j + c \tag{5.9}$$

where K_p, K_i and K_d are the proportional, integral and derivative compensation coefficients respectively and C_j is the new value of flow input. The PID performed well with a smoother transient response with no overshoot and settling time to steady state just over 5 seconds (Figure 5.2.2B). This contributed to a more accurate regulation of the flow, compared to the native digital control. The flow rate was settling to the desired value faster, while ensuring more stability and avoiding excessive variation.

5.2.3 *Volume estimation in microfluidic circuits*

A technique to estimate the volume of the system was developed. This was essential to assess the total amount of medium required to perfuse the entire setup to prepare for experiments, specifically for complex chip geometries and arrangements, where volume was initially unknown. The technique involved pre-filling the inlet tubes of known diameter and length with coloured liquid (V_1), then applying pressure over time T, whilst recording the flow rate Q, until the liquid is pushed through the elements of interest (V_2) and calculating the volume of the remaining outlet tubes (V_3). Flow rate is defined as the volume dV of liquid passing per unit time dt:

$$Q = \frac{dV}{dt} \tag{5.10}$$

Hence, the volume passed through the region of interest is:

$$V_2 = \int_{t=0}^{t=T} \frac{dV}{dt} dt \tag{5.11}$$

In the setting described above, k discretised measurements of the flow rate were collected by the flow sensor at sampling rate Δt :

$$V_2 = \sum_{n=1}^{n=k} Q_n \Delta t \tag{5.12}$$

Finally, the total volume, V_t , is given as the sum of V_1, V_2 and V_3 . For instance, in one of the setups the following measurements were taken:

Volume of inlet tubing, V_1	5.735 µl
Volume of microfluidic geometry, V_2	221.552 µl
Volume of outlet tubing, V_3	115.657 µl
Total volume, V_t	342.94 µl

Table 5.2.1 Volume estimation for a microfluidic setup.

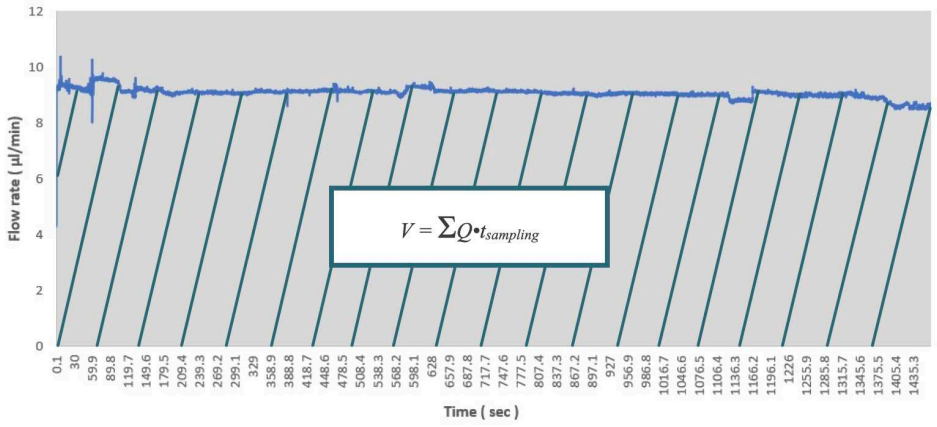

Figure 5.2.3 Volume estimation for a microfluidic setup.
The volume of the segment of interest was obtained by finding the sum of flow rate readings and multiplying by the sampling rate.

5.2.4 Bifurcation circuit

Parallel microfluidic channels were also considered as means of scaling the experimental capacity. In order to improve the statistical power of the experiment, a higher number of wells were considered to be perfused by the same pressure supply. For this, a bifurcation setup has been tested as an alternative to simple linear microfluidic circuit.

In this arrangement the liquid flow supply tubing was split into 2 channels with similar chip geometries connected in parallel. The lengths of the corresponding inlet and outlet tubing was ensured to have been of matching length. The resistance to flow values were obtained by measuring the flow rate for the complete system as well as for each of the two parallel channels during Q-P experiment. Due to the complexity of such setup, a simplified linearised *P-Q* relationship was used, only considering the contribution of the proportion part, corresponding to the resistance. For each branch of the bifurcation, pressure remains the same, while the flow is split according to the corresponding resistances:

$$P = Q_t R_t \tag{5.13}$$

$$P = P_1 = P_2 \tag{5.14}$$

$$Q_t = Q_1 + Q_2 \tag{5.15}$$

where P, Q_t and R_t are the total values of pressure, flow rate and resistance, respectfully for the system, and the branch parameters are indicated by 1 and 2. By substituting (5.13) to (5.14) and applying (5.15) the total resistance can be found:

$$\frac{P}{R_t} = \frac{P_1}{R_1} + \frac{P_2}{R_2} \tag{5.16}$$

$$R_t = \frac{R_1 R_2}{R_1 + R_2} \tag{5.17}$$

For the channels split perfectly in to the symmetric geometries and tubing of equal lengths, it can be assumed that:

$$R_1 = R_2 \tag{5.18}$$

$$R_t = \frac{1}{2}R_1 = \frac{1}{2}R_2 \tag{5.19}$$

The data collected in this experiment is presented in Figure 5.2.4 as plots of pressure (mbar) against flow rate (µl/min).

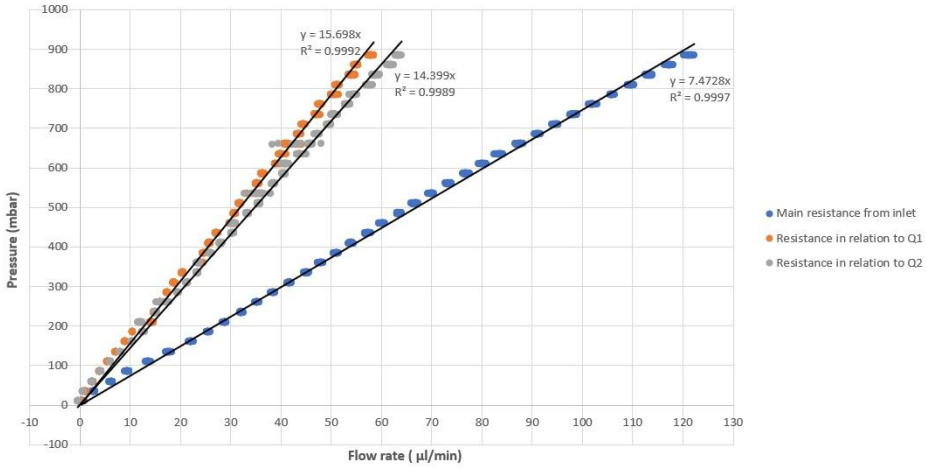

Figure 5.2.4 Pressure-flow curves of a bifurcation microfluidic setup.
Flow rate readings were taken for the total circuit Q_t (measured before the bifurcation split) and for each of the channels Q_1 and Q_2 (measured individually past the split).

Linear regression lines of best fit of the form $y = bx + c$ were obtained from the corresponding datasets. The slope, b, represented the corresponding resistance value in the circuit, whereas the y-intercept term c was either due to error in the measurements or hight variations in the tubing. The linear regression line for the Q_t, measured from flow rate sensor located before the bifurcation, was:

$$P = 7.4728Q_t + 11.42 \tag{5.20}$$

Hence, the total resistance of the circuit, R_t, was 7.47 mbar·min/µl. Similarly, the resistance values for each of the bifurcation channels were found as R_1 = 15.70 mbar·min/µl and R_2 = 14.40 mbar•min/µl. These measurements confirmed the equation (5.17). By substituting R_1 and R_2, the total resistance was calculated as 7.51 mbar•min/µl, close to the measured R_t.

At the same time, by applying the latter to the equation (5.19), the expected resistance in ideally split bifurcation channels is 14.95 mbar•min/µl. This value was close to the average resistance between R_1 and R_2, calculated as 15.05 mbar•min/µl.

5.2.5 Islets on chip

To confirm the results of the preliminary studies, a GSIS experiment has been performed in the perfusion conditions, using isolated mouse islets seeded on an ibidi® chip. During this experiment liquid samples were collected every 2 minutes to record the secretion dynamics in response to varied glucose concentration over time. The experiment was automatically controlled with Python algorithm (provided in Appendix 4). The GSIS curve appeared counter-intuitive to an

expectation: insulin concentration seemed high for low perfusion period and low for the high glucose perfusion period with about 6-fold difference, hence the effects of solution mixing had to be considered (Figure 5.2.5A).

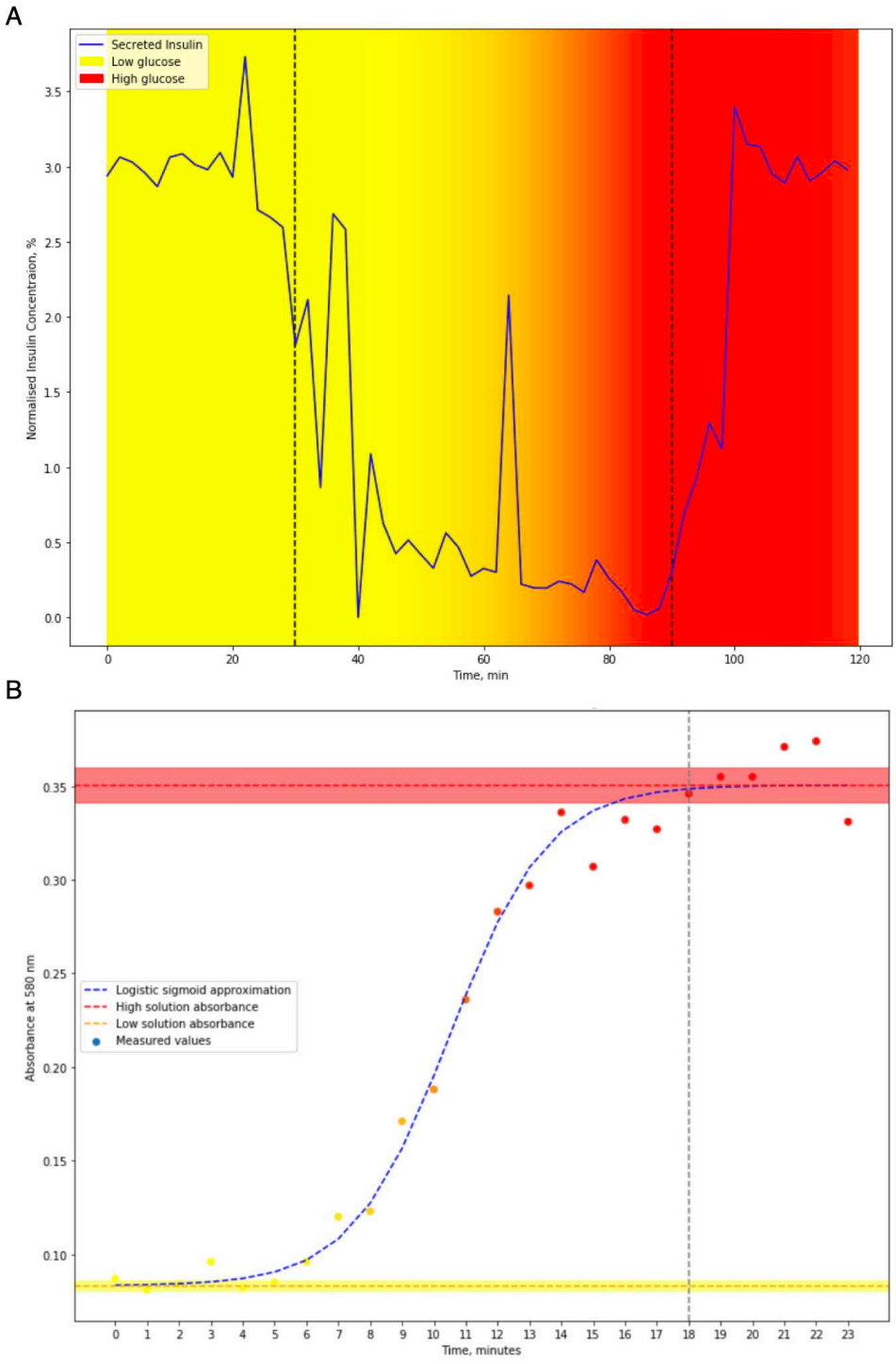

Figure 5.2.5 Islets on chip.
A - Insulin secretion by isolated mouse islets during perfusion on chip at 10 µl/min. Initially the islets were perfused with KRB low glucose solution (2.8 mM). KRB high glucose solution (16.8 mM) was introduced to the system at 30 min and changed back to low glucose after 1 hour. **B** - solution mixing dynamics estimation for the system at 50 µl/min. Colorimetry was used to determine the concentration of a dye.

The volume of the system had been estimated in advance as 412.5 µl, therefore, for a complete turnover from one solution to another at least 41 minutes 15 seconds would be required at the flow rate 10 µl/min. An additional experiment was run to investigate the mixing dynamics with dyed solutions of proportional dye concentrations to low and high glucose KRB solutions. Mixing was investigated colorimetrically with a resulting curve forming a sigmoid, as presented in Figure 5.2.5B. It was estimated that at 10 µl/min a complete solution turnover was taking about 90 minutes, hence the approximated glucose concentration information was added to the original GSIS graph. With this edit, insulin concentration was better conforming with the expectation. It was also observed that introduction of flow induced an extra stress onto the β-cells, which resulted in the higher insulin secretion in the beginning.

5.2.6 Hydrogel scaffold on chip

The synthetic extracellular scaffold matrices were tested in microfluidic setting with the aim to evaluate their performance under flow conditions. Cells-free matrix-treated PDMS chip was compared with empty chip of the same geometry in the Q-P experiment. The results of this study revealed the resistances to flow in both chips to be almost identical with R_{empty} = 1.999 mbar•min/µl and $R_{scaffold}$ = 2.015 mbar•min/µl. This was thanks to the high porosity of the hydrogel scaffold allowing unimpeded fluid flow through the pores. Experiments with MIN6-loaded scaffolds on chip could not be successfully completed in timely fashion due to encounter of leak and evaporation phenomena.

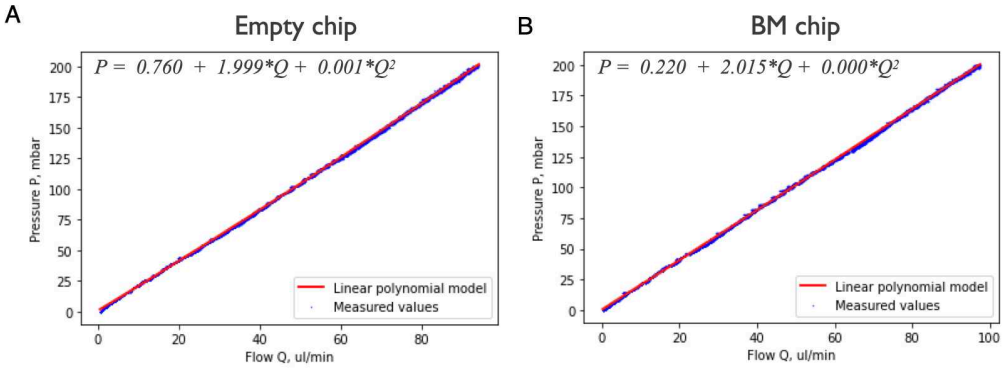

Figure 5.2.6 BIOMIMESYS® scaffold on chip.
Custom-made PDMS chip was connected with microfluidic tubing to Fluigent™ pressure generator and flow sensor. Pressure was changed in small increments, while flow was recorded. The data was fit to a 2nd degree polynomial regression to describe the *P-Q* relationship and estimate the resistance of the chip. **A** - empty chip, **B** - scaffold-loaded chip.

5.3 Microelectrodes

5.3.1 Design rationale confirmation

An MEA was proposed for continuous real-time on-chip electrochemical biosensing applications for analytes such as glucose and insulin. However, there exists a tradeoff between the electrode size and spacing. Highly dense array, where the electrodes are located very close to each other, would produce an inaccurate signal, whereas the signal's intensity scales with the area of the

electrode. In an effort to determine the optimal parameters for electrode size and density, an evaluation array was designed. The design rationale took into consideration the effect of diffusion zones in order to maximise the signal and minimise the detection time.

The evaluation array microfabrication protocol involved SU-8 passivation layer on glass substrate, giving rise to several crucial adjustments to the manufacturer's data sheet. More details on the optimisation are provided in the Table 5.3.1.

Spin	1) closed 500-100-10 2) closed 3000-300-30	1) closed 500-100-10 2) closed 3000-300-30	1) closed 500-100-10 2) closed 3000-300-30	1) open 500-100-10 2) closed 3000-300-30	1) Open 500-100-10 2) closed 3000-300-30	1) Open 500-100-10 2) closed 3000-300-30	1) Open 500-100-10 2) closed 3000-300-30	1) Open 500-100-10 2) closed 1000-300-30
SB	60 s	60 s	120 s	120 s	120 s	120 s	120 s	120 s
EXP	7 s	3 s	9 s	9 s	3 s	6 s	3 s	3 s
PEB	60 s	60 s	120 s	120 s	120 s	120 s	120 s	120 s
DEV	60 s	60 s	30 s	30 s	30 s	120 s	120 s	120 s
Track	0.25-0.7 µm (non-uniform, residue)	0.6 µm (clear)	0.2 µm (residue)	0.6 µm (residue)	1.2 µm+ (non-uniform residue)	1.2 µm (residue)	0.8 µm (clear)	2.5 µm (some residue)
Edge	0.6 µm (sloped)	0.6 µm (straight)	0.6 µm (sloped)	1.5 µm (sloped)	1.2 µm (straight)	1.2 µm (straight)	1.2 µm (straight)	2.5 µm

Table 5.3.1 Optimisation of deposition of SU-8 2002 on glass.
Microfabrication steps and their parameters are listed in the order of execution during the SU-8 deposition process. **Spin** - the first stage is to spread the resist on the substrate surface by spin coating. The process is done in 2 steps. Closed and open lid configurations were tested. The parameters are given as speed (rpm) - acceleration (rpm/s) - duration (s). **SB** - soft bake stage is used to evaporate all remaining solvent by placing the sample onto 100°C hotplate. **EXP** - exposure to UV radiation to initiate cross-linking in the photoresist. **PEB** - post-exposure bake used to complete the cross-linking reaction. **DEV** - submersion of the substrate into the developer solution to remove unreacted photoresist areas. **Track** and **Edge** rows contain profilometry observations of the passivation layer near the electrode opening area and at the far edge of the passivation layer, respectively.

Microfabrication parameters, such as spin-coating, soft bake, exposure, post exposure bake, and development — were being adjusted to achieve the desired structures on the glass substrate. Extra attention had to be paid to the temperature gradients and cooling of the substrate in order to avoid film stress. Profilometry was used to measure the profiles of the track areas and edges of the insulating layer. The track areas were required to be completely clear of the passivation SU-8 material with no residue in order to ensure the electrode exposure. Edge measurements were used to better understand nature of the defect, whether it was caused by delamination, unreacted resist leakage or underdeveloped residues. As a result, an optimised protocol has been developed and the

microelectrode arrays with reproducible insulation thickness of 2 micron were fabricated (presented in Figure 5.3.1).

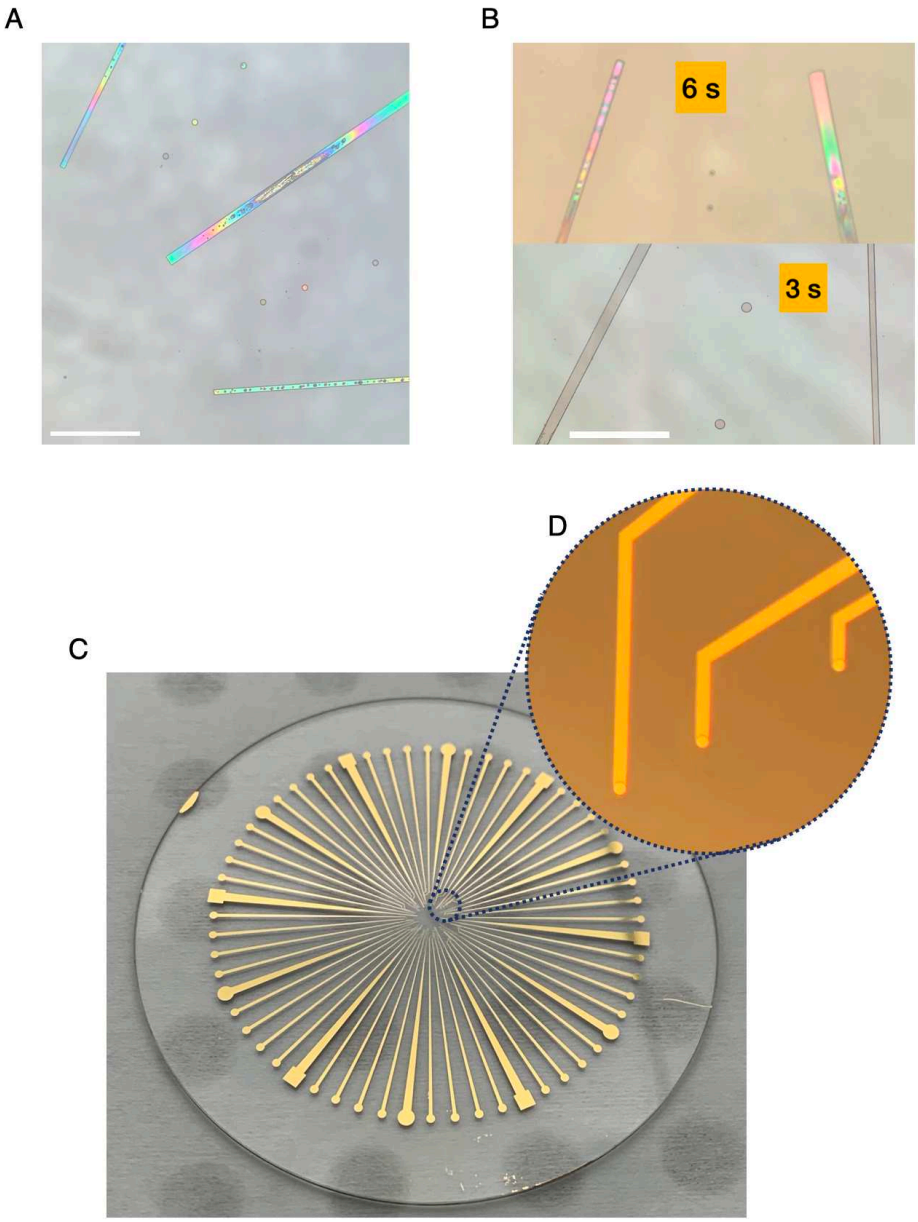

Figure 5.3.1 Fabricated MEA.
A and **B** - optimisation of photolithography process for SU-8 insulating layer deposition, scale bar = 500 µm. The manufacturer's protocol for SU-8 2002 was found to be not suited for fabrication on glass substrate due to excessive residue formation, as seen in **A**. Many parameters of the fabrication process had to be revisited including spin coating speed and mode, soft bake, post-exposure bake and development times, as well as exposure times as seen in **B**. **C** and **D** - the resulting array with Ti/Au tracks and SU-8 insulating layer with specific openings for electrode-solution interface.

In order to confirm the electrochemical and geometrical properties microelectreodes were then tested in a linear sweep voltammetry mode with a standard solution of ferricyanide at the potential scan from 0.25 V to -0.55 V and backward at 1 mv/s scan rate (Figure 5.3.2A). A more negative current was observed as the potential decreased from 0 V to -0.40 V, arising from ferricyanide reduction to ferrocyanide. On the contrary, further decrease in the potential from -0.40V to -0.55 V resulted in no significant change in current. This plateau was therefore identified as diffusion limited current region, since the rate of the reaction was limited by the mass transport of ferricyanide to the surface of the electrode (Figure 5.3.2B). The expected steady-state current in the diffusion limited region for the recessed electrodes is directly proportional to the bulk concentration of ferricyanide:

$$i_d = \frac{4\pi n F C D a^2}{4L + \pi a} \tag{5.21}$$

where i_d is the diffusion limited current, a is the electrode radius, L is the recess thickness of the insulating layer, F is the Faraday constant, C in the concentration of the analyte undergoing a redox reaction, n is the number of electrons in this reaction (n=1 for this case of single electron reduction reaction) and D is the diffusion coefficient. The current-voltage curves presented in Figure 5.3.2 C-E were obtained from the measured signal.

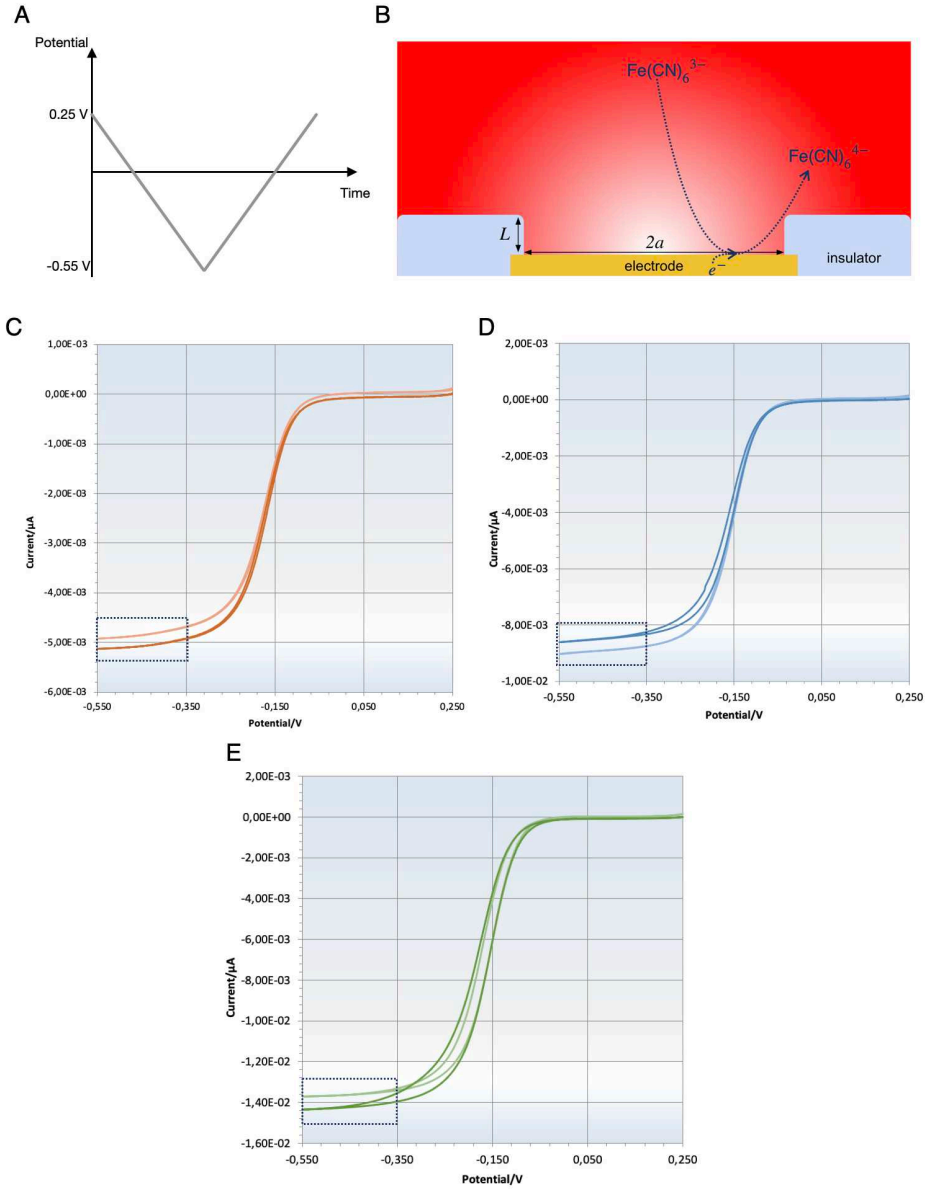

Figure 5.3.2 Sweep voltammetry with ferri-ferrocyanide in KCl solution.
A - the linear sweep of potential in the experiment. **B** - Schematic for the mass transport of electrons and ions at the electrode surface in the presence ferri-ferrocyanide redox. **C-E** - pairwise current-voltage curves resulting from the sweep voltammetry for each set of the electrodes on the MEA: a = 10 µm (**C**), a = 17.5 µm (**D**) and a = 25 µm (**E**). Rectangles highlight the diffusion-limited region.

Limited hysteresis was observed in the backward curves and the shape of the curve followed a sigmoid pattern, signifying the efficient mass transport around the microelectrodes. As well as this, pairwise tests revealed no significant effect of the neighbouring electrodes on each other's signals. The diffusion limited current values confirm the theoretical prediction from equation (5.21), thus validating the microfabrication protocol:

Electrode radius, a	10.0 µm	17.5 µm	25.0 µm
Expected current, i_d	4.97 nA	9.14 nA	13.33 nA
Observed reduction current, i_d	-4.92 ± 0.13 nA	-8.72 ± 0.21 nA	-13.37 ± 0.99 nA

Table 5.3.2 Diffusion limited current.

5.3.2 Graphene oxide deposition

Electrode surface modification with GO was performed aiming to enhance the signal and facilitate insulin detection using cyclic voltammetry technique. As the potential applied to modified electrodes was scanned from 0 to 0.75 V and backwards for 100 cycles (Figure 5.3.3A), an increase in current amplitude was observed on the voltammograms with each cycle, as presented in Figure 5.3.3B. Subsequently, a coverage of the electrodes' surfaces with GO films was shown on the SEM images of the modified electrodes (Figure 5.3.3D). Despite this, insulin detection in PBS solution was not demonstrated.

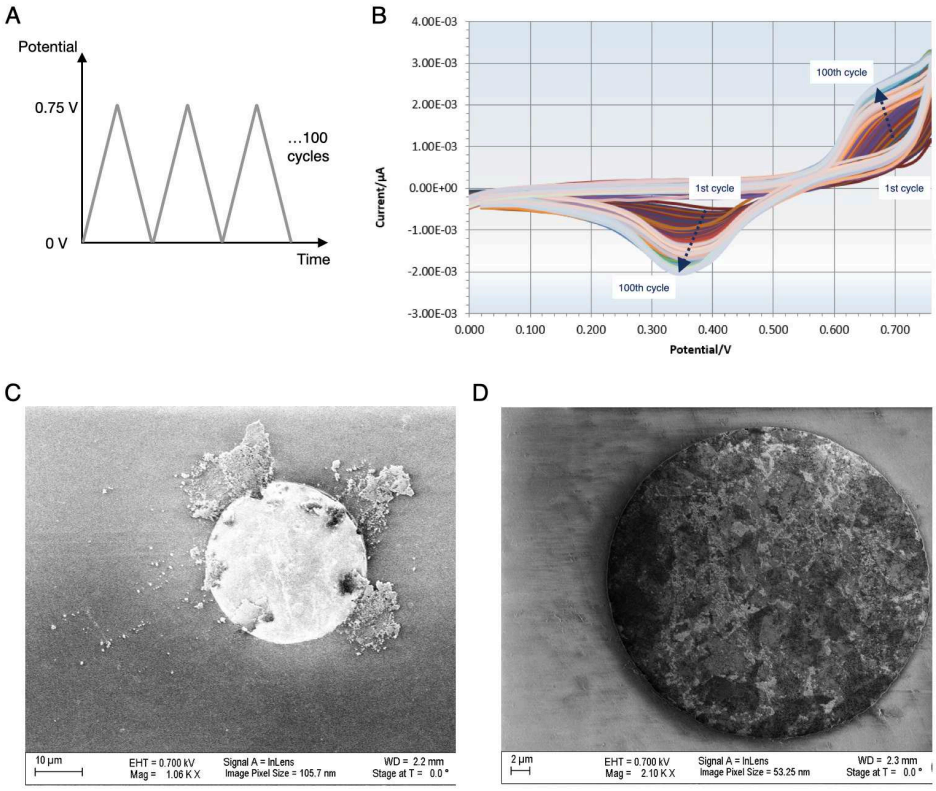

Figure 5.3.3 GO deposition on the MEA.
A - cyclic voltammetry sweep of the potential. **B** - current-voltage curve on one of the exposed electrodes of the MEA showing the increase of signal with each cycle more GO flakes get deposited on the electrode's surface. **C** - SEM image of an unexposed electrode. **D** - SEM image of an electrode after the GO deposition. Darker coloured structures observed on the electrode's surface signify the presence of the deposited GO flakes.

6. Discussion and Perspectives

6.1 Matrices

The findings of this work demonstrate the successful application of a synthesised biomimetic scaffold that emulates the pancreatic ECM for use in 3D cell cultures of MIN6 cells. The scaffold's porous architecture, viscoelastic properties, and inclusion of key ECM components create a more physiologically relevant environment for cell growth and function compared to traditional 2D culture systems.

Raman spectroscopy revealed that the key ECM components were present within the scaffold. As well as this, the cross-link formation between these components was confirmed. Peptide bonds are common for the biomolecules used in the scaffold's composition. These were evidently abundant, manifesting as the high intensity amide bands on the spectral curves. Furthermore, the correlation of several specific peaks between the spectra of scaffold and its constituents, suggests that the incorporation and cross-linking of HA, RGDS and collagens was successfully achieved via amide chemistry. Additionally, the observed conformational changes of these components within the scaffold may influence cell adhesion by providing niches for integrin binding. It is an important observation, since such cellular processes as proliferation, differentiation, and migration — depend on the interaction between the cells and the scaffold. In addition to this, the urea cross-links formed between the polysaccharide chains further enhance the stability and structural integrity of the scaffold. This makes the scaffold more robust and better suited for supporting cellular activity. These findings align with previous studies that have highlighted the importance of ECM composition in regulating cell behaviour and function [321, 322]. While HA and collagen type I were the dominant molecules based on the concentrations used during the synthesis, however the exact biomolecule densities in the scaffold composition were unclear. Despite its advantages at identifying the specific bonds due to exact location of characteristic peaks, Raman technique could not provide the precise information on the proportions of specific molecules. This could be important when considering the exact contribution of each of these chemicals to the mechanical and functional aspects of the scaffold. Also this information could confirm the reproducibility of the quantities of the biomolecules in the synthesis of the scaffold. For this, mass spectrometry or HPLC techniques could be employed to study liquid pre-lyophilised scaffolds.

Current literature provides limited data on the mechanical properties of pancreatic tissue. Elastography techniques have previously shown that the shear stiffness of the human pancreas ranges from 0.72 kPa to 1.54 kPa at 40 Hz [323, 324], while Wex et al. reported values between 0.64 and 1.17 kPa in rheological experiments, with $\tan(\delta)$ between 0.3 and 0.4 [325]. As such, the shear stress characteristics of BIOMIMESYS® scaffolds are comparable with the existing data on pancreatic tissue.

The production and storage of the scaffold were shown here to have had minimal impact on the response to loading of the fresh 'off-the-shelve' scaffolds. This work demonstrated both batch-

to-batch reproducibility and time stability during the storage, thereby confirming the robustness of the fabrication method. The double-exponent stress-relaxation model presented highlights the complexity of the material's time-dependent viscoelastic behaviour. The interaction between the two time constants, where T_2 is significantly shorter than T_1, and a steady state relaxation at 88.5% of the initial force, suggests dominant elastic characteristics. This implies a highly pronounced solid phase of the material. This is consistent with the rheological observations, where $G' > G''$ in the LVR. Conversely, a single-exponent model has been found to better fit the experimental results of human pancreas viscous relaxation in the study by Rubiano et al. [326]. Furthermore, relaxation to a lower steady-state force is often observed over a longer period [327]. Thus, although the scaffold's shear properties closely resemble those of the pancreas, its time-dependent dynamics fall short of fully replicating the biological tissue. However, given the scarcity of literature on the mechanical properties of pancreatic tissue, this area could be further explored by comparing the decellularised native ECM to BIOMIMESYS® in rheology and stress-relaxation experiments. Furthermore, the mechanical characterisation could be more complete with the use of compression-extension tests for more detailed stress-strain dynamics, and atomic force microscopy (AFM) for more precise measurement of stiffness, elasticity and adhesion forces at nano-scale. The latter, however could be challenging with the highly irregular distribution of the scaffold's fibres across its surface [328].

The observed slight modification of mechanical properties after one week incubation in the cell culture conditions (cell culture media only, 37°C, 5% CO_2) suggests potential fibre realignment and cross-link modification within the scaffolds, possibly influenced by the pH of the environment. Temperature change may have influenced polypeptide denaturation and conformational changes in the structural molecules. For instance, collagens are known for their dynamic denaturation properties at physiological temperatures [329]. However, the significance of this finding is questionable, considering, that the living cells, seeded onto the scaffold would also contribute to the structural modifications of the surrounding tissue by secreting the ECM remodelling enzymes, such as MMPs to degrade the polypeptide structures [89], and SPARC to influence the fibre alignment [88] as well as modification of laminins [330].

MIN6 cell line was chosen for this *in vitro* model of pancreatic tissue, thanks to its high experimental throughput and lower maintenance requirements, compared to other cell lines, such as INS 823/13 or EndoC-BH1. MIN6 line was best-functioning insulin-secreting model available for this work. It was used as a validation for the 3D culture with BIOMIMESYS® scaffolds as a preliminary step before applying more expensive, higher maintenance or less available cell types, such as primary cells. The use of the cell line for this model is also justified by the 3Rs initiative aiming to decrease animal experimentation. On the other hand, MIN6 cells have limited translational value due to their non-human origin and altered biological properties resulting from immortalisation. Although widely employed for studying pancreatic β-cell function, the inherent differences in gene expression and cellular signalling between mouse and human cells reduce the relevance of MIN6 findings to human pancreatic biology [203, 317]. In contrast, primary human

islets offer a more physiologically relevant model for understanding human-specific pancreatic function and diseases such as diabetes. However, their availability is severely limited due to the technical challenges of isolating islets from human donors and the global scarcity of suitable donor tissue [331, 332]. An alternative route for developing a highly relevant 3D pancreatic model would be iPSC-derived islets, however, it was not considered for this stage of the project due to an increased workload required for validation of the differentiation protocols existing in the literature [333].

The metabolic activity assays with MIN6 cells reveal an initial adaptation phase followed by a more gradual growth phase. During the latter stage, the spatial capacity provided by the scaffold's pores allows cells to continue proliferating without reaching confluence as rapidly as in 2D cultures. This is achieved by the scaffold more closely mimicking the native extracellular matrix, thereby providing a favourable microenvironment for cell growth and survival [334]. This is also supported by the long-term experiment, where the cells have been consistently proliferating over the course of 21 days.

Previous studies have utilised 'pseudoislet' generation methods with MIN6 cells to enhance insulin secretion compared to simple monolayer cultures, owing to increased cell-to-cell contact [319, 335-337]. Using BIOMIMESYS® ECM-mimicking scaffold has led to the formation of multiple MIN6 spheroids in 3D, which more closely resemble the islets of Langerhans found in native tissue. MIN6 insulin secretion was maintained over the course of a one-week culture in 3D, consistent with conventional culture.

The gene expression data in the short-term experiment confirmed the maintenance of key β-cell identity genes in the 3D culture. Interestingly, the slight increase of *Mafa* expression at day 7, albeit not statistically significant, could suggest a trend towards improved beta cell maturation in 3D culture over time [338]. In addition to this, the expression of *Gcg* and *Sst* (glucagon and somatostatin) appears to decrease in 3D culture over time, which could indicate a more specific beta cell phenotype, as these are typically expressed in other pancreatic endocrine cells. Although qRT-PCR was not performed in the long-term experiments, further gene expression investigation is needed to confirm these trends.

Despite the enhanced proliferation rate and cell viability in 3D culture compared to 2D, the total insulin content, as well as the expression of *Ins1* and *Ins2* genes, remained comparable in both conditions in the 1 week short-term evaluation. Klochendler et al. had previously shown that β-cell cycle progression in a transgenic mouse model (Ins-rtTA; TET-DTA) was linked to a decrease in the expression of genes specific to β-cells [339]. Similarly, Puri *et al.* demonstrated that in the INS-1 cell line, genes involved in insulin secretion and production were deregulated, and the efficiency of GSIS diminished when the cells entered the cell cycle [340]. Additionally, studies on the human β-cell line EndoC-βH have reported that GSIS could be improved by inhibiting cell proliferation [341]. This phenomenon might be due to partial β-cell de-differentiation during periods of high proliferative activity, as both insulin production and cell proliferation are energy-intensive processes that may need to trade off. In the model developed in

this work, however, both processes appear to occur simultaneously, suggesting that in 3D culture, MIN6 cells are able to sustain the expression of β-cell identity genes while proliferating. Further investigations are needed to fully understand this observation. On the other hand, the insulin secretion activity of the 3D cultured MIN6 cells in the long-term experiment has shown a promising result, especially with improvement on the day 21.

β-cell differentiation, survival and metabolism have been linked to mechanotransduction mechanisms acting on cell nuclei and mitochondria [342, 109]. Additionally, MIN6 cells have previously demonstrated increased glucose sensitivity when exposed to softer biomaterials, as opposed to the rigid surface of standard culture dishes. For instance, Nyitray et al. reported improved glucose response in cells cultured on 0.1 kPa scaffolds by accessing β-catenin signalling pathways [343]. As well as this, PIEZO1 transduction in β-cells has been shown to impact insulin secretion in response to encapsulation in increased stiffness materials [344]. In contrast, Zhang et al. observed increased insulin production and comparable secretion using hydrogels with stiffnesses of 40 and 70 kPa [345]. Although this thesis aimed to achieve a significant improvement in function by targeting the mechanical properties of native tissue, this was not observed.

The composition of the matrix may also have an impact on the insulin secretion function of the β-cells. The biomolecules incorporated into the hydrogel scaffold were designed to mimic those found in the natural pancreatic ECM. However, there is a challenge in achieving the appropriate balance of these molecules. For instance, despite reported positive effects of HA on insulin secretion [346], there is also evidence that HA becomes more abundant in T1D and T2D islets as the disease progresses, which leads to induced inflammation, damaging the β-cells [347, 348]. Further fine-tuning the scaffold components' concentrations is therefore crucial to achieving the desired effect.

Pseudoislet size has also been reported to influence the insulin-secreting capabilities of β-cells. For example, Mendelsohn et al. found that increasing the size of 832/13 insulinoma cell clusters from 40 to 60 and 120 μm led to a significant rise in the insulin index [349]. In this study, smaller spheroids were more prevalent, which may have negatively impacted the difference in insulin secretion between low and high glucose conditions. The scaffold's pores' size could have been the limiting factor dictating the capacity for pseudoislet formation. While the pores were studied on the dry samples under SEM, it remains unclear, what changes the pores had undergone, when culture media was introduced, causing size increase of the scaffold from 50% to 70%. On the one hand the pores could have been expanded due to swelling. On the other hand, the liquid could have been absorbed by the fibres thanks to the hydrophilic properties of the HA. The true pore size accommodating the cell cluster formation is therefore yet to be established. As well as this, cell-to-cell contacts as opposed to cell-scaffold attachments could also impact the insulin secretion functionality and it is unclear which one of these interactions plays a more dominant role. To capture the morphological aspects of the scaffold's porosity and cell interactions with the fibres, environmental SEM could be employed [350]. Also, fibre visualisation with fluorescent

staining could help to better observe the cell distribution within the pores of the scaffold. For this, HA-binding protein-streptavidin-FITC staining was attempted, however failed due to the modified chemical structure of HA in the scaffold [351].

It is hypothesised that further refinement of the hydrogel scaffold's mechanical properties, composition and pore size, along with longer incubation periods for MIN6 cells, could improve cell survival and maturation, leading to the formation of larger clusters and more cell-to-cell contacts, thereby enhancing insulin secretion under high glucose conditions.

The scaffold's performance has also been demonstrated in this work to be more advantageous and practical, compared to other 3D models, such as agarose and Matrigel®. Agarose gel spheroids were less physiologically relevant and more difficult to handle for the GSIS supernatant collection process. This could also be a drawback for utilising such model in a microfluidic setting with a continuous perfusion. Despite previously reported successful application of Matrigel® matrices with rodent cells [126], this approach was less efficient, compared to BIOMIMESYS® scaffolds, shown in this thesis. The Matrigel® samples exhibited more cell death, particularly at the spheroid core, while the insulin secretion remained unaffected by the glucose concentration. This suggests that nutrient diffusion is less efficient in Matrigel® — especially to the cells in the core of the spheroid, affecting cells' metabolic behaviour. Since cells in the centre are farther from the nutrient source, limited diffusion may lead to nutrient deprivation and cell death, a common problem in 3D cultures.

6.2 Microfluidics

The design and implementation of microfluidic perfusion circuits were intended to further improve the physiological relevance of the model developed in this thesis. Microfluidic methods established by this work were approached from control systems perspective. The fluid flow P-Q relationship in the microfluidic system was universally applicable across all chip geometries in this thesis, serving as an effective tool for determining the necessary pressure inputs to achieve the desired flow. Reducing the microchannel dimensions as well as diameters of the connecting tubes resulted in increase of the linear term b and diminished term a, as demonstrated by the experimental P-Q data, due to dominance of viscous forces over inertial forces. This finding is consistent with broader microfluidic literature, where resistance-based flow control is often used to describe fluid behaviour. A simplified linear model of fluid resistance to flow is conventionally employed in microfluidic circuit design [352, 353]. In contrast to the quadratic model, the linear model was more appropriate for the thinner geometries, in the range of 100-200 μm, and in the bifurcation flow setup. Furthermore, increasing the total resistance of the system improves the accuracy of flow control, since random small variations in pressure generator output transduce into less significant disturbance to the flow rate.

In the case of the bifurcation flow setup, the resistance estimation based on the flow measurements have confirmed the underlying principle of flow distribution in parallel channels, consistent with the existing literature on parallel flow investigations [354, 355]. This result also

provides an opportunity for controllable properties of split channel designs for high throughput experiments. Modular microfluidics is gaining significant attention within the microfluidics community, particularly in life sciences, due to its potential advantages, such as the ability to control distinct culture media independently [356, 220]. For instance, tissues derived from primary cells or cell lines such as 3T3-L1 often require tailored growth conditions to reach maturity. The modular approach allows individual tissue constructs on separate chips to mature under specific conditions before being interconnected. Once matured, the chips can be linked to investigate interactions between the different tissue types [357]. Understanding the flow characteristics enables the versatility of microfluidic circuit designs, such as parallel vs series connections and open vs recirculated flow.

System volume measurement technique was a useful tool in obtaining an estimate of the required liquid supply for known perfusion durations. However, this method has a limitation in assuming the uniform density of the air, that is being pushed by the liquid during the measurement process. On the contrary, air is a compressible fluid, meaning its density (and hence the volume) changes significantly under varying pressure conditions, according to Boyle's law [358]. When liquid is pushed through the microfluidic system, the displacement of air can result in pressure fluctuations that may not be directly proportional to the flow rate of the liquid. This compressibility can lead to inaccuracies in volume estimation, especially at higher flow rates or when large volumes of air are displaced rapidly. As well as this, the interaction between the liquid and the compressible air phase may lead to complex flow patterns due to viscous effects, that are not easily predictable or integrable. Surface tension at the air-liquid interface can also impact the flow and displacement dynamics, particularly in microfluidic systems where capillary forces are more pronounced. Nonetheless, the measured fluid flow profile presented in this work was rather uniform over time, suggesting low fluctuations of the pressure.

PID control method was shown to be a better alternative to the native adaptive control of the Fluigent™ equipment, providing a smother profile of steady-state flow. This offers an advantage for stable flow conditions to better control the perfusion experiments and avoid excessive stress on the cell culture. However, the impact of the shear stresses exerted onto the perfused cell culture resulting from the flow variations should be considered individually for the microwell geometry in question. On the other hand, the continuous flow monitoring and adjustment of pressure inputs in order to sustain constant flow rate may prove useful in the long-term experiments with cell cultures. As the cells proliferate, the resistance to flow is expected to increase, impacting the P-Q relationship of the system. Hence by implementing the PID control it would be possible to have automated pressure adjustment for the entire duration of the experiment.

The early GSIS experiment using a microfluidic ibidi® chip and isolated mouse islets exposed significant issues with the initial experimental design, particularly in controlling glucose delivery and flow-induced stress on β-cells. The counter-intuitive insulin secretion pattern, with higher insulin during low glucose periods, pointed to inadequate solution mixing, meaning that glucose concentrations were not as expected during insulin measurements. A follow-up

experiment revealed that the solution turnover time was underestimated due to transient mixing phenomena, taking 90 minutes to go from low to high glucose concentration, instead of the projected 41 minutes. This dead volume mixing effect is a technical issue, that needs to be considered in future experiments. Furthermore, elevated initial insulin secretion is hypothesised to be triggered by the flow-induced effects on β-cells, as opposed to static culture. The expected shear stress at the flow rate as low as 10 µl/min was not anticipated to impact the β-cell activity, since given the chamber size, even a tenfold increase in flow rate would have had no significant impact. Nonetheless, it was demonstrated by Jun et al. that the flow rate has impact on the localisation of paracrine factors, which regulate insulin secretion, when many islets were cultured on the same chip [248]. Future experiments need to test this hypothesis by measuring the insulin secretion, while varying the flow rate. In order to reduce the mixing time, possible improvements would include the use of smaller system volume and accelerated perfusion between the solution changes. The exact mixing dynamics could be analytically evaluated by employing finite element analysis modelling, considering diffusion-convection processes in the laminar flow.

With these considerations, a custom microfluidic PDMS chip design has been proposed in this thesis, featuring smaller channel geometry. The chip included a split into 4 separate parallel channels with microwells to improve the experimental throughput and facilitate direct incorporation of the BIOMIMESYS® scaffolds. PDMS was chosen as common soft elastomer material, often used for rapid prototyping in science thanks to its relatively low cost and good bonding to glass. The use of sandwich design, while offering a solution to liquid volume in the microwells, has also lead to significant fabrication complications, requiring PDMS concentration alteration, extra stages of PDMS deposition and bonding of the parts to ensure a good seal. On the one hand, increasing the monomer concentration may have an impact on cytotoxicity of the chip [359]. However, it was a trade off to improve the seal of the chip parts, since the pressure gradient across the entire chip geometry could not be compromised in order to avoid leaks and bubble formation. A possible solution for improved bonding of the sandwich parts would be the use of UV-curable OSTE+ polymer instead of PDMS [266], however it is more expensive. Other solutions would be rigid thermoplastics, such as PMMA, COC or PC, which could be thermally embossed into the desired geometries, however the bonding strategies would be more complicated for the proposed design of the chip. PTFE could be a non-toxic alternative to PDMS, although the fabrication would involve high melting temperatures [217]. Bubble traps were also considered, but not included in the chip design due to difficulty of implementation.

Expectedly, Q-P experiment on the proposed chip resulted in strong linearity between pressure input and flow rate output measured by the Fluigent™ sensor. This confirmed once again the dominance of viscous forces over the internal forces. The absence of any significant change in flow resistance during the cell-free application of the hydrogel scaffold within the chip demonstrates promising potential for perfusion experiments. This is explained by the scaffold's high porosity, which is ideal for efficient fluid flow. That said, the cell culture would impact the resistance, since the MIN6 cells have been shown in static experiments, described above, to grow

into spheroid structures, occupying the pores. Given the technical issues encountered with the cell culture and time constraints of the thesis, however, no further microfluidic experiments could be performed.

6.3 Microelectrodes

The perfusion GSIS experiment has also revealed the inefficiency of insulin measurements by ELISA due to lack of real-time monitoring and low temporal resolution. This has highlighted the need for on-chip environment monitoring and hence the electrochemical sensor development approach was taken by this work. The implementation of continuous on-chip insulin monitoring was planned to enable more detailed observations of the biphasic β-cell activity. The changes in these secretion patterns are known to be an important marker of T2D in the pancreas [60]. Hence real-time insulin tracing would provide an essential tool for observation of the β-cell dysfunction and disease progression, especially in the long-term experiments. At the same time, the electrochemical approach was viewed as a cheaper analytical method, compared to the ELISA kits to achieve this goal.

MEA used in sensing applications are typically comprised of a substrate, conductive electrode tracks, and a passivation layer. A key challenge in developing MEA for this thesis lied in maintaining reliability of the device, when exposed to liquid environments for microfluidic application. The choice of Ti/Au thin film for the microelectrodes was dictated by its favourable adhesion properties, high conductivity, chemical stability, and biocompatibility [360-362]. In addition to selecting appropriate materials for the electrodes, ensuring the quality of the passivation layer was equally important. This layer electrically insulates the interconnections from the liquid, exposing only the required regions of the electrodes. The use of SU-8 resin for this layer ensured it could produce high-aspect-ratio structures that are able to withstand both mechanical and chemical stresses, such as washes or exposure to harsh solvents. Additionally, SU-8 is widely used in biological interface devices due to its excellent biocompatibility and the fact that it does not release chemicals that could interfere with sensing processes [363-365].

The MEA fabrication was hindered by the deposition process of SU-8 insulating layer onto the glass substrate, which had to be optimised. The use of a transparent substrate was considered crucial to enable microscopy of the *diachip*. However, glass substrates are challenging in photoresist microfabrication due to different glass transition temperature and surface characteristics, compared to the traditional silicon wafers [366]. Optimising resist dispensing and spin coating parameters was important, as dispense volume and rate together with the temperature influence the film thickness. Furthermore, the substrate cooling post the soft bake stage needed careful management to avoid film stress. Exposure times were found to be overestimated in the data sheet and had to be shortened to avoid polymerisation and thickening of unexposed areas. The post-exposure bake was a critical stage, intended to activate cross-linking through the diffusion of Lewis acids. This stage also required careful temperature management to minimise internal stresses. While the robust SU-8 on glass fabrication method has been demonstrated by this

work, alternative insulation methods, such as oxide/nitride films or parylene C coating [367] could be also considered. For instance, SiO_2 sputtering, followed by photoresist patterning and etching is rather straightforward and cost-efficient and provides decent electrical insulation. Nonetheless, it can be prone to delamination at liquid interfaces, making it less suitable for electrochemical application. Parylene C has reliable electrical properties and is often an excellent choice for complex geometries. Despite this, to avoid delamination, the fabrication involves extra adhesion enhancement steps and dry etching patterning, making it more complex and expensive, compared to SU-8 deposition [365].

Ferri- ferrocyanide redox in KCl supporting electrolyte was chosen as the standard 1-electron quasi-reversible couple for characterisation of the microelectrodes in benchmark electrochemical tests, with well-studied oxidation potential and diffusion parameters [368-370]. Linear sweep voltammetry has been previously reported to be a robust technique for microelectrode diameter measurement as well as evaluation of interference, based on diffusion limited current [371]. By applying this method, the characterisation of MEAs in this thesis confirmed that the fabricated microelectrodes met the required geometrical criteria. Moreover, the observed forward-backward voltage-current curves had little to no hysteresis, suggesting low double-layer capacitance and dominance of the faradaic current [372, 290]. This is the consequence of using microscale electrodes with low surface areas, which leads to a higher signal-to-noise ratio, enhancing the sensitivity of the microelectrode as well as quicker response times. This is especially advantageous for detecting low analyte concentrations in solution, enabling real-time measurements, enhanced dynamic performance, and the simultaneous use of multiple electrodes in electrochemical sensing [373].

In addition to this, the MEA electrodes were studied both individually and simultaneously, with no impact on voltage-current characteristics observed, validating the electrode spacing. Interestingly, the diffusion zones on microelectrodes are influenced by the diffusion coefficients of the analytes. Ferricyanide, with a diffusion coefficient of 0.726×10^{-5} cm^2/s diffuses significantly faster than insulin, diffusion coefficient of which is 5×10^{-10} cm^2/s. Consequently, the diffusion zones around the microelectrode surface are wider for ferricyanide, compared to those for insulin over the same time scale. Therefore, the spacing between individual microelectrodes, validated by ferricyanide, should be more than sufficient to prevent signal overlap and interference between the individual microelectrodes in the case of insulin tracing. This finding, however, would need to be verified under perfusion conditions, since the diffusion zones would be affected by the fluid flow [374].

Cyclic voltammetry was found to be a more efficient GO deposition technique for microelectrode surface modification, compared to previously reported electrophoretic deposition [375]. The increase in current amplitude observed during the cyclic voltammetry on the MEA can be attributed to several factors. GO flakes exhibit large surface area, enhancing the electroactive surface available for electron transfer. As the cyclic voltammetry process continued, more of the electrode surface was becoming covered with GO, which lead to an increase in active sites and

improved the electron transfer. This resulted in a progressive rise in current amplitude with each cycle. The formation of a dense GO film, as shown in the SEM images, reduced contact resistance and improved overall conductivity of the microelectrodes, allowing for more efficient electron transfer during subsequent cycles.

The first attempts to find the oxidation potential of insulin in PBS solution in sweep voltammetry tests of the modified MEA have resulted in no notable change in current. Due to the time constraints of the project, the attempts were limited and more tests are needed to better understand the encountered problem. It is hypothesised, that the mass transport by diffusion of insulin, discussed above, was too small to produce a detectable flux at the given signal-to-noise ratio. Possible solution to this would be the simultaneous use of the array in order to scale the total signal. Another improvement could be reducing the GO layer to further enhance the conductivity. Removing oxygen-containing groups during the reduction would provide a more efficient electron transport mechanism and increase the availability of active sites for insulin adsorption [376]. Previously reported works on the use of reduced GO for insulin detection have utilised larger-scale electrode geometries enabling low limits of detection [278, 279, 377], hence scaling the total area of detection as well as reducing the GO layer should be considered. Another approach to amplifying the signal would be to increase the total surface area by using carbon nanotubes [280]. Thanks to their smaller dimension compared to the flakes, they could contribute to much more significant surface roughness increase at nanoscale, providing more sites for the electron transfer. Another hypothesis, explaining the lack of signal, could be that the characteristic oxidation potential did not reside within the applied range. This range was dictated by the use of gold as a conductive material for the electrode. It was observed in practice that gold was prone to corrosion and dissolution at the potential higher than 0.6 V. As an alternative, more resistant materials could be considered for the future experiments, such as glassy carbon [276], ruthenium oxide [275] or iridium oxide [280]. However, surface modification strategies, considered above would still be required to improve the conductivity and mass transport to these microelectrodes.

6.4 Further work

This work has taken several foundational development steps, centred around the key elements of the diachip device, as was outlined by the project's objectives. These approaches included the development of 3D matrices for the cell culture chamber, microfluidic circuits, and microelectrode sensors for the detection chamber. Despite significant progress in overcoming of numerous challenges, the work could not be fully completed due to the complexity of the tasks. Many important steps have been successfully undertaken, such as: scaffold characterisation and functionality test with MIN6 cells, microfluidic circuit characterisation and control, chip design and fabrication optimisation, MEA fabrication and characterisation, micro electrode surface modification. Nonetheless, each of these steps proved to carry time-consuming technical challenges, such as: MIN6 functional maintenance, insulin quantification with ELISA, scaffold size adjustment for the mechanical tests, optimisation of microfluidic chip to avoid leakages,

optimisation of SU-8 photolithography and GO deposition methods. Therefore, further work remains necessary to achieve the full scope of the project's objectives. The next steps will need to finalise the development of these individual elements and combine them into a single device.

While this thesis highlights the potential of the synthesised biomimetic scaffold in improving *in vitro* models of pancreatic islets, several limitations and future directions must be considered. First, the use of MIN6 cells, although a convenient and well-established model, may not fully replicate the behaviour of primary human islets [317]. MIN6 cell line has been routinely used in this laboratory and it appeared to be the most reliable model available for this work, for the purpose of initial validation of the scaffold. Future studies should validate these findings using primary human islets or hiPSC-derived β-cells to enhance the scaffold's relevance to human biology. hiPSC strategies have already shown promise in 3D models of the pancreas [378-380]. Furthermore, the long-term effects of the scaffold on cell viability, function, and differentiation should be further investigated. This work presents promising results over a 7-day period and a 3-week culture. However, more longer-term experiments are necessary to confirm the scaffold's ability to maintain cell function and phenotype over extended durations [381] as well as to test for the stability and degradation characteristics. While stiffness of the scaffold has been satisfactory, the dynamic viscoelastic properties and chemical composition may require further optimisation to more closely mimic native pancreatic ECM. The incorporation of additional ECM components, such as laminin [125], nidogen [127] and heparan sulphate [382], or modulation of cross-linking density, could be explored to fine-tune the scaffold's properties and enhance its biological relevance.

Further *in vitro* studies are needed to evaluate the scaffold's performance in more complex environments. Thanks to its high porosity, the scaffold has demonstrated the potential to be used in a microfluidic OOC setup with dynamic fluid supply across the seeded matrix. Such an application has already been reported with a similarly synthesised matrix that mimics the liver ECM [383]. The next step for the validation of the model presented in this work would be an on-chip 3D β-cell functionality evaluation in the short-term and long-term context. Both open and closed-loop (recirculation) perfusion systems should be considered. For the latter, a peristaltic pump can be employed. Furthermore, this work has underlined the impact of the shear forces exerted on the β-cells by the scaffold and fluid flow on the insulin secreting functionality. This could be further investigated by studying the mechanotransduction mechanisms, such as PIEZO1 and YAP/TAZ in sequencing analyses.

Preliminary results have reported the successful utilisation of the hydrogel scaffold with 3T3-L1 adipocytes [294]. Further direction for Micro3DBeta project would be to create a multi-organ on chip device in order to investigate the cross-talk between pancreatic and adipose tissues, particularly insulin secretion by β-cells and lipid metabolism in adipocytes. Currently there exist several gaps in our understanding of the detailed sequence of molecular events linking obesity, insulin resistance and T2D. Therefore, pancreas-adipose-on-chip presents a novel opportunity to study the closed-loop processes involved in this cross-talk and how they impact the cell activity of

both tissues, leading to loss of insulin secretion and β-cell mass. Compared to the existing *in vivo* models, such device would have an advantage of better environmental control, high temporal resolution, quick access to molecular biology. With the 3D culture of β-cells validated by this thesis, further work should focus on studying their co-culture with adipocytes. The secretory activity of the latter can be probed under dynamic glucose and forskolin stimulations [384]. To enable these experiments, whilst ensuring physiological relevance, a crucial step would be to optimise the ratio of the two cell types and their respective culture media. For this, allometric and functional scaling approaches should be considered, adjusting the proportions based on the metabolic rates and secretory function. Metabolic activity, together with viability and functionality assays need to be performed on the co-cultured cells, maintained in a varying range of the cell numbers as well as respective media ratios. Functional outputs should be assessed, targeting the physiological ranges of main hormones, such as insulin (50-70 pM), adiponectin (70-1200 nM) and leptin (30-900 PM). qRT-PCR analysis of mRNA expression of the co-culture should also be performed as part of this investigation to confirm the identity of the cells.

The use of microfluidic system developed in this thesis enables open-loop flow conditions by perfusing the dedicated cell co-culture chambers in series. This arrangement could be used to study how direct secretion from one tissue type affects the function of the other by artificially generating hormone gradients. For instance, GSIS could be applied to trigger insulin response in the β-cells, which in turn would affect the lipolytic activity of adipocytes as well as adiponectin and leptin secretion. Furthermore, closed-loop flow system could be designed to more closely mimic the circulatory environment of the organism. For this, a peristaltic pump could be used to recirculate the liquid across the cell culture chambers. In this scenario, the consequent regulation of β-cell activity by the adipocytes would be included in the model. The key advantage of 3D model demonstrated in this thesis is its ability to support long-term viable and functional culture. Perfusion experiments lasting a couple of weeks could be designed featuring regular functionality evaluations every few days. In order to enable this, however, sterile conditions have to be ensured as well as sufficient flow control to avoid evaporation. If made possible, such approach would be useful to investigate the feedback cross-talk responses in the stimulated conditions of glucotoxicity, hyperinsulinemia or lipotoxicity, deconstructing the black box of the homeostasis disruptions.

With successful GO deposition onto the microelectrodes the next steps include reduction of the GO layer and increasing the total surface area of the MEA. To enable continuous glucose and insulin sensing, cyclic voltammetry can be used to first identify the characteristic oxidation potentials, which will then be applied as reference for amperometry. Additional surface modifications, including aptamers or molecular imprinting could be explored [385, 386]. On the other hand, given the limitations of electrochemical methods for detecting certain biomolecules, alternative analytical techniques could be employed for *diachip*. For example, impedance spectroscopy can be tested for other biomarkers, such as leptin and adiponectin [387]. Alternatively, fluorescent antibody labelling or gene modification for optical sensing could be

integrated into the *diachip* to broaden the range of traced analytes. These techniques could be essential for understanding the cross-talk between pancreatic and adipose cells, providing insights into the dynamics of hormonal regulation of and metabolism during T2D.

As outlined by the thesis objectives, after the successful fabrication and validation of the *diachip*, further automation of the device could be explored. Extended environmental control could be achieved by integrating temperature chamber and CO_2 supply platforms with programmable microcontrollers, such as Arduino. Further monitoring of metabolic conditions in the microfluidic system could be performed with additional sensors for O_2 and pH, complementing the glucose biosensors under development and providing a more comprehensive understanding of cellular activity on the chip [388].

This work presents the approach to mimic the peninsular basement membrane, surrounding the islets of Langerhans. To further improve the physiological relevance of the *diachip*, perivascular basement membrane could be modelled by incorporation of vascularisation strategies. Vascularisation is essential for nutrient and oxygen delivery in *in vivo* environments, and its absence in *in vitro* models remains a significant limitation, providing inaccurate gradient models. Co-culture systems involving endothelial cells or the incorporation of pre-vascularised scaffolds could be explored to address this issue [252]. Additionally, integration of immune cells could provide a more complete representation of the diabetic microenvironment, since inflammation affects β-cells in both T1D and T2D physiopathology [389, 390].

The model developed in this thesis could also serve as a platform for testing pharmaceutical agents. Future work could focus on using the *diachip* for drug screening applications, enabling high-throughput testing of T2D treatments in a controlled, physiologically relevant setting. This approach is expected to improve the drug development efficiency, also enabling personalised medicine if patient derived cells are to be used in the model [391].

Finally, a complementary *in silico* model could also be considered for the cross-talk of islets and adipocytes (Figure 6.4.1). Development of the *diachip* will lead to the increased volume of the experiments, which is anticipated to produce a dataset where varying input conditions will have an effect on the secretion levels of insulin and adipokines. Thus, the dataset could be used for the development of a mathematical model describing the *diachip* system, which in turn can shine the light on the black box mechanisms in the metabolic disease. Certain assumptions and linearisation steps will need to be taken to translate the model to the real biological system, which is oftentimes non-linear [392]. Hence, system identification, fuzzy rules-based system and machine learning approaches can be explored to tackle this problem [393-396].

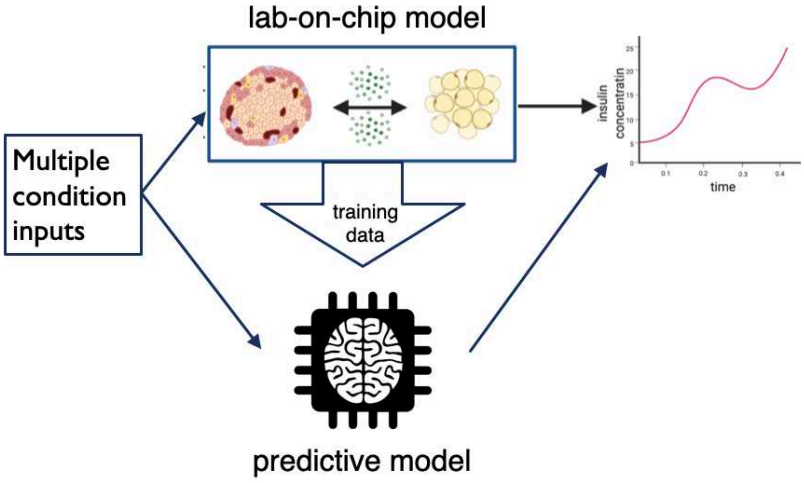

Figure 6.4.1 Lab-on-chip and predictive model to describe biological activity. Development of multi-organ-on-chip device can generate data, that together with existing biological research results could be used to derive a computational model of cellular signalling and behaviour. Using both *in vitro* and *in silico* models in tandem could improve the understanding of complex biological interactions during T2D and drive predictions about them.

7. Conclusion

Microfluidic 3D multi-OOC models show promising potential in T2D physiopathology research by studying inter-organ signalling details, while better mimicking natural environments, compared to the conventional models.

This work has laid the foundations for creating a microfluidic 3D model of pancreatic tissue, envisioned to be used for T2D progression studies of the cross-talk between the adipose tissue and pancreas, proposed as *diachip*. The project aimed to provide an improved physiological relevance, compared to the existing *in vitro* models, and an extensive analytical functionality. In order to achieve this, the thesis work focused on several key aspects, including: use of ECM for 3D culture, design and charactrisation of microfluidic circuits and automation methods for perfusion experiments, as well as biosensor development for biomarker monitoring.

BIOMIMESYS 3D hydrogel scaffolds used in this work were synthesised incorporating key ECM components, mimicking the composition of native pancreatic tissue, including HA, collagens and RGDS. Chemical characterisation has confirmed the presence of these molecules and their cross-linking. The scaffold's stiffness was found comparable to the pancreatic ECM in rheological tests. A stress-relaxation model has been developed in this work, based on the experimental data, to evaluate the viscoelastic properties of the biomaterial, highlighting the key mechanical behaviour characteristics. The high porosity of the scaffold provides multiple sites for cell adhesion and facilitates effective microfluidic perfusion.

3D culture of MIN6 cells on the scaffolds has resulted in enhanced proliferation and formation of islet-like structures as well as maintained insulin secretion and differentiation over the short term. Furthermore, the insulin-secreting function was demonstrated to be maintained over the long term. The hydrogel scaffolds were also shown here to be an advantageous 3D pancreatic model, compared to Matrigel and agarose. At the same time, the results of this study indicate that the interaction between scaffold properties and β-cell behaviour is more intricate than previously expected, emphasising the necessity for further refinement of the scaffold design and chemical composition.

Microfluidic techniques explored by this thesis can be used to characterise and control open-loop perfusion systems. Understanding the mixing dynamics and flow impact on β-cell activity will be crucial for further experiments. Biosensor MEA design, fabrication and characterisation methodologies, presented in this work can be used as basis for the development of on-chip analytic tools, such as glucose and insulin sensors.

Refining the *diachip* platform by co-culturing β-cells and adipocytes as well as implementing biosensors, automation and vascularisation, will be essential steps in improving the physiological relevance and utility of the model. Additionally, the development of mathematical models will contribute to a deeper understanding of the complex interactions between pancreatic and adipose tissues during T2D progression, ultimately supporting the development of more effective therapeutic strategies.

References

1. American Diabetes Association, 2021. 2. Classification and diagnosis of diabetes: standards of medical care in diabetes—2021. Diabetes care, 44(Supplement_1), pp.S15-S33.
2. DeFronzo, R.A., Ferrannini, E., Groop, L., Henry, R.R., Herman, W.H., Holst, J.J., Hu, F.B., Kahn, C.R., Raz, I., Shulman, G.I. and Simonson, D.C., 2015. Type 2 diabetes mellitus. Nature reviews Disease primers, 1(1), pp.1-22.
3. Magliano, D.J., Boyko, E.J. and Atlas, I.D., 2021. What is diabetes?. In IDF DIABETES ATLAS [Internet]. 10th edition. International Diabetes Federation.
4. Zheng, Y., Ley, S.H. and Hu, F.B., 2018. Global aetiology and epidemiology of type 2 diabetes mellitus and its complications. Nature reviews endocrinology, 14(2), pp.88-98.
5. Abdul Basith Khan, M., Hashim, M.J., King, J.K., Govender, R.D., Mustafa, H. and Al Kaabi, J., 2020. Epidemiology of type 2 diabetes—global burden of disease and forecasted trends. Journal of epidemiology and global health, 10(1), pp.107-111.
6. Forbes, J.M. and Cooper, M.E., 2013. Mechanisms of diabetic complications. Physiological reviews, 93(1), pp.137-188.
7. Bommer, C., Heesemann, E., Sagalova, V., Manne-Goehler, J., Atun, R., Bärnighausen, T. and Vollmer, S., 2017. The global economic burden of diabetes in adults aged 20–79 years: a cost-of-illness study. The lancet Diabetes & endocrinology, 5(6), pp.423-430.
8. Bommer, C., Sagalova, V., Heesemann, E., Manne-Goehler, J., Atun, R., Bärnighausen, T., Davies, J. and Vollmer, S., 2018. Global economic burden of diabetes in adults: projections from 2015 to 2030. Diabetes care, 41(5), pp.963-970.
9. Chatterjee, S., Khunti, K. and Davies, M.J., 2017. Type 2 diabetes. The lancet, 389(10085), pp.2239-2251.
10. Guh, D.P., Zhang, W., Bansback, N., Amarsi, Z., Birmingham, C.L. and Anis, A.H., 2009. The incidence of co-morbidities related to obesity and overweight: a systematic review and meta-analysis. BMC public health, 9, pp.1-20.
11. Popkin, B.M., Adair, L.S. and Ng, S.W., 2012. Global nutrition transition and the pandemic of obesity in developing countries. Nutrition reviews, 70(1), pp.3-21.
12. Knowler, W.C., Barrett-Connor, E., Fowler, S.E., Hamman, R.F., Lachin, J.M., Walker, E.A., Nathan, D.M., Watson, P.G., Mendoza, J.T., Smith, K.A. and Caro, J., 2002. Reduction in the incidence of type 2 diabetes with lifestyle intervention or metformin.
13. American Diabetes Association Professional Practice Committee and American Diabetes Association Professional Practice Committee:, 2022. 4. Comprehensive medical evaluation and assessment of comorbidities: Standards of Medical Care in Diabetes—2022. Diabetes Care, 45(Supplement_1), pp.S46-S59.
14. Powers, M.A., Bardsley, J.K., Cypress, M., Funnell, M.M., Harms, D., Hess-Fischl, A., Hooks, B., Isaacs, D., Mandel, E.D., Maryniuk, M.D. and Norton, A., 2020. Diabetes self-management education and support in adults with type 2 diabetes: a consensus report of the American Diabetes Association, the Association of Diabetes Care & Education Specialists, the Academy of Nutrition and Dietetics, the American Academy of Family Physicians, the American Academy of PAs, the American Association of Nurse Practitioners, and the American Pharmacists Association. Journal of the American Pharmacists Association, 60(6), pp.e1-e18.
15. Tahrani, A.A., Piya, M.K., Kennedy, A. and Barnett, A.H., 2010. Glycaemic control in type 2 diabetes: targets and new therapies. Pharmacology & therapeutics, 125(2), pp.328-361.
16. Stumvoll, M., Goldstein, B.J. and Van Haeften, T.W., 2005. Type 2 diabetes: principles of pathogenesis and therapy. The Lancet, 365(9467), pp.1333-1346.
17. Tahrani, A. A., Barnett, A. H., & Bailey, C. J. (2016). Pharmacology and therapeutic implications of current drugs for type 2 diabetes mellitus. Nature Reviews Endocrinology, 12(10), 566-592.
18. Kleinert, M., Clemmensen, C., Hofmann, S.M., Moore, M.C., Renner, S., Woods, S.C., Huypens, P., Beckers, J., De Angelis, M.H., Schürmann, A. and Bakhti, M., 2018. Animal models of obesity and diabetes mellitus. Nature Reviews Endocrinology, 14(3), pp.140-162.

19. Zhang, X., Kupczyk, E., Schmitt-Kopplin, P. and Mueller, C., 2022. Current and future approaches for in vitro hit discovery in diabetes mellitus. Drug Discovery Today, 27(10), p.103331.

20. Pantaleao, S.Q., Fujii, D.G., Maltarollo, V.G., da C Silva, D., Trossini, G.H., Weber, K.C., Scott, L.P. and Honorio, K.M., 2017. The role of qsar and virtual screening studies in type 2 diabetes drug discovery. Medicinal Chemistry, 13(8), pp.706-720.

21. Moffat, J.G., Vincent, F., Lee, J.A., Eder, J. and Prunotto, M., 2017. Opportunities and challenges in phenotypic drug discovery: an industry perspective. Nature reviews Drug discovery, 16(8), pp.531-543.

22. Saladin, K.S. and Miller, L., 1998. Anatomy & Physiology. New York: WCB.

23. Da Silva Xavier, G., 2018. The cells of the islets of Langerhans. Journal of clinical medicine, 7(3), p.54.

24. Ionescu-Tirgoviste, C., Gagniuc, P.A., Gubceac, E., Mardare, L., Popescu, I., Dima, S. and Militaru, M., 2015. A 3D map of the islet routes throughout the healthy human pancreas. Scientific reports, 5(1), p.14634.

25. Rorsman, P. and Ashcroft, F.M., 2018. Pancreatic β-cell electrical activity and insulin secretion: of mice and men. Physiological reviews, 98(1), pp.117-214.

26. Eliasson, L., Abdulkader, F., Braun, M., Galvanovskis, J., Hoppa, M.B. and Rorsman, P., 2008. Novel aspects of the molecular mechanisms controlling insulin secretion. The Journal of physiology, 586(14), pp.3313-3324.

27. Rorsman, P. and Renström, E., 2003. Insulin granule dynamics in pancreatic beta cells. Diabetologia, 46, pp.1029-1045.

28. Röder, P.V., Wu, B., Liu, Y. and Han, W., 2016. Pancreatic regulation of glucose homeostasis. Experimental & molecular medicine, 48(3), pp.e219-e219.

29. Quesada, I., Tudurí, E., Ripoll, C. and Nadal, A., 2008. Physiology of the pancreatic α-cell and glucagon secretion: role in glucose homeostasis and diabetes. Journal of endocrinology, 199(1), pp.5-19.

30. Hauge-Evans, A.C., King, A.J., Carmignac, D., Richardson, C.C., Robinson, I.C., Low, M.J., Christie, M.R., Persaud, S.J. and Jones, P.M., 2009. Somatostatin secreted by islet δ-cells fulfills multiple roles as a paracrine regulator of islet function. Diabetes, 58(2), pp.403-411.

31. Petersen, M.C. and Shulman, G.I., 2018. Mechanisms of insulin action and insulin resistance. Physiological reviews, 98(4), pp.2133-2223.

32. Muoio, D.M. and Newgard, C.B., 2008. Molecular and metabolic mechanisms of insulin resistance and β-cell failure in type 2 diabetes. Nature reviews Molecular cell biology, 9(3), pp.193-205.

33. Riaz, S., 2014. Obesity as a risk factor for diabetes mellitus in the local population of Pakistan. Univers. J. Clin. Med, 2(3), pp.58-64.

34. Zierath, J.R., He, L., Guma, A., Wahlström, E.O., Klip, A. and Wallberg-Henriksson, H., 1996. Insulin action on glucose transport and plasma membrane GLUT4 content in skeletal muscle from patients with NIDDM. Diabetologia, 39, pp.1180-1189.

35. Lawrence Jr, J.C. and Roach, P.J., 1997. New insights into the role and mechanism of glycogen synthase activation by insulin. Diabetes, 46(4), pp.541-547.

36. Chow, L.S., Gerszten, R.E., Taylor, J.M., Pedersen, B.K., Van Praag, H., Trappe, S., Febbraio, M.A., Galis, Z.S., Gao, Y., Haus, J.M. and Lanza, I.R., 2022. Exerkines in health, resilience and disease. *Nature Reviews Endocrinology*, *18*(5), pp.273-289.

37. Steinberg, G.R. and Hardie, D.G., 2023. New insights into activation and function of the AMPK. Nature reviews Molecular cell biology, 24(4), pp.255-272.

38. Laviola, L.; Perrini, S.; Cignarelli, A.; Giorgino, F. Insulin signalling in human adipose tissue. Arch. Physiol. Biochem. 2006, 112, 82–88.

39. Titchenell PM, Quinn WJ, Lu M, Chu Q, Lu W, Li C, Chen H, Monks BR, Chen J, Rabinowitz JD, Birnbaum MJ. Direct Hepatocyte Insulin Signaling Is Required for Lipogenesis but Is Dispensable for the Suppression of Glucose Production. Cell Metab 23: 1154–1166, 2016.

40. Perry, R.J., Peng, L., Abulizi, A., Kennedy, L., Cline, G.W. and Shulman, G.I., 2017. Mechanism for leptin's acute insulin-independent effect to reverse diabetic ketoacidosis. The Journal of clinical investigation, 127(2), pp.657-669.

41. Poitout V, Rouault C, Guerre-Millo M, et al. Inhibition of insulin secretion by leptin in normal rodent islets of Langerhans. Endocrinology 1998;139:822-6.

42. Chen NG, Swick AG, Romsos DR. Leptin constrains acetylcholine-induced insulin secretion from pancreatic islets of ob/ob mice. J Clin Invest 1997;100:1174-9

43. Shimabukuro M, Koyama K, Chen G, et al. Direct antidiabetic effect of leptin through triglyceride depletion of tissues. Proc Natl Acad Sci U S A 1997;94:4637-41.

44. Lee, Y.H., Magkos, F., Mantzoros, C.S. and Kang, E.S., 2011. Effects of leptin and adiponectin on pancreatic β-cell function. Metabolism, 60(12), pp.1664-1672.

45. Elliott, A.D., Ustione, A. and Piston, D.W., 2015. Somatostatin and insulin mediate glucose-inhibited glucagon secretion in the pancreatic α-cell by lowering cAMP. American Journal of Physiology-Endocrinology and Metabolism, 308(2), pp.E130-E143.

46. Bruning, J.C., Gautam, D., Burks, D.J., Gillette, J., Schubert, M., Orban, P.C., Klein, R., Krone, W., Muller-Wieland, D. and Kahn, C.R., 2000. Role of brain insulin receptor in control of body weight and reproduction. Science, 289(5487), pp.2122-2125.

47. Obici, S., Zhang, B.B., Karkanias, G. and Rossetti, L., 2002. Hypothalamic insulin signaling is required for inhibition of glucose production. Nature medicine, 8(12), pp.1376-1382.

48. Heni, M., Wagner, R., Kullmann, S., Gancheva, S., Roden, M., Peter, A., Stefan, N., Preissl, H., Häring, H.U. and Fritsche, A., 2017. Hypothalamic and striatal insulin action suppresses endogenous glucose production and may stimulate glucose uptake during hyperinsulinemia in lean but not in overweight men. Diabetes, 66(7), pp.1797-1806.

49. Kim, K.S., Seeley, R.J. and Sandoval, D.A., 2018. Signalling from the periphery to the brain that regulates energy homeostasis. Nature Reviews Neuroscience, 19(4), pp.185-196.

50. Perry, R.J., Peng, L., Barry, N.A., Cline, G.W., Zhang, D., Cardone, R.L., Petersen, K.F., Kibbey, R.G., Goodman, A.L. and Shulman, G.I., 2016. Acetate mediates a microbiome–brain–β-cell axis to promote metabolic syndrome. Nature, 534(7606), pp.213-217.

51. Xiao, C., Dash, S., Morgantini, C., Koulajian, K. and Lewis, G.F., 2015. Evaluation of the effect of enteral lipid sensing on endogenous glucose production in humans. Diabetes, 64(8), pp.2939-2943.

52. Cnop, M., Welsh, N., Jonas, J.C., Jorns, A., Lenzen, S. and Eizirik, D.L., 2005. Mechanisms of pancreatic β-cell death in type 1 and type 2 diabetes: many differences, few similarities. Diabetes, 54(suppl_2), pp.S97-S107.

53. Poitout, V. and Robertson, R.P., 2008. Glucolipotoxicity: fuel excess and β-cell dysfunction. Endocrine reviews, 29(3), pp.351-366.

54. Giacca, A., Xiao, C., Oprescu, A.I., Carpentier, A.C. and Lewis, G.F., 2011. Lipid-induced pancreatic β-cell dysfunction: focus on in vivo studies. American Journal of Physiology-Endocrinology and Metabolism, 300(2), pp.E255-E262.

55. Donath, M.Y., Böni-Schnetzler, M., Ellingsgaard, H. and Ehses, J.A., 2009. Islet inflammation impairs the pancreatic β-cell in type 2 diabetes. Physiology, 24(6), pp.325-331.

56. Ashcroft, F.M. and Rorsman, P., 2013. KATP channels and islet hormone secretion: new insights and controversies. Nature Reviews Endocrinology, 9(11), pp.660-669.

57. Rorsman, P. and Ashcroft, F.M., 2018. Pancreatic β-cell electrical activity and insulin secretion: of mice and men. Physiological reviews, 98(1), pp.117-214.

58. Mulder, H. and Ling, C., 2009. Mitochondrial dysfunction in pancreatic β-cells in type 2 diabetes. Molecular and cellular endocrinology, 297(1-2), pp.34-40.

59. Olofsson, C.S., Salehi, A., Holm, C. and Rorsman, P., 2004. Palmitate increases L-type Ca2+ currents and the size of the readily releasable granule pool in mouse pancreatic β-cells. The Journal of physiology, 557(3), pp.935-948.

60. Weir, G.C. and Bonner-Weir, S., 2004. Five stages of evolving beta-cell dysfunction during progression to diabetes. Diabetes, 53(suppl_3), pp.S16-S21.

61. Nauck, M.K., Stöckmann, F., Ebert, R. and Creutzfeldt, W., 1986. Reduced incretin effect in type 2 (non-insulin-dependent) diabetes. Diabetologia, 29(1), pp.46-52.

62. Gandasi, N.R., Yin, P., Riz, M., Chibalina, M.V., Cortese, G., Lund, P.E., Matveev, V., Rorsman, P., Sherman, A., Pedersen, M.G. and Barg, S., 2017. Ca 2+ channel clustering with insulin-containing granules is disturbed in type 2 diabetes. The Journal of clinical investigation, 127(6), pp.2353-2364.

63. Nagarajan A, Petersen MC, Nasiri AR, Butrico G, Fung A, Ruan H-B, Kursawe R, Caprio S, Thibodeau J, Bourgeois-Daigneault M-C, Sun L, Gao G, Bhanot S, Jurczak MJ, Green MR, Shulman GI, Wajapeyee N. MARCH1 regulates insulin sensitivity by controlling cell surface insulin receptor levels. Nat Commun 7: 12639, 2016

64. James, D.E., Stöckli, J. and Birnbaum, M.J., 2021. The aetiology and molecular landscape of insulin resistance. Nature Reviews Molecular Cell Biology, 22(11), pp.751-771.

65. Garvey, W.T., Maianu, L., Zhu, J.H., Brechtel-Hook, G., Wallace, P. and Baron, A.D., 1998. Evidence for defects in the trafficking and translocation of GLUT4 glucose transporters in skeletal muscle as a cause of human insulin resistance. The Journal of clinical investigation, 101(11), pp.2377-2386.

66. Cusi, K., Maezono, K., Osman, A., Pendergrass, M., Patti, M.E., Pratipanawatr, T., DeFronzo, R.A., Kahn, C.R. and Mandarino, L.J., 2000. Insulin resistance differentially affects the PI 3-kinase–and MAP kinase–mediated signaling in human muscle. The Journal of clinical investigation, 105(3), pp.311-320.

67. Gross, D.N., Van Den Heuvel, A.P.J. and Birnbaum, M.J., 2008. The role of FoxO in the regulation of metabolism. Oncogene, 27(16), pp.2320-2336.

68. Yoon, J.C., Puigserver, P., Chen, G., Donovan, J., Wu, Z., Rhee, J., Adelmant, G., Stafford, J., Kahn, C.R., Granner, D.K. and Newgard, C.B., 2001. Control of hepatic gluconeogenesis through the transcriptional coactivator PGC-1. Nature, 413(6852), pp.131-138.

69. Bugianesi, E., Moscatiello, S.I.M.O.N.A., Ciaravella, M.F. and Marchesini, G., 2010. Insulin resistance in nonalcoholic fatty liver disease. Current pharmaceutical design, 16(17), pp.1941-1951.

70. Kadowaki, T., Yamauchi, T., Kubota, N., Hara, K., Ueki, K. and Tobe, K., 2006. Adiponectin and adiponectin receptors in insulin resistance, diabetes, and the metabolic syndrome. The Journal of clinical investigation, 116(7), pp.1784-1792.

71. Myers, M.G., Cowley, M.A. and Münzberg, H., 2008. Mechanisms of leptin action and leptin resistance. Annu. Rev. Physiol., 70(1), pp.537-556.

72. Randle, P.J., Garland, P.B., Hales, C.N. and Newsholme, E.A., 1963. The glucose fatty-acid cycle its role in insulin sensitivity and the metabolic disturbances of diabetes mellitus. The Lancet, 281(7285), pp.785-789.

73. Krssak, M.F.P.K., Petersen, K.F., Dresner, A., DiPietro, L., Vogel, S.M., Rothman, D.L., Shulman, G.I. and Roden, M., 1999. Intramyocellular lipid concentrations are correlated with insulin sensitivity in humans: a 1H NMR spectroscopy study. Diabetologia, 42(1), pp.113-116.

74. Griffin, M.E., Marcucci, M.J., Cline, G.W., Bell, K., Barucci, N., Lee, D., Goodyear, L.J., Kraegen, E.W., White, M.F. and Shulman, G.I., 1999. Free fatty acid-induced insulin resistance is associated with activation of protein kinase C theta and alterations in the insulin signaling cascade. Diabetes, 48(6), pp.1270-1274.

75. Cignarelli, A., Genchi, V.A., Perrini, S., Natalicchio, A., Laviola, L. and Giorgino, F., 2019. Insulin and insulin receptors in adipose tissue development. International journal of molecular sciences, 20(3), p.759.

76. Kahn, S.E., Hull, R.L. and Utzschneider, K.M., 2006. Mechanisms linking obesity to insulin resistance and type 2 diabetes. Nature, 444(7121), pp.840-846.

77. Stendahl, J.C., Kaufman, D.B. and Stupp, S.I., 2009. Extracellular matrix in pancreatic islets: relevance to scaffold design and transplantation. Cell transplantation, 18(1), pp.1-12.

78. Patel, S.N., Mathews, C.E., Chandler, R. and Stabler, C.L., 2022. The foundation for engineering a pancreatic islet niche. Frontiers in Endocrinology, 13, p.881525.

79. Llacua, L.A., Faas, M.M. and de Vos, P., 2018. Extracellular matrix molecules and their potential contribution to the function of transplanted pancreatic islets. Diabetologia, 61, pp.1261-1272.

80. Pierschbacher, M.D. and Ruoslahti, E., 1984. Cell attachment activity of fibronectin can be duplicated by small synthetic fragments of the molecule. Nature, 309(5963), pp.30-33.

81. Jiang, F.X., Naselli, G. and Harrison, L.C., 2002. Distinct distribution of laminin and its integrin receptors in the pancreas. Journal of Histochemistry & Cytochemistry, 50(12), pp.1625-1632.

82. Weng, X., Maxwell-Warburton, S., Hasib, A., Ma, L. and Kang, L., 2022. The membrane receptor CD44: novel insights into metabolism. Trends in Endocrinology & Metabolism, 33(5), pp.318-332.

83. Singleton, P.A. and Bourguignon, L.Y., 2004. CD44 interaction with ankyrin and IP3 receptor in lipid rafts promotes hyaluronan-mediated Ca2+ signaling leading to nitric oxide production and endothelial cell adhesion and proliferation. Experimental cell research, 295(1), pp.102-118.

84. McCarthy, K.J., 2015. The basement membrane proteoglycans perlecan and agrin: something old, something new. Current topics in membranes, 76, pp.255-303.

85. Zertal-Zidani, S., Bounacer, A. and Scharfmann, R., 2007. Regulation of pancreatic endocrine cell differentiation by sulphated proteoglycans. Diabetologia, 50, pp.585-595.

86. Crawford, S.E., Stellmach, V., Murphy-Ullrich, J.E., Ribeiro, S.M., Lawler, J., Hynes, R.O., Boivin, G.P. and Bouck, N., 1998. Thrombospondin-1 is a major activator of TGF-β1 in vivo. Cell, 93(7), pp.1159-1170.

87. Esposito, I., Penzel, R., Chaib-Harrireche, M., Barcena, U., Bergmann, F., Riedl, S., Kayed, H., Giese, N., Kleeff, J., Friess, H. and Schirmacher, P., 2006. Tenascin C and annexin II expression in the process of pancreatic carcinogenesis. The Journal of Pathology: A Journal of the Pathological Society of Great Britain and Ireland, 208(5), pp.673-685.

88. Ryall, C.L., Viloria, K., Lhaf, F., Walker, A.J., King, A., Jones, P., Mackintosh, D., McNeice, R., Kocher, H., Flodstrom-Tullberg, M. and Edling, C., 2014. Novel role for matricellular proteins in the regulation of islet β cell survival. Journal of Biological Chemistry, 289(44), pp.30614-30624.

89. Phillips, P.A., McCarroll, J.A., Park, S., Wu, M.J., Pirola, R., Korsten, M., Wilson, J.S. and Apte, M.V., 2003. Rat pancreatic stellate cells secrete matrix metalloproteinases: implications for extracellular matrix turnover. Gut, 52(2), pp.275-282.

90. Bramhall, S.R., Neoptolemos, J.P., Stamp, G.W. and Lemoine, N.R., 1997. Imbalance of expression of matrix metalloproteinases (MMPs) and tissue inhibitors of the matrix metalloproteinases (TIMPs) in human pancreatic carcinoma. The Journal of Pathology: A Journal of the Pathological Society of Great Britain and Ireland, 182(3), pp.347-355.

91. Vining, K.H. and Mooney, D.J., 2017. Mechanical forces direct stem cell behaviour in development and regeneration. Nature reviews Molecular cell biology, 18(12), pp.728-742.

92. Thivolet, C.H., Chatelain, P., Nicoloso, H., Durand, A. and Bertrand, J., 1985. Morphological and functional effects of extracellular matrix on pancreatic islet cell cultures. Experimental cell research, 159(2), pp.313-322.

93. Maniotis, A.J., Chen, C.S. and Ingber, D.E., 1997. Demonstration of mechanical connections between integrins, cytoskeletal filaments, and nucleoplasm that stabilize nuclear structure. Proceedings of the National Academy of Sciences, 94(3), pp.849-854.

94. Lombardi, M.L., Jaalouk, D.E., Shanahan, C.M., Burke, B., Roux, K.J. and Lammerding, J., 2011. The interaction between nesprins and sun proteins at the nuclear envelope is critical for force transmission between the nucleus and cytoskeleton. Journal of Biological Chemistry, 286(30), pp.26743-26753.

95. Lou, J. and Mooney, D.J., 2022. Chemical strategies to engineer hydrogels for cell culture. Nature Reviews Chemistry, pp.1-19.

96. Gnanasambandam, R., Bae, C., Gottlieb, P. A. & Sachs, F. Ionic selectivity and permeation properties of human PIEZO1 channels. PLoS ONE 10, e0125503 (2015).

97. M. Yao, A. Tijore, D. Cheng, J.V. Li, A. Hariharan, B. Martinac, G.T. Van Nhieu, C.D. Cox, M. Sheetz Force- and cell state-dependent recruitment of piezo1 drives focal adhesion dynamics and calcium entry Sci. Adv., 8 (45) (2022), pp. 1-15, 10.1126/sciadv.abo1461

98. Deivasikamani, V. et al. Piezo1 channel activation mimics high glucose as a stimulator of insulin release. Sci. Rep. 9, 16876 (2019).

99. Ye, Y., Barghouth, M., Dou, H., Luan, C., Wang, Y., Karagiannopoulos, A., Jiang, X., Krus, U., Fex, M., Zhang, Q. and Eliasson, L., 2022. A critical role of the mechanosensor PIEZO1 in glucose-induced insulin secretion in pancreatic β-cells. Nature Communications, 13(1), p.4237.

100. Dupont, S., Morsut, L., Aragona, M., Enzo, E., Giulitti, S., Cordenonsi, M., Zanconato, F., Le Digabel, J., Forcato, M., Bicciato, S. and Elvassore, N., 2011. Role of YAP/TAZ in mechanotransduction. Nature, 474(7350), pp.179-183.

101. George, N.M., Day, C.E., Boerner, B.P., Johnson, R.L. and Sarvetnick, N.E., 2012. Hippo signaling regulates pancreas development through inactivation of Yap. Molecular and cellular biology, 32(24), pp.5116-5128.

102. Rosado-Olivieri, E.A., Anderson, K., Kenty, J.H. and Melton, D.A., 2019. YAP inhibition enhances the differentiation of functional stem cell-derived insulin-producing β cells. Nature communications, 10(1), p.1464.

103. Cebola, I., Rodríguez-Seguí, S.A., Cho, C.H., Bessa, J., Rovira, M., Luengo, M., Chhatriwala, M., Berry, A., Ponsa-Cobas, J., Maestro, M.A. and Jennings, R.E., 2015. TEAD and YAP regulate the enhancer network of human embryonic pancreatic progenitors. Nature cell biology, 17(5), pp.615-626.

104. Bartolák-Suki, E., Imsirovic, J., Nishibori, Y., Krishnan, R. and Suki, B., 2017. Regulation of mitochondrial structure and dynamics by the cytoskeleton and mechanical factors. International journal of molecular sciences, 18(8), p.1812.

105. Liesa, M. and Shirihai, O.S., 2013. Mitochondrial dynamics in the regulation of nutrient utilization and energy expenditure. Cell metabolism, 17(4), pp.491-506.

106. Anesti, V. and Scorrano, L., 2006. The relationship between mitochondrial shape and function and the cytoskeleton. Biochimica et Biophysica Acta (BBA)-Bioenergetics, 1757(5-6), pp.692-699.

107. Boldogh, I.R. and Pon, L.A., 2006. Interactions of mitochondria with the actin cytoskeleton. Biochimica et Biophysica Acta (BBA)-Molecular Cell Research, 1763(5-6), pp.450-462.

108. Galli, A., Maffioli, E., Sogne, E., Moretti, S., Di Cairano, E.S., Negri, A., Nonnis, S., Norata, G.D., Bonacina, F., Borghi, F. and Podestà, A., 2018. Cluster-assembled zirconia substrates promote long-term differentiation and functioning of human islets of Langerhans. Scientific Reports, 8(1), p.9979.

109. Maffioli, E., Galli, A., Nonnis, S., Marku, A., Negri, A., Piazzoni, C., Milani, P., Lenardi, C., Perego, C. and Tedeschi, G., 2020. Proteomic analysis reveals a mitochondrial remodeling of βTC3 cells in response to nanotopography. Frontiers in Cell and Developmental Biology, 8, p.508.

110. Homo-Delarche, F., Calderari, S., Irminger, J.C., Gangnerau, M.N., Coulaud, J., Rickenbach, K., Dolz, M., Halban, P., Portha, B. and Serradas, P., 2006. Islet inflammation and fibrosis in a spontaneous model of type 2 diabetes, the GK rat. Diabetes, 55(6), pp.1625-1633.

111. Böni-Schnetzler, M. and Meier, D.T., 2019, July. Islet inflammation in type 2 diabetes. In Seminars in immunopathology (Vol. 41, pp. 501-513). Springer Berlin Heidelberg.

112. Zhu, Y., Shu, T., Lin, Y., Wang, H., Yang, J., Shi, Y. and Han, X., 2011. Inhibition of the receptor for advanced glycation endproducts (RAGE) protects pancreatic β-cells. Biochemical and biophysical research communications, 404(1), pp.159-165.

113. Teissier, T. and Boulanger, É., 2019. The receptor for advanced glycation end-products (RAGE) is an important pattern recognition receptor (PRR) for inflammaging. Biogerontology, 20(3), pp.279-301.

114. Bollyky, P.L., Bogdani, M., Bollyky, J.B., Hull, R.L. and Wight, T.N., 2012. The role of hyaluronan and the extracellular matrix in islet inflammation and immune regulation. Current diabetes reports, 12, pp.471-480.

115. Moon, S.J., Jung, I. and Park, C.Y., 2021. Current advances of artificial pancreas systems: a comprehensive review of the clinical evidence. *Diabetes & metabolism journal*, *45*(6), pp.813-839.

116. Phelps, E.A., Templeman, K.L., Thulé, P.M. and García, A.J., 2015. Engineered VEGF-releasing PEG–MAL hydrogel for pancreatic islet vascularization. *Drug delivery and translational research*, *5*(2), pp.125-136.

117. Yang, X.D., Li, H.M., Chen, M., Zou, X.H., Zhu, L.Y., Wei, C.J. and Chen, G.Q., 2010. Enhanced insulin production from murine islet beta cells incubated on poly (3-hydroxybutyrate-co-3-hydroxyhexanoate). Journal of Biomedical Materials Research Part A: An Official Journal of The Society for Biomaterials, The Japanese Society for Biomaterials, and The Australian Society for Biomaterials and the Korean Society for Biomaterials, 92(2), pp.548-555.

118. Ito, M. and Taguchi, T., 2009. Enhanced insulin secretion of physically crosslinked pancreatic β-cells by using a poly (ethylene glycol) derivative with oleyl groups. *Acta Biomaterialia*, *5*(8), pp.2945-2952.

119. Qi, M., Gu, Y., Sakata, N., Kim, D., Shirouzu, Y., Yamamoto, C., Hiura, A., Sumi, S. and Inoue, K., 2004. PVA hydrogel sheet macroencapsulation for the bioartificial pancreas. *Biomaterials*, *25*(27), pp.5885-5892.

120. Mao, G.H., Chen, G.A., Bai, H.Y., Song, T.R. and Wang, Y.X., 2009. The reversal of hyperglycaemia in diabetic mice using PLGA scaffolds seeded with islet-like cells derived from human embryonic stem cells. *Biomaterials*, *30*(9), pp.1706-1714.

121. Vegas, A.J., Veiseh, O., Gürtler, M., Millman, J.R., Pagliuca, F.W., Bader, A.R., Doloff, J.C., Li, J., Chen, M., Olejnik, K. and Tam, H.H., 2016. Long-term glycemic control using polymer-encapsulated human stem cell–derived beta cells in immune-competent mice. *Nature medicine*, *22*(3), pp.306-311.

122. Buchwald, P., Tamayo-Garcia, A., Manzoli, V., Tomei, A.A. and Stabler, C.L., 2018. Glucose-stimulated insulin release: parallel perifusion studies of free and hydrogel encapsulated human pancreatic islets. *Biotechnology and bioengineering*, *115*(1), pp.232-245.

123. Borg, D.J. and Bonifacio, E., 2011. The use of biomaterials in islet transplantation. *Current diabetes reports*, *11*, pp.434-444.

124. Lin, C.C. and Anseth, K.S., 2009. Glucagon-like peptide-1 functionalized PEG hydrogels promote survival and function of encapsulated pancreatic β-cells. *Biomacromolecules*, *10*(9), pp.2460-2467.

125. Daoud, J., Petropavlovskaia, M., Rosenberg, L. and Tabrizian, M., 2010. The effect of extracellular matrix components on the preservation of human islet function in vitro. Biomaterials, 31(7), pp.1676-1682.

126. Nagata, N., Gu, Y., Hori, H., Balamurugan, A.N., Touma, M., Kawakami, Y., Wang, W., Baba, T.T., Satake, A., Nozawa, M. and Tabata, Y., 2001. Evaluation of insulin secretion of isolated rat islets cultured in extracellular matrix. Cell transplantation, 10(4-5), pp.447-451.

127. Zbinden, A., Urbanczyk, M., Layland, S.L., Becker, L., Marzi, J., Bosch, M., Loskill, P., Duffy, G.P. and Schenke-Layland, K., 2021. Collagen and endothelial cell coculture improves β-cell functionality and rescues pancreatic extracellular matrix. *Tissue Engineering Part A*, *27*(13-14), pp.977-991.

128. Santini-González, J., Simonovich, J.A., Castro-Gutiérrez, R., González-Vargas, Y., Abuid, N.J., Stabler, C.L., Russ, H.A. and Phelps, E.A., 2021. In vitro generation of peri-islet basement membrane-like structures. *Biomaterials*, *273*, p.120808.

129. Pal, V., Wang, Y., Regeenes, R., Kilkenny, D.M. and Rocheleau, J.V., 2022. Laminin matrix regulates beta-cell FGFR5 expression to enhance glucose-stimulated metabolism. *Scientific Reports*, *12*(1), p.6110.

130. Brandhorst, D., Brandhorst, H., Layland, S.L., Acreman, S., Schenke-Layland, K. and Johnson, P.R., 2022. Basement membrane proteins improve human islet survival in hypoxia: Implications for islet inflammation. *Acta Biomaterialia*, *137*, pp.92-102.

131. Guruswamy Damodaran, R. and Vermette, P., 2018. Decellularized pancreas as a native extracellular matrix scaffold for pancreatic islet seeding and culture. Journal of tissue engineering and regenerative medicine, 12(5), pp.1230-1237.

132. Goh, S.K., Bertera, S., Olsen, P., Candiello, J.E., Halfter, W., Uechi, G., Balasubramani, M., Johnson, S.A., Sicari, B.M., Kollar, E. and Badylak, S.F., 2013. Perfusion-decellularized pancreas as a natural 3D scaffold for pancreatic tissue and whole organ engineering. Biomaterials, 34(28), pp.6760-6772.

133. Sackett, S.D., Tremmel, D.M., Ma, F., Feeney, A.K., Maguire, R.M., Brown, M.E., Zhou, Y., Li, X., O'Brien, C., Li, L. and Burlingham, W.J., 2018. Extracellular matrix scaffold and hydrogel derived from decellularized and delipidized human pancreas. *Scientific Reports*, *8*(1), p.10452.

134. Bi, H., Karanth, S.S., Ye, K., Stein, R. and Jin, S., 2020. Decellularized tissue matrix enhances self-assembly of islet organoids from pluripotent stem cell differentiation. *ACS biomaterials science & engineering*, *6*(7), pp.4155-4165.

135. Narayanan, K., Lim, V.Y., Shen, J., Tan, Z.W., Rajendran, D., Luo, S.C., Gao, S., Wan, A.C. and Ying, J.Y., 2014. Extracellular matrix-mediated differentiation of human embryonic stem cells: differentiation to insulin-secreting beta cells. *Tissue Engineering Part A*, *20*(1-2), pp.424-433.

136. Kim, J., Shim, I.K., Hwang, D.G., Lee, Y.N., Kim, M., Kim, H., Kim, S.W., Lee, S., Kim, S.C., Cho, D.W. and Jang, J., 2019. 3D cell printing of islet-laden pancreatic tissue-derived extracellular matrix bioink constructs for enhancing pancreatic functions. *Journal of Materials Chemistry B*, *7*(10), pp.1773-1781.

137. Kim, J.J., Park, J.Y., Nguyen, V.V.T., Bae, M., Kim, M., Jang, J., Won, J.Y. and Cho, D.W., 2023. Pathophysiological reconstruction of a tissue-specific multiple-organ on-a-chip for Type 2 diabetes emulation using 3D cell printing. *Advanced Functional Materials*, *33*(22), p.2213649.

138. Saldin, L.T., Cramer, M.C., Velankar, S.S., White, L.J. and Badylak, S.F., 2017. Extracellular matrix hydrogels from decellularized tissues: Structure and function. *Acta biomaterialia*, *49*, pp.1-15.

139. Chaudhuri, O., Cooper-White, J., Janmey, P.A., Mooney, D.J. and Shenoy, V.B., 2020. Effects of extracellular matrix viscoelasticity on cellular behaviour. Nature, 584(7822), pp.535-546.

140. Wu, D.T., Jeffreys, N., Diba, M. and Mooney, D.J., 2022. Viscoelastic Biomaterials for Tissue Regeneration. Tissue Engineering Part C: Methods, 28(7), pp.289-300.

141. Schulze, M.B., Hoffmann, K., Boeing, H., Linseisen, J., Rohrmann, S., Mohlig, M.A.T.T.H.I.A.S., Pfeiffer, A.F., Spranger, J., Thamer, C., Haring, H.U. and Fritsche, A., 2007. An accurate risk score based on anthropometric, dietary, and lifestyle factors to predict the development of type 2 diabetes. Diabetes care, 30(3), pp.510-515.

142. Hu, F.B., Manson, J.E., Stampfer, M.J., Colditz, G., Liu, S., Solomon, C.G. and Willett, W.C., 2001. Diet, lifestyle, and the risk of type 2 diabetes mellitus in women. New England journal of medicine, 345(11), pp.790-797.

143. Qin, J., Li, Y., Cai, Z., Li, S., Zhu, J., Zhang, F., Liang, S., Zhang, W., Guan, Y., Shen, D. and Peng, Y., 2012. A metagenome-wide association study of gut microbiota in type 2 diabetes. nature, 490(7418), pp.55-60.

144. Köbberling J, Tillil H. Empirical risk figures for first-degree relatives of non-insulin dependent diabetics. In: Köbberling J, Tattersall R eds. The genetics of diabetes mellitus. London: Academic Press; 1982:201–9.

145. Groop L, Forsblom C, Lehtovirta M, Tuomi T, Karanko S, Nissen M et al. Metabolic consequences of a family history of NIDDM (the Botnia study): evidence for sex-specific parental effects. Diabetes 1996;45:1585–93.

146. Willemsen, G., Ward, K.J., Bell, C.G., Christensen, K., Bowden, J., Dalgård, C., Harris, J.R., Kaprio, J., Lyle, R., Magnusson, P.K. and Mather, K.A., 2015. The concordance and heritability of type 2 diabetes in 34,166 twin pairs from international twin registers: the discordant twin (DISCOTWIN) consortium. Twin Research and Human Genetics, 18(6), pp.762-771.

147. Ahlqvist, E., Ahluwalia, T.S. and Groop, L., 2011. Genetics of type 2 diabetes. Clinical chemistry, 57(2), pp.241-254.

148. Prasad, R.B. and Groop, L., 2015. Genetics of type 2 diabetes—pitfalls and possibilities. Genes, 6(1), pp.87-123.

149. Scott, R.A., Scott, L.J., Mägi, R., Marullo, L., Gaulton, K.J., Kaakinen, M., Pervjakova, N., Pers, T.H., Johnson, A.D., Eicher, J.D. and Jackson, A.U., 2017. An expanded genome-wide association study of type 2 diabetes in Europeans. Diabetes, 66(11), pp.2888-2902.

150. Fox, C.S., Coady, S., Sorlie, P.D., D'Agostino Sr, R.B., Pencina, M.J., Vasan, R.S., Meigs, J.B., Levy, D. and Savage, P.J., 2007. Increasing cardiovascular disease burden due to diabetes mellitus: the Framingham Heart Study. Circulation, 115(12), pp.1544-1550.

151. Turner, R.C., 1998. The UK prospective diabetes study: a review. Diabetes care, 21(Supplement_3), pp.C35-C38.

152. Zinman, B., Wanner, C., Lachin, J.M., Fitchett, D., Bluhmki, E., Hantel, S., Mattheus, M., Devins, T., Johansen, O.E., Woerle, H.J. and Broedl, U.C., 2015. Empagliflozin, cardiovascular outcomes, and mortality in type 2 diabetes. New england journal of medicine, 373(22), pp.2117-2128.

153. Kahn, S.E., Haffner, S.M., Heise, M.A., Herman, W.H., Holman, R.R., Jones, N.P., Kravitz, B.G., Lachin, J.M., O'Neill, M.C., Zinman, B. and Viberti, G., 2006. Glycemic durability of rosiglitazone, metformin, or glyburide monotherapy. New England Journal of Medicine, 355(23), pp.2427-2443.

154. Berry, S., Drew, D., Linenberg, I., Wolf, J., Hadjigeorgiou, G., Davies, R., Al Khatib, H., Hart, D., Surdulescu, G., Yarand, D. and Nessa, A., 2020. Personalised REsponses to DIetary Composition Trial (PREDICT): an intervention study to determine inter-individual differences in postprandial response to foods.

155. L. Peltonen and V. A. McKusick, "Genomics and medicine: dissecting human disease in the postgenomic era," Science, vol. 291, no. 5507, pp. 1224–1229, 2001.

156. Buettner, R., Schölmerich, J. and Bollheimer, L.C., 2007. High-fat diets: modeling the metabolic disorders of human obesity in rodents. *Obesity*, *15*(4), pp.798-808.

157. Caterson, I.D. and Taylor, K.W., 1982. Islet cell function in gold thioglucose-induced obesity in mice. *Diabetologia*, *23*, pp.119-123.

158. King, A.J., 2012. The use of animal models in diabetes research. British journal of pharmacology, 166(3), pp.877-894.

159. Coleman, D.L., 1978. Obese and diabetes: two mutant genes causing diabetes-obesity syndromes in mice. Diabetologia, 14, pp.141-148.

160. Portha, B., Giroix, M.H., Tourrel-Cuzin, C., Le-Stunff, H. and Movassat, J., 2012. The GK rat: a prototype for the study of non-overweight type 2 diabetes. animal models in diabetes research, pp.125-159.

161. Renner, S., Fehlings, C., Herbach, N., Hofmann, A., von Waldthausen, D.C., Kessler, B., Ulrichs, K., Chodnevskaja, I., Moskalenko, V., Amselgruber, W. and Göke, B., 2010. Glucose intolerance and reduced proliferation of pancreatic β-cells in transgenic pigs with impaired glucose-dependent insulinotropic polypeptide function. Diabetes, 59(5), pp.1228-1238.

162. Pound, L.D., Kievit, P. and Grove, K.L., 2014. The nonhuman primate as a model for type 2 diabetes. Current Opinion in Endocrinology, Diabetes and Obesity, 21(2), pp.89-94.

163. Wagner, J.D., Kavanagh, K., Ward, G.M., Auerbach, B.J., Harwood Jr, H.J. and Kaplan, J.R., 2006. Old world nonhuman primate models of type 2 diabetes mellitus. ILAR journal, 47(3), pp.259-271.

164. Asfari, M., Janjic, D., Meda, P.A.O.L.O., Li, G.U.O.D.O.N.G., Halban, P.A. and Wollheim, C.B., 1992. Establishment of 2-mercaptoethanol-dependent differentiated insulin-secreting cell lines. Endocrinology, 130(1), pp.167-178.

165. Miyazaki, J.I., Araki, K., Yamato, E., Ikegami, H., Asano, T., Shibasaki, Y., Oka, Y. and YAMAMURA, K.I., 1990. Establishment of a pancreatic β cell line that retains glucose-inducible insulin secretion: special reference to expression of glucose transporter isoforms. Endocrinology, 127(1), pp.126-132.

166. Hohmeier, H.E., Mulder, H., Chen, G., Henkel-Rieger, R., Prentki, M. and Newgard, C.B., 2000. Isolation of INS-1-derived cell lines with robust ATP-sensitive K+ channel-dependent and-independent glucose-stimulated insulin secretion. Diabetes, 49(3), pp.424-430.

167. Ravassard, P., Hazhouz, Y., Pechberty, S., Bricout-Neveu, E., Armanet, M., Czernichow, P. and Scharfmann, R., 2011. A genetically engineered human pancreatic β cell line exhibiting glucose-inducible insulin secretion. *The Journal of clinical investigation*, *121*(9).

168. Hall, E., Jönsson, J., Ofori, J.K., Volkov, P., Perfilyev, A., Dekker Nitert, M., Eliasson, L., Ling, C. and Bacos, K., 2019. Glucolipotoxicity alters insulin secretion via epigenetic changes in human islets. *Diabetes*, *68*(10), pp.1965-1974.

169. von Hanstein, A.S., Tsikas, D., Lenzen, S., Jörns, A. and Plötz, T., 2023. Potentiation of Lipotoxicity in Human EndoC-βH1 β-Cells by Glucose is Dependent on the Structure of Free Fatty Acids. *Molecular Nutrition & Food Research*, *67*(5), p.2200582.

170. Brozzi, F., Nardelli, T.R., Lopes, M., Millard, I., Barthson, J., Igoillo-Esteve, M., Grieco, F.A., Villate, O., Oliveira, J.M., Casimir, M. and Bugliani, M., 2015. Cytokines induce endoplasmic reticulum stress in human, rat and mouse beta cells via different mechanisms. *Diabetologia*, *58*, pp.2307-2316.

171. Frørup, C., Gerwig, R., Svane, C.A.S., Mendes Lopes de Melo, J., Henriksen, K., Fløyel, T., Pociot, F., Kaur, S. and Størling, J., 2023. Characterization of the functional and transcriptomic effects of pro-inflammatory cytokines on human EndoC-βH5 beta cells. *Frontiers in Endocrinology*, *14*, p.1128523.

172. Green, H. and Meuth, M., 1974. An established pre-adipose cell line and its differentiation in culture. Cell, 3(2), pp.127-133.

173. Yaffe, D., 1968. Retention of differentiation potentialities during prolonged cultivation of myogenic cells. Proceedings of the National Academy of Sciences, 61(2), pp.477-483.

174. Aden, D.P., Fogel, A., Plotkin, S., Damjanov, I. and Knowles, B.B., 1979. Controlled synthesis of HBsAg in a differentiated human liver carcinoma-derived cell line. Nature, 282(5739), pp.615-616.

175. Zeng, X.Y., Zhou, X., Xu, J., Chan, S.M., Xue, C.L., Molero, J.C. and Ye, J.M., 2012. Screening for the efficacy on lipid accumulation in 3T3-L1 cells is an effective tool for the identification of new anti-diabetic compounds. Biochemical pharmacology, 84(6), pp.830-837.

176. Henquin, J.C., Nenquin, M., Stiernet, P. and Ahren, B., 2006. In vivo and in vitro glucose-induced biphasic insulin secretion in the mouse: pattern and role of cytoplasmic Ca2+ and amplification signals in β-cells. Diabetes, 55(2), pp.441-451.

177. Mosser, R.E., Maulis, M.F., Moullé, V.S., Dunn, J.C., Carboneau, B.A., Arasi, K., Pappan, K., Poitout, V. and Gannon, M., 2015. High-fat diet-induced β-cell proliferation occurs prior to insulin resistance in C57Bl/6J male mice. American Journal of Physiology-Endocrinology and Metabolism, 308(7), pp.E573-E582.

178. Ahren, B., Pacini, G., Foley, J.E. and Schweizer, A., 2005. Improved meal-related β-cell function and insulin sensitivity by the dipeptidyl peptidase-IV inhibitor vildagliptin in metformin-treated patients with type 2 diabetes over 1year. Diabetes care, 28(8), pp.1936-1940.

179. Kitamura, T., Nakae, J., Kitamura, Y., Kido, Y., Biggs, W.H., Wright, C.V., White, M.F., Arden, K.C. and Accili, D., 2002. The forkhead transcription factor Foxo1 links insulin signaling to Pdx1 regulation of pancreatic β cell growth. The Journal of clinical investigation, 110(12), pp.1839-1847.

180. Marselli, L., Thorne, J., Dahiya, S., Sgroi, D.C., Sharma, A., Bonner-Weir, S., Marchetti, P. and Weir, G.C., 2010. Gene expression profiles of Beta-cell enriched tissue obtained by laser capture microdissection from subjects with type 2 diabetes. PloS one, 5(7), p.e11499.

181. El-Assaad, W., Buteau, J., Peyot, M.L., Nolan, C., Roduit, R., Hardy, S., Joly, E., Dbaibo, G., Rosenberg, L. and Prentki, M., 2003. Saturated fatty acids synergize with elevated glucose to cause pancreatic β-cell death. Endocrinology, 144(9), pp.4154-4163.

182. Ciaraldi, T.P., Ryan, A.J., Mudaliar, S.R. and Henry, R.R., 2016. Altered myokine secretion is an intrinsic property of skeletal muscle in type 2 diabetes. PloS one, 11(7), p.e0158209.

183. Kroon, E., Martinson, L.A., Kadoya, K., Bang, A.G., Kelly, O.G., Eliazer, S., Young, H., Richardson, M., Smart, N.G., Cunningham, J. and Agulnick, A.D., 2008. Pancreatic endoderm derived from human embryonic stem cells generates glucose-responsive insulin-secreting cells in vivo. Nature biotechnology, 26(4), pp.443-452.

184. Pagliuca, F.W., Millman, J.R., Gürtler, M., Segel, M., Van Dervort, A., Ryu, J.H., Peterson, Q.P., Greiner, D. and Melton, D.A., 2014. Generation of functional human pancreatic β cells in vitro. Cell, 159(2), pp.428-439.

185. Nair, G.G., Liu, J.S., Russ, H.A., Tran, S., Saxton, M.S., Chen, R., Juang, C., Li, M.L., Nguyen, V.Q., Giacometti, S. and Puri, S., 2019. Recapitulating endocrine cell clustering in culture promotes maturation of human stem-cell-derived β cells. Nature cell biology, 21(2), pp.263-274.

186. Hogrebe, N.J., Maxwell, K.G., Augsornworawat, P. and Millman, J.R., 2021. Generation of insulin-producing pancreatic β cells from multiple human stem cell lines. Nature protocols, 16(9), pp.4109-4143.

187. Velazco-Cruz, L., Song, J., Maxwell, K.G., Goedegebuure, M.M., Augsornworawat, P., Hogrebe, N.J. and Millman, J.R., 2019. Acquisition of dynamic function in human stem cell-derived β cells. *Stem cell reports*, *12*(2), pp.351-365.

188. Chmielowiec, J., Szlachcic, W.J., Yang, D., Scavuzzo, M.A., Wamble, K., Sarrion-Perdigones, A., Sabek, O.M., Venken, K.J. and Borowiak, M., 2022. Human pancreatic microenvironment promotes β-cell differentiation via non-canonical WNT5A/JNK and BMP signaling. *Nature Communications*, *13*(1), p.1952.

189. Benner, C., van der Meulen, T., Cacéres, E., Tigyi, K., Donaldson, C.J. and Huising, M.O., 2014. The transcriptional landscape of mouse beta cells compared to human beta cells reveals notable species differences in long non-coding RNA and protein-coding gene expression. BMC genomics, 15, pp.1-17.

190. Baron, M., Veres, A., Wolock, S.L., Faust, A.L., Gaujoux, R., Vetere, A., Ryu, J.H., Wagner, B.K., Shen-Orr, S.S., Klein, A.M. and Melton, D.A., 2016. A single-cell transcriptomic map of the human and mouse pancreas reveals inter-and intra-cell population structure. Cell systems, 3(4), pp.346-360.

191. Bosco, D., Armanet, M., Morel, P., Niclauss, N., Sgroi, A., Muller, Y.D., Giovannoni, L., Parnaud, G. and Berney, T., 2010. Unique arrangement of α-and β-cells in human islets of Langerhans. Diabetes, 59(5), pp.1202-1210.

192. Steiner, D.J., Kim, A., Miller, K. and Hara, M., 2010. Pancreatic islet plasticity: interspecies comparison of islet architecture and composition. Islets, 2(3), pp.135-145.

193. Stancill, J.S., Cartailler, J.P., Clayton, H.W., O'Connor, J.T., Dickerson, M.T., Dadi, P.K., Osipovich, A.B., Jacobson, D.A. and Magnuson, M.A., 2017. Chronic β-cell depolarization impairs β-cell identity by disrupting a network of Ca2+-regulated genes. Diabetes, 66(8), pp.2175-2187.

194. Cabrera, O., Berman, D.M., Kenyon, N.S., Ricordi, C., Berggren, P.O. and Caicedo, A., 2006. The unique cytoarchitecture of human pancreatic islets has implications for islet cell function. Proceedings of the National Academy of Sciences, 103(7), pp.2334-2339.

195. Johnston, N.R., Mitchell, R.K., Haythorne, E., Pessoa, M.P., Semplici, F., Ferrer, J., Piemonti, L., Marchetti, P., Bugliani, M., Bosco, D. and Berishvili, E., 2016. Beta cell hubs dictate pancreatic islet responses to glucose. Cell metabolism, 24(3), pp.389-401.

196. Kilimnik, G., Zhao, B., Jo, J., Periwal, V., Witkowski, P., Misawa, R. and Hara, M., 2011. Altered islet composition and disproportionate loss of large islets in patients with type 2 diabetes. PloS one, 6(11), p.e27445.

197. Brissova, M., Shostak, A., Fligner, C.L., Revetta, F.L., Washington, M.K., Powers, A.C. and Hull, R.L., 2015. Human islets have fewer blood vessels than mouse islets and the density of islet vascular structures is increased in type 2 diabetes. Journal of Histochemistry & Cytochemistry, 63(8), pp.637-645.

198. Cross, S.E., Vaughan, R.H., Willcox, A.J., McBride, A.J., Abraham, A.A., Han, B., Johnson, J.D., Maillard, E., Bateman, P.A., Ramracheya, R.D. and Rorsman, P., 2017. Key matrix proteins within the pancreatic islet basement membrane are differentially digested during human islet isolation. American Journal of Transplantation, 17(2), pp.451-461.

199. Llacua, A., de Haan, B.J., Smink, S.A. and de Vos, P., 2016. Extracellular matrix components supporting human islet function in alginate-based immunoprotective microcapsules for treatment of diabetes. Journal of biomedical materials research Part A, 104(7), pp.1788-1796.

200. Otonkoski, T., Banerjee, M., Korsgren, O., Thornell, L.E. and Virtanen, I., 2008. Unique basement membrane structure of human pancreatic islets: implications for β-cell growth and differentiation. Diabetes, obesity and metabolism, 10, pp.119-127.

201. Virtanen, I., Banerjee, M., Palgi, J., Korsgren, O., Lukinius, A., Thornell, L.E., Kikkawa, Y., Sekiguchi, K., Hukkanen, M., Konttinen, Y.T. and Otonkoski, T., 2008. Blood vessels of human islets of Langerhans are surrounded by a double basement membrane. Diabetologia, 51, pp.1181-1191.

202. Russell Wms, B., 1992. The principles of humane experimental technique. London: UFAW.

203. NC3Rs. (2021). The 3Rs. National Centre for the Replacement, Refinement and Reduction of Animals in Research. [accessed 08.09.2024]. https://www.nc3rs.org.uk/the-3rs

204. Shi, Y., Inoue, H., Wu, J.C. and Yamanaka, S., 2017. Induced pluripotent stem cell technology: a decade of progress. Nature reviews Drug discovery, 16(2), pp.115-130.

205. Ronaldson-Bouchard, K. and Vunjak-Novakovic, G., 2018. Organs-on-a-chip: a fast track for engineered human tissues in drug development. Cell stem cell, 22(3), pp.310-324.

206. Shaw, R., Festing, M. F., Peers, I., & Furlong, L. (2002). Use of factorial designs to optimize animal experiments and reduce animal use. ILAR Journal, 43(4), 223-232.

207. Prescott, M. J., & Lidster, K. (2017). Improving quality of science through better animal welfare: The NC3Rs strategy. Lab Animal, 46(4), 152-156.

208. Eriksson, O., Laughlin, M., Brom, M., Nuutila, P., Roden, M., Hwa, A., Bonadonna, R. and Gotthardt, M., 2016. In vivo imaging of beta cells with radiotracers: state of the art, prospects and recommendations for development and use. *Diabetologia*, *59*, pp.1340-1349.

209. Tannenbaum, J. and Bennett, B.T., 2015. Russell and Burch's 3Rs then and now: the need for clarity in definition and purpose. Journal of the American association for laboratory animal science, 54(2), pp.120-132.

210. Kong, Y., Duan, J., Liu, F., Han, L., Li, G., Sun, C., Sang, Y., Wang, S., Yi, F. and Liu, H., 2021. Regulation of stem cell fate using nanostructure-mediated physical signals. Chemical Society Reviews, 50(22), pp.12828-12872.

211. Hutchinson, E., Avery, A. and VandeWoude, S., 2005. Environmental enrichment for laboratory rodents. ILAR journal, 46(2), pp.148-161.

212. Sanchez-Alavez, M., Alboni, S. and Conti, B., 2011. Sex-and age-specific differences in core body temperature of C57Bl/6 mice. Age, 33, pp.89-99.

213. Doke, S.K. and Dhawale, S.C., 2015. Alternatives to animal testing: A review. Saudi Pharmaceutical Journal, 23(3), pp.223-229.

214. Gerdts, V., Wilson, H.L., Meurens, F., van Drunen Littel-van den Hurk, S., Wilson, D., Walker, S., Wheler, C., Townsend, H. and Potter, A.A., 2015. Large animal models for vaccine development and testing. ILAR journal, 56(1), pp.53-62.

215. Burden, N., Chapman, K., Sewell, F. and Robinson, V., 2015. Pioneering better science through the 3Rs: an introduction to the national centre for the replacement, refinement, and reduction of animals in research (NC3Rs). Journal of the American Association for Laboratory Animal Science, 54(2), pp.198-208.

216. Ma, C., Peng, Y., Li, H. and Chen, W., 2021. Organ-on-a-chip: a new paradigm for drug development. Trends in pharmacological sciences, 42(2), pp.119-133.

217. Nielsen, J.B., Hanson, R.L., Almughamsi, H.M., Pang, C., Fish, T.R. and Woolley, A.T., 2019. Microfluidics: innovations in materials and their fabrication and functionalization. *Analytical chemistry*, *92*(1), pp.150-168.

218. Esch, E.W., Bahinski, A. and Huh, D., 2015. Organs-on-chips at the frontiers of drug discovery. Nature reviews Drug discovery, 14(4), pp.248-260.

219. Palasantzas, V.E., Tamargo-Rubio, I., Le, K., Slager, J., Wijmenga, C., Jonkers, I.H., Kumar, V., Fu, J. and Withoff, S., 2023. iPSC-derived organ-on-a-chip models for personalized human genetics and pharmacogenomics studies. Trends in Genetics, 39(4), pp.268-284.

220. Picollet-D'hahan, N., Zuchowska, A., Lemeunier, I. and Le Gac, S., 2021. Multiorgan-on-a-chip: a systemic approach to model and decipher inter-organ communication. Trends in Biotechnology, 39(8), pp.788-810.

221. Roper, M.G., Shackman, J.G., Dahlgren, G.M. and Kennedy, R.T., 2003. Microfluidic chip for continuous monitoring of hormone secretion from live cells using an electrophoresis-based immunoassay. Analytical chemistry, 75(18), pp.4711-4717.

222. Dishinger, J.F. and Kennedy, R.T., 2007. Serial immunoassays in parallel on a microfluidic chip for monitoring hormone secretion from living cells. Analytical chemistry, 79(3), pp.947-954.

223. Dishinger, J.F., Reid, K.R. and Kennedy, R.T., 2009. Quantitative monitoring of insulin secretion from single islets of Langerhans in parallel on a microfluidic chip. Analytical chemistry, 81(8), pp.3119-3127.

224. Rocheleau, J.V., Walker, G.M., Head, W.S., McGuinness, O.P. and Piston, D.W., 2004. Microfluidic glucose stimulation reveals limited coordination of intracellular Ca2+ activity oscillations in pancreatic islets. Proceedings of the National Academy of Sciences, 101(35), pp.12899-12903.

225. Lam, A.K., Silva, P.N., Altamentova, S.M. and Rocheleau, J.V., 2012. Quantitative imaging of electron transfer flavoprotein autofluorescence reveals the dynamics of lipid partitioning in living pancreatic islets. Integrative Biology, 4(8), pp.838-846.

226. Regeenes, R., Wang, Y., Piro, A., Au, A., Yip, C.M., Wheeler, M.B. and Rocheleau, J.V., 2023. Islet-on-a-chip device reveals first phase glucose-stimulated respiration is substrate limited by glycolysis independent of Ca2+ activity. Biosensors and Bioelectronics: X, 13, p.100285.

227. Mohammed, J.S., Wang, Y., Harvat, T.A., Oberholzer, J. and Eddington, D.T., 2009. Microfluidic device for multimodal characterization of pancreatic islets. Lab on a Chip, 9(1), pp.97-106.

228. Adewola, A.F., Lee, D., Harvat, T., Mohammed, J., Eddington, D.T., Oberholzer, J. and Wang, Y., 2010. Microfluidic perifusion and imaging device for multi-parametric islet function assessment. Biomedical microdevices, 12, pp.409-417.

229. Lo, J.F., Wang, Y., Blake, A., Yu, G., Harvat, T.A., Jeon, H., Oberholzer, J. and Eddington, D.T., 2012. Islet preconditioning via multimodal microfluidic modulation of intermittent hypoxia. Analytical chemistry, 84(4), pp.1987-1993.

230. Nourmohammadzadeh, M., Xing, Y., Lee, J.W., Bochenek, M.A., Mendoza-Elias, J.E., McGarrigle, J.J., Marchese, E., Chun-Chieh, Y., Eddington, D.T., Oberholzer, J. and Wang, Y., 2016. A microfluidic array for real-time live-cell imaging of human and rodent pancreatic islets. Lab on a Chip, 16(8), pp.1466-1472.

231. Zhang, X. and Roper, M.G., 2009. Microfluidic perfusion system for automated delivery of temporal gradients to islets of Langerhans. Analytical chemistry, 81(3), pp.1162-1168.

232. Yi, L., Wang, X., Dhumpa, R., Schrell, A.M., Mukhitov, N. and Roper, M.G., 2015. Integrated perfusion and separation systems for entrainment of insulin secretion from islets of Langerhans. Lab on a Chip, 15(3), pp.823-832.

233. Dhumpa, R., Truong, T.M., Wang, X. and Roper, M.G., 2015. Measurement of the entrainment window of islets of Langerhans by microfluidic delivery of a chirped glucose waveform. Integrative Biology, 7(9), pp.1061-1067.

234. Schrell, A.M., Mukhitov, N., Yi, L., Adablah, J.E., Menezes, J. and Roper, M.G., 2017. Online fluorescence anisotropy immunoassay for monitoring insulin secretion from islets of Langerhans. Analytical Methods, 9(1), pp.38-45.

235. Glieberman, A.L., Pope, B.D., Zimmerman, J.F., Liu, Q., Ferrier, J.P., Kenty, J.H., Schrell, A.M., Mukhitov, N., Shores, K.L., Tepole, A.B. and Melton, D.A., 2019. Synchronized stimulation and continuous insulin sensing in a microfluidic human Islet on a Chip designed for scalable manufacturing. Lab on a Chip, 19(18), pp.2993-3010.

236. Eaton, W.J. and Roper, M.G., 2021. A microfluidic system for monitoring glucagon secretion from human pancreatic islets of Langerhans. Analytical Methods, 13(32), pp.3614-3619.

237. Raoux, M., Bornat, Y., Quotb, A., Catargi, B., Renaud, S. and Lang, J., 2012. Non-invasive long-term and real-time analysis of endocrine cells on micro-electrode arrays. The Journal of Physiology, 590(5), pp.1085-1091.

238. Lebreton, F., Pirog, A., Belouah, I., Bosco, D., Berney, T., Meda, P., Bornat, Y., Catargi, B., Renaud, S., Raoux, M. and Lang, J., 2015. Slow potentials encode intercellular coupling and insulin demand in pancreatic beta cells. Diabetologia, 58, pp.1291-1299.

239. Perrier, R., Pirog, A., Jaffredo, M., Gaitan, J., Catargi, B., Renaud, S., Raoux, M. and Lang, J., 2018. Bioelectronic organ-based sensor for microfluidic real-time analysis of the demand in insulin. Biosensors and Bioelectronics, 117, pp.253-259.

240. Abarkan, M., Gaitan, J., Lebreton, F., Perrier, R., Jaffredo, M., Mulle, C., Magnan, C., Raoux, M. and Lang, J., 2019. The glutamate receptor GluK2 contributes to the regulation of glucose homeostasis and its deterioration during aging. Molecular metabolism, 30, pp.152-160.

241. Jaffredo, M., Bertin, E., Pirog, A., Puginier, E., Gaitan, J., Oucherif, S., Lebreton, F., Bosco, D., Catargi, B., Cattaert, D. and Renaud, S., 2021. Dynamic uni-and multicellular patterns encode biphasic activity in pancreatic islets. Diabetes, 70(4), pp.878-888.

242. Abarkan, M., Pirog, A., Mafilaza, D., Pathak, G., N'Kaoua, G., Puginier, E., O'Connor, R., Raoux, M., Donahue, M.J., Renaud, S. and Lang, J., 2022. Vertical Organic Electrochemical Transistors and Electronics for Low Amplitude Micro-Organ Signals. Advanced Science, 9(8), p.2105211.

243. Pfeiffer, T., Kraushaar, U., Düfer, M., Schönecker, S., Haspel, D., Günther, E., Drews, G. and Krippeit-Drews, P., 2011. Rapid functional evaluation of beta-cells by extracellular recording of membrane potential oscillations with microelectrode arrays. Pflügers Archiv-European Journal of Physiology, 462, pp.835-840.

244. Heileman, K., Daoud, J., Hasilo, C., Gasparrini, M., Paraskevas, S. and Tabrizian, M., 2015. Microfluidic platform for assessing pancreatic islet functionality through dielectric spectroscopy. Biomicrofluidics, 9(4).

245. Brouwer, S., Hoffmeister, T., Gresch, A., Schönhoff, L. and Düfer, M., 2018. Resveratrol influences pancreatic islets by opposing effects on electrical activity and insulin release. Molecular Nutrition & Food Research, 62(5), p.1700902.

246. Alassaf, A., Ishahak, M., Bowles, A. and Agarwal, A., 2020. Microelectrode array based functional testing of pancreatic islet cells. Micromachines, 11(5), p.507.

247. Schönecker, S., Kraushaar, U., Düfer, M., Sahr, A., Härdtner, C., Guenther, E., Walther, R., Lendeckel, U., Barthlen, W., Krippeit-Drews, P. and Drews, G., 2014. Long-term culture and functionality of pancreatic islets monitored using microelectrode arrays. Integrative Biology, 6(5), pp.540-544.

248. Jun, Y., Lee, J., Choi, S., Yang, J.H., Sander, M., Chung, S. and Lee, S.H., 2019. In vivo–mimicking microfluidic perfusion culture of pancreatic islet spheroids. Science Advances, 5(11), p.eaax4520.

249. Lee, S.H., Hong, S., Song, J., Cho, B., Han, E.J., Kondapavulur, S., Kim, D. and Lee, L.P., 2018. Microphysiological analysis platform of pancreatic islet β-cell spheroids. Advanced Healthcare Materials, 7(2), p.1701111.

250. Misun, P.M., Yesildag, B., Forschler, F., Neelakandhan, A., Rousset, N., Biernath, A., Hierlemann, A. and Frey, O., 2020. In vitro platform for studying human insulin release dynamics of single pancreatic islet microtissues at high resolution. Advanced biosystems, 4(3), p.1900291.

251. Wu Jin, P., Rousset, N., Hierlemann, A. and Misun, P.M., 2021. A microfluidic hanging-Drop-Based islet perifusion system for studying glucose-stimulated insulin secretion from multiple individual pancreatic islets. Frontiers in Bioengineering and Biotechnology, 9, p.674431.

252. Bender, R.H.F., T O'Donnell, B., Shergill, B., Pham, B.Q., Tahmouresie, S., Sanchez, C.N., Juat, D.J., Hatch, M.M., Shirure, V.S., Wortham, M. and Nguyen-Ngoc, K.V., 2024. A vascularized 3D model of the human pancreatic islet for ex vivo study of immune cell-islet interaction. Biofabrication, 16(2), p.025001.

253. Quintard, C., Tubbs, E., Jonsson, G., Jiao, J., Wang, J., Werschler, N., Laporte, C., Pitaval, A., Bah, T.S., Pomeranz, G. and Bissardon, C., 2024. A microfluidic platform integrating functional vascularized organoids-on-chip. *Nature communications*, *15*(1), p.1452.

254. Patel, S.N., Ishahak, M., Chaimov, D., Velraj, A., LaShoto, D., Hagan, D.W., Buchwald, P., Phelps, E.A., Agarwal, A. and Stabler, C.L., 2021. Organoid microphysiological system preserves pancreatic islet function within 3D matrix. Science advances, 7(7), p.eaba5515.

255. Ortega, M.A., Rodríguez-Comas, J., Yavas, O., Velasco-Mallorquí, F., Balaguer-Trias, J., Parra, V., Novials, A., Servitja, J.M., Quidant, R. and Ramón-Azcón, J., 2021. In situ LSPR sensing of secreted insulin in organ-on-chip. Biosensors, 11(5), p.138.

256. Castiello, F.R. and Tabrizian, M., 2018. Multiplex surface plasmon resonance imaging-based biosensor for human pancreatic islets hormones quantification. Analytical chemistry, 90(5), pp.3132-3139.

257. Nguyen, D.T.T., Van Noort, D., Jeong, I.K. and Park, S., 2017. Endocrine system on chip for a diabetes treatment model. Biofabrication, 9(1), p.015021.

258. Bauer, S., Wennberg Huldt, C., Kanebratt, K.P., Durieux, I., Gunne, D., Andersson, S., Ewart, L., Haynes, W.G., Maschmeyer, I., Winter, A. and Ämmälä, C., 2017. Functional coupling of human pancreatic islets and liver spheroids on-a-chip: Towards a novel human ex vivo type 2 diabetes model. Scientific reports, 7(1), p.14620.

259. Essaouiba, A., Okitsu, T., Kinoshita, R., Jellali, R., Shinohara, M., Danoy, M., Legallais, C., Sakai, Y. and Leclerc, E., 2020. Development of a pancreas-liver organ-on-chip coculture model for organ-to-organ interaction studies. Biochemical Engineering Journal, 164, p.107783.

260. Baudoin, R., Griscom, L., Prot, J.M., Legallais, C. and Leclerc, E., 2011. Behavior of HepG2/C3A cell cultures in a microfluidic bioreactor. Biochemical Engineering Journal, 53(2), pp.172-181.

261. Essaouiba, A., Okitsu, T., Jellali, R., Shinohara, M., Danoy, M., Tauran, Y., Legallais, C., Sakai, Y. and Leclerc, E., 2020. Microwell-based pancreas-on-chip model enhances genes expression and functionality of rat islets of Langerhans. Molecular and Cellular Endocrinology, 514, p.110892.

262. IEssaouiba, A., Jellali, R., Gilard, F., Gakière, B., Okitsu, T., Legallais, C., Sakai, Y. and Leclerc, E., 2022. Investigation of the Exometabolomic Profiles of Rat Islets of Langerhans Cultured in Microfluidic Biochip. Metabolites, 12(12), p.1270.

263. Hirano, K., Konagaya, S., Turner, A., Noda, Y., Kitamura, S., Kotera, H. and Iwata, H., 2017. Closed-channel culture system for efficient and reproducible differentiation of human pluripotent stem cells into islet cells. Biochemical and Biophysical Research Communications, 487(2), pp.344-350.

264. Tao, T., Wang, Y., Chen, W., Li, Z., Su, W., Guo, Y., Deng, P. and Qin, J., 2019. Engineering human islet organoids from iPSCs using an organ-on-chip platform. Lab on a Chip, 19(6), pp.948-958.

265. Tao, T., Deng, P., Wang, Y., Zhang, X., Guo, Y., Chen, W. and Qin, J., 2022. Microengineered multi-organoid system from hiPSCs to recapitulate human liver-islet axis in normal and type 2 diabetes. Advanced Science, 9(5), p.2103495.

266. Zandi Shafagh, R., Youhanna, S., Keulen, J., Shen, J.X., Taebnia, N., Preiss, L.C., Klein, K., Büttner, F.A., Bergqvist, M., van der Wijngaart, W. and Lauschke, V.M., 2022. Bioengineered pancreas–liver crosstalk in a microfluidic coculture chip identifies human metabolic response signatures in prediabetic hyperglycemia. Advanced Science, 9(34), p.2203368.

267. Fernández-Costa, J.M., Ortega, M.A., Rodríguez-Comas, J., Lopez-Muñoz, G., Yeste, J., Mangas-Florencio, L., Fernández-González, M., Martin-Lasierra, E., Tejedera-Villafranca, A. and Ramon-Azcon, J., 2023. Training-on-a-chip: a multi-organ device to study the effect of muscle exercise on insulin secretion in vitro. Advanced Materials Technologies, 8(7), p.2200873.

268. Xiu, Y., Xiu-Li, Z., Yong, L., Li-Chao, L., Wei-Jie, Z. and Bing-Cheng, L., 2019. Establishment of 3D organ chip for multiplexed assessment of type 2 diabetes drugs. PROGRESS IN BIOCHEMISTRY AND BIOPHYSICS, 46(6), pp.620-630.

269. Yin, J., Meng, H., Lin, J., Ji, W., Xu, T. and Liu, H., 2022. Pancreatic islet organoids-on-a-chip: how far have we gone?. Journal of Nanobiotechnology, 20(1), p.308.

270. Bowsher, R.R. and Nowatzke, W.L., 2011. Insights in regulated bioanalysis of human insulin and insulin analogs by immunoanalytical methods. Bioanalysis, 3(8), pp.883-898.

271. Freckmann, G., Hagenlocher, S., Baumstark, A., Jendrike, N., Gillen, R.C., Rössner, K. and Haug, C., 2007. Continuous glucose profiles in healthy subjects under everyday life conditions and after different meals. Journal of diabetes science and technology, 1(5), pp.695-703.

272. Weyer, C., Hanson, R.L., Tataranni, P.A., Bogardus, C. and Pratley, R.E., 2000. A high fasting plasma insulin concentration predicts type 2 diabetes independent of insulin resistance: evidence for a pathogenic role of relative hyperinsulinemia. Diabetes, 49(12), pp.2094-2101.

273. Darby, S.M., Miller, M.L., Allen, R.O. and LeBeau, M., 2001. A mass spectrometric method for quantitation of intact insulin in blood samples. Journal of analytical toxicology, 25(1), pp.8-14.

274. Luong, A.D., Roy, I., Malhotra, B.D. and Luong, J.H., 2021. Analytical and biosensing platforms for insulin: A review. Sensors and Actuators Reports, 3, p.100028.

275. Salimi, A., Roushani, M., Soltanian, S. and Hallaj, R., 2007. Picomolar detection of insulin at renewable nickel powder-doped carbon composite electrode. Analytical Chemistry, 79(19), pp.7431-7438.

276. Salimi, A., Noorbakhash, A., Sharifi, E. and Semnani, A., 2008. Highly sensitive sensor for picomolar detection of insulin at physiological pH, using GC electrode modified with guanine and electrodeposited nickel oxide nanoparticles. Biosensors and Bioelectronics, 24(4), pp.792-798.

277. Jaafariasl, M., Shams, E. and Amini, M.K., 2011. Silica gel modified carbon paste electrode for electrochemical detection of insulin. Electrochimica acta, 56(11), pp.4390-4395.

278. Yagati, A.K., Park, J. and Cho, S., 2016. Reduced graphene oxide modified the interdigitated chain electrode for an insulin sensor. Sensors, 16(1), p.109.

279. Yagati, A.K., Choi, Y., Park, J., Choi, J.W., Jun, H.S. and Cho, S., 2016. Silver nanoflower–reduced graphene oxide composite based micro-disk electrode for insulin detection in serum. Biosensors and Bioelectronics, 80, pp.307-314.

280. Arvinte, A., Westermann, A.C., Sesay, A.M. and Virtanen, V., 2010. Electrocatalytic oxidation and determination of insulin at CNT-nickel–cobalt oxide modified electrode. Sensors and Actuators B: Chemical, 150(2), pp.756-763.

281. Lin Y, Hu L, Li L, Wang K (2014) Facile synthesis of nickel hydroxide–graphene nanocomposites for insulin detection with enhanced electro-oxidation properties. RSC Adv 4:46208–46213

282. Cruz, A.G., Haq, I., Cowen, T., Di Masi, S., Trivedi, S., Alanazi, K., Piletska, E., Mujahid, A. and Piletsky, S.A., 2020. Design and fabrication of a smart sensor using in silico epitope mapping and electro-responsive imprinted polymer nanoparticles for determination of insulin levels in human plasma. Biosensors and Bioelectronics, 169, p.112536.

283. Wardani, N.I., Kangkamano, T., Wannapob, R., Kanatharana, P., Thavarungkul, P. and Limbut, W., 2023. Electrochemical sensor based on molecularly imprinted polymer cryogel and multiwalled carbon nanotubes for direct insulin detection. Talanta, 254, p.124137.

284. Thévenot, D.R., Toth, K., Durst, R.A. and Wilson, G.S., 2001. Electrochemical biosensors: recommended definitions and classification. Biosensors and bioelectronics, 16(1-2), pp.121-131.

285. Rackus, D.G., Shamsi, M.H. and Wheeler, A.R., 2015. Electrochemistry, biosensors and microfluidics: a convergence of fields. Chemical Society Reviews, 44(15), pp.5320-5340.

286. Nernst, W., 1888. Zur kinetik der in lösung befindlichen körper. Zeitschrift für physikalische Chemie, 2(1), pp.613-637.

287. Nernst, W., 1889. Die elektromotorische wirksamkeit der jonen. Zeitschrift für physikalische Chemie, 4(1), pp.129-181.

288. Planck, M., 1935. Zur Theorie der Elektrizitätserregung in Elektrolyten. Zeitschrift für Physik, 94(7), pp.469-472.

289. Labib, M., Sargent, E.H. and Kelley, S.O., 2016. Electrochemical methods for the analysis of clinically relevant biomolecules. Chemical reviews, 116(16), pp.9001-9090.

290. Heinze, J., 1993. Ultramicroelectrodes in electrochemistry. Angewandte Chemie International Edition in English, 32(9), pp.1268-1288.

291. Compton, R.G. and Banks, C.E., 2018. Understanding voltammetry. World Scientific.

292. Hood,S.J.,Kampouris,D.K.,Kadara,R.O.,Jenkinson,N.,DelCampo,F. J., Muñoz, F. X. & Banks, C. E. (2009) Why ‘the bigger the better’is not always the case when utilising microelectrode arrays: high density vs. low density arrays for the electroanalytical sensing of chromium (VI). Analyst. 134 (11), 2301-2305.

293. Roudaut, M., Caillaud, A., Souguir, Z., Bray, L., Girardeau, A., Rimbert, A., Croyal, M., Lambert, G., Patitucci, M., Delpouve, G. and Vandenhaute, É., 2024. Human induced pluripotent stem cells-

derived liver organoids grown on a Biomimesys® hyaluronic acid-based hydroscaffold as a new model for studying human lipoprotein metabolism. Bioengineering & Translational Medicine, p.e10659.

294. Louis, F., Pannetier, P., Souguir, Z., Le Cerf, D., Valet, P., Vannier, J.P., Vidal, G. and Demange, E., 2017. A biomimetic hydrogel functionalized with adipose ECM components as a microenvironment for the 3D culture of human and murine adipocytes. Biotechnology and bioengineering, 114(8), pp.1813-1824.

295. Alkhouli, N., Mansfield, J., Green, E., Bell, J., Knight, B., Liversedge, N., Tham, J.C., Welbourn, R., Shore, A.C., Kos, K. and Winlove, C.P., 2013. The mechanical properties of human adipose tissues and their relationships to the structure and composition of the extracellular matrix. American Journal of Physiology-Endocrinology and Metabolism, 305(12), pp.E1427-E1435.

296. Buchwald, P., Wang, X., Khan, A., Bernal, A., Fraker, C., Inverardi, L. and Ricordi, C., 2009. Quantitative assessment of islet cell products: estimating the accuracy of the existing protocol and accounting for islet size distribution. *Cell transplantation*, *18*(10-11), pp.1223-1235.

297. Miri, T., 2011. Viscosity and oscillatory rheology. Practical food rheology: An interpretive approach, pp.7-28.

298. Seabold, S. and Perktold, J., 2010. Statsmodels: econometric and statistical modeling with python. SciPy, 7(1).

299. Virtanen, P., Gommers, R., Oliphant, T.E., Haberland, M., Reddy, T., Cournapeau, D., Burovski, E., Peterson, P., Weckesser, W., Bright, J. and Van Der Walt, S.J., 2020. SciPy 1.0: fundamental algorithms for scientific computing in Python. Nature methods, 17(3), pp.261-272.

300. Pedregosa, F., Varoquaux, G., Gramfort, A., Michel, V., Thirion, B., Grisel, O., Blondel, M., Prettenhofer, P., Weiss, R., Dubourg, V. and Vanderplas, J., 2011. Scikit-learn: Machine learning in Python. the Journal of machine Learning research, 12, pp.2825-2830.

301. Harris, C.R., Millman, K.J., Van Der Walt, S.J., Gommers, R., Virtanen, P., Cournapeau, D., Wieser, E., Taylor, J., Berg, S., Smith, N.J. and Kern, R., 2020. Array programming with NumPy. Nature, 585(7825), pp.357-362.

302. McKinney, W., 2010, June. Data structures for statistical computing in Python. In SciPy (Vol. 445, No. 1, pp. 51-56).

303. Hunter, J.D., 2007. Matplotlib: A 2D graphics environment. Computing in science & engineering, 9(03), pp.90-95.

304. Li, C.H. and Lee, C.K., 1993. Minimum cross entropy thresholding. Pattern recognition, 26(4), pp.617-625.

305. Oger, F., Bourouh, C., Friano, M.E., Courty, E., Rolland, L., Gromada, X., Moreno, M., Carney, C., Rabhi, N., Durand, E. and Amanzougarene, S., 2023. β-cell–specific E2f1 deficiency impairs glucose homeostasis, β-cell identity, and insulin secretion. Diabetes, 72(8), pp.1112-1126.

306. Rabhi, N.; Denechaud, P.-D.; Gromada, X.; Hannou, S.A.; Zhang, H.; Rashid, T.; Salas, E.; Durand, E.; Sand, O.; Bonnefond, A.; et al. KAT2B Is Required for Pancreatic Beta Cell Adaptation to Metabolic Stress by Controlling the Unfolded Protein Response. Cell Rep. 2016, 15, 1051–1061.

307. Guo, J. and Lindner, E., 2009. Cyclic voltammograms at coplanar and shallow recessed microdisk electrode arrays: guidelines for design and experiment. Analytical chemistry, 81(1), pp.130-138.

308. Rodgers, P.J. and Amemiya, S., 2007. Cyclic voltammetry at micropipet electrodes for the study of ion- transfer kinetics at liquid/liquid interfaces. Analytical chemistry, 79(24), pp.9276-9285.

309. Andersson, M., Axelsson, A. and Zacchi, G., 1997. Diffusion of glucose and insulin in a swelling N-isopropylacrylamide gel. International journal of Pharmaceutics, 157(2), pp.199-208.

310. McColl, I.H., Blanch, E.W., Gill, A.C., Rhie, A.G., Ritchie, M.A., Hecht, L., Nielsen, K. and Barron, L.D., 2003. A new perspective on β-sheet structures using vibrational Raman optical activity: from poly (L-lysine) to the prion protein. Journal of the American Chemical Society, 125(33), pp.10019-10026.

311. Martinez, M.G., Bullock, A.J., MacNeil, S. and Rehman, I.U., 2019. Characterisation of structural changes in collagen with Raman spectroscopy. Applied Spectroscopy Reviews, 54(6), pp.509-542.

312. Talari, A.C.S., Movasaghi, Z., Rehman, S. and Rehman, I.U., 2015. Raman spectroscopy of biological tissues. Applied spectroscopy reviews, 50(1), pp.46-111.

313. Essendoubi, M., Gobinet, C., Reynaud, R., Angiboust, J.F., Manfait, M. and Piot, O.J.S.R., 2016. Human skin penetration of hyaluronic acid of different molecular weights as probed by Raman spectroscopy. Skin Research and Technology, 22(1), pp.55-62.

314. Ahearne, M., Yang, Y., El Haj, A.J., Then, K.Y. and Liu, K.K., 2005. Characterizing the viscoelastic properties of thin hydrogel-based constructs for tissue engineering applications. Journal of the Royal Society Interface, 2(5), pp.455-463.

315. Efremov, Y.M., Okajima, T. and Raman, A., 2020. Measuring viscoelasticity of soft biological samples using atomic force microscopy. Soft matter, 16(1), pp.64-81.

316. Miyazaki, J.I., Araki, K., Yamato, E., Ikegami, H., Asano, T., Shibasaki, Y., Oka, Y. and YAMAMURA, K.I., 1990. Establishment of a pancreatic β cell line that retains glucose-inducible insulin secretion: special reference to expression of glucose transporter isoforms. Endocrinology, 127(1), pp.126-132.

317. Skelin, M., Rupnik, M. and Cencič, A., 2010. Pancreatic beta cell lines and their applications in diabetes mellitus research. ALTEX-Alternatives to animal experimentation, 27(2), pp.105-113.

318. Kleinman, H.K. and Martin, G.R., 2005, October. Matrigel: basement membrane matrix with biological activity. In Seminars in cancer biology (Vol. 15, No. 5, pp. 378-386). Academic Press.

319. Chao, X., Zhao, F., Hu, J., Yu, Y., Xie, R., Zhong, J., Huang, M., Zeng, T., Yang, H., Luo, D. and Peng, W., 2023. Comparative study of two common in vitro models for the pancreatic islet with MIN6. Tissue engineering and regenerative medicine, 20(1), pp.127-141.

320. Crowe, J., Chen, G.R., Ferdous, R., Greenwood, D.R., Grimble, M.J., Huang, H.P., Jeng, J.C., Johnson, M.A., Katebi, M.R., Kwong, S. and Lee, T.H., 2005. *PID control: new identification and design methods*. Springer-Verlag London Limited.

321. Rozario, T. and DeSimone, D.W., 2010. The extracellular matrix in development and morphogenesis: a dynamic view. Developmental biology, 341(1), pp.126-140.

322. Khademhosseini, A. and Langer, R., 2016. A decade of progress in tissue engineering. Nature protocols, 11(10), pp.1775-1781.

323. Shi, Y., Glaser, K.J., Venkatesh, S.K., Ben-Abraham, E.I. and Ehman, R.L., 2015. Feasibility of using 3D MR elastography to determine pancreatic stiffness in healthy volunteers. Journal of Magnetic Resonance Imaging, 41(2), pp.369-375.

324. Lennartz, S., Laukamp, K.R., Neuhaus, V., Hokamp, N.G., Le Blanc, M., Maus, V., Kabbasch, C., Mpotsaris, A., Maintz, D. and Borggrefe, J., 2018. Dual-layer detector CT of the head: initial experience in visualization of intracranial hemorrhage and hypodense brain lesions using virtual monoenergetic images. European Journal of Radiology, 108, pp.177-183.

325. Wex, C., Fröhlich, M., Brandstädter, K., Bruns, C. and Stoll, A., 2015. Experimental analysis of the mechanical behavior of the viscoelastic porcine pancreas and preliminary case study on the human pancreas. Journal of the mechanical behavior of biomedical materials, 41, pp.199-207.

326. Rubiano, A., Delitto, D., Han, S., Gerber, M., Galitz, C., Trevino, J., Thomas, R.M., Hughes, S.J. and Simmons, C.S., 2018. Viscoelastic properties of human pancreatic tumors and in vitro constructs to mimic mechanical properties. Acta biomaterialia, 67, pp.331-340.

327. Schmuck, R.B., Lippens, E., Wulsten, D., Garske, D.S., Strönisch, A., Pratschke, J., Sauer, I.M., Duda, G.N., Bahra, M. and Cipitria, A., 2021. Role of extracellular matrix structural components and tissue mechanics in the development of postoperative pancreatic fistula. Journal of biomechanics, 128, p.110714.

328. Norman, M.D., Ferreira, S.A., Jowett, G.M., Bozec, L. and Gentleman, E., 2021. Measuring the elastic modulus of soft culture surfaces and three-dimensional hydrogels using atomic force microscopy. *Nature Protocols*, *16*(5), pp.2418-2449.

329. Leikina, E., Mertts, M.V., Kuznetsova, N. and Leikin, S., 2002. Type I collagen is thermally unstable at body temperature. Proceedings of the National Academy of Sciences, 99(3), pp.1314-1318.

330. Huang, G. and Greenspan, D.S., 2012. ECM roles in the function of metabolic tissues. Trends in Endocrinology & Metabolism, 23(1), pp.16-22.

331. Gloyn, A.L., Ibberson, M., Marchetti, P., Powers, A.C., Rorsman, P., Sander, M. and Solimena, M., 2022. Every islet matters: improving the impact of human islet research. Nature metabolism, 4(8), pp.970-977.

332. Kulkarni, R.N. and Stewart, A.F., 2014. Summary of the Keystone islet workshop (April 2014): the increasing demand for human islet availability in diabetes research. Diabetes, 63(12), pp.3979-3981.

333. Du, Y., Liang, Z., Wang, S., Sun, D., Wang, X., Liew, S.Y., Lu, S., Wu, S., Jiang, Y., Wang, Y. and Zhang, B., 2022. Human pluripotent stem-cell-derived islets ameliorate diabetes in non-human primates. *Nature medicine*, *28*(2), pp.272-282.

334. Pampaloni, F., Reynaud, E.G. and Stelzer, E.H., 2007. The third dimension bridges the gap between cell culture and live tissue. Nature reviews Molecular cell biology, 8(10), pp.839-845.

335. Hauge-Evans, A.C., Squires, P.E., Persaud, S.J. and Jones, P.M., 1999. Pancreatic beta-cell-to-beta-cell interactions are required for integrated responses to nutrient stimuli: enhanced Ca2+ and insulin secretory responses of MIN6 pseudoislets. Diabetes, 48(7), pp.1402-1408.

336. Chowdhury, A., Dyachok, O., Tengholm, A., Sandler, S. and Bergsten, P., 2013. Functional differences between aggregated and dispersed insulin-producing cells. Diabetologia, 56, pp.1557-1568.

337. Bae, C.Y., Min, M.K., Kim, H. and Park, J.K., 2014. Geometric effect of the hydrogel grid structure on in vitro formation of homogeneous MIN6 cell clusters. Lab on a Chip, 14(13), pp.2183-2190.

338. Nishimura, W., Iwasa, H. and Tumurkhuu, M., 2022. Role of the Transcription Factor MAFA in the Maintenance of Pancreatic β-Cells. International journal of molecular sciences, 23(9), p.4478.

339. Klochendler, A., Caspi, I., Corem, N., Moran, M., Friedlich, O., Elgavish, S., Nevo, Y., Helman, A., Glaser, B., Eden, A. and Itzkovitz, S., 2016. The genetic program of pancreatic β-cell replication in vivo. Diabetes, 65(7), pp.2081-2093.

340. Puri, S., Roy, N., Russ, H.A., Leonhardt, L., French, E.K., Roy, R., Bengtsson, H., Scott, D.K., Stewart, A.F. and Hebrok, M., 2018. Replication confers β cell immaturity. Nature Communications, 9(1), p.485.

341. Blanchi, B., Taurand, M., Colace, C., Thomaidou, S., Audeoud, C., Fantuzzi, F., Sawatani, T., Gheibi, S., Sabadell-Basallote, J., Boot, F.W. and Chantier, T., 2023. EndoC-βH5 cells are storable and ready-to-use human pancreatic beta cells with physiological insulin secretion. *Molecular metabolism*, *76*, p.101772.

342. Alessandra, G., Algerta, M., Paola, M., Carsten, S., Cristina, L., Paolo, M., Elisa, M., Gabriella, T. and Carla, P., 2020. Shaping pancreatic β-cell differentiation and functioning: the influence of mechanotransduction. Cells, 9(2), p.413.

343. Nyitray, C.E., Chavez, M.G. and Desai, T.A., 2014. Compliant 3D microenvironment improves β-cell cluster insulin expression through mechanosensing and β-catenin signaling. Tissue Engineering Part A, 20(13-14), pp.1888-1895.

344. Johansen, C.G., Holcomb, K., Sela, A., Morrall, S., Park, D. and Farnsworth, N.L., 2024. Extracellular matrix stiffness mediates insulin secretion in pancreatic islets via mechanosensitive Piezo1 channel regulated Ca2+ dynamics. Matrix Biology Plus, 22, p.100148.

345. Zhang, M., Yan, S., Xu, X., Yu, T., Guo, Z., Ma, M., Zhang, Y., Gu, Z., Feng, Y., Du, C. and Wan, M., 2021. Three-dimensional cell-culture platform based on hydrogel with tunable microenvironmental properties to improve insulin-secreting function of MIN6 cells. Biomaterials, 270, p.120687.

346. Cañibano-Hernández, A., Del Burgo, L.S., Espona-Noguera, A., Orive, G., Hernández, R.M., Ciriza, J. and Pedraz, J.L., 2019. Hyaluronic acid enhances cell survival of encapsulated insulin-producing cells in alginate-based microcapsules. International journal of pharmaceutics, 557, pp.192-198.

347. Hull, R.L., Bogdani, M., Nagy, N., Johnson, P.Y. and Wight, T.N., 2015. Hyaluronan: a mediator of islet dysfunction and destruction in diabetes?. Journal of Histochemistry & Cytochemistry, 63(8), pp.592-603.

348. Bogdani, M., 2016. Thinking outside the cell: a key role for hyaluronan in the pathogenesis of human type 1 diabetes. Diabetes, 65(8), pp.2105-2114.

349. Mendelsohn, A.D., Nyitray, C., Sena, M. and Desai, T.A., 2012. Size-controlled insulin-secreting cell clusters. Acta biomaterialia, 8(12), pp.4278-4284.

350. Al-Abboodi, A., Fu, J., Doran, P.M. and Chan, P.P., 2013. Three-dimensional nanocharacterization of porous hydrogel with ion and electron beams. *Biotechnology and bioengineering*, *110*(1), pp.318-326.

351. Barberio, C., Saez, J., Withers, A., Nair, M., Tamagnini, F. and Owens, R.M., 2022. Conducting polymer-ECM scaffolds for human neuronal cell differentiation. *Advanced Healthcare Materials*, *11*(20), p.2200941.

352. Akers, A., Gassman, M. and Smith, R., 2006. Hydraulic power system analysis. CRC press.

353. Koo, J. and Kleinstreuer, C., 2003. Liquid flow in microchannels: experimental observations and computational analyses of microfluidics effects. Journal of Micromechanics and Microengineering, 13(5), p.568.

354. Huang, Y., Han, T., Xuan, J., Xu, H., Wang, Y. and Zhang, L., 2018. Design criteria and applications of multi-channel parallel microfluidic module. Journal of Micromechanics and Microengineering, 28(10), p.105021.

355. Choi, Sungyoung; Lee, Myung Gwon; Park, Je-Kyun (2010). Microfluidic parallel circuit for measurement of hydraulic resistance. Biomicrofluidics, 4(3), 034110–. doi:10.1063/1.3486609

356. Wu, J., Fang, H., Zhang, J. and Yan, S., 2023. Modular microfluidics for life sciences. Journal of Nanobiotechnology, 21(1), p.85.

357. Esch, M.B., Ueno, H., Applegate, D.R. and Shuler, M.L., 2016. Modular, pumpless body-on-a-chip platform for the co-culture of GI tract epithelium and 3D primary liver tissue. Lab on a Chip, 16(14), pp.2719-2729.

358. Fredlund, D.G., 1976. Density and compressibility characteristics of air–water mixtures. Canadian Geotechnical Journal, 13(4), pp.386-396.

359. Regehr, K.J., Domenech, M., Koepsel, J.T., Carver, K.C., Ellison-Zelski, S.J., Murphy, W.L., Schuler, L.A., Alarid, E.T. and Beebe, D.J., 2009. Biological implications of polydimethylsiloxane-based microfluidic cell culture. Lab on a Chip, 9(15), pp.2132-2139.

360. Todeschini, M., Bastos da Silva Fanta, A., Jensen, F., Wagner, J.B. and Han, A., 2017. Influence of Ti and Cr adhesion layers on ultrathin Au films. ACS applied materials & interfaces, 9(42), pp.37374-37385.

361. Ravariu, C., Manea, E. and Babarada, F., 2017. Masks and metallic electrodes compounds for silicon biosensor integration. Journal of Alloys and Compounds, 697, pp.72-79.

362. Olejnik, A., Śliwiński, G., Karczewski, J., Ryl, J., Siuzdak, K. and Grochowska, K., 2021. Laser-assisted approach for improved performance of Au-Ti based glucose sensing electrodes. Applied Surface Science, 543, p.148788.

363. Chen, Z. and Lee, J.B., 2021. Biocompatibility of su-8 and its biomedical device applications. Micromachines, 12(7), p.794.

364. Vernekar, V.N., Cullen, D.K., Fogleman, N., Choi, Y., García, A.J., Allen, M.G., Brewer, G.J. and LaPlaca, M.C., 2009. SU-8 2000 rendered cytocompatible for neuronal bioMEMS applications. Journal of Biomedical Materials Research Part A: An Official Journal of The Society for Biomaterials, The Japanese Society for Biomaterials, and The Australian Society for Biomaterials and the Korean Society for Biomaterials, 89(1), pp.138-151.

365. Temiz, Y., Ferretti, A., Leblebici, Y. and Guiducci, C., 2012. A comparative study on fabrication techniques for on-chip microelectrodes. Lab on a Chip, 12(22), pp.4920-4928.

366. Liu, J., Song, D., Zong, G., Yin, P., Zhang, X., Xu, Z., Du, L., Liu, C. and Wang, L., 2014. Fabrication of SU-8 moulds on glass substrates by using a common thin negative photoresist as an adhesive layer. Journal of Micromechanics and Microengineering, 24(3), p.035009.

367. Susloparova, A., Halliez, S., Begard, S., Colin, M., Buée, L., Pecqueur, S., Alibart, F., Thomy, V., Arscott, S., Pallecchi, E. and Coffinier, Y., 2021. Low impedance and highly transparent microelectrode arrays (MEA) for in vitro neuron electrical activity probing. Sensors and Actuators B: Chemical, 327, p.128895.

368. O'Reilly, J.E., 1973. Oxidation-reduction potential of the ferro-ferricyanide system in buffer solutions. Biochimica et Biophysica Acta (BBA)-Bioenergetics, 292(3), pp.509-515.

369. Bortels, L., Van den Bossche, B., Deconinck, J., Vandeputte, S. and Hubin, A., 1997. Analytical solution for the steady-state diffusion and migration involving multiple reaction ions Application to the identification of Butler-Volmer kinetic parameters for the ferri-/ferrocyanide redox couple. Journal of Electroanalytical Chemistry, 429(1-2), pp.139-155.

370. Konopka, S.J. and McDuffie, B., 1970. Diffusion coefficients of ferri-and ferrocyanide ions in aqueous media, using twin-electrode thin-layer electrochemistry. Analytical Chemistry, 42(14), pp.1741-1746.

371. Patel, B.A., Arundell, M., Quek, R.G., Harvey, S.L., Ellis, I.R., Florence, M.M., Cass, A.E., Schor, A.M. and O'Hare, D., 2008. Individually addressable microelectrode array for monitoring oxygen and nitric oxide release. Analytical and bioanalytical chemistry, 390, pp.1379-1387.

372. Helmholtz, H.V., 1879. Studien über electrische Grenzschichten. Annalen der Physik, 243(7), pp.337-382.

373. Orozco, J., Fernández-Sánchez, C. and Jiménez-Jorquera, C., 2010. Ultramicroelectrode array based sensors: A promising analytical tool for environmental monitoring. Sensors, 10(1), pp.475-490.

374. Ayliffe, H.E. and Rabbitt, R.D., 2003. An electric impedance based microelectromechanical system flow sensor for ionic solutions. Measurement science and Technology, 14(8), p.1321.

375. Wang, Q., Vasilescu, A., Wang, Q., Coffinier, Y., Li, M., Boukherroub, R. and Szunerits, S., 2017. Electrophoretic approach for the simultaneous deposition and functionalization of reduced graphene oxide nanosheets with diazonium compounds: application for lysozyme sensing in serum. ACS Applied Materials & Interfaces, 9(14), pp.12823-12831.

376. Tarcan, R., Todor-Boer, O., Petrovai, I., Leordean, C., Astilean, S. and Botiz, I., 2020. Reduced graphene oxide today. Journal of Materials Chemistry C, 8(4), pp.1198-1224.

377. Noorbakhsh, A. and Alnajar, A.I.K., 2016. Antifouling properties of reduced graphene oxide nanosheets for highly sensitive determination of insulin. Microchemical Journal, 129, pp.310-317.

378. Bi, H., Karanth, S.S., Ye, K., Stein, R. and Jin, S., 2020. Decellularized tissue matrix enhances self-assembly of islet organoids from pluripotent stem cell differentiation. ACS biomaterials science & engineering, 6(7), pp.4155-4165.

379. Abazari, M.F., Soleimanifar, F., Aleagha, M.N., Torabinejad, S., Nasiri, N., Khamisipour, G., Mahabadi, J.A., Mahboudi, H., Enderami, S.E., Saburi, E. and Hashemi, J., 2018. PCL/PVA nanofibrous scaffold improve insulin-producing cells generation from human induced pluripotent stem cells. Gene, 671, pp.50-57.

380. Enderami, S.E., Kehtari, M., Abazari, M.F., Ghoraeian, P., Nouri Aleagha, M., Soleimanifar, F., Soleimani, M., Mortazavi, Y., Nadri, S., Mostafavi, H. and Askari, H., 2018. Generation of insulin-producing cells from human induced pluripotent stem cells on PLLA/PVA nanofiber scaffold. Artificial cells, nanomedicine, and biotechnology, 46(sup1), pp.1062-1069.

381. Jiang, K., Chaimov, D., Patel, S.N., Liang, J.P., Wiggins, S.C., Samojlik, M.M., Rubiano, A., Simmons, C.S. and Stabler, C.L., 2019. 3-D physiomimetic extracellular matrix hydrogels provide a supportive microenvironment for rodent and human islet culture. Biomaterials, 198, pp.37-48.

382. Takahashi, I., Noguchi, N., Nata, K., Yamada, S., Kaneiwa, T., Mizumoto, S., Ikeda, T., Sugihara, K., Asano, M., Yoshikawa, T. and Yamauchi, A., 2009. Important role of heparan sulfate in postnatal islet growth and insulin secretion. Biochemical and biophysical research communications, 383(1), pp.113-118.

383. Messelmani, T., Le Goff, A., Souguir, Z., Maes, V., Roudaut, M., Vandenhaute, E., Maubon, N., Legallais, C., Leclerc, E. and Jellali, R., 2022. Development of liver-on-chip integrating a hydroscaffold mimicking the liver's extracellular matrix. Bioengineering, 9(9), p.443.

384. Ho, R.J. and Shi, Q.H., 1982. Forskolin as a novel lipolytic agent. Biochemical and Biophysical Research Communications, 107(1), pp.157-164.

385. Wu, Y., Midinov, B. and White, R.J., 2019. Electrochemical aptamer-based sensor for real-time monitoring of insulin. ACS sensors, 4(2), pp.498-503.;

386. Mazzotta, E., Di Giulio, T. and Malitesta, C., 2022. Electrochemical sensing of macromolecules based on molecularly imprinted polymers: challenges, successful strategies, and opportunities. Analytical and Bioanalytical Chemistry, 414(18), pp.5165-5200.

387. Mihailescu, C.M., Stan, D., Savin, M., Moldovan, C.A., Dinulescu, S., Radulescu, C.H., Firtat, B., Muscalu, G., Brasoveanu, C., Ion, M. and Dragomir, D., 2020. Platform with biomimetic electrochemical sensors for adiponectin and leptin detection in human serum. Talanta, 210, p.120643.

388. Tanumihardja, E., Slaats, R.H., van der Meer, A.D., Passier, R., Olthuis, W. and van den Berg, A., 2020. Measuring both pH and O2 with a single on-chip sensor in cultures of human pluripotent stem cell-derived cardiomyocytes to track induced changes in cellular metabolism. ACS sensors, 6(1), pp.267-274.

389. Lehuen, A., Diana, J., Zaccone, P. and Cooke, A., 2010. Immune cell crosstalk in type 1 diabetes. Nature Reviews Immunology, 10(7), pp.501-513.

390. Kolb, H. and Mandrup-Poulsen, T., 2005. An immune origin of type 2 diabetes?. Diabetologia, 48, pp.1038-1050.

391. van Berlo, D., Nguyen, V.V., Gkouzioti, V., Leineweber, K., Verhaar, M.C. and van Balkom, B.W., 2021. Stem cells, organoids, and organ-on-a-chip models for personalized in vitro drug testing. Current Opinion in Toxicology, 28, pp.7-14.

392. Snowden, T.J., van der Graaf, P.H. and Tindall, M.J., 2017. Methods of model reduction for large-scale biological systems: a survey of current methods and trends. Bulletin of mathematical biology, 79, pp.1449-1486.

393. Alsharaiah, M.A., Samarasinghe, S. and Kulasiri, D., 2023. Proteins as fuzzy controllers: Auto tuning a biological fuzzy inference system to predict protein dynamics in complex biological networks. Biosystems, 224, p.104826.

394. Volk, Michael Jeffrey; Lourentzou, Ismini; Mishra, Shekhar; Vo, Lam Tung; Zhai, Chengxiang; Zhao, Huimin (2020). Biosystems Design by Machine Learning. ACS Synthetic Biology, (), acssynbio.0c00129–. doi:10.1021/acssynbio.0c00129

395. Ma, J., Yu, M.K., Fong, S., Ono, K., Sage, E., Demchak, B., Sharan, R. and Ideker, T., 2018. Using deep learning to model the hierarchical structure and function of a cell. Nature methods, 15(4), pp.290-298.;

396. Erbe, R., Gore, J., Gemmill, K., Gaykalova, D.A. and Fertig, E.J., 2022. The use of machine learning to discover regulatory networks controlling biological systems. Molecular cell, 82(2), pp.260-273.

Appendix 1

1st author scientific research article accepted to Springer 'In Vitro Models' journal.

Mechanical and functional characterisation of a 3D porous biomimetic extracellular matrix to study insulin secretion from pancreatic β-cell lines

Leonid Pliner[1] (ORCID 0000-0001-5823-3868), Nathan Laneret[2], Meryl Roudaut[3] (ORCID 0000-0003-2373-7593), Alejandra Mogrovejo-Valdivia[3] (ORCID 0000-0002-1532-6631), Elodie Vandenhaute[3], Nathalie Maubon[3], Robert-Alain Toillon[2] (ORCID 0000-0001-5483-2118), Youness Karrout[4], Anthony Treizebre[5, 6, *] (ORCID 0000-0002-2265-8095) and Jean-Sebastien Annicotte[1, 6, *] (ORCID 0000-0002-2109-4849)

[1] Univ. Lille, Inserm, CHU Lille, Institut Pasteur Lille, U1167 - RID-AGE - Facteurs de risque et déterminants moléculaires des maladies liées au vieillissement, F-59000 Lille, France

[2] Univ. Lille, CNRS, Inserm, CHU Lille, UMR9020-U1277 – CANTHER – Cancer Heterogeneity Plasticity and Resistance to Therapies, F-59000 Lille, France

[3] HCS Pharma, F-59000 Lille, France

[4] Univ. Lille, Inserm, CHU Lille, U1008, F-59000 Lille, France

[5] Univ. Lille, CNRS, Univ Polytechnique Hauts-de-France, Junia, UMR 8520 - IEMN – Institut d'Électronique de Microélectronique et de Nanotechnologie, F-59000 Lille, France

[6]Co-senior authors

*Corresponding authors: jean-sebastien.annicotte@inserm.fr, anthony.treizebre@univ-lille.fr

Abstract

Background Extracellular matrix (ECM) is a three-dimensional (3D) structure found around cells in the tissues of many organisms. It is composed mainly of fibrous proteins, such as collagen and elastin, adhesive glycoproteins, such as fibronectin and laminin — as well as proteoglycans, such as hyaluronic acid. The ECM performs several essential functions, including structural support of tissues, regulation of cell communication, adhesion, migration and differentiation by providing biochemical and biomechanical cues

to the cells. Pancreatic β-cells have been previously shown to be responsive to the surrounding mechanical stress, impacting their insulin-secreting function.

Purpose We aimed to derive a physiologically relevant *in vitro* model of pancreatic tissue by using an innovative synthesised porous ECM, that mimics the native tissue microenvironment and mechanical properties.

Methods Here we performed mechanical, physico-chemical and functional characterisation of a synthetic hydrogel ECM, composed of hyaluronic acid cross-linked with collagen type I and VI and modified with fibronectin. The hydrogel was used as a 3D cell culture scaffold for the MIN6 insulinoma cell line. Cell proliferation, viability, gene expression and insulin secretion in response to glucose stimulus were assessed and contrasted with classic monolayer culture.

Results The biomaterial exhibited a shear modulus of 815.37 kPa and a distinctive viscoelastic response. MIN6 cells showed a higher proliferation and viability rates and maintained insulin secretion in response to glucose stimulus and β-cell identity gene expression when cultured in the 3D hydrogel compared to monolayer culture.

Conclusion Our study demonstrated the potential of this biomimetic hydrogel scaffold as an innovative matrix enabling better *in vitro* models to study disease physiopathology.

Keywords

Biomaterial, extracellular matrix, 3d cell culture, pancreatic β-cells

Acknowledgements

The authors thank US 41 - UMS 2014 - PLBS for confocal imaging facilities and UMET CNRS UMR 8207, especially Cédric Zobrist, for assisting with rheological experiments. The authors would like to thank Mrs. Myriam Moreau for her help in carrying out the work on the micro Raman system facility of the Advanced Characterization Platform of the Chevreul Institute. The Chevreul Institute is thanked for supporting CPER projects funded by the “Ministère de l’Enseignement Supérieur et de la Recherche”, the region “Hauts-de-France”, the ERDF program of the European Union and the “Métropole Européenne de Lille”. We thank Laure Rolland and Vaihere Cheung for excellent technical guidance with cell culture. We also thank Emilie Courty, Véronique de Conto, Zied Sougir, Cécile Legallais, Yannick Coffinier and members of INSERM UMR1167 and IEMN UMR8520 for their contributions in scientific discussions.

Declarations

Funding

This project has received funding from the European Union's Horizon 2020 research and innovation program under the Marie Skłodowska-Curie grant agreement no 847568, from the French government through the Programme Investissement d'Avenir (I-SITE ULNE/ ANR-16-IDEX-0004 ULNE) managed by the Agence Nationale de la Recherche (ANR). This work was supported by the ANR grants (ANR EpiRNA-T2D ANR-23-CE14-0040), INSERM, Université de Lille, Institut Pasteur de Lille, Fondation pour la Recherche Médicale (EQU202103012732).

Competing interests

M.R., A.M.V., E.V., N.M. are board members and/or employees of HCS Pharma, which provided BIOMIMESYS® scaffold. N.M. owns stocks in HCS Pharma. The other authors have no relevant financial or non-financial interests to disclose.

Author contributions

Conceptualisation, J.S.A. and A.T.; Methodology, L.P., M.R., A.M.V., Y.K., J.S.A. and A.T; Investigation, L.P., N.L., M.R., A.M.V., Y.K., J.S.A. and A.T; Resources, E.V., N.M., Y.K., R.A.T.; Data curation, L.P., N.L., M.R., A.M.V., A.T and J.S.A.; Writing - original draft, L.P.; Writing - Review & Editing, A.T. and J.S.A.; Visualisation, L.P.; Supervision, A.T. and J.S.A.; Funding acquisition, A.T. and J.S.A.

Materials availability

All unique/stable reagents generated in this study are available from the lead contact with a completed Materials Transfer Agreement.

Data and code availability

All original data and code reported in this paper will be shared by the lead contact upon request. Any additional information required to reanalyse the data reported in this paper is available from the lead contact upon request.

Introduction

Diabetes mellitus, a chronic metabolic disorder characterised by hyperglycaemia, affects millions of people worldwide. While type 1 diabetes (T1D) results from autoimmune destruction of pancreatic β-cells, type 2 diabetes (T2D) is associated with insulin resistance of peripheral tissues such as muscle, liver, adipose tissue and progressive loss of β-cell mass and function [1]. Pancreatic islet transplantation has emerged as a promising treatment for T1D [2], which gave rise to the development of porous scaffold grafts to enhance long-term survival and function of the transplanted islets [3]. Moreover, the development of effective therapies for T2D requires a better understanding of the mechanisms underlying pancreatic β-cell dysfunction, which can be facilitated by advanced *in vitro* models [4].

The extracellular matrix (ECM) plays a crucial role in providing structural support and regulating cellular behaviour, growth, and differentiation in living tissues [5, 6]. ECM is a complex network of proteins and polysaccharides that exhibits viscoelastic mechanical properties, which are essential for tissue-specific functions [7-9]. The influence of ECM on pancreatic islet cell differentiation, attachment, and proliferation has been well-established [10, 11], highlighting the need for incorporating ECM components in three-dimensional (3D) *in vitro* models to improve their relevance and predictive power.

Current *in vitro* models of pancreatic islets involve synthetic polymer matrices, such as polyethylene glycol (PEG), polylactic acid (PLA), poly(lactic-co-glycolic acid) (PLGA) [12]. These materials often lack the complexity and biomechanical cues provided by the native ECM, leading to limitations in their ability to recapitulate the in vivo behaviour of islet cells. Various strategies, such as protein hydrogels, scaffolds, and decellularised matrices, have been employed to address this issue. For instance, Daoud *et al.* demonstrated that the presence of ECM components, such as collagen and laminin, improved the survival and function of human islets *in vitro*. Nagata *et al.* showed that culturing rat islets in an ECM-derived scaffold enhanced insulin secretion compared to conventional culture methods [13-18]. However, there remains a need for a more comprehensive and biomimetic approach that combines the key structural and functional components of the ECM to enhance the performance of *in vitro* islet models.

In this study, we aimed to bridge the gap between current *in vitro* models and the native islet microenvironment by developing a synthesised biomimetic scaffold that serves as an extracellular matrix for 3D cell culture. By incorporating key ECM components, such as

fibrous proteins (collagen type I and VI), proteoglycans (hyaluronic acid, HA), and adhesive glycoproteins (fibronectin), we sought to provide the necessary biomechanical cues and cell-matrix interactions that are essential for maintaining pancreatic β-cell function and viability [19, 20]. By fine-tuning the composition and structure of our synthesised scaffold, we aimed to achieve viscoelastic properties that closely mimic the native tissue, thus providing an optimal microenvironment for islet cell function.

Our work focused on MIN6 cells, a well-established mouse pancreatic β-cell line, relatively easy to maintain and capable of robust insulin secretion in response to glucose stimulus. We used this cell line to validate the performance of the synthesised biomimetic scaffold as a model for studying glucose-stimulated insulin secretion [21, 22]. By comparing the behaviour of MIN6 cells cultured in our 3D scaffold with those in conventional two-dimensional (2D) cultures, we aimed to evaluate cell metabolic activity and insulin secretion in response to glucose stimulation.

Materials and Methods

Hydrogel scaffold fabrication

The hydrogel scaffold was prepared as previously described [23]. Briefly, the BIOMIMESYS® Adipose Tissue scaffolds were synthesised in two steps. Initially, HA (9067-32-7, Baoding Faithful Industry Co., Ltd, China) was completely dissolved in pure water at the concentration of 4 g/L, followed by the addition of 10 mg of Arg-Gly-Asp-Ser motif (RGDS, 91037-65-9, Cayman Chemicals, U.S.A.), 7.22 µmol of type I collagen (c-136157, Santa Cruz Biotechnology, Inc., U.S.A.) and 2 µmol of type VI collagen (ab7538, Abcam, U.K.). The mixture was stirred for 1 hour until achieving a homogeneous solution. In the second step, the hydrazide cross-linker (ADH, TCI Europe, Belgium) was dissolved in deionised water at the concentration of 18 g/L and incorporated into the solution, while the pH was adjusted to 4.75 using 1 M HCl (Fisher Scientific, France). The carbodiimide reagent (EDCI, TCI Europe, Belgium) was dissolved in deionised water, introduced into the reaction mixture, and allowed to gel for 2 hours under gentle agitation. The resulting hydrogels were then dialysed against deionised

water to remove unreacted ADH and EDCI. The purified hydrogel was cast in 96-well plates, frozen, and subsequently lyophilised for 24 hours using a freeze dryer (Crios, Cryotec, France; performance: 3 kg ice/24 h, T = 55°C). Finally, the hydrogel-loaded plates were sterilised through ultraviolet (UV) irradiation over the course of 30 minutes.

Rheological measurements

Rheological measurements were performed using Discovery HR10 from Ta Instruments (New Castle, U.S.A.), using a Peltier plane and a 25mm plane geometry, sustained at 37°C. The scaffold was subjected to shear stress with an oscillation measurement in a logarithmic amplitude sweep from 1 to 500 Pa at a frequency of 1 Hz. Optimal gap between the plates for the samples used in this study was found to be 100 µm. Shear modulus (G^*) was determined as the square root of the sum of squares of the shear storage and loss moduli recorded in the linear viscoelastic region (LVR). The loss factor was obtained by taking the ratio of loss modulus to storage modulus. Young's modulus (E) was derived using the shear modulus and Poisson's ratio of 0.5 for hydrogels [24], using the following equation.

$$E = 2(1 + 0.5)G^*$$

Stress-relaxation assays

For stress-relaxation experiment, 2 batches of 6-well plate shaped samples were prepared in two separate syntheses, as mentioned above. One plate each of Batch 1 and Batch 2 were evaluated on the day 1 after synthesis. A separate plate of Batch 2 was stored at 4°C and used on the day 30 after synthesis.

The experiment was carried out with the use of TA.XTplusC Texture Analyser (Stable Micro Systems, U.K.). A spherical probe of 6 mm diameter was utilised in conjunction with a 5g loadcell. The experiment involved a close to instantaneous application of mechanical stress with a solid probe onto the biomaterial fixed between two parallel plates, sustained for 60 seconds and released after, during which the reaction force exerted by the biomaterial onto the probe was measured.

The time-series data was analysed by a home-made Python program, that used Statsmodels, SciPy and Scikit-learn libraries for model fitting and assessment [25-27] as well as Pandas, NumPy and Matplotlib libraries for data processing and visualisation [28-30]. The signal was filtered using lowess smoothing and then used to fit a two-exponent model using non-linear least squares curve fitting. The goodness of the fit was assessed by R^2 value and mean square error of the residuals. The models were then normalised around the maximum value.

Raman spectroscopy

Raman spectra of the scaffold and its constituents: HA, RGDS and collagens type I and VI - were recorded in the range of 380-3800 cm^{-1} with HR Evolution spectroscope by Horiba Scientific (Horiba, Japan). HA and RGDS were examined in powder form, while collagen samples were produced by freeze-drying 2 mL of collagen I and VI at -50°C for 24 hours. Scaffold samples were prepared as described above. For HA, RGDS and collagen type I, a 632.8 nm laser was used as an excitation source with a 100x objective lens focusing 15 mW at the sample in air interface at ambient conditions, resulting in an approximately 1 μm^2 laser spot. The spectrometer was equipped with diffraction grating of 300 grooves/mm which gave rise to the spatial resolution of 2 wavenumber per pixel. Prior to data collection, the instrument was calibrated with Raman line of silicon at 520.7 cm^{-1}. During the recording, single spectral acquisitions of 120 s duration were performed for each sample. Collagen type VI spectra were collected using 785 nm laser with double spectral acquisitions, 100 s long. Data processing was performed in LabSpec 5 software (Horiba Jobyn Yvon). An 8-degree polynomial baseline correction was applied to remove any fluorescence noise. Average spectra were produced for 3 specimens of each chemical.

Scanning Electron Microscopy

Scaffolds were imaged with a scanning electron microscope (SEM) ULTRA 55 (Carl Zeiss Microscopy GmbH, Germany) at 10 keV, working distance around 12 mm. Pores were measured using ImageJ software. Pore identification was achieved by applying ‘Band Pass Filter’ smoothing tool followed by pixel intensity histogram thresholding with 'Li Thresholding’ tool [31] to separate the foreground, represented by fibres, and background, represented by pores. After this, the resulting binary image was quantified

using the ‘Analyze Particles’ tool. The porosity was assessed by taking the ratio of cumulative area of all openings against the total observed area of the SEM image, given as a percentage.

Cell culture, glucose stimulated insulin secretion and insulin quantification

MIN6 cells (RRID:CVCL_0431, AddexBio, U.S.A.) were cultivated in complete MIN6 medium, which comprised DMEM medium with a glucose concentration of 4.5 g/L (31966-021, Gibco, U.S.A.). The medium was supplemented with 15% foetal bovine serum, 100 µg/ml penicillin-streptomycin, and 55 µM β-mercaptoethanol (M6250, Sigma Aldrich, U.S.A.). The cells were cultured at a temperature of 37°C with a CO_2 concentration of 5%. At the day 0 of the experiment, the cells were detached from a T75 flask with trypsin and seeded on a 96-well plate (353072, Corning, U.S.A.) in the concentration 100 $x10^3$ cells/well. For the 3D condition, the 96-well plates contained the matrix in each well. The plates were incubated in the same conditions, as described above for 7 days. Media changes took place every two days. Glucose-stimulated insulin secretion (GSIS) was performed on the days 3 and 7 of culture. MIN6 cells underwent a 1-hour starvation period using Krebs-Ringer bicarbonate buffer (KRB) supplemented with 0.5% Bovine Serum Albumin (BSA, A7030, Sigma Aldrich, U.S.A.) and 2.8 mM glucose (G8769, Sigma Aldrich, U.S.A.). Subsequently, cells were treated with 2.8 mM glucose KRB for 1 hour, followed by 20 mM glucose KRB treatment for 1 hour. Insulin content was determined after cell lysis with 180 mM HCl and 75% ethanol, followed by neutralisation with 1 M Na_2CO_3. After each treatment stage and lysis, supernatant was sampled from the wells to a sampling plate. Secreted and content insulin concentrations were evaluated using enzyme-linked immunosorbent assay (ELISA, mouse ELISA insulin kit, Mercodia). Results were expressed as a percentage of insulin content. The experiment was repeated twice.

Metabolic activity and viability measurements

The metabolic activity of the MIN6 cells was evaluated on the days 0, 3 and 7 with resazurin reduction assay. Resazurin sodium salt (B21187, Fisher Scientific, France) was dissolved in deionised water to make a 1mM working solution. The solution was sterilised with 0.22 µm syringe filter. MIN6 cells were seeded as described above. Prior to the assay, fresh media was added to each well. Next, a total of 100 µl of working solution

was added to each well and samples were incubated for 4 hours at 37°C, 5% CO_2. 100 µl of media was collected to a sampling plate (353072, Corning, U.S.A.), which was read with Infinite 200 PRO microplate reader (Tecan Group Ltd., Switzerland). Fluorescence signal was recorded using 550/9 nm excitation and 590/20 nm emission monochromators. A standard curve was produced and was used to determine the cell number based on the fluorescence value, arising from the overall metabolic activity of the cells in the sampled wells. For this, the assay was performed for a range of varied cell densities (0, 10, 20, 40, 100, 200, 400 $x10^3$ cells per well) on the day 0, after complete cell attachment on the bottom of the well was observed. Cell viability was measured using MTT assay. Measurements were performed on the days 3 and 5 of culture. At each time point, 20 µL of MTT (475989, Sigma Aldrich, U.S.A.) solution (5 mg/mL in PBS) was added to each well of a 96-well plate containing either 2D or 3D cultures. The plate was incubated for 4 hours at 37°C, 5% CO_2 in the dark. After incubation, the supernatant was removed, and 150 µL of dimethyl sulfoxide (DMSO) was added and the plates were incubated for 20 minutes at room temperature. Absorbance was measured at 540 nm. Each experimental set consisted of 6 data points, including 1 control and 5 cell-cultured samples. The data was given as a percentage viability relative to the day 3.

Immunostaining and fluorescence imaging

For fluorescence imaging, after 7 days of culture, the cell-loaded scaffold wells and chamber slides (Lab-Tek™ II CC2™ Chamber Slide, 154941, Thermo Fisher Scientific, France) were filled with a fixing solution of paraformaldehyde (4%) in PBS and kept at room temperature for 20 minutes. Following fixation, blocking was performed using a blocking buffer of 1% BSA. Guinea pig anti-insulin primary antibodies (IR00261-2, Agilent Technologies, U.S.A.) were then applied and incubated overnight at 4°C. Subsequently, cells were washed with PBS and incubated with anti-guinea pig 647 nm secondary antibodies (A21450, Invitrogen, U.S.A.) for 1 hour at room temperature to visualise intracellular insulin. Lastly, nuclear staining was achieved using 4',6-diamidino-2-phenylindole (DAPI) for 15 minutes, followed by thorough washing with PBS. Confocal imaging was conducted using Zeiss Axio Observer Z1 inverted microscope (Carl Zeiss Microscopy GmbH, Germany) equipped with CSU-X1 spinning-disc unit (Yokogava Electric Corporation, Japan) and a sCMOS PRIME 95B camera (Teledyne Photometrics, U.S.A.). 2D slides were imaged with 40x objective lens. For three-dimensional scaffold samples, a z-stack was obtained containing 100-200 images focused at a range of

equally spaced planes across the z-axis with a 63x objective lens. Image processing was performed using ZEN Microscopy Software (Carl Zeiss Microscopy GmbH, Germany). A single 2D-projection image was compiled from the z-stack, based on the maximum intensity of the pixels for each x-y coordinate, thus producing a pseudo-3D image as viewed from the top. Additionally, 3D reconstruction images were obtained from the z-stacks. Control experiments excluding primary antibodies were performed to assess the specificity of staining.

RNA extraction and qRT-PCR analysis

RNA samples were extracted using TRIzol agent (15596026, Invitrogen, U.S.A.). Prior to extraction, hydroscaffolds were transferred into an Eppendorf tube whit Trizol agent and homogenised using a 1-mL syringe fitted with a 19G needle to ensure efficient disruption of the scaffolds. After homogenisation, 200 µL of chloroform was added, and samples were vigorously shaken for 10 seconds, followed by incubation at room temperature for 3 minutes. Centrifugation was performed at 12,000 g for 15 minutes at 4°C to separate the phases. The aqueous phase was transferred to a new tube and 500 µL of isopropanol was added to precipitate RNA. Samples were incubated at room temperature for 15 minutes, followed by centrifugation at 12,000 g for 10 minutes at 4°C. The RNA pellet was washed twice with 1 mL of 75% ethanol, air dried, and resuspended in 10-20 µL of RNase-free water. mRNA expression was measured after reverse transcription by quantitative RT-PCR (qRT-PCR) as previously described [32] with FastStart SYBR Green master mix (Roche, Switzerland) using a LC480 instrument (Roche, Switzerland). qRT-PCR results were normalized to endogenous cyclophilin reference mRNA levels. Results are expressed as the relative mRNA levels of a specific gene expression using the formula $2^{-\Delta Ct}$. The complete list of primers is presented in Supplemental Table 1.

Statistical Analysis

Data are presented as mean ± s.d. or s.e.m. 2-sided Grubbs test was systematically performed to identify outliers, using Prism 10.0 (GraphPad software). Statistical analyses were performed using a two-tailed unpaired Mann-Whitney U-test or two-way ANOVA with Fisher's LSD tests. Differences were considered statistically significant at $p < 0.05$ (*$p < 0.05$, ** $p < 0.01$, *** $p < 0.001$ and **** $p < 0.0001$).

Results

Mechanical characterisation of the scaffold

Rheological analysis was first performed to evaluate the shear mechanical properties of the matrix. BIOMIMESYS® scaffold, transformed in its hydrogel form by adding MIN6 culture medium, was subjected to harmonically varying loading to evaluate the shear property of the material. Storage modulus (*G'*) and the loss modulus (*G"*) are presented as plots against deformation (γ) in Fig. 1a. The dynamics of these moduli under oscillatory loading characterised the contribution of solid and liquid phase to the mechanical properties of the scaffold, reflected in *G'* and *G"* respectively. Notably, the storage modulus exceeded the loss modulus, indicating that the scaffold exhibited gel-like behaviour of a viscoelastic solid. Within the range of low deformations (<10%), both *G'* and *G"* remained constant, indicating an undisturbed scaffold structure. This region is called Linear Viscoelastic Region (LVR). Consequently, the moduli began to decrease, signifying structural perturbation. The backward sweep curves (i.e., decreasing deformation) demonstrated the reversibility of the scaffold's structure, characterised by a return close to the original values of *G'* and *G"*. The plateau values observed for *G'* and *G''* within the LVR related to the scaffold's mechanical properties, such as rigidity or elasticity. The shear modulus G^* was found 815.37 ± 165.08 Pa and the average loss factor $\tan(\delta)$=0.187. Young's modulus *E*, or elastic modulus, was calculated using Poisson's equation, producing the value of 2446.1 ± 495.23 Pa.

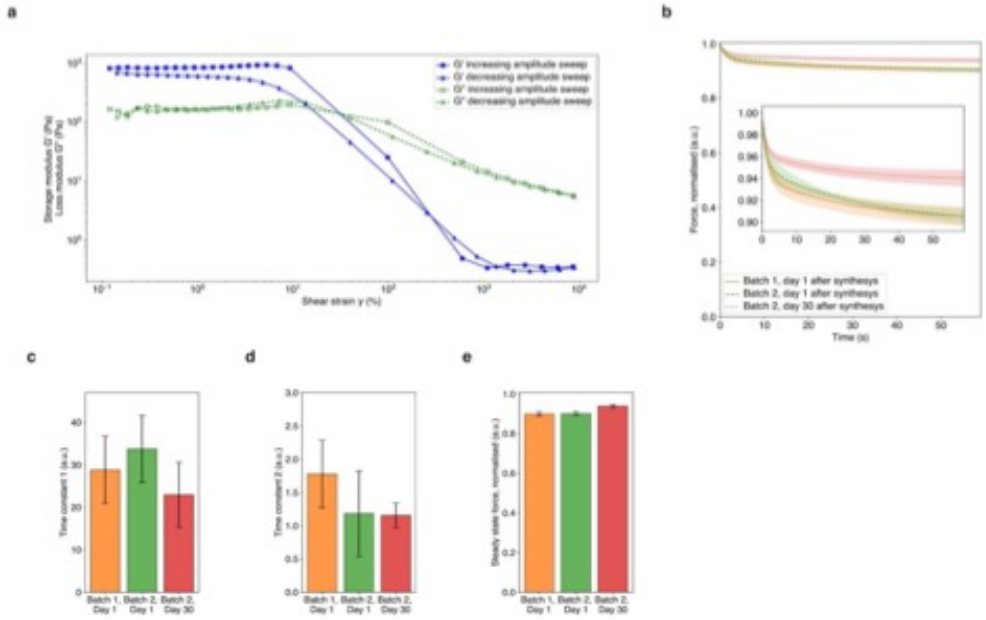

Fig. 1 Mechanical characterisation of the hydrogel scaffold. Scaffold's mechanical properties were evaluated in rheological shear oscillation test (**a**) and stress-relaxation test (**b-f**). In rheological evaluation an oscillatory shear stress was applied from 1 to 500 Pa at a frequency of 1 Hz, 37°C and storage (*G'*) and loss (*G"*) moduli were recorded. In stress-relaxation experiment, samples were fixed between two parallel plates with an opening and subjected to a constant loading applied for 60 seconds through a spherical probe (**b**). The stress-relaxation curves were filtered and fitted a 2-exponent Maxwell model, normalised against the maximum value. Averages and standard deviations of the curves for Batch 1 (*n*=6) and Batch 2 (*n*=4) on the 1st day after synthesis and Batch 2 one month after synthesis (*n*=6) are presented in **c**. Two time constants and steady state force were extracted from the 2-exponent model parameters and compared in **c**, **d**, and **e**, respectively.

During the stress-relaxation experiment, the scaffold was subjected to a constant loading by applying a fixed deformation and sustaining it for 60 seconds, while the stress was recorded. The setup is shown in Supplemental Fig. 1. The response of the material was a dynamic non-linear relaxation to a steady state from an initial value. A transient response was observed with an initial steep negative gradient converging to zero over time. This provided further insight into the viscoelastic characteristic of the complex material. A Generalised Maxwell model [33] was used in order to describe the behaviour of the scaffold with spring-dashpot elements connected in parallel (details are provided in Suppplemental Fig 2). Springs represent the elastic property of the scaffold while dashpots – viscous. It was found that second order model with 2 parallel elements was sufficient to represent the observed relaxation response:

$$\sigma(t) = \sigma + \left(\frac{\eta_1}{E_1} + \frac{\eta_2}{E_2}\right)\frac{d\sigma}{dt} + \frac{\eta_1\eta_2}{E_1E_2}\frac{d^2\sigma}{dt^2}$$,

(1)

where σ is the stress, η_1 and η_2 are the viscosity coefficients of the corresponding dashpot element and E_1 and E_2 are the corresponding spring coefficients. An exponential solution to this model consisted of 2 exponential elements and was expressed as:

$$F(t) = Ce^{\frac{-t}{T_1}} + (F(t=0) - C - F_{ss})e^{\frac{-t}{T_2}} + F_{ss}$$,

(2)

where $F(t=0)$ is the initial reaction force, F_{ss} is the steady state force and C is the parametric coefficient and T_1 and T_2 are the time constants, describing the speed of relaxation of the biomaterial. These time constants were related to the differential form parameters as the ratio η/E. The experimental data was fit to the model (2) and the average fits are presented in Fig. 1b. The model parameters were shown to be repeatable between samples, giving aggressive T_1 = 36.43 ± 3.10 and a steadier T_2 = 1.49 ± 0.36, with the reaction force converging to F_{ss} = 0.8850 ± 0.0076 (normalised against the initial force). This behaviour was also shown to be consistent between batches and repeatable after 1 month of storage at 4°C, as presented in Fig. 1c, 1d and 1e.

Physico-chemical characterisation of the scaffold

Raman spectroscopy was performed on the scaffold and the major chemicals in its composition: HA, collagens type I and VI and RGDS. The average spectra of 3 specimen each are presented in Fig. 2. Collagen type VI spectrum is given in the range of 380-2800 cm^{-1}, due to poor sensitivity of the sensor at higher wavenumber for the laser configuration used. The spectral patterns of both collagen types appeared alike, since they were similar in their chemical composition. The presence of the amide bands was observed in the spectra of HA, RGDS, collagens and the scaffold. For instance, amide I band is observed in 1630-1690 cm^{-1} region, arising from the C=O stretching vibration. While it occurs at higher wavenumber for HA, RGDS and collagen samples, the peak is downshifted to 1640 cm^{-1} in the scaffold suggesting a conformational change from β-

sheet to α-helix [34]. As well as this, amide III peaks at 1238 cm^{-1} and 1266 cm^{-1} are observed in all spectra, arising from C-N stretching and N-H bending. N-H in plane deformations were also observed in the scaffold spectrum at 1426 cm^{-1}, same as in collagens' and RGDS spectra. The peaks in the 890 cm^{-1} and 938 cm^{-1} bands appear in the scaffold spectrum and relate to breathing of proline ring and C-C stretching of collagen and RGDS backbone respectively. At the same time, together with the 1125 cm^{-1} peak, they can also be associated with stretching of C-O-C glycosidic bond, forming the polysaccharide backbone of the HA. Furthermore, the 1049 cm^{-1} peak is both manifested in HA and as a shoulder on the scaffold spectrum, assigned to C-O stretching vibration of the alcoholic group (-OH). Similar vibrations are inherited by the scaffold from RGDS, visible at 1078 cm^{-1}. The 1374 cm^{-1} peak arising from C-H and CH_2 out of plane deformations can be observed in both HA and scaffold's spectra, as well as the CH stretching peak at 2907 cm^{-1}. In addition to this, the scaffold inherits the CH_3 and CH_2 deformation peaks at 1450 cm^{-1} and 2937 cm^{-1} regions from collagen. A pronounced peak at 1156 cm^{-1} corresponding to C-N stretching signifies new cross-links formed between the carbonyl and amine groups of HA and collagen. A notable peak in 1296 cm^{-1} in the scaffold's spectrum has resulted from the CH_2 methylene twisting of the cross-linking agent ADH. As well as this, a group of high intensity peaks in 3150-3350 cm^{-1} wavenumber region in the spectrum of the scaffold can be associated with N-H stretching arising from EDCI/NHS urea linkages formed between the polysaccharide chains during the synthesis [35-37].

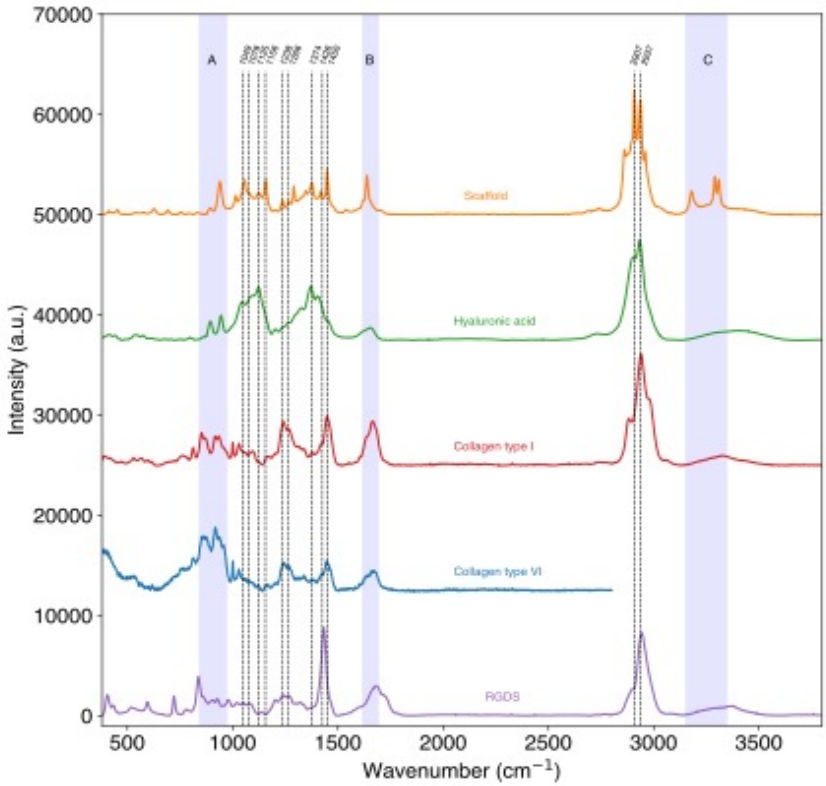

Fig. 2 Chemical characterisation of scaffold and its constituents. Raman spectroscopy curves of scaffold (yellow), hyaluronic acid (green), collagen type I (red), collagen type VI (blue) and RGDS (purple). The highlighted regions are C-C and C-O-C stretching bands (**a**), amide I band (**b**) and N-H stretching bands (**c**). Three samples were prepared for each material and spectra were collected in dry conditions at ambient temperature. Fluorescence noise was removed with polynomial baseline correction and average curve for each chemical is presented (*n*=3). For collagen type VI a longer wavelength laser was used to avoid autofluorescence. Hence, only 380-2800 cm^{-1} range is presented due to limited sensitivity of the spectrometer in this laser configuration.

Physical structure of cell-free scaffolds was then examined under the SEM (Fig. 3a). The biomaterial can be characterised as a mesh of interlinked thin non-uniform irregular concave-shaped structures of varied sizes, arising from the cross-linked HA-collagen fibres. A homogeneous network of highly open and interconnected pores formed between the fibres. The pores appear evenly distributed across the entire volume of the scaffold, as evident from top (Fig. 3b), cross-section (Fig. 3c) and bottom (Fig. 3d) images. The average porosity was determined as 47.76 ± 4.48% with pore diameter ranging from 1.82 to 135.07 μm, providing enough volume for structural support of biological cells. The scaffold was thus demonstrated to exhibit both the expected chemical and structural composition.

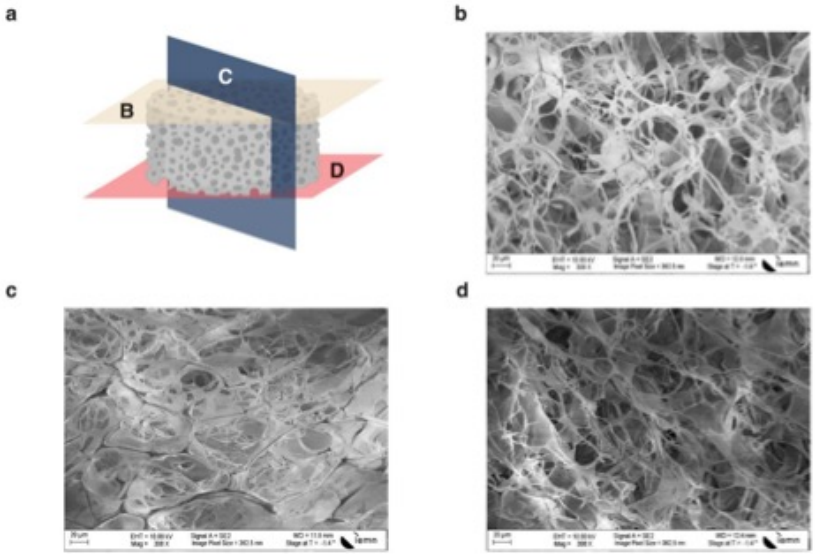

Fig. 3 Surface characterisation of the hydrogel scaffold. SEM images, as explained on the schematic **a,** showing the microstructure of the top (**b**), section (**c**) and bottom (**d**) of the scaffold. The scaffolds were freeze dried prior to imaging. No sputter coating was required, as fibres were detectable at 10 kV with minimal charging effect. Porosity of the scaffold was assessed by observing the open areas between the fibres.

MIN6 proliferation, viability, gene expression and insulin secretion in 2D versus 3D culture

MIN6 cell line was used to assess the functionality of the scaffold as a 3D pancreatic *in vitro* model in the context of cell proliferation and insulin secretion in response to glucose stimulation. The proliferation and viability of MIN6 cells was evaluated during 5 to 7 days of incubation and assessed by measuring metabolic activity using resazurin and MTT assays, respectively, as shown in Fig. 4a and b. The growth rates followed a similar pattern for both 2- and 3-dimensional cultures. There was a rapid increase in metabolic activity at the day 3, compared to the day 0, followed by a more gradual growth until day 7. Nonetheless, the proliferation rate at both day 3 and 7 appeared faster in the 3D culture compared to 2D culture. Scaffold seeded cells reached 400% by the day 3 and 550% by the day 7, compared to the steadier 260% and 320% proliferation in the classic culture on the corresponding days, relative to the day 0 metabolic activity. This can be accounted for by the observation that confluence is reached in the 2D condition. In MTT assays, we observed that cells in 2D had the same viability at day 3 and day 5 in 2D (Fig. 4b). However, viability of MIN6 cells were much more improved at day 5 compared to day 3 in 3D, suggesting that 3D culture could improve viability of MIN6 cells with time.

After 7 days of culture, MIN6 cells cultured on the classic plastic 2D surface reached confluence, spreading flat over the entire available surface (Fig. 4c). On the other hand, z-stack immunofluorescent imaging of the 3D culture, presented in Fig. 4d, 4e and 4f, revealed the organisation of MIN6 cells into clustered spheroid structures that express insulin at the protein level. The clusters of 20-40 cells were observed to have been scattered across the entire volume of the scaffold. The shape of the clusters was rather asymmetrical in x- and y-directions and oblate in z-direction, with width ranging from 40 to 120 µm and thickness from 20 to 40 µm. These observations suggested that the cells have migrated, adhered and divided within the pores of the scaffold, self-distributing over the available space in 3D during the 7-day culture. To evaluate whether 2D or 3D culture could modify gene expression, we assessed mRNA expression levels of key β-cell identity genes (*Ins1, Ins2, Slc2a2, Pcsk1, Glp1r, Ucn3, Pdx1, Mafa, Nkx6.1*) and other pancreatic islet genes (*Gcg, Sst*) through qRT-PCR. Although most of the gene expression were found similar in MIN6 cells cultivated in 2D and 3D for 3 and 7 days, we observed that the expression of the transcription factor *Nkx6.1*, a key gene involved in insulin secretion and β-cell identity, was increased in 3D condition at day 3 compared to 2D (Fig. 4g). These data suggest that 2D or 3D cultures may have biological effects in modifying the transcriptome of MIN6 cells.

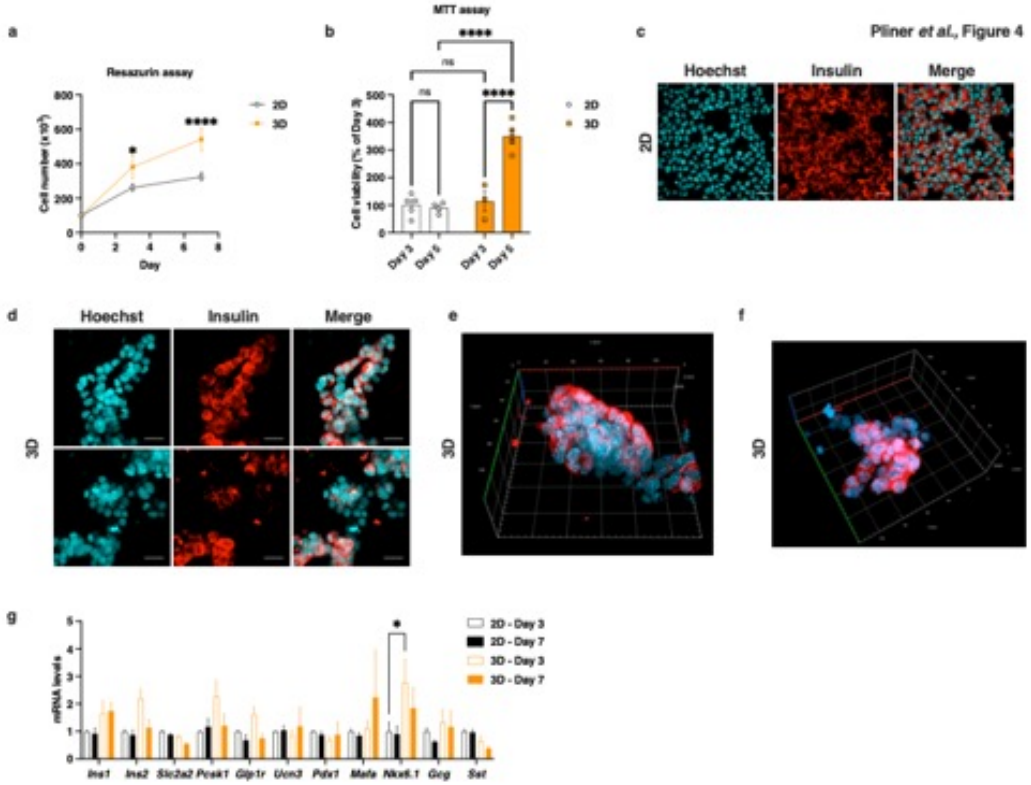

Fig. 4 MIN6 proliferation, viability, confocal imaging and gene expression analysis of MIN6 cells in 2D and 3D culture. (**a**) MIN6 cells were cultivated on classic 2D plastic surface and in 3D culture on scaffolds in 96 well plates for 7 days at the concentration 10^{-5} cells/well. Proliferation was assessed with resazurin assay performed on day 3 and 7. Standard curve was produced to relate the fluorescence to cell number by assessing the activity of cells seeded at various concentrations and resazurin assay taken on day 0 after cell sedimentation. Obtained cell number data is presented as averages with standard deviations in **a** (*n*=3). (**b**) Viability assays using MTT was performed on day 3 and day 7 of MIN6 cells cultured in 2D and 3D. Data are presented as percentage over 2D at day 3 (*n*=3-5). (**c-f**) Immunofluorescence confocal images of MIN6 cells demonstrate high level of confluence in 2D and cluster formation in 3D after 7 days of culture. Cells were fixed and stained for nuclei (cyan) and insulin (red). The images of 2D samples were obtained from a single focal plane (**c**). Scale bar = 20 μm. For 3D samples, confocal spin disc microscope was used to take a stack of images at 100-200 focal planes in z-direction, separated by 0.2 μm. **d** - Maximum intensity projection image of z-stack, depicting an example of β-cell cluster. Scale bar = 20 μm. **e-f** - 3D reconstructions of z-stack confocal fluorescent images showing two MIN6 spheroids in the spatial domain. (**g**) mRNA expression levels of key β-cell identity genes (*Ins1, Ins2, Slc2a2, Pcsk1, Glp1r, Ucn3, Pdx1, Mafa, Nkx6.1*) and other pancreatic islet genes (*Gcg, Sst*) in MIN6 cells cultivated in 2D and 3D for 3 and 7 days. Results in **a**, **b** and **g** are displayed as means +/- SEM. * $p<0.05$, **** $p<0.0001$. ns, not significant.

The regulation of insulin secretion by the MIN6 cells in response to variation of glucose concentration in GSIS experiment was then measured as presented in Supplemental Fig. 3 and Fig. 5. The increase of secreted insulin in 20 mM glucose conditions was maintained for both conditions on the day 3 and 7 (Fig. 5a and b, respectively). Despite the increased cell number, insulin content was not significantly different in MIN6 cells maintained in 2D or 3D at day 3 (Fig. 5b) and day 7 (Fig. 5d). When normalised against total insulin content, the percentage of secreted insulin was maintained after 7 days of culture in 2D, although the amplitude of the response was decreased. In the 3D condition, MIN6 cells were still responding to a 20 mM glucose stimulation, yet again the response was diminished compared to day 3. Overall, the data suggest that the secretory activity of MIN6 was analogous for 2D and 3D cultures in short-term conditions, confirming the maintained functionality of the cells seeded on the scaffold.

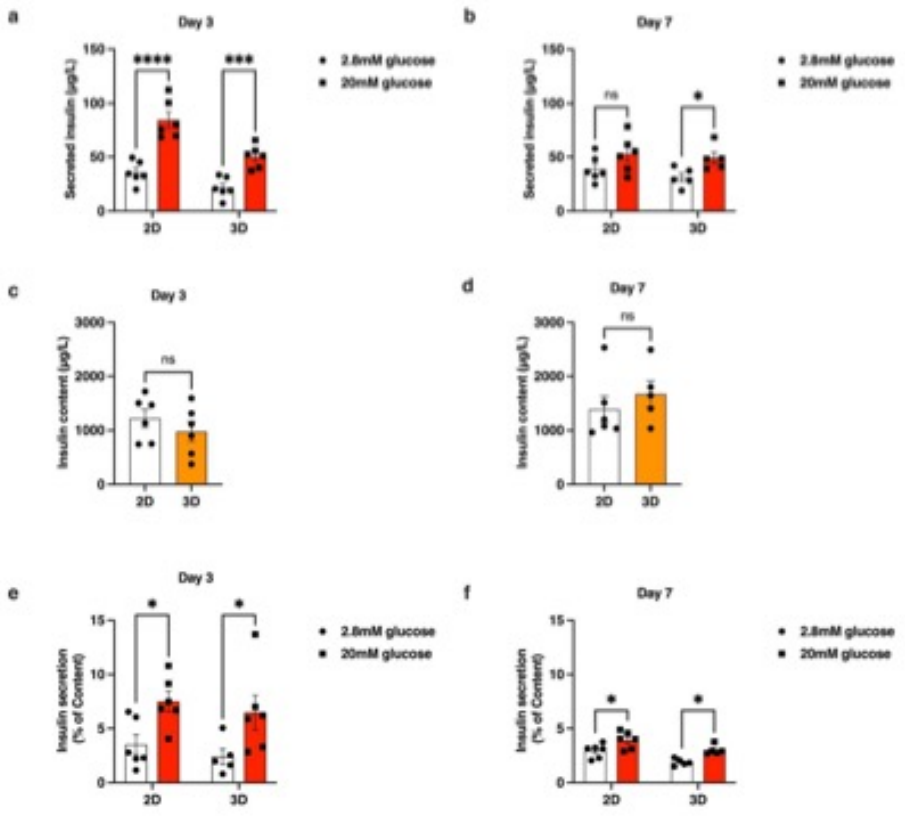

Fig. 5 Insulin secretion in response to glucose in 2D and 3D cultivated-MIN6 cells. GSIS assay was performed on days 3 and 7. Secreted insulin concentration values after stimulation with 2.8 and 20 mM glucose (**a-b**) were normalised against total insulin content (**c-d**) in each well and given as percentage of content (**e-f**). Average and standard deviation values of insulin secretion and content are presented (n=6). *p < 0.05, *** p < 0.001 and **** p < 0.0001.

Discussion

The results presented in this study demonstrate the successful synthesis of a biomimetic scaffold that mimics the pancreatic ECM for application with a 3D cell culture of MIN6 cells. The scaffold's viscoelastic properties, porous structure, and incorporation of key ECM components provide a more physiologically relevant environment for cell growth and function compared to traditional 2D culture systems.

Current literature lacks sufficient data on the mechanical properties of pancreatic tissue. The elastography approaches have previously demonstrated shear stiffness of human pancreas to range from 0.72 kPa to 1.54 kPa at 40 Hz [38, 39], whereas Wex *et al.*

reported 0.64 to 1.17 kPa in rheological experiments with tan(δ) between 0.3 and 0.4 [40]. Therefore, the shear stress attributes of the synthesised ECM scaffolds are comparable with the existing data on the pancreatic tissue.

The production and storage of the scaffold are demonstrated here to have little to no effect on the response to loading, thus confirming the reproducibility of the fabrication method. The double-exponent stress-relaxation model presented here highlights the complexity of the time-dependent viscoelastic behaviour of the material. Thus, the dynamics between the two time constants, where T_2 is significantly less than T_1 and steady state at 88.5% of the initial force suggest pronounced elastic characteristics. The latter implies strong dominance of the solid phase of the material, in line with the rheological observations. Conversely, a single exponent model has been found to be a better fit for the experimental results of human pancreas viscous relaxation in the study of Rubiano *et al.* [41]. As well as this, the relaxation to lower steady state force is often observed over a longer time frame [42]. Thus, despite shear properties closely resembling those of pancreas, the time-transient dynamic of the scaffold falls short of the biological tissue. That said, the available literature on the mechanical properties of pancreatic tissue is scarce and this topic could be further explored.

Raman spectroscopy confirmed the presence of key ECM components in the scaffold. The appearance of amide bands, indicative of peptide bonds, as well as correlation of specific vibrations suggest successful incorporation and cross-linking of HA and type I collagen through amide chemistry. Furthermore, the observed conformational changes of these components within the scaffold may have implications for cell attachment and growth, presenting niches for integrin binding. As well as this, urea cross-links formed between the polysaccharide chains enhance the stability and structural integrity of the scaffold. These findings are consistent with previous studies that have demonstrated the importance of ECM composition in regulating cell behaviour and function [43, 44].

Our metabolic activity experiments involving MIN6 cells demonstrate an initial adaptation phase followed by a more gradual growth phase. During the latter stage, the spatial capacity provided by the pores within the scaffold allows cells to continue proliferating without reaching confluence as quickly as in the 2D culture. This is achieved as a result of the scaffold mimicking the native extracellular matrix more closely and providing a favourable microenvironment for cell growth and survival [45].

‘Pseudoislet’ generation methods with MIN6 cells have been previously employed to improve the insulin secreting function compared to simple monolayer cultures thanks to increased cell-to-cell contact [46-49]. Using our ECM-mimicking scaffold, we demonstrate the formation of multiple MIN6 spheroids in 3D, closer resembling the islets of Langerhans in native tissue. We have shown that MIN6 insulin secretion functionality was maintained over the course of 1 week culture in 3D, consistent with classic culture. Despite the higher proliferation rate and viability, compared to the 2D culture, the total insulin content values, *Ins1* and *Ins2* gene expression were similar in both conditions. Klochendler *et al.* had reported that cell cycle progression in β-cells, isolated from a transgenic mouse model (Ins-rtTA; TET-DTA), was associated with reduced expression of β-cell-specific genes [50]. Similarly, it has been shown by Puri *et al.* that INS-1 cell line had deregulated insulin secretion and production linked genes and showed diminished GSIS as the cells were entering the cell cycle [51]. In addition to this, the studies on human β-cell lines EndoC-βH reported that GSIS efficiency could be improved by removing proliferating properties [52]. Such phenomenon could be explained by partial β-cell de-differentiation observed during high proliferative activity, since both processes (*i.e.* insulin production and cell proliferation) have high energy demand and require to shut down one or the other. In our model, both processes are operating at the same time, suggesting that in 3D, MIN6 cells are capable of maintaining β-cell identity gene levels while proliferating. Further studies are required to better understand this observation.

β-cell survival, differentiation and metabolism have been linked to mechanotransduction mechanisms acting on cell nuclei and mitochondria [53, 54]. Furthermore, MIN6 cells have been shown before to have an increased glucose sensitivity when exposed to lower stiffness biomaterials as opposed to the plastic surface of classic culture. Thus Nyitray *et al.* have reported improved response to glucose stimulation in cells cultured on 0.1kPa scaffolds, by accessing β-catenin signalling pathways [55]. On the other hand, Zhang *et al.* demonstrated increased insulin production and comparable secretion, utilising hydrogels as stiff as 40 and 70 kPa [56]. By targeting the mechanical properties of native tissue we aimed to achieve a significant improvement of function, however this was not observed. Pseudoislet size has also been reported to affect the insulin secreting capabilities of β-cells. For instance, Mendelsohn *et al.* have found that increasing the size of 832/13 insulinoma cell clusters from 40 to 60 and 120 μm had resulted in a dramatic rise of insulin index [57]. In our study, smaller spheroids were more prevalent, which

could negatively impact the contrast in insulin secretion between low and high glucose conditions. We hypothesise, that further fine-tuning the mechanical properties and pore size of our scaffold as well as longer incubation period of MIN6 could positively affect cell survival and maturation, at the same time producing larger clusters and developing higher number of cell-to-cell contacts, which in turn could further improve the insulin secreting function during high glucose exposure.

While the current study demonstrates the potential of the synthesised biomimetic scaffold in improving *in vitro* models of pancreatic islets, there are several limitations and future directions to consider. First, the use of MIN6 cells, while providing a convenient and well-established model as well as decreasing animal experimentation to satisfy the 3Rs initiative (Reduce, Replace, Refine) [58], may not fully recapitulate the behaviour of primary human islets [22]. MIN6 cell line was the most reliable model on our hands, which allowed high experimental throughput thanks to its lower maintenance requirements, compared to other cell lines, such as INS 823/13 or EndoC-BH1. Nonetheless, the immortalised properties and the mouse origin of MIN6 have diminished the translational relevance to human pancreas biology. At the same time, primary human islets availability is highly limited worldwide [59, 60]. Future studies should validate these findings using primary human islets or induced pluripotent stem cells (iPSC) derived β-cells to improve the scaffold's relevance to human biology. iPSC strategies have already demonstrated their potential to be utilised in 3D models of pancreas [17, 61, 62].

Second, the long-term effects of the scaffold on cell viability, function, and differentiation should be investigated. While the current study demonstrates promising results over a 7-day period, longer-term experiments are necessary to evaluate the scaffold's ability to maintain cell function and phenotype over extended periods [18].

Third, the mechanical properties of the scaffold, such as stiffness and stress-relaxation rate, may require further optimisation to more closely mimic the native pancreatic ECM. The incorporation of additional ECM components, such as laminin [14] and heparan sulphate [63], or the modulation of cross-linking density could be explored to fine-tune the scaffold's properties and enhance its biological relevance.

Finally, further *in vitro* studies are necessary to assess the scaffold's performance in a more complex environment. Thanks to its high porosity the scaffold has a potential to be

utilised in a microfluidic organ-on-chip setting with dynamic fluid supply applied across the seeded matrix. Such application has already been demonstrated with a similarly synthesised matrix, mimicking the ECM of liver [64]. Additionally, vascularisation strategies or co-culture experiments with immune cells or adipose tissue could be explored in such setting as an improved model for the tissue function and/or to better understand T1D and T2D physiopathology.

Conclusion

The synthesised biomimetic scaffold presented in this study represents a promising platform for improving *in vitro* models of pancreatic islet studies and β-cell function. Interestingly, the scaffold's viscoelastic properties, porous structure, and incorporation of key ECM components provide a more physiologically relevant environment for MIN6 cell growth and function. The enhanced proliferation and formation of islet-like structures in the scaffold highlight its potential for advancing the understanding of islet biology and facilitating the development of novel cell-based therapies for diabetes. Our findings suggest that the relationship between scaffold properties and cell behaviour is more complex than initially anticipated, highlighting the need for further optimisation of the scaffold design. Future studies should focus on the optimisation of scaffold properties and validation of these findings using human cells to fully realise its potential for drug screening or diagnostic applications.

References

1. American Diabetes Association. Diagnosis and classification of diabetes mellitus. Diabetes Care. 2014; 37 (Supplement_1). https://doi.org/10.2337/dc14-S081
2. Shapiro AJ, Pokrywczynska M, Ricordi C. Clinical pancreatic islet transplantation. Nat Rev Endocrinol. 2017; https://doi.org/10.1038/nrendo.2016.178
3. Kang D, Kim J, Jang J. Advancements in biomaterials and biofabrication for enhancing islet transplantation. Int J Bioprinting. 2023; https://doi.org/10.18063/ijb.v9i6.1024

4. Weir GC, Bonner-Weir S. Islet β cell mass in diabetes and how it relates to function, birth, and death. Ann N Y Acad Sci. 2013; https://doi.org/10.1111/nyas.2013.1281.issue-1
5. Frantz C, Stewart KM, Weaver VM. The extracellular matrix at a glance. J Cell Sci. 2010; https://doi.org/10.1242/jcs.023820
6. Vining KH, Mooney DJ. Mechanical forces direct stem cell behaviour in development and regeneration. Nat Rev Mol Cell Biol. 2017; https://doi.org/10.1038/nrm.2017.108
7. Chaudhuri O, Cooper-White J, Janmey PA, Mooney DJ, Shenoy VB. Effects of extracellular matrix viscoelasticity on cellular behaviour. Nat. 2020; https://doi.org/10.1038/s41586-020-2612-2
8. Lou J, Mooney DJ. Chemical strategies to engineer hydrogels for cell culture. Nat Rev Chem. 2022; https://doi.org/10.1038/s41570-022-00364-4
9. Wu DT, Jeffreys N, Diba M, Mooney DJ. Viscoelastic biomaterials for tissue regeneration. Tissue Eng Part C Methods. 2022; https://doi.org/10.1089/ten.TEC.2021.0386
10. Thivolet CH, Chatelain P, Nicoloso H, Durand A, Bertrand J. Morphological and functional effects of extracellular matrix on pancreatic islet cell cultures. Exp Cell Res. 1985; https://doi.org/10.1016/0014-4827(85)90510-1
11. Llacua LA, Faas MM, de Vos P. Extracellular matrix molecules and their potential contribution to the function of transplanted pancreatic islets. Diabetologia. 2018; https://doi.org/10.1007/s00125-018-4560-8
12. Jiang L, Shen Y, Liu Y, Zhang L, Jiang W. Making human pancreatic islet organoids: progresses on the cell origins, biomaterials and three-dimensional technologies. Theranostics. 2022; https://doi.org/10.7150/thno.59252
13. Guruswamy Damodaran R, Vermette P. Decellularized pancreas as a native extracellular matrix scaffold for pancreatic islet seeding and culture. J Tissue Eng Regen Med. 2018; https://doi.org/10.1002/term.2648
14. Daoud J, Petropavlovskaia M, Rosenberg L, Tabrizian M. The effect of extracellular matrix components on the preservation of human islet function in vitro. Biomater. 2010; https://doi.org/10.1016/j.biomaterials.2009.11.050
15. Nagata N, Gu Y, Hori H, Balamurugan AN, Touma M, Kawakami Y, Wang W, Baba TT, Satake A, Nozawa M, Tabata Y. Evaluation of insulin secretion of isolated rat islets cultured in extracellular matrix. Cell Transplant. 2001; https://doi.org/10.3727/000000001783986678
16. Goh SK, Bertera S, Olsen P, Candiello JE, Halfter W, Uechi G, Balasubramani M, Johnson SA, Sicari BM, Kollar E, Badylak SF. Perfusion-decellularized pancreas as a natural 3D scaffold for pancreatic tissue and whole organ engineering. Biomater. 2013; https://doi.org/10.1016/j.biomaterials.2013.05.065

17. Bi H, Karanth SS, Ye K, Stein R, Jin S. Decellularized tissue matrix enhances self-assembly of islet organoids from pluripotent stem cell differentiation. ACS Biomater Sci Eng. 2020; https://doi.org/10.1021/acsbiomaterials.0c00169
18. Jiang K, Chaimov D, Patel SN, Liang JP, Wiggins SC, Samojlik MM, Rubiano A, Simmons CS, Stabler CL. 3-D physiomimetic extracellular matrix hydrogels provide a supportive microenvironment for rodent and human islet culture. Biomater. 2019; https://doi.org/10.1016/j.biomaterials.2018.03.023
19. Theocharis AD, Skandalis SS, Gialeli C, Karamanos NK. Extracellular matrix structure. Adv Drug Deliv Rev. 2016; https://doi.org/10.1016/j.addr.2015.11.001
20. Plow EF, Haas TA, Zhang L, Loftus J, Smith JW. Ligand binding to integrins. J Biol Chem. 2000; https://doi.org/10.1074/jbc.R000003200
21. Miyazaki JI, Araki K, Yamato E, Ikegami H, Asano T, Shibasaki Y, Oka Y, Yamamura KI. Establishment of a pancreatic β cell line that retains glucose-inducible insulin secretion: special reference to expression of glucose transporter isoforms. Endocrinol. 1990; https://doi.org/10.1210/endo-127-1-126
22. Skelin M, Rupnik M, Cencič A. Pancreatic beta cell lines and their applications in diabetes mellitus research. ALTEX. 2010; https://doi.org/10.14573/altex.2010.2.105
23. Louis F, Pannetier P, Souguir Z, Le Cerf D, Valet P, Vannier JP, Vidal G, Demange E. A biomimetic hydrogel functionalized with adipose ECM components as a microenvironment for the 3D culture of human and murine adipocytes. Biotechnol Bioeng. 2017; https://doi.org/10.1002/bit.26305
24. Ahearne M, Yang Y, El Haj AJ, Then KY, Liu KK. Characterizing the viscoelastic properties of thin hydrogel-based constructs for tissue engineering applications. J R Soc Interface. 2005; https://doi.org/10.1098/rsif.2005.0054
25. Seabold S, Perktold J. Statsmodels: econometric and statistical modeling with Python. SciPy. 2010; https://doi.org/10.25080/Majora-92bf1922-011
26. Virtanen P, Gommers R, Oliphant TE, Haberland M, Reddy T, Cournapeau D, Burovski E, Peterson P, Weckesser W, Bright J, Van Der Walt SJ. SciPy 1.0: fundamental algorithms for scientific computing in Python. Nat Methods. 2020; https://doi.org/10.1038/s41592-019-0686-2
27. Pedregosa F, Varoquaux G, Gramfort A, Michel V, Thirion B, Grisel O, Blondel M, Prettenhofer P, Weiss R, Dubourg V, Vanderplas J. Scikit-learn: Machine learning in Python. J Mach Learn Res. 2011; https://doi.org/10.5555/1953048.2078195
28. Harris CR, Millman KJ, Van Der Walt SJ, Gommers R, Virtanen P, Cournapeau D, Wieser E, Taylor J, Berg S, Smith NJ, Kern R. Array programming with NumPy. Nat. 2020; https://doi.org/10.1038/s41586-020-2649-2

29. McKinney W. Data structures for statistical computing in Python. SciPy. 2010; https://doi.org/10.25080/Majora-92bf1922-00a

30. Hunter JD. Matplotlib: A 2D graphics environment. Comput Sci Eng. 2007; https://doi.org/10.1109/MCSE.2007.55

31. Li CH, Lee CK. Minimum cross entropy thresholding. Pattern Recognit. 1993; https://doi.org/10.1016/0031-3203(93)90115-D

32. Oger F, Bourouh C, Friano ME, Courty E, Rolland L, Gromada X, Moreno M, Carney C, Rabhi N, Durand E, Amanzougarene S. β-cell–specific E2f1 deficiency impairs glucose homeostasis, β-cell identity, and insulin secretion. Diabetes. 2023; https://doi.org/10.2337/db22-0604

33. Efremov YM, Okajima T, Raman A. Measuring viscoelasticity of soft biological samples using atomic force microscopy. Soft Matter. 2020; https://doi.org/10.1039/C9SM02004B

34. McColl IH, Blanch EW, Gill AC, Rhie AG, Ritchie MA, Hecht L, Nielsen K, Barron LD. A new perspective on β-sheet structures using vibrational Raman optical activity: from poly(L-lysine) to the prion protein. J Am Chem Soc. 2003; https://doi.org/10.1021/ja029310d

35. Martinez MG, Bullock AJ, MacNeil S, Rehman IU. Characterisation of structural changes in collagen with Raman spectroscopy. Appl Spectrosc Rev. 2019; https://doi.org/10.1080/05704928.2018.1533085

36. Talari ACS, Movasaghi Z, Rehman S, Rehman IU. Raman spectroscopy of biological tissues. Appl Spectrosc Rev. 2015; https://doi.org/10.1080/05704928.2014.923902

37. Essendoubi M, Gobinet C, Reynaud R, Angiboust JF, Manfait M, Piot O. Human skin penetration of hyaluronic acid of different molecular weights as probed by Raman spectroscopy. Skin Res Technol. 2016; https://doi.org/10.1111/srt.12239

38. Shi Y, Glaser KJ, Venkatesh SK, Ben-Abraham EI, Ehman RL. Feasibility of using 3D MR elastography to determine pancreatic stiffness in healthy volunteers. J Magn Reson Imaging. 2015; https://doi.org/10.1002/jmri.24651

39. Shi Y, Cang L, Zhang X, Cai X, Wang X, Ji R, Wang M, Hong Y. The use of magnetic resonance elastography in differentiating autoimmune pancreatitis from pancreatic ductal adenocarcinoma: a preliminary study. Eur J Radiol. 2018; https://doi.org/10.1016/j.ejrad.2018.09.010

40. Wex C, Fröhlich M, Brandstädter K, Bruns C, Stoll A. Experimental analysis of the mechanical behavior of the viscoelastic porcine pancreas and preliminary case study on the human pancreas. J Mech Behav Biomed Mater. 2015; https://doi.org/10.1016/j.jmbbm.2014.10.014

41. Rubiano A, Delitto D, Han S, Gerber M, Galitz C, Trevino J, Thomas RM, Hughes SJ, Simmons CS. Viscoelastic properties of human pancreatic tumors and in vitro constructs to mimic mechanical properties. Acta Biomater. 2018; https://doi.org/10.1016/j.actbio.2017.11.051

42. Schmuck RB, Lippens E, Wulsten D, Garske DS, Strönisch A, Pratschke J, Sauer IM, Duda GN, Bahra M, Cipitria A. Role of extracellular matrix structural components and tissue mechanics in the development of postoperative pancreatic fistula. J Biomech. 2021; https://doi.org/10.1016/j.jbiomech.2021.110714

43. Rozario T, DeSimone DW. The extracellular matrix in development and morphogenesis: a dynamic view. Dev Biol. 2010; https://doi.org/10.1016/j.ydbio.2009.10.026

44. Khademhosseini A, Langer R. A decade of progress in tissue engineering. Nat Protoc. 2016; https://doi.org/10.1038/nprot.2016.123

45. Pampaloni F, Reynaud EG, Stelzer EH. The third dimension bridges the gap between cell culture and live tissue. Nat Rev Mol Cell Biol. 2007; https://doi.org/10.1038/nrm2236

46. Hauge-Evans AC, Squires PE, Persaud SJ, Jones PM. Pancreatic beta-cell-to-beta-cell interactions are required for integrated responses to nutrient stimuli: enhanced Ca2+ and insulin secretory responses of MIN6 pseudoislets. Diabetes. 1999; https://doi.org/10.2337/diabetes.48.7.1402

47. Chowdhury A, Dyachok O, Tengholm A, Sandler S, Bergsten P. Functional differences between aggregated and dispersed insulin-producing cells. Diabetologia. 2013; https://doi.org/10.1007/s00125-013-2891-4

48. Bae CY, Min MK, Kim H, Park JK. Geometric effect of the hydrogel grid structure on in vitro formation of homogeneous MIN6 cell clusters. Lab Chip. 2014; https://doi.org/10.1039/C4LC00230H

49. Chao X, Zhao F, Hu J, Yu Y, Xie R, Zhong J, Huang M, Zeng T, Yang H, Luo D, Peng W. Comparative study of two common in vitro models for the pancreatic islet with MIN6. Tissue Eng Regen Med. 2023; https://doi.org/10.1007/s13770-022-00406-8

50. Klochendler A, Caspi I, Corem N, Moran M, Friedlich O, Elgavish S, Nevo Y, Helman A, Glaser B, Eden A, Itzkovitz S, Dor Y. The genetic program of pancreatic β-cell replication in vivo. Diabetes. 2016; https://doi.org/10.2337/db16-0003

51. Puri S, Roy N, Russ HA, et al. Replication confers β-cell immaturity. Nat Commun. 2018; https://doi.org/10.1038/s41467-018-02939-0

52. Blanchi B, Taurand M, Colace C, Thomaidou S, Audeoud C, Fantuzzi F, Sawatani T, Gheibi S, Sabadell-Basallote J, Boot FW, Chantier T. EndoC-βH5 cells are storable and ready-to-use human pancreatic beta cells with physiological insulin secretion. Mol Metab. 2023; https://doi.org/10.1016/j.molmet.2023.101772

53. Alessandra G, Algerta M, Paola M, Carsten S, Cristina L, Paolo M, Elisa M, Gabriella T, Carla P. Shaping pancreatic β-cell differentiation and functioning: the influence of mechanotransduction. Cells. 2020; https://doi.org/10.3390/cells9020413

54. Galli A, Maffioli E, Sogne E, Moretti S, Di Cairano ES, Negri A, Nonnis S, Norata GD, Bonacina F, Borghi F, Podestà A. Cluster-assembled zirconia substrates promote long-term differentiation and functioning of human islets of Langerhans. Sci Rep. 2018; https://doi.org/10.1038/s41598-018-28271-4

55. Nyitray CE, Chavez MG, Desai TA. Compliant 3D microenvironment improves β-cell cluster insulin expression through mechanosensing and β-catenin signaling. Tissue Eng Part A. 2014; https://doi.org/10.1089/ten.TEA.2013.0532

56. Zhang M, Yan S, Xu X, Yu T, Guo Z, Ma M, Zhang Y, Gu Z, Feng Y, Du C, Wan M. Three-dimensional cell-culture platform based on hydrogel with tunable microenvironmental properties to improve insulin-secreting function of MIN6 cells. Biomater. 2021; https://doi.org/10.1016/j.biomaterials.2021.120687

57. Mendelsohn AD, Nyitray C, Sena M, Desai TA. Size-controlled insulin-secreting cell clusters. Acta Biomater. 2012; https://doi.org/10.1016/j.actbio.2012.07.033

58. Singh J. The National Centre for the Replacement, Refinement, and Reduction of Animals in Research. J Pharmacol Pharmacother. 2012

59. Gloyn AL, Ibberson M, Marchetti P, Powers AC, Rorsman P, Sander M, Solimena M. Every islet matters: improving the impact of human islet research. Nat Metab. 2022; https://doi.org/10.1038/s42255-022-00607-8

60. Kulkarni RN, Stewart AF. Summary of the Keystone islet workshop (April 2014): the increasing demand for human islet availability in diabetes research. Diabetes. 2014; https://doi.org/10.2337/db14-1303

61. Abazari MF, Soleimanifar F, Aleagha MN, Torabinejad S, Nasiri N, Khamisipour G, Mahabadi JA, Mahboudi H, Enderami SE, Saburi E, Hashemi J. PCL/PVA nanofibrous scaffold improve insulin-producing cells generation from human induced pluripotent stem cells. Gene. 2018; https://doi.org/10.1016/j.gene.2018.05.082

62. Enderami SE, Kehtari M, Abazari MF, Ghoraeian P, Nouri Aleagha M, Soleimanifar F, Soleimani M, Mortazavi Y, Nadri S, Mostafavi H, Askari H. Generation of insulin-producing cells from human induced pluripotent stem cells on PLLA/PVA nanofiber scaffold. Artif Cells, Nanomed and Biotechnol. 2018; https://doi.org/10.1080/21691401.2018.1443466

63. Takahashi I, Noguchi N, Nata K, Yamada S, Kaneiwa T, Mizumoto S, Ikeda T, Sugihara K, Asano M, Yoshikawa T, Yamauchi A. Important role of heparan sulfate in postnatal islet growth and insulin secretion. Biochem and Biophys Res Commun. 2009; https://doi.org/10.1016/j.bbrc.2009.03.140

64. Messelmani T, Le Goff A, Souguir Z, Maes V, Roudaut M, Vandenhaute E, Maubon N, Legallais C, Leclerc E, Jellali R. Development of liver-on-chip integrating a hydroscaffold mimicking the liver's extracellular matrix. Bioeng,. 2022; https://doi.org/10.3390/bioengineering9090443

Supplemental Information

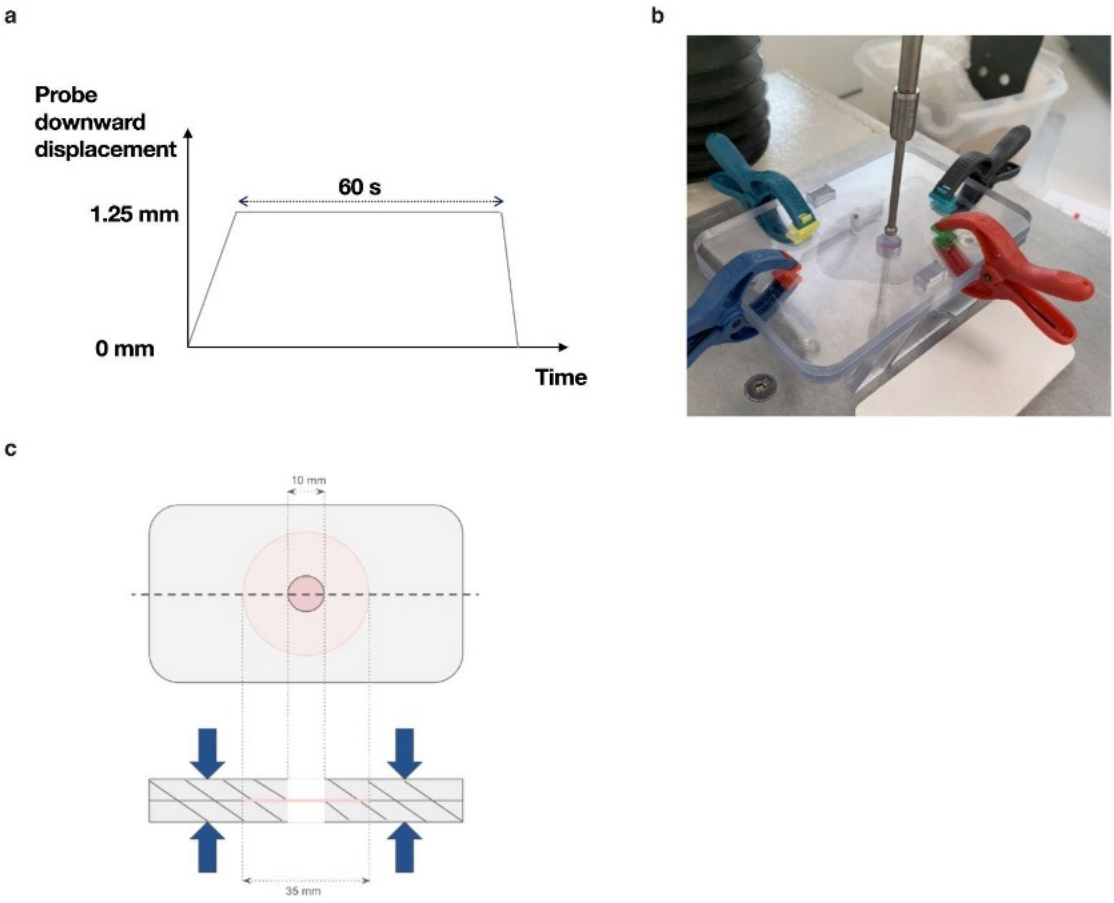

Supplementary Fig. 1 Stress-relaxation experimental set up. The sample was fixed between 2 parallel plates with an exposed opening of 10 mm in diameter (**c**), and pressure was applied with clams. A spherical probe shown in the photograph **b** was used to swiftly apply stress through the opening and sustain it for 60 s (**a**), while the relaxation response of the samples was being recorded.

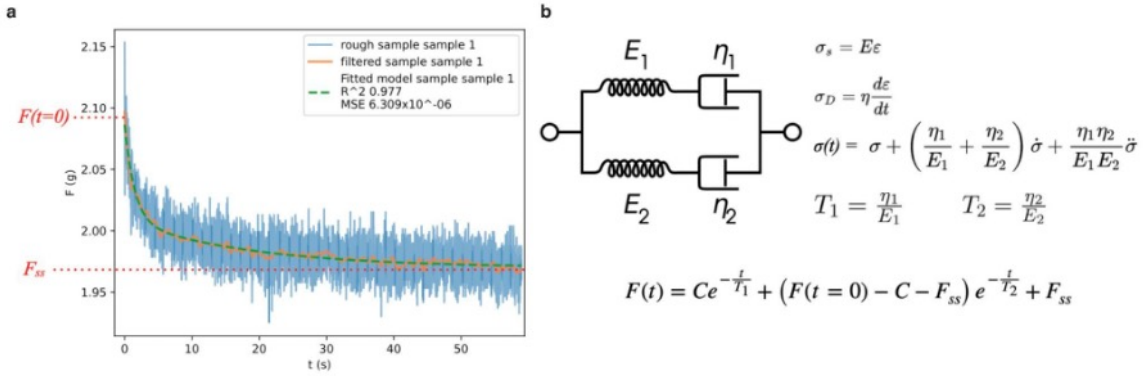

Supplementary Fig. 2 Filtering and fitting of the stress-relaxation curves. The time series data of the force exerted onto the probe by the scaffold (**a**) was first filtered using lowess function to remove the noise. It was then fitted to double exponent model (**b**) referencing the parameters for *F(t=0)* as the initial value and F_{ss} as the steady state value, which was obtained by taking the average of the final 15% of the series. The two-exponent model was based on the solution to a second order differential equation, which described the sterss-train relationship of two spring-dashpot elements connected in parallel. For a spring, the stress was proportionally related to the strain, whereas for a dashpot – to the derivative of the strain. These relationships were defined by the corresponding spring and viscosity coefficients, *E* and *η,* respectively. The ratio of the latter gave rise to the corresponding time constants T_1 and T_2 for each of the parallel element series. These time constants were discovered during the non-linear least squares fitting process for each sample and were used to infer the speed of its relaxation. It should be noted that this representation is merely a lump model and it does not provide a direct interpretation of the particular properties of the molecules in the scaffold's composition. On the other hand, it was found to be a useful tool in describing the complex viscoelastic behaviour of the biomaterial as a commonly employed technique.

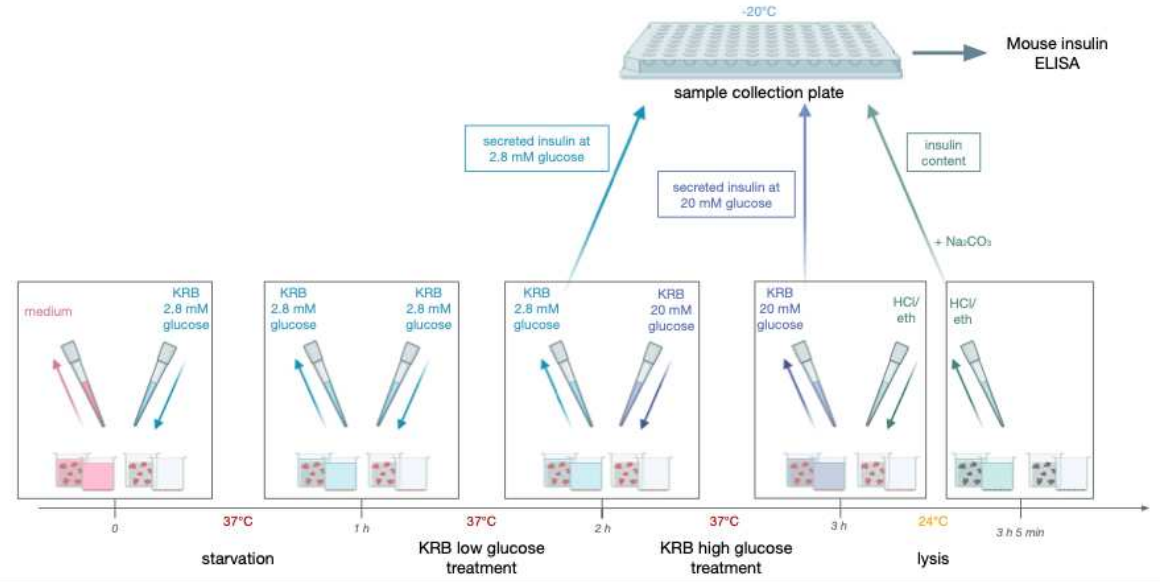

Supplementary Fig. 3 Process diagram of GSIS protocol. 2D 96-well plates and 3D scaffold-containing 96-well plates were used, seeded with MIN6 cells. First, cell culture medium was removed from the wells and replaced with KRB low glucose (2.8 mM) solution. The plates were incubated for 1 hour at 37°C with a CO_2 concentration of 5%. Next, the liquid was completely replaced with KRB low glucose solution and the plates were incubated for 1 hour during the low glucose treatment. The supernatant then was sampled to a separate sampling plate kept at -20°C. After this, KRB low glucose (20 mM) solution was added to each well and the cell-seeded plates were incubated for high glucose treatment. The supernatant was then collected to the sampling plate and HCl/ ethanol solution was applied to each well for 5 minutes at room temperature to lyse the cells. The supernatant was then collected to the sampling plate and mixed with neutralisation solution of Na_2CO_3. The sampling plate was preserved at -20°C until the secreted insulin was quantified using mouse insulin ELISA kit.

Gene Name	Gene symbol	Species	Primer
Cyclophilin	Cyclo	Mouse	ATGGCACTGGCGGCAGGTCC
			TTGCCATTCCTGGACCCAAA
Insulin1	Ins1	Mouse	GCCAAACAGCAAAGTCCAGG
			GTTGAAACAATGACCTGCTTGC
Insulin2	Ins2	Mouse	CAGCAAGCAGGAAGCCTATCT
			CAGGTGGGAACCACAAAGGT
Solute carrier family 2 (facilitated glucose transporter)	Slc2a2	Mouse	GTGACATCCTCAGTTCCTCTTAG
			GTCCAGAAAGCCCCAGATACC
Proprotein convertase subtilisin/kexin type1	Pcsk1	Mouse	TGATGATCGTGTGACGTGGG
			GGCAGAGCTGCAGTCATTCT
Glucagon-like peptide 1 receptor	Glp1r	Mouse	GTTTCCTCACGGAAGCGCCA
			AAGGAACCTGGGGGCCCATC
Urocortin 3	Ucn3	Mouse	TGATGCCCACCTACTTCCTG
			CTGTGTTGAGGCAGCTGAAG
Pancreatic and duodenal homebox 1	Pdx1	Mouse	CCCCAGTTTACAAGCTCGCT
			CTCGGTTCCATTCGGGAAAGG
v-maf musculoaponeurotic fibrosarcoma oncogene family, protein A	MafA	Mouse	CCTGTAGAGGAAGCCGAGGAA
			CCTCCCCCAGTCGAGTATAGC
Homebox protein Nkx6.1	Nkx6.1	Mouse	TCAGGTCAAGGTCTGGTTCC
			GTCTCCGAGTCCTGCTTCTT
Glucagon	Gcg	Mouse	AGGCCGAGGAAGGCGAGACT
			GGAGCCATCAGCGTGCCTGC
Somatostatin	Sst	Mouse	TCCGTCAGTTTCTGCAGAAGTCTC
			GTACTTGGCCAGTTCCTGTTTCCC

Supplementary Table 1 List of primers used for qRT-PCR analysis.

Appendix 2

Python code for stress-relaxation data processing.

```
'''
B********S(R) Stress relaxation experiment

A stress relaxation experiment was performed using a texture
analyser 'Stable Micro Systems' with a 500 g sensor and a
spherical 5 mm probe on the 12 well plate samples held between
2 plated with 8 mm opening for the probe. The aim of the
experiment was to evaluate the transient response of the
viscoelastic samples to the continuously applied constant load,
also referred to as stress-relaxation curve.

The plots of the stress response are produced in this script.
The section of data is used starting from peak value and ending
at the t=t_peak+59s (steady state observed). Sampling rate is
0.005 s.

The data is then fitted to a double exponent model representing
the 2nd order Maxwell model, expressed as the Prony series:

F(t)=C1e^-t/T1 + (F(t=0)-F(t=59)-C1)e^-t/T2 + F(t=59)


'''

import numpy as np
import matplotlib.pyplot as plt
import pandas as pd
import statsmodels.api as sm
import os.path
from scipy.optimize import curve_fit
from sklearn.metrics import r2_score
from scipy.stats import shapiro, kstest, probplot


#Example sheet_name='sample 4'

#Define the model (double exponent in this case)
def secondmodel(t,F_1,T_1,F_0,F_f,T_2):
    return F_1*np.exp(-t/T_1) + (F_0-F_f-F_1)*np.exp(-t/T_2) + F_f


def transient_fit(filename,sheet_name, usecols, filtered):

    datapath=os.path.abspath(filename)
    data=pd.read_excel(datapath, sheet_name=sheet_name, skiprows=2,
usecols=usecols, names=['F','t'])


#=============================================================================
    #Identifying the region of interest and resetting the time

    t_sampling=0.005

    #Start at the maximum force value
    starting_index=data['F'].idxmax()

    #Finish after 59 seconds since the maximum force reading, assuming the
steady state is reached at this timepoint
    finishing_index = int(59/t_sampling + starting_index+1)

    #Cutoff the unwanted regions
```

```
    segment_of_interest=
data.loc[starting_index:finishing_index].reset_index(drop=True)

    #Reset the time
    segment_of_interest['t']=segment_of_interest['t']-
segment_of_interest['t'].iloc[0]


#=============================================================================
    # Fit the data to a double exponential model

    #Select the data for fitting
    if filtered==False:

        xdata=np.array(segment_of_interest['t'])
        ydata=np.array(segment_of_interest['F'])

        plotlabel='rough'

    else:

        lowess = sm.nonparametric.lowess
        #Set an appropriate fraction
        f=70
        #Apply smoothing
        smoothoperator=lowess(segment_of_interest['F'],segment_of_interest['t'],
frac=1/f)

        xdata=np.array(smoothoperator[:,0])
        ydata=np.array(smoothoperator[:,1])

        plotlabel='filtered'

    #Specify parameter bounds: for the initial value +- 1% of the max, for the
steady state value +- 1% of the final 15% of the series and for the T - chose
appropriate
    F_0_min=0.99*np.max(ydata)
    F_0_max=1.01*np.max(ydata)

    F_f_min=0.99*np.mean(ydata[int(0.85*len(ydata)):])
    F_f_max=1.01*np.mean(ydata[int(0.85*len(ydata)):])

    F_1_min=-np.inf
    F_1_max=np.inf

    T_1_min=10
    T_1_max=60

    T_2_min=0.1
    T_2_max=3

    bounds=([F_1_min, T_1_min, F_0_min, F_f_min, T_2_min], [F_1_max, T_1_max,
F_0_max, F_f_max, T_2_max])

    #Generate the fit
    popt, pcov = curve_fit(secondmodel, xdata, ydata , bounds=bounds)
    popt
    model=secondmodel(xdata,*popt)


    #Determine the R^2 value of the model
    r2 = r2_score(ydata, model)

    #Do residual analysis: Mean square error, Shapiro-Wilk test and Kologomorov-
Smirnov test for normality
    residuals = ydata - model

    mse = np.mean(residuals**2)
```

```
    sw, sw_p_value = shapiro(residuals)

    ks, ks_p_value = kstest(residuals, 'norm')



    fig = plt.figure(2)

    # Plot the fitted model and rough data
    #plt.subplot(121)
    plt.plot(segment_of_interest['t'],segment_of_interest['F'], '-', alpha=0.6,
label='rough'+' sample '+sheet_name)
    plt.plot(xdata,ydata, '-', alpha=0.8, lw=2, label=plotlabel+' sample
'+sheet_name)
    plt.plot(xdata,model, '--', lw=2, label='Fitted model'+' sample
'+sheet_name+'\nR^2 '+str(format(r2,'.3f'))+'\nMSE
'+str(format(mse,'.3e').replace('e', 'x10^')))
    plt.xlim(-1.5,80)
    plt.xlabel('t (s)')
    plt.ylabel('F (g)')
    plt.title('Fitted models')
    plt.legend()

    # Plot Q-Q plot to assess the normality of the model residuals
    #plt.subplot(122)
    #probplot(residuals, plot=plt)


#=============================================================================
    # Normalise the data and model around the max values

    data_norm=ydata/np.max(ydata)
    model_norm=model/np.max(ydata)

    tc1=format(popt[1],'.2f')
    tc2=format(popt[4],'.2f')
    ffn=format(popt[3]/np.max(ydata),'.2f')
    f1n=format(popt[0]/np.max(ydata),'.2f')

    yrough=segment_of_interest['F']
    ysmooth=np.array(smoothoperator[:,1])


    return yrough, ysmooth, model_norm, xdata, tc1, tc2, data_norm, model, ffn,
r2, mse, sw_p_value, ks_p_value, f1n



#=============================================================================
# %% Plot several data

def batchplot(filename,samplerange,reps):
    #filename example: 'texture analyser bma 6wp 18_01_24.xls'
    #samplerange example: [1,2,3,4,5,6]
    #reps example: [3,5]

    fig, (td) = plt.subplots(1, 1)
    fig.set_size_inches(12, 10)

    Normalised_ydata={}
    Parameters={}

    for sample in samplerange:
        sheet_name='sample '+str(sample)

        if sample in reps:
```

```
            usecols=[3,5]
        else:
            usecols=[0,2]

        #if sample==4:
        #    filtered=True
        #else:
        #    filtered=False

        filtered=True
        #filtered=False

        yrough, ysmooth, sample_responce_fit, sample_time, tc1, tc2, data_norm,
model, ffn, r2, mse, sw_p_value, ks_p_value, f1n = transient_fit(filename,
sheet_name, usecols, filtered)
        td.plot(sample_time, sample_responce_fit, color='C'+str(sample+5), label
= 'Sample '+str(sample)+' time constants '+str(tc1)+', '+str(tc2))

        print(sample, tc1, tc2, ffn, r2, mse)


        #Store y-values
        Normalised_ydata['Sample' +str(sample)]=sample_responce_fit

        #Store parameters
        Parameters['Sample' +str(sample)] = [f1n,tc1,1,ffn,tc2]


    Normalised_ydata=pd.DataFrame(Normalised_ydata)

    Normalised_ydata['mean'] = Normalised_ydata.mean(axis=1)
    Normalised_ydata['std'] = Normalised_ydata.std(axis=1)



    Parameters=pd.DataFrame(Parameters)
    Parameters=Parameters.astype(float)

    Parameters['mean'] = Parameters.mean(axis=1)
    Parameters['std'] = Parameters.std(axis=1)



    td.set_xlabel('Time, s)')
    td.set_ylabel('Normalised force, au')
    td.set_title('Time domain (normalised)')
    td.legend()


    return Normalised_ydata['mean'], Normalised_ydata['std'], sample_time,
Parameters['mean'], Parameters['std']
```

Appendix 3

Optimal MIN6 seeding density determination.

As the primary step, optimal seeding density was determined in a 7-day-long study featuring 2D and 3D (on BM hydroscaffold) cell cultures in static condition on 96 well plate. The seeding densities for the two conditions were ranging from 1 thousand to 1 million cells per well. The procedure involved culture for 4 days followed by live/dead nuclei staining (hoechst blue/draq7 red) and confocal imaging performed from day 4 to day 7. Cell culture media was changed every 3 days. The 3D images were obtained by taking a z-stack of 15-20 images focused at a range of equally spaced planes across the z-axis. Afterwards a single 2D-projection image was compiled from the stack, based on the maximum intensity of the pixels for each x-y coordinate, thus producing a pseudo-3D image. Initially, digital image processing and Computer Vision methods were applied using Python programming language to evaluate the observed cell density - provided below. Despite being mostly satisfactory, the algorithm needs further work, since some contradictory results were obtained due to the procedural errors in experiment conduction and image collection. Therefore, visual assessment of the images was preferred. It was decided to opt for the lower seeding densities in the range of 10-50 thousand cells per well for the long-term experiments and higher densities of 50-200 thousand cells per well for the short term experiments.

An automated image processing method was implemented using OpenCV library in Python programming language for the images taken during MIN6 cell density experiment on 2D and 3D. Blue channel was used representing the nuclei of live MIN6 cells. The images were partitioned into the segments corresponding to cells the percentage density was estimated as the ratio between area covered by these segments and the total image space area. Although it should be noted that the area is ambiguous in the case of two-dimensional projection of the z-stack images of 3D scaffolds. The following techniques have been applied:

- thresholding;
- dilation;
- distance transform;
- subtraction (background from foreground)
- connected components;
- watershed segmentation.

Below is the demonstration of the computer vision. Images from left to right: orginal, segmented and overlay. Top 3 are sourced from 2D cell culture image taken on day 5 after initial seeding density 10k cells per well. Bottom 3 - 2D projection of z-stack images of 3D culture in BM, taken on day 4, initially seeded with 200k cells.

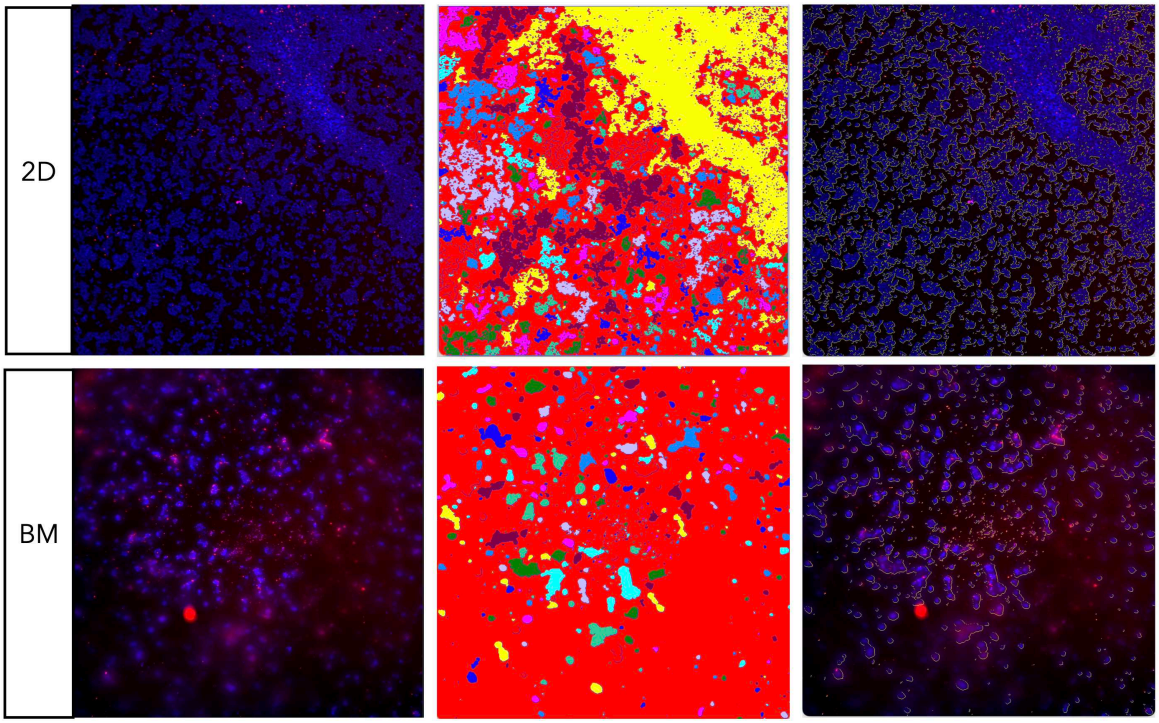

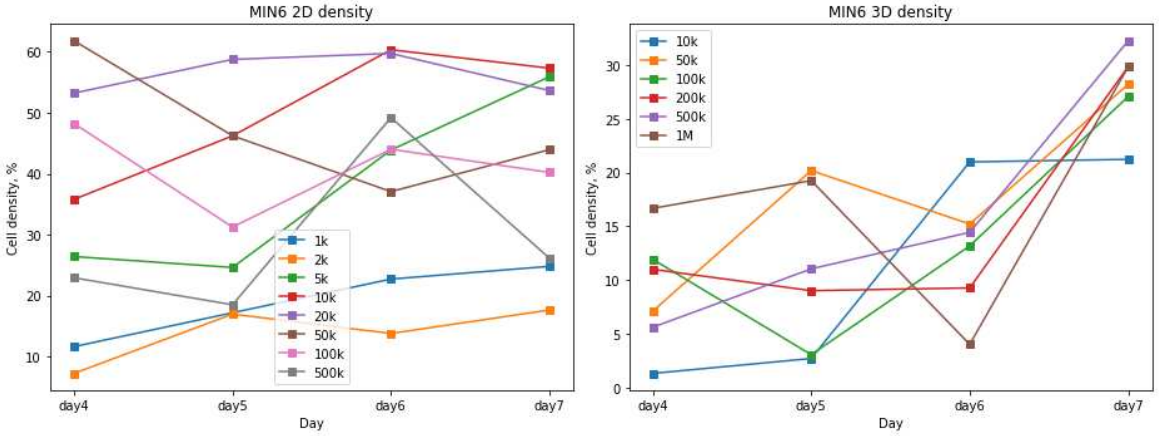

Area estimation summarised in the plots above is rather inconclusive for most of the samples, especially in 2D. Evidently, the efficiency of the algorithm was limited by the image quality, affected by the factors including: artefacts, bubbles, overexposure, intensity imbalance, poor focus, cell culture contamination, distribution of cells across the area of the well not visible in the field of view, etc. In future more work could be dedicated to experiment design, pre-processing of images and improving the algorithm, however, it is not the scope of this thesis.

Automated image processing Python code

```
"""
Cell density analysis

In the cell density experiment 2D and 3D cell cultures were prepared by seeding
MIN6 cells onto a 2D well plate at 8 different cell concentrations and also
onto a 3D B********S(R) hydroscaffold plate at 6 different concentrations.

    2D (cells per well):
        1k 2k 5k 10k 20k 50k 100k 500k

    3D (cells per well):
        10k 50k 100k 200k 500k 1M

Fluorescent imaging was performed for 4 days starting from Day 4 with Hoechst
staining on the blue channel to determine the cell nuclei of the live cells,
and with draq7 on the red channel to determine the dead cells. 2D images were
collected using fluorescent microscopy, and 3D images - using confocal
fluorescence microscopy. For 3D imaging a z-stack of 15-20 images taken at
different focal planes along the z-axis spaced by approximately 20 um to
capture the cells that have proliferated into the hydroscaffold. The stack
images were then combined into a single 2D projection image.

Percentage cell density is worked out as the ratio between the high-intensity
blue channel pixels indicating the cells to the total area of the image.

Some of the code related to image processing was borrowed from Sreenivas
Bhattiprolu, "Python for Microscopists":
https://github.com/bnsreenu/python_for_microscopists/blob/master/033-
grain_size_analysis_using_wateshed_segmentation.py

"""

import pandas as pd
import numpy as np
import matplotlib.pyplot as plt

import os.path
import cv2
from scipy import ndimage
from skimage import measure, color, io


def celldensity(datapath,pixel_to_um=1.7, show=True):

    img=cv2.imread(datapath)

#pixel_to_um=1.7

    #Take the blue channel
    dapi=img[:,:,0]

    #Threshold image to binary using OTSU. ALl thresholded pixels will be set to
255
    ret1, thresh=cv2.threshold(dapi, 0, 255, cv2.THRESH_BINARY+cv2.THRESH_OTSU)

    #Create a working kernel matrix
    kernel3 = np.ones((3,3),np.uint8)
    kernel2 = np.ones((2,2),np.uint8)

    #Define a background around the cells that is definitely not cells by using
the function 'dilate'
    sure_bg = cv2.dilate(thresh,kernel2,iterations=1)

    #Apply distance transform method to the foreground.
    dist_transform = cv2.distanceTransform(thresh,cv2.DIST_L2,3)
```

```
    #Threshold the distance transform
    ret2, sure_fg =
cv2.threshold(dist_transform,0.01*dist_transform.max(),255,0)

    #The unknown region is the difference between sure background and sure
foreground
    sure_fg = np.uint8(sure_fg)
    unknown = cv2.subtract(sure_bg,sure_fg)

    #Perform connected components algorithm without the border
    ret3, markers = cv2.connectedComponents(sure_fg)
    markers = markers+10
    markers[unknown==255] = 0
    #plt.imshow(markers, cmap='jet')

    #Perform the watershed to find the boundaries and color them yellow,
excluding the borders of the image
    markers = cv2.watershed(img,markers)
    for i in range(1,len(img)-1):
        for j in range(1,len(img)-1):
            if markers[i,j]==-1:
                img[i,j]=[0,255,255]

        #img[markers == -1] = [0,255,255]

    #Produce an image with marked cells
    img1 = color.label2rgb(markers, bg_label=0)

    #Extracting the properties of detected cells
    regions = measure.regionprops(markers, intensity_image=dapi)

    #For cell density estimation, area is imortant
    Areas=[]
    for prop in regions:
        Areas.append(prop.area)
    #Remove the background area
    Areas.pop(0)

    Total_area=float(len(img)**2)
    Cells_area=float(sum(Areas))

    density_percent=100*Cells_area/Total_area

    #Show the original image and the colored cells that were found
    if show==True:
        cv2.destroyAllWindows()
        cv2.imshow('Overlay on original image', img)
        cv2.imshow('Colored Grains', img1)
        cv2.waitKey(1000)

    return density_percent

#print('\nCell density =',round(density,2),'%')


#%%
#Display the image
cv2.destroyAllWindows()
cv2.imshow('Overlay on original image', img)
cv2.imshow('Colored Grains', img1)
cv2.waitKey(0)

#%%
#Insert here the path to the image folder
common=''

#Create results table
Cond=['2D','3D','3D_wb']
```

```
Day=['day4','day5','day6','day7']
Cell_conc=['1k', '2k', '5k', '10k', '20k', '50k', '100k', '200k','500k', '1M']

Results={'Condition':[], 'Day':[], 'Cell concentration':[], 'Density':[]}

for cond in Cond:
    for day in Day:
        for conc in Cell_conc:
            if (cond=='2D' and (conc=='200k' or conc=='1M')) or ((cond=='3D' or
cond=='3D_wb') and (conc=='1k' or conc=='2k' or conc== '5k' or conc=='20k')) or
(cond=='3D_wb' and day!='day7'):
                continue
            datapath=common+cond+'_'+day+'_'+conc+'.tif'
            density=celldensity(datapath,pixel_to_um=1.7, show=True)
            Results['Condition'].append(cond)
            Results['Day'].append(day)
            Results['Cell concentration'].append(conc)
            Results['Density'].append(density)
            #print (cond,day,conc,density,'%')

Results_df=pd.DataFrame(Results)
#%%

#Plot the density results for the specified condition
plt.figure()
plt.plot(np.arange(len(Day)),Results_df['Density']
[(Results_df['Condition']=='2D')&(Results_df['Cell concentration']=='1k')])
plt.xticks(np.arange(len(Day)),labels=Day)
```

Appendix 4

Q-P experiment Python code

```
'''
Experiment to determine the pressure-flow relationship in the microfluidic
system, containing pressure generator Fluigent™ Flow EZ, a microfluidic set-up
and Flow Unit sensor.

The pressure range for this experiment is [0,200] mbar and the step is 1 mbar.
The time step is 10 sec. A set pressure is applied and then given 5 seconds
for pressure to settle. Then measurements of pressure and flow are taken for
5 seconds.
'''

import pandas as pd
import numpy as np
import matplotlib.pyplot as plt
import time
from datetime import date

from Fluigent.SDK import fgt_init, fgt_close
from Fluigent.SDK import fgt_set_pressure, fgt_get_pressure, fgt_get_sensorValue



#%% The experiment

#initialise the session with Fluigent

fgt_init()

#set the ranges and experimental parameters

P_min=0

P_max=999

P_step=1

t_halfstep=5

t_sampling=0.1



number_of_measurements=(P_max-P_min)/P_step + 1

number_of_repeats_per_measurement=(t_halfstep/t_sampling)

number_of_datapoints=number_of_repeats_per_measurement*number_of_measurements



pressure_measured=[]

flow_measured=[]

volume_utilised=0

#each measurement is an iteration of the while loop
```

```
P_in=P_min

while P_in<=P_max:
    #first check there is enough liquid
    if volume_utilised >= 10000:
        #pause the experiment and set pressure to 0 untill the required volume
is restored
        fgt_set_pressure(0, 0)
        input('\nLow liquid volume. Pour more liquid and press Enter to
continue...')
        volume_utilised=0
    else:
        pass

    #Set the pressure to a new value
    fgt_set_pressure(0,P_in)
    #allow the pressure to settle
    time.sleep(t_halfstep)
    #take the measuremets over the course of 5 seconds at the sampling frequency
    for t in range (int(number_of_repeats_per_measurement)):
        pressure_measured.append(fgt_get_pressure(0))
        flow_measured.append(fgt_get_sensorValue(0))
        time.sleep(t_sampling)
    #add the used volume as mean flow * time passed
    volume_utilised +=
2*t_halfstep*np.mean(flow_measured[int(number_of_repeats_per_measurement*(P_in-1
)):int(number_of_repeats_per_measurement*P_in)])
    #define the next input pressure
    P_in += P_step


#At the end of the experiment, set the presure to zero and finish the session

fgt_set_pressure(0, 0)
fgt_close()


#save the data

dict = {'P':pressure_measured, 'Q':flow_measured}

df=pd.DataFrame(dict)

today=date.today()
```

```
date_of_experiment = today.strftime('%d_%b_%Y')

filename='pressure_flow_'+ date_of_experiment +'.csv'

df.to_csv(filename)

#%% Data visualisation

#plot a scatterplot

threshold=int(number_of_repeats_per_measurement*224)
cutoff=int(number_of_repeats_per_measurement*1)

plt.figure()
plt.scatter(flow_measured[:threshold],pressure_measured[:threshold],s=0.1)
plt.xlabel('Measured flow Q, ul/min')
plt.ylabel('Measured pressure P, mbar')

x=[]
y=[]
for n in range (600):
    x.append(n)
    y.append(0.33*n)

plt.plot(x,y,'r')
```

Q-P regression code

```
"""
Fluigent™ Pressure - Flow experiment data processing.
The aim of this experiment was to determine the pressure-flow relationship.
This will be done by fitting a polynomial regression model to the obtained
dataset.

"""
import pandas as pd
import numpy as np
import matplotlib.pyplot as plt

#Enter file name
dataset = pd.read_csv('empty_chip_pressure_flow_12_Jul_2022.csv')


#Extract the data
P= dataset.P[:]
Q= dataset.Q[:]

P=P[:,np.newaxis]
Q=Q[:,np.newaxis]

#%%
#Make a scatter plot of the measured values
plt.figure()
plt.scatter(Q,P,s=0.1)
plt.xlabel('Measured flow Q, ul/min')
plt.ylabel('Measured pressure P, mbar')


#%%
#Split the data into training and testing sets, 80:20

from sklearn.model_selection import train_test_split
Q_train, Q_test, P_train, P_test =
train_test_split(Q,P,test_size=0.2,random_state=0)



#%%
#Use a 2nd degree polynomial model
from sklearn.preprocessing import PolynomialFeatures
poly = PolynomialFeatures(degree=2)
x_poly= poly.fit_transform(Q_train)


#%%
#Fit the data to the model
from sklearn.linear_model import LinearRegression
reg=LinearRegression()

reg.fit(x_poly,P_train)

y_pred=reg.predict(x_poly)

#%%
#Display the model equation
print ('The model equation: \nP = ',str(reg.intercept_[0]),' +
',str(reg.coef_[0,1])+'*Q + ',str(reg.coef_[0,2])+'*Q^2')


#%%
#Plot the regression

import operator
```

```
sort_axis = operator.itemgetter(0)
sorted_zip = sorted(zip(Q_train,y_pred), key=sort_axis)
Q_train, y_pred = zip(*sorted_zip)

#%%
plt.figure()
plt.scatter(Q, P, color = 'blue', s=0.1, label='Measured values')
plt.plot(Q_train, y_pred, color = 'red', linewidth=2, markersize=2,
label='Linear polynomial model')
plt.xlabel('Flow Q, ul/min')
plt.ylabel('Pressure P, mbar')
plt.legend(loc='lower right')
plt.show()
```

Digital PID control Python code

```
'''
PID control of setting the flowrate to a certain value via adjusting pressure.
'''

import pandas as pd
import numpy as np
import matplotlib.pyplot as plt
import time

from Fluigent.SDK import fgt_init, fgt_close
from Fluigent.SDK import fgt_set_pressure, fgt_get_pressure, fgt_get_sensorValue


#%% The experiment

#initialise the session with Fluigent

fgt_init()

LineUP = LineUPClassicalSessionFactory().Create(0)

#set the ranges and experimental parameters

Q_d = 10

t_step=20

t_sampling=0.1

pressure_measured=[]

flow_measured=[]

timepoint=[]

volume_utilised=0

time_passed=0

Kp=1

Ki=1

Kd=1

Error_Q = []

E=0
Input_Q=[]

Q_in = 0

#take the measuremets over the course of 10 seconds at the sampling frequency

while time_passed<= t_step:

    #Perform measurements

    pressure_measured.append(fgt_get_pressure(0))

    flow_measured.append(fgt_get_sensorValue(0))

    Error_Q.append(Q_d-fgt_get_sensorValue(0))

    Input_Q.append(Q_in)
```

```
    timepoint.append(time_passed)

    time_passed += t_sampling

    #Adjust the input according to PID

    E=Error_Q[len(Error_Q)-1]

    Q_in = Kp*E + Ki*t_sampling*np.sum(Error_Q) +
Kd*(flow_measured[len(flow_measured)-1] - flow_measured[len(flow_measured)-2])/
t_sampling

    #add the used volume as measured flow * measurement time

    volume_utilised += t_sampling*flow_measured[len(flow_measured)-1]

    time.sleep(t_sampling)

    #Set the flow to the imput value

    LineUP.SetFlowrate(0, Q_in)

#At the end of the experiment, set the presure to zero and finish the session

fgt_set_pressure(0, 0)
fgt_close()
```

GSIS perfusion experiment automation Python code

```
'''
Experiment to determine the dependance of insulin secretion on the glucose
concentration in media/buffer.

The protocol includes passing different solutions through the microfluidic
device with seeded islets in the following order:

    1) KRB Low glucose 30 min
    2) KRB High glucose 60 min
    3) KRB Low glucose 30 min

The flowrate is 10 ul/min. The collection of samples is done every 2 mins onto
the 96 well plate to then be taken for ELISA.

The pressure for this experiment is ___ mbar and is determined from
p-q experiment preseeding this and in accordance with the total volume of the
system.
'''

import winsound as ws
import pandas as pd
import numpy as np
import matplotlib.pyplot as plt
import time
from datetime import date

from Fluigent.SDK import fgt_init, fgt_close
from Fluigent.SDK import fgt_set_pressure


#%% The experiment

#Set pressure to the desired value
P_in= 42

Step_duration = [30*60, 60*60, 30*60]
Message = ['\nChange the tube for KRB High Glucose and press Enter to
continue...\n',
           '\nChange the tube for KRB Low Glucose and press Enter to continue...
\n',
           '\nPress Enter to finish\n',]

#initialise the session with Fluigent

fgt_init()

for i in range(len(Step_duration)):

    #set the pressure to the desired value for the desired flow

    fgt_set_pressure(0, P_in)

    #no sample collection during the first and last step

    if i ==-1 or i == 4:

        time.sleep(Step_duration[i])

    #The sample is collected during the Steps 2)-4)

    else:

        time_end= time.time()+Step_duration[i]

        while time.time() < time_end:
```

```
            print('\nCollect now')
            ws.Beep(600,986)
            time.sleep(59)
            print('\nStop collecting\n')
            time.sleep(60)

    fgt_set_pressure(0, 0)

    #change the tube with the solution
    input(Message[i])

#At the end of the experiment, set the presure to zero and finish the session

fgt_set_pressure(0, 0)
fgt_close()
```

Appendix 5

Microelectrode array mask

Top view

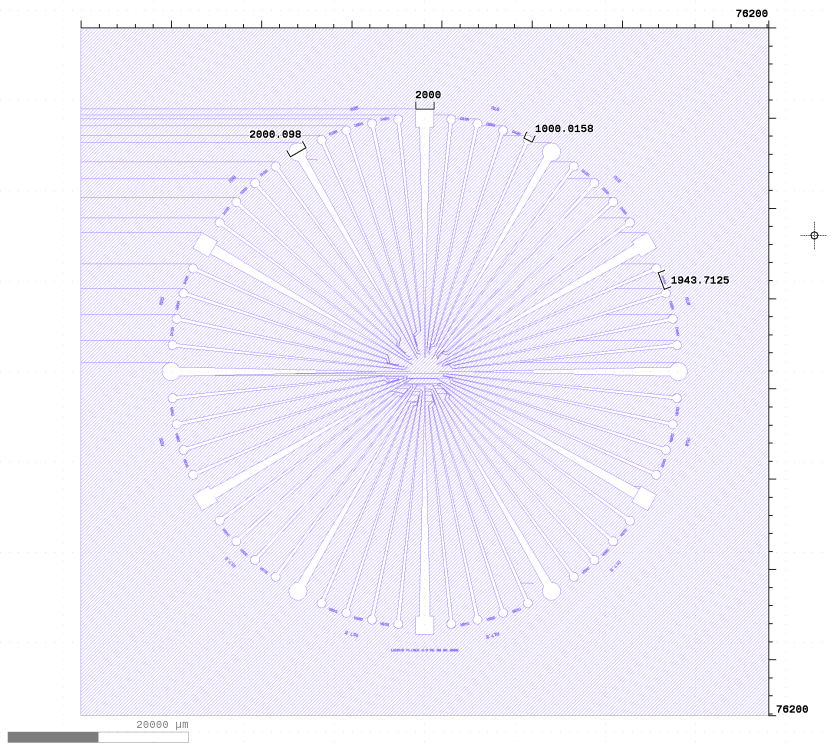

Zoom in

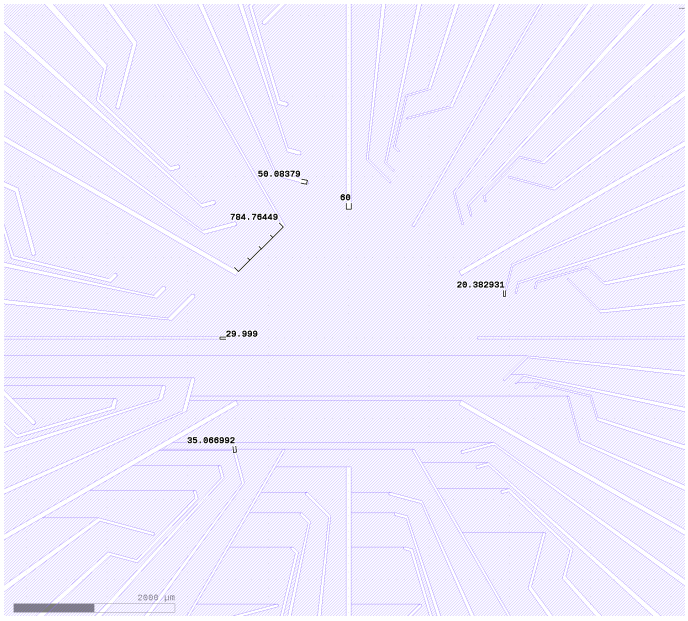

Insulation layer mask

Top view

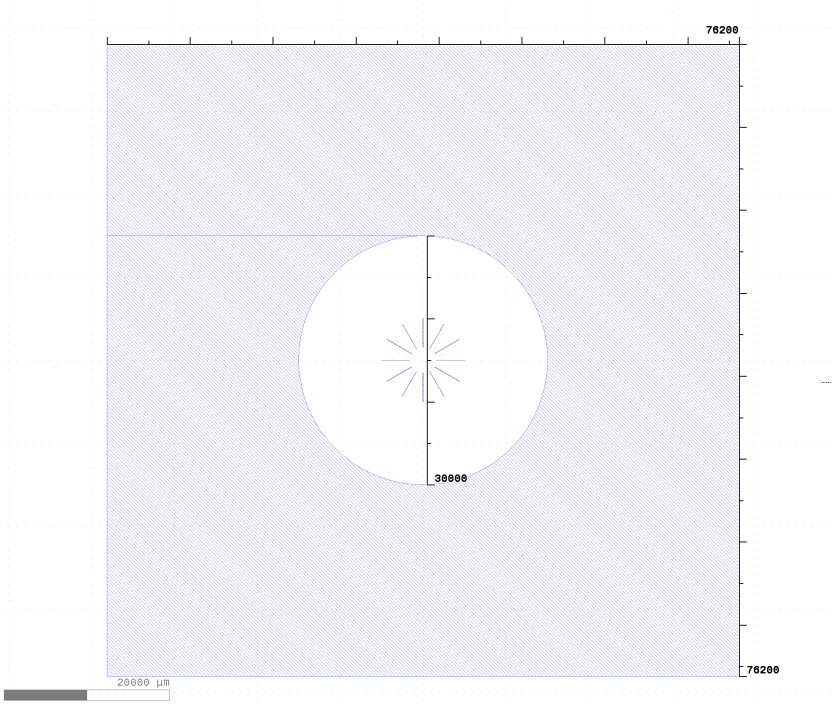

Zoom in